Tuning the Mechanical and Thermal Responses of Emissive β-Diketones: Modification of Electronic and Molecular Packing Effects.

Tristan Phillips Butler
Cheney, Washington

M.S., Western Washington University, 2012

A Dissertation presented to the Graduate Faculty
of the University of Virginia in Candidacy for the
Degree of Doctor of Philosophy

Department of Chemistry

University of Virginia
April, 2017

Abstract

New stimuli responsive luminescent materials are incorporated into emerging technologies such as optical memory storage devices and force sensors. In particular, difluoroboron coordinated β-diketones (BF$_2$bdk), which are easily synthesized from commercially available starting materials, exhibit impressive solid-state optical properties and show emission changes in response to thermal and mechanical perturbations. In some cases, mechanically responsive BF$_2$bdk dyes even self-erase at room temperature, a rare property in other materials. Prior studies with BF$_2$bdk dyes explored halide and alkyl chain substituent effects on mechanoresponsive properties, however, clear design strategies for tuning optical properties had yet to be elucidated.

While exploring methods for modulating the properties of BF$_2$bdk materials, it was discovered that boron-free β-diketones (bdk) also possess thermally and mechanically responsive emission. Substitution of bdk dyes with donor and acceptor groups resulted in tunable emission wavelengths. In combination with BF$_2$ coordination, a series of mechano-responsive dyes were synthesized that encompassed the entire visible spectrum. Additionally, rapid self-erasure was observed for a trimethoxy-substituted bdk derivative, which was used to evaluate processing effects (i.e. substrate and film thickness) on smeared state recovery. Diketone dyes incorporating donor-acceptor motifs also exhibited stable supercooled liquid phases upon cooling after melting. In some cases, shear-induced crystallization was observed, a new property for this class of dyes. Given rich thermal and mechanical properties, responsive bdk and BF$_2$bdk materials show great promise for practical applications.

Table of Contents

Chapter 1: Introduction to Luminescence and Mechanochromic Luminescent Materials Design

Chapter 2: Mechanochromic Luminescence and Aggregation Induced Emission in Metal-Free β-Diketones

Chapter 3: Mechanochromic Luminescence and Aggregation Induced Emission of Dinaphthoylmethane β-Diketones and their Boronated Counterparts

Chapter 4: Camera Method for Monitoring a Mechanochromic Luminescent β-Diketone Dye with Rapid Recovery

Chapter 5: Controlling Solid-State Optical Properties of
Stimuli Responsive Dimethylamino-Substituted Dibenzoylmethane Materials

Chapter 6: Color Tuning of High Contrast Mechanochromic
β-Diketonate Materials

Chapter 7: Arene and Alkyl Chain Length Effects on the Thermal Stability of Luminescent Supercooled Liquid Phases of Trimethoxy Substituted β-Diketones

Chapter 8: Future Directions

Acknowledgements

I owe a tremendous debt of gratitude to the tireless support of many wonderful people. Many thanks to my graduate advisor, Dr. Cassandra Fraser, who welcomed me into her lab and gave me the opportunity to work hard, and learn how to become a scientist. She provided me with financial support and taught me the value of organizing my thoughts and always having a plan. Without her encouragement, this thesis surely would not have seen the light of day.

Special thanks to all the members of the Fraser Lab, but especially Dr. Christopher DeRosa, who was my colleague, sounding board, literature guru, inspiration, and most importantly, friend. Other than my wife, I have spent more time around him than any other person these last five years. His passion, humor, and insight has kept me sane, motivated, and laughing during many long days and late nights. I will truly miss drinking coffee with him every morning and getting set for the day ahead. Big thank you, Dr. William Morris, my fellow ML teammate. Our conversations about music, Star Trek, movies, and science were always a pleasure, and often a needed distraction. Thank you to Alexander Mathew, who helped design the camera detection method and taught me what little I know about programing. I would also like to thank Maggie Daly and Caroline Kerr for their positive attitude and willingness to help me whenever possible. Their optimism interjected a breath of fresh air into the Fraser Lab from the moment they joined.

Big thanks to the UVA faculty members Dr. Carl. O. Trindle, Dr. Jiwei Liu, Dr., Michal Sabat, and Dr. James N. Demas who were always there to answer my questions. Thank you to the staff in Chemistry Department who are all great at their jobs. Thanks to Danny who runs the stockroom like a Swiss watch, and Michael Brickhead who makes ordering general lab supplies an absolute delight. I would also like to thank our lab custodian and friend, Josef. He unlocked

doors for me when I forgot my keys, taught me how to say some general phrases in French and tolerated my atrocious pronunciation.

Thank you to my many wonderful friends here in Cville, Brandon and Danielle Thompson, Kyle Bartholomew and Jacquelyn Duvall. You guys have become my support system and family since moving to Virginia. It has been an absolute pleasure to have spent the last five years drinking, talking, laughing, and drinking some more with you all. I can't imagine my life without you. Finally, the biggest thanks to my wife Courtney. Words can't begin to describe how grateful I am for your patience, wisdom, and unwavering support. I am constantly amazed by your ability to say and do the right thing at the precisely the right moment. Your encouragement over these last few years has meant everything to me. I could not have done it without you, Court.

Dedication

This thesis is dedicated to Mom and Dad. Thank you for giving me the inspiration to pursue my dreams.

List of Tables

List of Figures

xv

Chapter 1

Introduction to Luminescence and Mechanochromic Luminescent Materials Design

1.1 Luminescent Materials and Their Applications

1.1.1 Current Applications of Luminescent Materials

Luminescent dyes, and materials exploiting their properties, have become increasingly ubiquitous in our daily lives.[1] The integration of high performance light emitting diodes (LEDs) into the screens of battery operated mobile devices allow for the convenient display of information.[2] Energy saving organic light emitting diodes (OLEDs) have been incorporated into our TV screens, enabling us to watch our favorite programs in high definition and save money on our energy bills.[3] Similarly, cutting-edge energy producing technologies rely on luminescent materials to improve their viability. For example, the fluorescent bulbs we use to light our homes may soon be powered with low-cost dye-sensitized solar cells.[4,5] In addition, luminescent probes have enabled the monitoring of cellular processes and the measurement of changes to the physiological environment.[6,7] While these examples demonstrate the important role luminescent materials play in current technology, the incorporation of dyes into developing materials such as security inks, shape memory materials and new sensors represent the focus of current research.[8,9]

1.1.2 Types of Luminescent Molecules

There are many different types of photoluminescent materials that have proven useful for applications, however they can generally be categorized according to their molecular structure as organic, inorganic, or organometallic luminogens.[1] Some examples of purely inorganic emissive materials are metallic nanoparticles (e.g. luminescent gold nanoparticles), as well as nanocrystalline semiconductors, commonly referred to as quantum dots. Among their many features, these materials are widely utilized due to their size dependent optical properties, which allows them to be easily tailored for specific applications. Commonly used luminescent organometallic materials include ruthenium and copper complexes, metalloporphyrin derivatives

as well as luminescent lanthanide compounds. Organometallic luminogens are desirable synthetic targets due to their tunable emission, as well as their ability to produce phosphorescence.[1]

Luminescent organic dyes, which are the main topic of this work, possess certain commonalities which imbue them with emissive properties. Many molecules possess a conjugated network of π-bonds which allows them to absorb and emit visible light.[10] This structural feature introduces electronic transitions excitable by photons deriving from ultraviolet (UV) and visible regions of the electromagnetic spectrum. Strategic manipulations of molecular structure can predictably alter the energy of these transitions, resulting in tunable absorption and emission. Perhaps the most basic organic luminogens are polycyclic aromatic hydrocarbons such as anthracene, phenanthracene, pyrene, and perylene. Organic dye families, including xanthenes, cyanines, and coumarins, contain highly conjugated dye scaffolds derivative of polycyclic aromatics dyes. Many current studies of luminescent materials often involve substitution of these and other dye families in order to improve luminescent properties (Figure 1.1).[11]
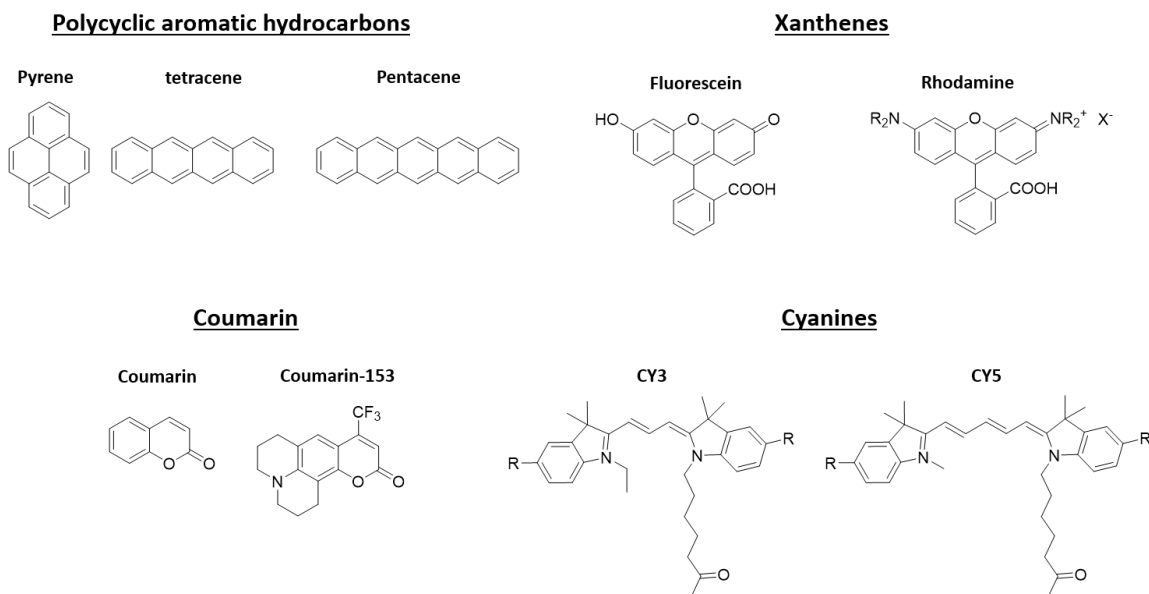
Figure 1.1. Chemical Structures of Common Organic Dye Families.

1.2 Properties of Photoluminescent Molecules

There are many different ways to produce luminescence. Light can be produced as a result of chemical (chemiluminescence) or biochemical (bioluminescence) reactions. Application of an electric current across a material (electroluminescence) and the absorption of a photon (photoluminescence) are other common mechanisms to produce luminescence. Many different factors must be considered when designing materials including the mechanism used to produce luminescence and the applications of interest. For photoluminescent materials, these parameters include the absorption and emission energy, molar absorptivity (ε), lifetime (τ), quantum yield (φ), photostability, and more.

1.2.1 Luminescence Theory

The spectroscopic features of organic molecules are determined by the relative energies of their excited states, as well as the relationship between radiative processes that originate in the excited state. These processes are typically illustrated using a Jablonski diagram (Figure 1.2). In general, an electron is promoted from the ground state (S_0) to an excited state (S_1) of the same spin multiplicity when a fluorophore is irradiated with light of sufficient energy. Depending on the energy of incident photons, excitation to higher energy singlet states (S_2, S_3,…) can occur, however, relaxation to the lowest energy excited state typically occurs prior to emission (Kasha's Rule).[10] There are several different mechanisms by which excited energy may be dissipated. Non-radiative pathways include the release of heat due to molecular rotations or vibrations. Additionally, emission can be quenched through collisions with other molecules. Radiative decay occurs when energy is released through the emission of a photon. The most common radiative pathway, fluorescence, occurs when energy is released from an excited singlet state (S_1) to the ground singlet state (S_0) through emission of a photon. Though less commonly observed in organic

dyes at room temperature, phosphorescence can occur when there is spin orbit coupling between excited singlet state (S_1) and triplet states (T_1). In this mechanism, energy is transferred from matching excited singlet state to a triplet state through intersystem crossing (ISC), followed by the release of a lower energy photon. Additionally, thermal repopulation of S_1 from T_1, and subsequent radiative relaxation to the ground state is a process called thermally activated delayed fluorescence (TADF). The optical properties of organic molecules are determined via a complex interplay of these processes which can often be controlled through dye modifications and substitutions.[10]
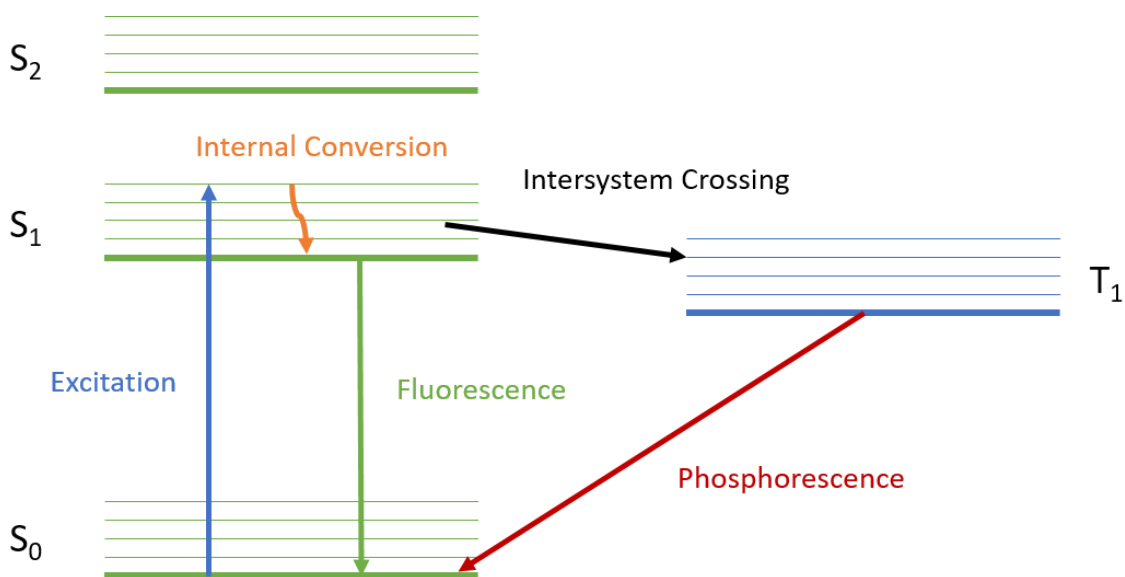
Figure 1.2. Jablonski Diagram. Diagram depicting photoexcitation of an electron from a singlet ground state (S_0) to a singlet excited state (S_1 or S_2) followed by internal conversion and emission of a photon from S_1 (fluorescence). Alternatively, intersystem crossing (ISC) can occur leading to emission from the first triplet excited state (T_1) to the ground state (phosphorescence).

1.2.2 *Optical Characterization*

The optical properties of luminescent molecules are measured spectroscopically using a UV-vis spectrophotometer (absorption) and fluorimeter (emission). For absorption measurements, which give information about the ground state, an analyte sample and blank are prepared and

illuminated separately with UV and visible light. The difference in transmitted light between the sample and blank yields an absorption spectrum (Figure 1.3).[10] To obtain an emission spectrum using a fluorimeter, an excitation monochromator is used to selectively illuminate a sample with a single wavelength of light. The emission of the illuminated sample is then filtered by wavelength using a subsequent emission monochromator, and the intensity at each wavelength is detected. The emission intensity as a function of wavelength is defined as the emission spectrum, and is typically independent of the excitation wavelength for pure monomeric samples. A fluorimeter can also be used to obtain an excitation spectrum where emission intensity is detected at a single wavelength, and the wavelength used to excite the sample is varied.[10]
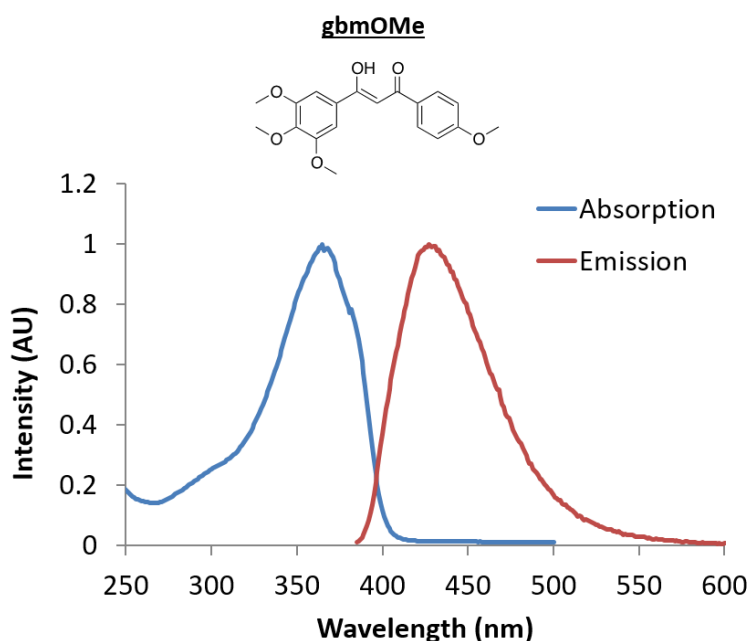
Figure 1.3. Example of Spectral Characterization. Absorption and emission spectra of 3-hydroxy-1-(4-methoxyphenyl)-3-(3,4,5-trimethoxyphenyl)prop-2-en-1-one (gbmOMe).

The spectra of a given dye can be used to calculate many important luminescent parameters. One example is the Stokes' shift, which is defined as the energy difference between the peak absorption and emission of a dye (Figure 1.3). Larger Stokes' shifts are observed for polar dyes and are also dependent on the medium in which the absorption and emission spectra are

measured. In general, when a polar dye is dissolved in a polar solvent, larger Stokes' shifts are observed. This also implies that dyes that are sensitive to the polarity of their environment possess larger Stokes' shifts. Additionally, the overlap between the two spectra represents the energy of emitted photons that can be reabsorbed by the same dye. This is significant for many applications with high dye loadings because reabsorption results in a loss in emission intensity. While the Stokes' shift of a dye can be easily calculated directly from the absorption and emission spectra of a material, it is important to consider the basic theory of photoluminescence in order to describe other important quantities.[10]

1.2.3 Luminescent Parameters

There are many different quantities that describe the luminescence properties of a molecule, however they can generally be divided into two different categories: absorption, and emission. As mentioned previously, the absorption of a dye is typically measured by irradiating a dye solution with UV and visible light and detecting the light transmitted. This process can be modeled using the Beer-Lambert Law (Equation 1.1).[10] In this equation, the absorbance of a dye (A) is equal to its molar absorptivity (ε) multiplied by the product of the absorbing medium path length (b), and its concentration. For a typical absorbance measurement performed with a spectrophotometer and a quartz cuvette, the path length is 1 cm and the concentration is variable.

$$A = \varepsilon bc \qquad\qquad (1.1)$$

According to the Beer-Lambert equation, the only parameter which is intrinsic to the dye is ε. The molar absorptivity is related to the size of the dye absorbing region, or molecular cross section.[12] Molecules with large molecular cross sections typically have large ε values. Additionally, the Beer-Lambert relationship indicates that absorbance only depends on concentration and ε, therefore absorbance can be tuned through the manipulation of these factors.

7

The emission of a dye is also defined using a various parameters. For example, the probability that an excited molecule will fluoresce is defined as the fluorescence quantum yield (ϕ). This can also be described as the ratio of photons emitted compared to the photons absorbed (Equation 1.2).[10]

$$\phi = \frac{k_e}{k_e + \sum k_d} = \frac{n_E}{n_A} \tag{1.2}$$

In 1.2, k_e is the rate constant of emissive decay, $\sum k_d$ is the sum of the rate constants for all other elaxation mechanisms (i.e. non-radiative decay pathways), n_E is the number of photons emitted, and n_A is the number absorbed. Many applications require luminescent materials to exhibit quantum yields near unity. Quantum yields approaching unity can be observed for fluorescent molecules in solution at room temperature, however, phosphorescent quantum yields are typically much smaller under the same conditions.[10] Examination of Equation 1.2 indicates that one strategy for improving quantum yields is to decrease the probability of non-radiative decay. This can be accomplished by increasing rigidity in order to prevent molecular rotations and vibrations, factors influencing the quantum yield. Additionally, the quantum yield of a dye is highly dependent on the surrounding matrix. Elevated quantum yields are often observed in more viscous solvents that slow molecular motions.[13] While designing organic dyes with highly rigid structures is an effective strategy to improve quantum yield in solution it often leads to aggregate formation from increased π-stacking interactions, and quenched solid-state emission. Strategies for improving the solid-state quantum yield will be discussed in a subsequent section.

$$\phi_f = \phi_{f,ref} \left(\frac{A_{ref}}{I_{ref}} \right) \left(\frac{n^2}{n_{ref}^2} \right) \left(\frac{I}{A} \right) \tag{1.3}$$

The measurement of quantum yield in solution is typically accomplished by comparison to dye standards with well know quantum yields using Equation 1.3, where Φ_{ref} denotes the fluorescence quantum yield of the standard, A is the absorbance at the excitation wavelength, and

I and I_{ref} are the integrated fluorescence intensities of the sample and reference emission spectra. The refractive indices of the dye and standard solutions are denoted by n and n_{ref}, respectively. Care must be taken in order to ensure that the absorption and emission of the dye and reference have comparable wavelengths and that both solutions are dilute such that the absorbance at the excitation wavelength is less than 0.10 AU. Concentrated samples increase the probability of self-absorption which can produce artificially low quantum yields.

Another characteristic emission parameter is the average time a molecule occupies the excited state prior to depopulation and relaxation back to the ground state. This is called the excited-state lifetime (τ) (Equation 1.4). Typical lifetimes for fluorescent molecules are on the order of nanoseconds (ns) whereas the lifetimes of phosphorescent molecules are often on the order of milliseconds (ms) or longer. Similar to quantum yield, lifetime is dependent on the rate constants of the radiative (k_e) and non-radiative (k_d) rate constants.[10]

$$\tau = \frac{1}{k_e + \sum k_d} \tag{1.4}$$

The design of luminescent materials with variable lifetimes is desirable for applications. For example, lifetime-based imaging is widely-used in biological and sensing applications.[14] In order to rationally design materials suitable for these purposes, many different strategies have been developed to modulate lifetime. One example is heavy atom substitution (e.g. Br or I) which can lead to increased spin-orbit coupling between the excited singlet and triplet states.[15] This increases the rate of intersystem crossing to the longer-lived triplet state, thereby decreasing the rate of emission and thus increasing the lifetime.

There are two different methods of observing the excited state lifetime of a fluorophore, time-resolved and frequency-resolved measurements. Because only time-resolved measurements were performed in this work, they serve as the focus of this discussion. Specifically, time correlated

single photon counting (TCSPC) was used to measure lifetimes. This involves using a pulsed light source to excite the dye and measuring the intensity over different decay time intervals once the light is off. This cycle is repeated until a histogram representative of the excited state decay is produced.[16] This exponential decay is then fit to single or multiexponential decay functions and the pre-exponential weighted lifetime can be calculated. The amount of exponential decay is correlated with the number of emissive species and can be used to evaluate energy transfer (when more than one molecule is present), excimer formation, and other important luminescent properties.[10]

1.3 Strategies for Modulating Optical Properties

Depending on the application, the optical properties required of a given luminescent dye can be wide-ranging. For instance, longer wavelength light (e.g. red and near infrared) is well suited for biological imaging applications because lower energy light is less affected by intrinsic autofluorescence in vivo, and a reduction in light scattering and re-absorbance by surrounding tissue is observed, leading to greater tissue penetration.[17–19] Low energy fluorophores with high absorbance are also useful for dye-sensitized solar cells.[4] In order to modulate the properties of emissive materials, several different strategies are employed. Through modifications to dye structure, including increasing π-conjugation of the luminescent core and substitution with donor and acceptor groups, the emission energy, quantum yield, fluorescence lifetime and type of emissive species can be manipulated.[10] While these strategies allow for the rational design of luminescent molecules, different optical properties are intertwined such that multiple parameters are affected depending on the type of structural modification.

1.3.1 Conjugation Length Effects

The effect of increased π-conjugation can be illustrated through examination of the optical properties of polycyclic aromatic hydrocarbons (e.g. naphthalene, anthracene, tetracene).[20,21] In these systems, red-shifted absorption and emission peaks are observed as the conjugation length is increased. Given more π-type molecular orbitals are formed as the π-system is extended, a narrowing of the energy gap between the highest occupied molecular orbital (HOMO) and lowest unoccupied molecular orbital (LUMO) is observed.[10] In addition to wavelength effects, the degree of conjugation also has an effect on the molar absorptivity of an organic compound. As π-conjugation is increased, so does the molecular cross-section, and thus, the molar absorptivity.[12,17]

This strategy has been used to adjust the optical properties within a family of dyes. For example, Park *et al.,* employed this strategy to produce a series of excited state intramolecular proton transfer (ESIPT) dyes with red, green, and blue emission. These molecules were used as a molecular pixel system because molecular crosstalk was not observed (Figure 1.4).[22] In this system, all emissive materials were structurally similar, but subtle modifications were made to tune the properties of each dye. Multiple methods were employed to produce molecular pixels with suitable emission, including the extension of π-conjugation length. For example, the green emitter (p-MHPIC) was produced *via* replacement of the biphenyl moiety in its blue counterpart (m-MHPI) with a fluorenyl group (p-MHPIC), thereby increasing π-conjugation. Furthermore, a naphthyl substituent, instead of a phenyl group, was incorporated in the design of the red pixel (HPNO) in order to lower the energy of emission. Though extended π-conjugation helped produce red-shifted emission, further structural modifications via the addition of donor and acceptor groups were required to tune the optical properties of each dye.
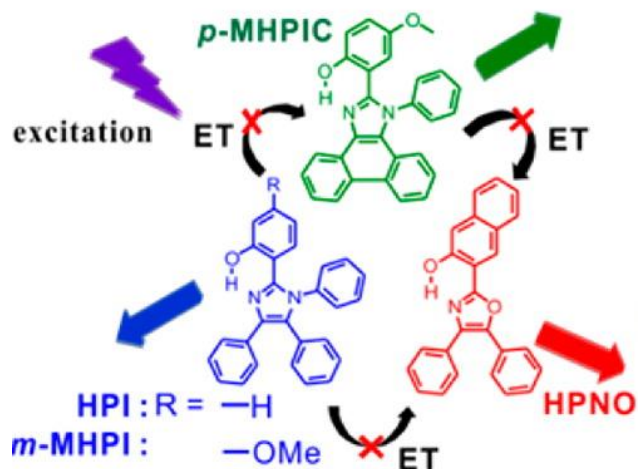
Figure 1.4. Molecular Pixel System. Schematic showing the excited state intramolecular proton transfer (ESIPT) red (HPNO), green (p-MHPIC) and blue (HPI, m-MHPI) molecular pixels. Image published with permission of Park *et al.*, *J. Am. Chem. Soc.* **2013**, *135*, 11239–11246. Copyright American Chemical Society 2013.[22]

1.3.2 Donor and Acceptor Effects

Substitution of luminescent dyes with donor and acceptor groups is an effective strategy for the rational design of stimuli responsive fluorophores.[23–26] Depending on the substitution position and electron donating or withdrawing strength of the substituent, the relative molecular orbital (MO) energies can be greatly affected. In general, substitution with electron withdrawing groups lowers MO energy, whereas incorporating electron donating groups into molecular structures results in their destabilization.[10] As seen in the previous example, Park *et al.*, replaced the imidazole core of the blue and green molecular pixel (m-MHPI and p-MHPIC, respectively) with an oxazole, in order to increase charge transfer to the core of the red-emitter (HPNO) (Figure 1.4).[22] Additionally, methoxy donating groups were added to the meta position of the blue (m-MHPI) dye and the para position of the green (p-MHPIC) emitter to further adjust emission. This strategy has been widely used to modulate the emission of organic fluorophores, but often results in the formation of charge transfer (CT) states which have been known to quench emission in

solution and the solid state. Compared to molecules that undergo π-π* transitions, CT dyes generally possess lower quantum yields and longer lifetimes.[10]

Dyes that exhibit intramolecular charge transfer (ICT) are also known as push-pull fluorophores.[27,28] This term stems from the transfer of electron density from an electron donor group to an acceptor group on the same dye (Figure 1.5). As a result, a highly polar excited state is formed which can be stabilized or destabilized depending on its surrounding environment.[29] Evidence of charge transfer can be found in the MO diagrams of molecules like the difluoroboron β-diketonate, $BF_2dbmp(OMe)_2$ (Figure 1.5).[30] Examination of the highest occupied molecular orbital (HOMO) shows electron density localized on the dioxaborine ring. Upon UV excitation to the lowest unoccupied molecular orbital (LUMO), electron density shifts to the out-of-plane phenyl ring, demonstrating charge transfer.
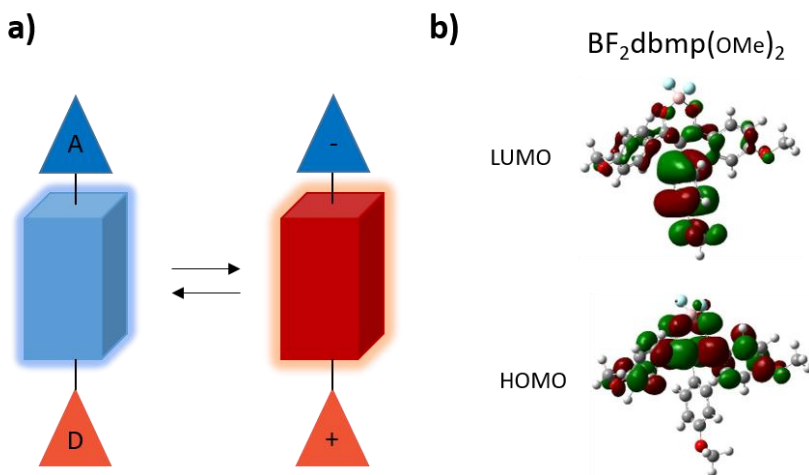
Figure 1.5. Charge Transfer Diagram. Schematic illustrating charge transfer in luminescent dyes (a). Chemical structure of 3-hydroxy-3-(6-methoxynaphthalen-2-yl)-1-(naphthalen-2-yl)prop-2-en-1-one ($BF_2dbmp(OMe)_2$) and frontier molecular orbitals depicting charge transfer (b).

Depending on the steric bulk of a substituent (e.g. t-butyl), substitution pattern, and the viscosity and polarity of the solvent, twisted intramolecular charge transfer (TICT) states can form.[31–33] This process is similar to ICT, however a change in molecular geometry is also observed upon excitation. Dyes with TICT often exhibit red shifted emission, longer lifetimes, and low

13

quantum yields in fluid solvents as a result of non-radiative decay from molecular twisting.[23,33–35] The introduction of TICT states can be useful in designing viscosity probes, where molecular twisting can be hindered by viscous solvents.[34] Often called molecular rotors,[36] dyes exhibiting TICT have been used to probe lipid membranes due to their ability to distinguish lipid ordered (L_o) and disordered (L_d) phases.[6,37]

1.4 Responsive Properties in Solution

Many different biological applications require dye sensitivity toward the surrounding environment. In solution, these responses can result from many different factors including pH, viscosity, polarity, and temperature. Different molecular design strategies have been utilized to tune dye sensitivity toward these different properties.

1.4.1 Solvatochromism

As previously discussed, dyes that exhibit ICT transitions often possess environmentally sensitive optical properties. One example of this is solvatochromism, where polar dyes in the excited state are stabilized through electrostatic interactions with solvent molecules (Figure 1.6). Because the lifetime of fluorescence (~1-10 ns) is typically longer than solvent relaxation times (~0.1 ns), solvent molecules can arrange themselves to lower the energy of the excited state through dipole-dipole interactions.[10] For more polar solvents, the stabilization of the excited state is greater and emission is red-shifted compared to dyes in weakly or non-polar solvents. In general, the absorption spectra of dyes show much less dependence on solvent polarity in comparison to their emission.[38] Polar dyes that exhibit solvatochromism are often used as sensors in biological contexts. For example, the diethylamino-substituted push-pull derivative, NR12S, was utilized as a membrane probe by Klymchenko *et al*.[39,40]
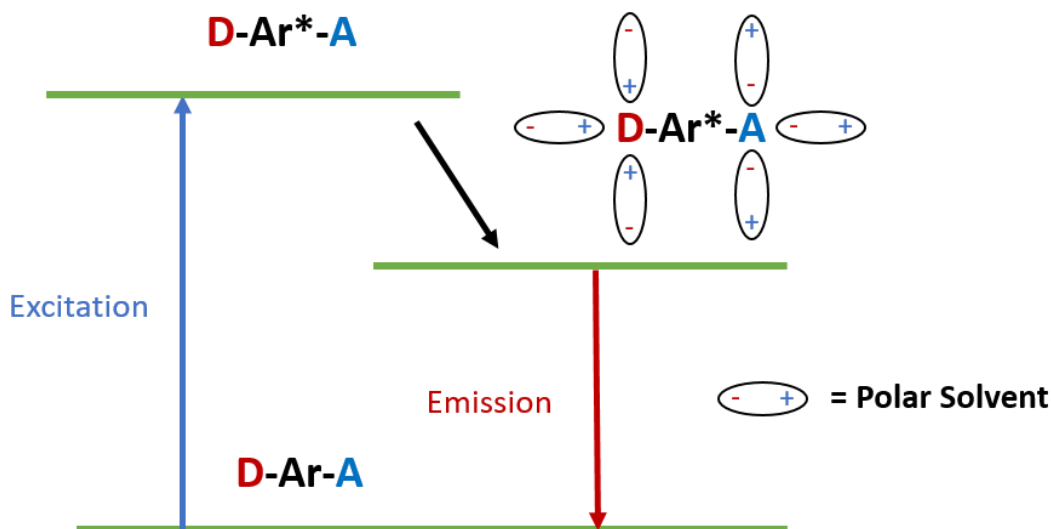
Figure 1.6. Polarity Effects on Emission. Schematic illustrating solvatochromism where polar solvent molecules stabilize the excited state species.

The degree of solvatochromic shift can be approximated according to Lippert-Mataga theory (Equations 1.5 and 1.6)[41,42] where ν_{ab} and ν_{em} are the peak absorption and emission in wavenumbers, h is Plank's constant, c is the speed of light, a is the Onsanger cavity radius, μ_e and μ_g are the excited and ground state dipolar moments, and n and ε are the refractive index and dielectric constant of the solvent, respectively.

$$\Delta\nu = \nu_{ab} - \nu_{em} = \frac{2\Delta f}{hca^3}\left(\mu_e - \mu_g\right)^2 + constant \tag{1.5}$$

$$\Delta f = f(\varepsilon) - f(n^2) \approx \frac{\varepsilon-1}{2\varepsilon+1} - \frac{n^2-1}{2n^2+1} \tag{1.6}$$

According to this treatment, the Stokes' shift ($\Delta\nu$) of a dye is linearly dependent on the solvent polarity parameter (Δf). The slope of the line is indicative of dye sensitivity toward polar environments.

1.4.2 Excited State Intramolecular Proton Transfer (ESIPT)

There are numerous examples of proton transfer reactions throughout the many disciplines of chemistry, both intermolecular and intramolecular.[43,44] One type of proton transfer reaction that

is commonly utilized in the design of luminophores is excited state intramolecular proton transfer (ESIPT) (Figure 1.7).[45] These molecules require the presence of a hydrogen bond in the lowest energy ground, or normal (N) state. Typical ESIPT molecules have 5- or 6-membered H-bonding rings.[46] Upon excitation to the normal excited state (N*), rapid proton transfer (time scale ~ 10^{-12} s) can occur which results in the formation of a transient tautomeric state (T*). Emission from T* to the corresponding ground state (T) results in redshifted emission, followed by reverse proton transfer to the lower energy ground state conformer (i.e. N).[43]

Excited state intramolecular propton transfer (ESIPT) can be detected spectroscopically, where dual emission from N* and T* species is observed. Depending on the surrounding environment and the molecular structure of the dye, the relative energies of these peaks can be controlled.[45] For example, when dissolved in protic solvents, hydrogen bonding between the solvent and dye can hinder the proton transfer and produce emission from N*.[32,47] Thus, blue-shifted emission is expected for ESIPT dyes when dissolved in protic solvents. This process has been utilized for a variety of applications including molecular probes that use the ESIPT reaction to sense various cellular processes.[48] As mentioned previously, the red-shifted emission of ESIPT fluorophores has also been harnessed by Park *et al.*, to fabricate a molecular pixel system with red, green and blue emitting ESIPT dyes. These dyes can be mixed in precise ratios to yield materials with predictable composite emission because the large Stokes shift characteristic of ESIPT dyes prevents energy transfer or molecular cross talk.[22]
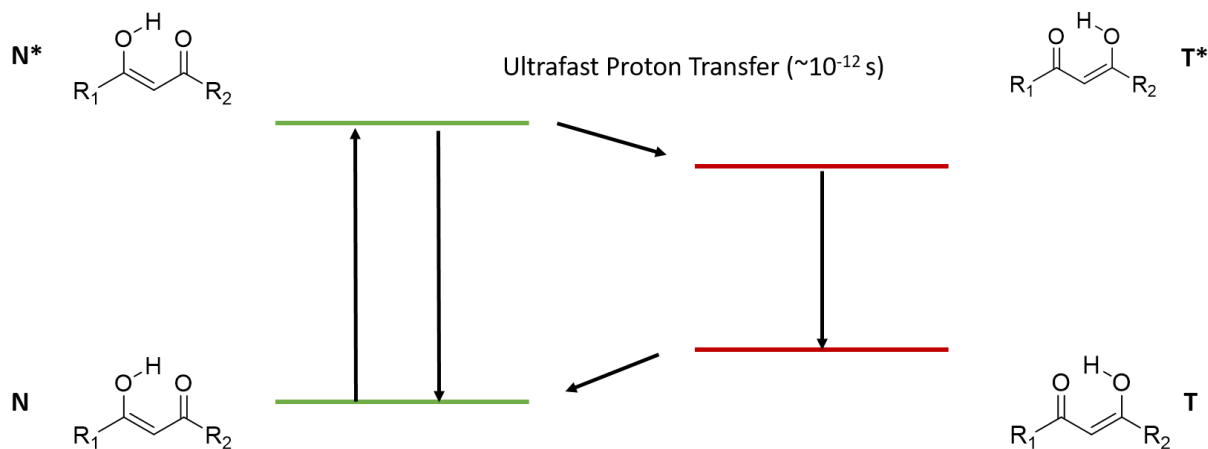
Figure 1.7. Illustration of ESIPT. Schematic illustrating excited state intramolecular proton transfer (ESIPT) for enol moieties. Excitation occurs from a normal ground state (N) to its corresponding excited state (N*) where it undergoes an ultra-fast proton transfer reaction to produce an excited state tautomeric species (T*) before relaxation to its ground state (T). Once in the ground state, reverse tatuomerization occurs back to the normal state.

1.5 Designing Solid-State Emissive Materials

Many applications require efficient solid-state emission, however, luminophores that are emissive in solution are often dark in the solid state due to aggregation caused quenching (ACQ).[49] Instead of emitting a photon, ACQ dyes dissipate energy through non-radiative pathways arising from intermolecular interactions in the aggregate. Dyes that exhibit ACQ often contain fused aromatic systems, such as polycyclic aromatic hydrocarbons, that can π-stack and quench emission.[50]

1.5.1 Aggregation Induced Emission (AIE)

In order to circumvent ACQ, Tang *et al.,* used the propeller-shaped hexaphenylsilole (HPS) system to show that some materials become emissive upon aggregation.[51] This was accomplished by measuring the emission of dyes in acetone/H_2O mixtures, wherein dyes aggregate with increasing the concentration of H_2O, a non-solvent. This phenomenon has been explained through the restriction of molecular motions (RIM) as aggregates are formed.[52] With this in mind, many different compounds have been developed that show aggregation-induced emission (AIE) or

aggregation-induced enhanced emission (AIEE).[49] These include triarylamine, tetraphenylethene, silole, and cyanostilbene based materials, which have found use in OLEDs, optical devices, and biomedical applications.[50,53–56] Recently, Chujo *et al.*, reported stimuli responsive boron coordinated diiminate materials showing dynamic aggregation induced emission (AIE) properties that were modulated through incorporation of donor and acceptor substituents.[57] Many of these materials also exhibit mechanochromic luminescence (ML), a focus of our work.

One example that illustrates the differences between molecules exhibiting ACQ and AIE are the α-substituted boron difluoride β-diketonates, $BF_2dbe(OMe)_2$ and $BF_2dbt(OMe)_2$ (Figure 1.8).[30] The β-tetralone derivative, $BF_2dbt(OMe)_2$, is strapped and molecular motion is hindered. Therefore, blue emission is seen when $BF_2dbt(OMe)_2$ is dissolved in DMSO. Addition of H_2O induces aggregation and quenches emission; that is, ACQ is observed. In contrast, the dibenzoylethane dye, $BF_2dbe(OMe)_2$, is initially non-emissive in solution owing to the molecular motions associated with its non-planar structure. As the concentration of non-solvent is increased and aggregates are formed, these rotations are restricted and blue-green emission is observed.
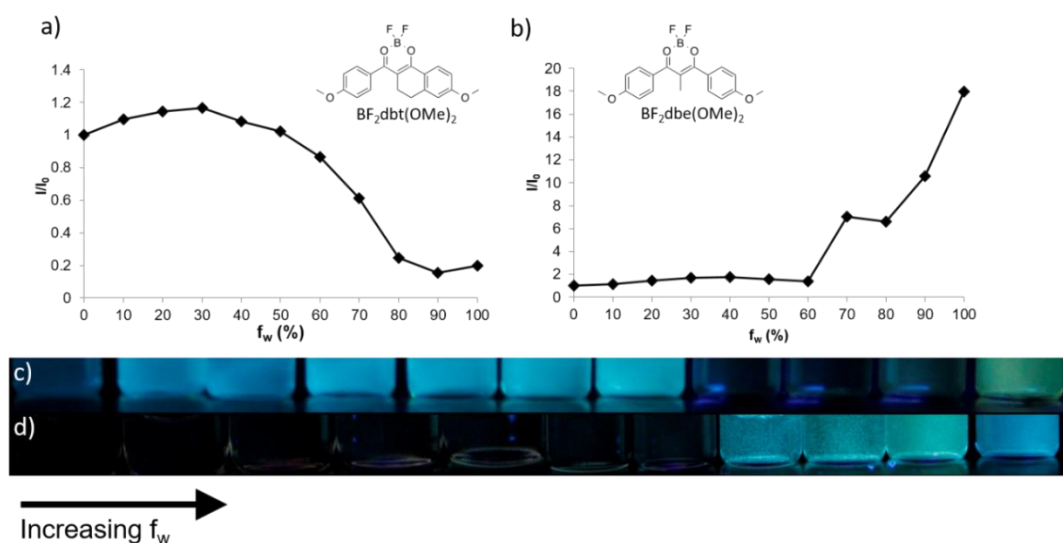
Figure 1.8. AIE and ACQ Comparison. Intensity plots (I/I_0) of $BF_2dbt(OMe)_2$ (a) and $BF_2dbe(OMe)_2$ (b) in DMSO/H_2O solutions. Images of DMSO/H_2O solutions of $BF_2dbt(OMe)_2$ (c) and $BF_2dbe(OMe)_2$ (d) under UV irradiation. (λ_{ex} = 369 nm)

1.5.2 Emission of Aggregates

For many stimuli responsive materials, different optical properties can be observed for crystalline and amorphous aggregate species. The emission of aggregate species has been described using exciton coupling theory by Kasha *et al.*[58] According to this treatment, a splitting of energy levels (Davydov splitting) occurs as aggregates are formed which results in higher and lower energy transitions relative to the energy of the monomer (Figure 1.9).[59] When dyes aggregate in a face-to-face arrangement, H-aggregates are formed and transition to the higher energy state is allowed. Transition to the lower energy state is observed for J-aggregates, which are comprised of offset dimers.[60] Based on this theory, the formation of aggregates can be monitored using absorption spectroscopy where the peak absorbance of H-aggregates and J-aggregates are blue-shifted and red-shifted, respectively, relative to the absorbance of the monomer.[61] Comparatively, J-aggregates exhibit brighter emission than typically non-emissive H-aggregate species. Materials that form J-aggregates have been utilized as sensitizers for silver halide photographic films.[62]
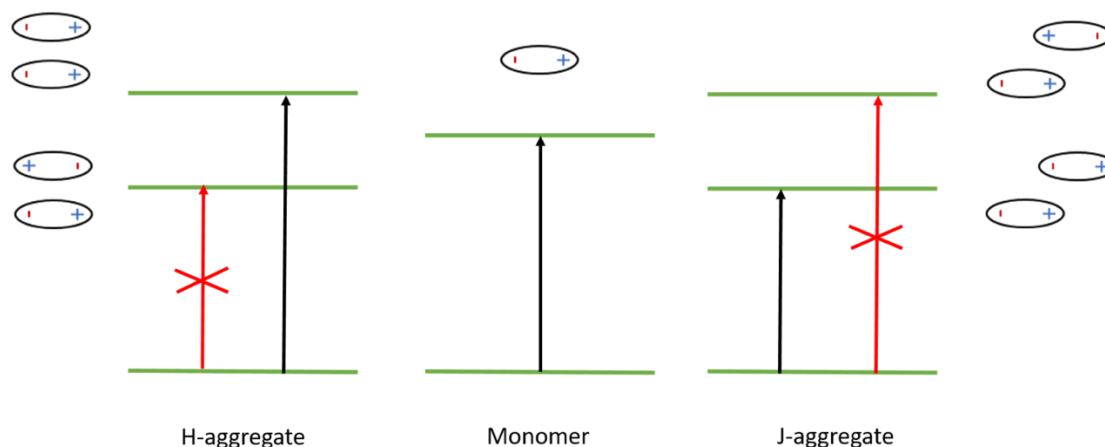
Figure 1.9. Aggregation Effects. Schematic showing the different energetic properties when dyes associate in H and J aggregate forms.

1.6 Mechanochromic Luminescent Materials

Materials respond to a variety of different kinds of stimuli. For example, some have been engineered to react to temperature (thermochromism) and pH, while others show emission changes

in response to the presence of chemical species (e.g. O_2, amines, ions).[63–66] In particular, mechanochromic luminescent (ML) dyes, which change emission wavelength in response to external mechanical stimuli such as hydrostatic pressure or shear force, are an emerging class of responsive material.[67] In some cases, spectral changes vary depending on the type of force being applied.[68] There are different types of ML materials including metal,[69] organic,[10] polymer,[70] and liquid crystalline compounds.[9] Though some mechanophores have been known for some time, many have only been reported in the past decade. These systems show promise for luminescent data storage, security inks, and other technologies.[8] The development of ML materials with tunable optical properties is a main focus of this research.

1.6.1 Properties of Mechanoresponsive Dyes

Similar to strategies for modulating emissive properties of dyes in solution, the optical properties of solid-state materials often incorporate donor (D) and acceptor (A) motifs.[55,71,72] Solid-state emission is determined by intermolecular interactions[61,73] and crystal packing.[60,74] For example, cyanostilbene-based materials have shown emission switching due to the sliding of molecular sheets, controlled via C-H···N and C-H···O hydrogen bonding interactions.[75] Additionally, Kato *et al.,* fabricated water soluble mechanoresponsive micelles in water that change emission wavelength when vortexed due to the formation of different molecular assemblies (Figure 1.10).[76] In this study, pyrene based amphiphiles formed dumbbell-shapes when self-assembled in H_2O and linked to glass beads. In the initial assembly, pyrene molecules were in close enough proximity to form excimers, and yellow emission was observed. Upon vortexing the glass beads, the morphology of the micelles changed, breaking up pyrene excimers, and producing green emission. These examples illustrate that it is not only important to consider how substituents

modify the optical properties of individual dyes, but also how the intermolecular association and supramolecular structure are impacted by substitution.
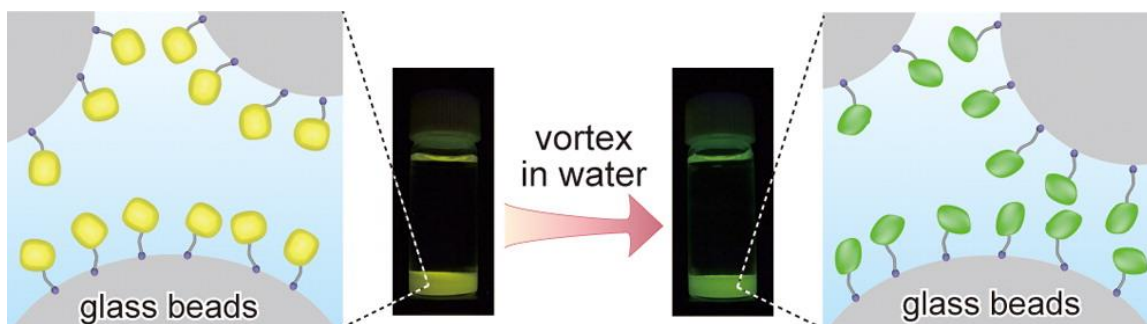
Figure 1.10. Mechano-Responsive Molecular Assemblies. Water soluble emissive micelles that change emission upon vortexing in H_2O due to change in molecular assembly. Published with permission from Kato *et al.*, *J. Am. Chem. Soc.* **2014**, *136*, 4273–4280. Copyright American Chemical Society 2014.[76]

Material processing conditions such as temperature, dye-substrate interactions, film thickness and repeated smearing also influence ML properties. The thermal properties of luminophores are important both for fabrication and because the mechanically triggered changes in optical properties are often the result of temperature dependent crystalline-to-amorphous phase transitions.[68] For example, Mizuguchi *et al.*, reported a triphenyl amine (TPA) material that showed rapid ML recovery of a green-yellow emissive state. Furthermore, the red-shifted emission was also produced *via* melting and cooling to room temperature in addition to smearing.[79] The identity of this emissive melted state was determined to be a supercooled liquid with red-shifted emission resulting from a twisted intramolecular charge transfer (TICT) state.

Recently, Kim *et al.*, reported an alkylated diketopyrrolopyrrole (DPP8) with high contrast emission changes, due to shear-triggered crystallization of a thermally stable supercooled liquid state (Figure 1.11).[80] The phase transition was attributed to a small Gibbs free energy difference between the crystalline and supercooled liquid states. Crystallization was localized to the smeared region at 25 ºC, which enabled direct writing of spin cast DPP8 films. However, propagation was

observed when the supercooled liquid was smeared at 120 ℃. Furthermore, such minute forces were required to trigger crystallization and associated emission changes, that they could even be induced *via* live cell attachment. This example demonstrates an application for thermally stable amorphous solids, namely, as cell force sensors. Despite their potential for optical and optoelectronic uses,[81,82] and for improving the solubility of various active pharmaceutical ingredients and excipients,[83] supercooled liquids are relatively rare.
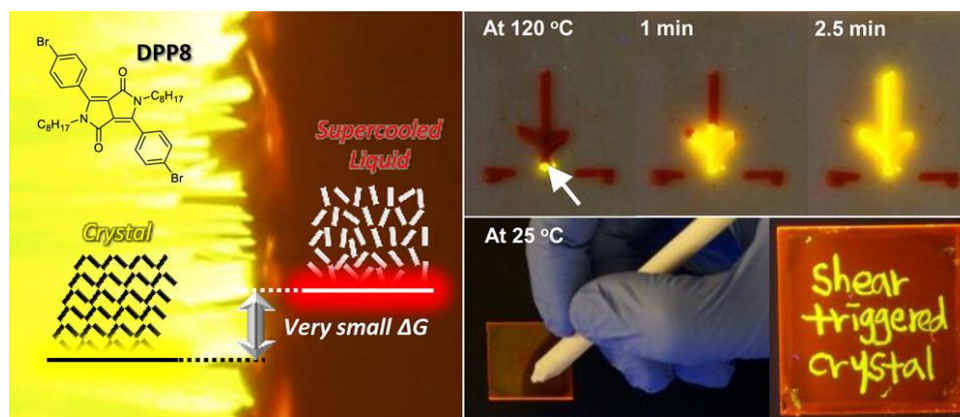
Figure 1.11. Mechano-Responsive Supercooled Liquids. Shear triggered crystallization of a DPP8 supercooled liquid. At elevated temperatures (120 ℃) crystallization propagates, however at room temperature (25 ℃) crystallization is localized. Published with permission from Kim *et al., ACS Cent. Sci.* **2015**, *1*, 94–102. Copyright American Chemical Society 2015.[80]

While a hypsochromic shift is observed upon smearing in the previous example, the wavelength shift of many solid-state ML materials is the product of a mechanically produced phase transition from an initially crystalline state to an amorphous, red-shifted one.[67] However, in rare instances, mechanically produced emission changes are the result of crystal-to-crystal transformations. From a mechanistic perspective, these systems are particularly compelling, since single crystal X-ray analysis can be used to probe the ML states both before and after smearing. One example of a crystal-to-crystal ML material was developed by Ito *et al.*, where a crystalline triethylene-substituted Au (I) complex with blue emission initially occupied a transient amorphous state, before forming a separate yellow-emissive crystal upon smearing.[84]

In order to produce new ML materials with crystal-to-crystal transitions, many derivatives based on this Au(I) system were synthesized with different aromatic donor and acceptor groups (Figure 1.12).[85] While the vast majority of these derivatives showed peaks in their XRD patterns before grinding that disappeared after mechanical perturbation, the CF_3-CN derivative ($R_1 = CF_3$, $R_2 = CN$) exhibited peaks in the XRD spectra for both states, indicating a crystal-crystal phase transition. Furthermore, DFT calculations coupled with single crystal obtained before and after grinding indicate that the change in emission is due to aurophilic interactions, and that weak intermolecular interactions in the initial crystal are important for producing ML materials that undergo crystal-to-crystal transformations. This is a unique ML system and illustrates an approach to designing materials with different optical properties.
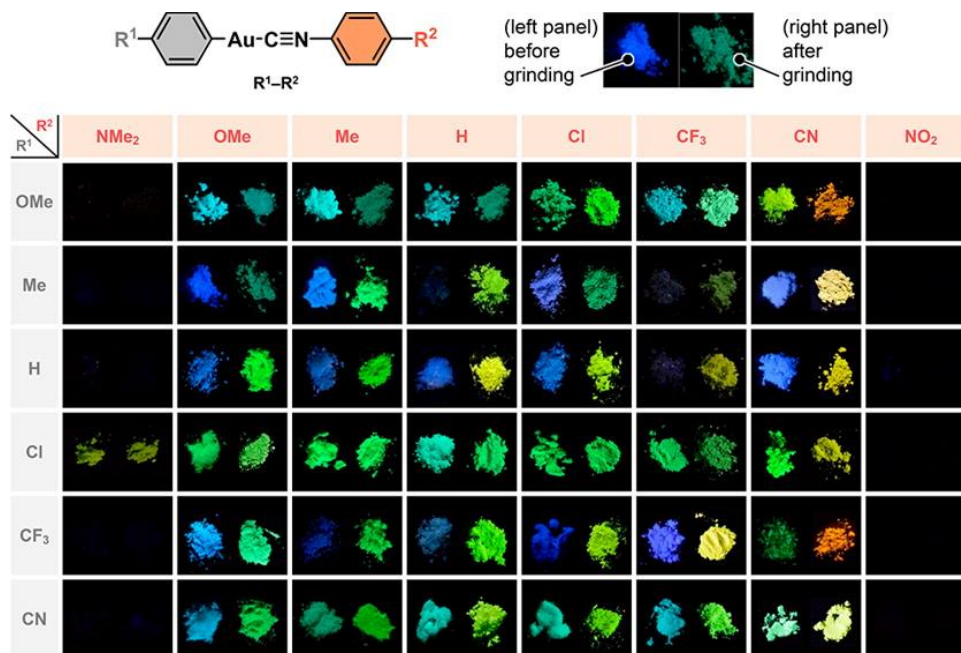
Figure 1.12. Color Tuning of ML Materials. Emission before and after grinding of donor and acceptor substituted Au(I) complexes. Published with permission from Ito *et al.*, *J. Am. Chem. Soc.* **2016**, *138*, 6252–6260. Copyright American Chemical Society 2016.[85]

1.6.2 Mechanochromic Luminescence of Difluoroboron β–Diketonates

Difluoroboron β-diketonate (BF$_2$bdk) materials display impressive optical properties including high extinction coefficients,[12] room temperature phosphorescence in poly(lactic acid) matrices that is sensitive to molecular weight effects,[86] efficient solid-state emission, as well as ML behavior.[87] They are also easily synthesized from a variety of commercially available starting materials. Additionally, certain BF$_2$bdk ML materials self-erase at room temperature and can withstand multiple cycles of smearing and annealing without degradation of ML properties.[88] The first reported example of an ML active BF$_2$bdk by Fraser *et al.,* was the avobenzone derivative BF$_2$AVB.[89] Mechanical perturbation of BF$_2$AVB thin films on weighing paper elicited an emission response that could be erased by gentle heating. At room temperature, the smeared emission gradually faded back to the original unperturbed state after a few minutes, demonstrating self-erasing (i.e. smeared state recovery) behavior. Films could be sheared and erased multiple times without degradation of optical properties. It was also discovered that different polymorphs of BF$_2$AVB could be accessed, which displayed different optical and mechanical properties.[90] While ML was barely detectable for brittle green crystals, more elastic crystals with cyan emission could also be deformed to produced yellow emission.

Figure 1.13. Film of BF$_2$AVB on Weigh Paper Showing ML. Published with permission by Fraser *et al.*, *J. Am. Chem. Soc.* **2010**, *132*, 2160–2162. Copyright of the American Chemical Society 2010.[91]

In addition to BF$_2$AVB, many other BF$_2$bdk ML materials have been synthesized. For instance, the Fraser lab has modulated optical properties of stimuli responsive BF$_2$bdk materials

via alkyl chain length,[92,93] substitution at the α-position, and with arenes substitution.[30,88] Recently, Sket *et al.*, have shown that the ML active, methoxy-substituted BF_2bdk 1-phenyl-3-(3,5-dimethoxyphenyl)-propane-1,3-dione can be crystallized as uniquely emissive polymorphs whose formation is partially governed by the different conformations of the methoxy substituents.[73] Furthermore, heavy atom substitution results in mechanochromic luminescence quenching (MLQ) where emission is quenched upon smearing due to enhanced intersystem crossing to the oxygen sensitive triplet state.[15] Additionally, the MLQ properties of BF_2bdks with C_{12} alkyl chains can be modulated through halide substitution.[77] And in a follow-up study, it was found that the triplet energies of iodo-substituted BF_2bdks were sensitive to alkyl chain length.[93]

Though a variety of ML active materials have been developed, some BF_2bdk compounds also show reversible emission changes in response to thermal stimuli. Recently, thiophene (BF_2tbmOC12) and furan (BF_2fbmOC12) BF_2bdks analogues have shown emission shifts produced *via* thermal and mechanical perturbation.[94] In particular, weigh paper films of BF_2fbmOC12 showed dynamic thermal responses depending on how heat was applied (Figure 1.14). Films were prepared by smearing a small amount of dye across a 5 x 5 cm sheet of weigh paper. When films were gently heated with a heat gun, uniform green emission was observed. However, when heated above the melting temperature and cooled in air (i.e. melt quenching) films glowed orange under UV light. Orange emission could also be produced by stamping films with heated objects in order to produce the melt quench state. The green emissive films were regenerated through gentle heating of melt quenched films, which demonstrated switchable thermoresponsive luminescence for BF_2fbmOC12. Like most ML active BF_2bdk materials, the emission change induced by thermal stimulation is the result of a crystalline (green) to amorphous (orange) phase transition.
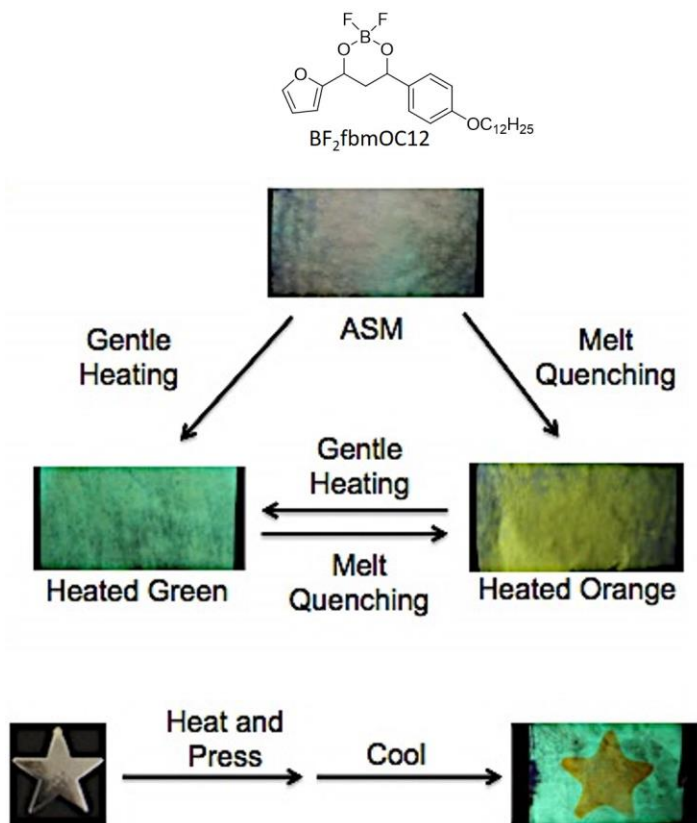
Figure 1.14. Thermally Responsive Behavior of $BF_2fbmOC12$.

1.6.3 Mechanistic Investigation of ML-Active BF_2bdks

Based on these examples, it is clear that the thermally and mechanically produced emission changes of BF_2bdk materials are due to the formation of uniquely emissive states (i.e. crystalline, amorphous). Through the analysis of packing motifs, strategies for tuning the emission of crystalline species can be developed and tested. However, information about the emissive species in the amorphous state is more difficult to obtain. Mechanistic studies of BF_2bdk ML by Sun *et al*., suggest that optical responses are the result of mechanically generated ground state aggregates (Figure 1.15).[61]

Spectroscopic investigation of monomeric, dimeric, and polymeric boron difluoride dibenzoylmethane (BF$_2$dbm) derivatives indicate that dyes can form face-to-face H-aggregates. As discussed previously, H-aggregates exhibit lower energy singlet energies compared to J-stacked dimers. Therefore, excitons could be funneled to mechanically generated H-aggregates, resulting in red-shifted emission. According to this mechanism, uniform amorphous states are not required in order to observe ML shifts because the overall emission of the smeared state is the result of exciton migration to low energy states.
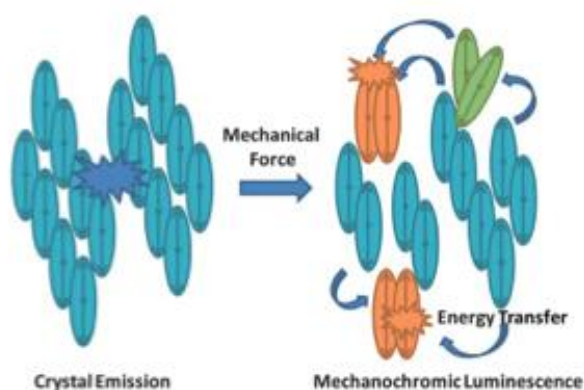
Figure 1.15. Proposed Mechanism of ML BF$_2$bdk Materials. Scheme describing mechanochromic luminescence (ML) of BF$_2$bdk materials. Published with permission by Zhang *et al.*, *J. Mater. Chem. C.* **2012**, *132*, 2160–2162. Copyright of Royal Society of Chemistry 2012.[61]

1.7 Goals

The goal of this work is to determine the structure property relationships and processing effects (e.g. substrate and film thickness) that determine the ML properties of β-diketonate materials. These properties include the emission of dyes before and after smearing as well as the rate of ML recovery at room temperature. Additionally, it was discovered that some β-diketones exhibit mechanically and thermally produced emission responses so these properties were also investigated. Many of these dyes also exhibit AIE in different THF/H$_2$O mixtures. Based on the

stimuli responsive properties investigated herein, design strategies are also presented for optimizing AIE and ML properties in both ligands and boron complexes.

1.8 References

1   G. Blasse and B. C. Grabmaier, *Luminescent Materials*, Springer, New York, NY, 1994.

2   R.-J. Xie, *Nitride Phosphors and Solid-State Lighting*, CRC Press, Boca Raton, FL, 2011.

3   A. M. Bagher, *Am. J. Opt. Photonics*, 2014, **2**, 32–36.

4   J. Gong, K. Sumathy, Q. Qiao and Z. Zhou, *Renew. Sustain. Energy Rev.*, 2017, **68**, 234–246.

5   A. Hagfeldt, G. Boschloo, L. Sun, L. Kloo and H. Pettersson, *Chem. Rev.*, 2010, **110**, 6595–6663.

6   A. S. Klymchenko, *Acc. Chem. Res.*, 2017, **50**, 366–375.

7   M. T. Z. Spence and I. D. Johnson, *The Molecular Probes Handbook : a Guide to Fluorescent Probes and Labeling Technologies*, Life Technologies Corporation, 2010.

8   Y. Jiang, *Mater. Sci. Eng. C*, 2014, **45**, 682–689.

9   Y. Sagara, S. Yamane, M. Mitani, C. Weder and T. Kato, *Adv. Mater.*, 2016, **28**, 1073–1095.

10   J. R. Lakowicz, *Principles of Fluorescence Spectroscopy*, Springer, New York, 2006.

11   L. D. Lavis and R. T. Raines, *ACS Chem. Biol.*, 2014, **9**, 855–866.

12   E. Cogné-Laage, J.-F. Allemand, O. Ruel, J.-B. Baudin, V. Croquette, M. Blanchard-

Desce and L. Jullien, *Chem. - A Eur. J.*, 2004, **10**, 1445–1455.

13   J. B. Grimm, B. P. English, J. Chen, J. P. Slaughter, Z. Zhang, A. Revyakin, R. Patel, J. J. Macklin, D. Normanno, R. H. Singer, T. Lionnet and L. D. Lavis, *Nat. Methods*, 2015, **12**, 244–250.

14   M. K. Kuimova, G. Yahioglu, J. A. Levitt and K. Suhling, *J. Am. Chem. Soc.*, 2008, **130**, 6672–6673.

15   G. Zhang, J. Lu and C. L. Fraser, *Inorg. Chem.*, 2010, **49**, 10747–10749.

16   D. V. O'Connor and D. Phillips, *Appl. Opt.*, 1986, **25**, 460–463.

17   X. Zhang, Y. Xiao, J. Qi, J. Qu, B. Kim, X. Yue and K. D. Belfield, *J. Org. Chem.*, 2013, **78**, 9153–9160.

18   A. J. Nichols, E. Roussakis, O. J. Klein and C. L. Evans, *Angew. Chem. Int. Ed. Engl.*, 2014, **53**, 3671–3674.

19   G. M. Palmer, A. N. Fontanella, S. Shan, G. Hanna, G. Zhang, C. L. Fraser and M. W. Dewhirst, *Nat. Protoc.*, 2011, **6**, 1355–1366.

20   D. Lee, X. Ma, J. Jung, E. J. Jeong, H. Hashemi, A. Bregman, J. Kieffer and J. Kim, *Phys. Chem. Chem. Phys.*, 2015, **17**, 19096–19103.

21   Y. Yang, R. P. Hughes and I. Aprahamian, *J. Am. Chem. Soc.*, 2012, **134**, 15221–15224.

22   J. E. Kwon, S. S. Y. Park and S. S. Y. Park, *J. Am. Chem. Soc.*, 2013, **135**, 11239–11246.

23   S. Kumar, P. Singh, P. Kumar, R. Srivastava, S. K. Pal and S. Ghosh, *J. Phys. Chem. C*, 2016, **120**, 12723–12733.

24 B. Jędrzejewska, A. Zakrzewska, G. Mlostoń, Š. Budzák, K. Mroczyńska, A. M. Grabarz, M. A. Kaczorowska, D. Jacquemin and B. Ośmiałowski, *J. Phys. Chem. A*, 2016, **120**, 4116–4123.

25 J. R. Hemmer, S. O. Poelma, N. Treat, Z. A. Page, N. D. Dolinski, Y. J. Diaz, W. Tomlinson, K. D. Clark, J. P. Hooper, C. Hawker and J. Read de Alaniz, *J. Am. Chem. Soc.*, 2016, **138**, 13960–13966.

26 A. Felouat, A. D'Aléo, A. Charaf-Eddin, D. Jacquemin, B. Le Guennic, E. Kim, K. J. Lee, J. H. Woo, J.-C. Ribierre, J. W. Wu and F. Fages, *J. Phys. Chem. A*, 2015, **119**, 6283–6295.

27 I. A. Karpenko, Y. Niko, V. P. Yakubovskyi, A. O. Gerasov, D. Bonnet, Y. P. Kovtun and A. S. Klymchenko, *J. Mater. Chem. C*, 2016, **4**, 3002–3009.

28 J. Grolleau, F. Gohier, C. Cabanetos, M. Allain, S. Legoupy and P. Frère, *Org. Biomol. Chem.*, 2016, **14**, 10516–10522.

29 L. Giordano, V. V Shvadchak, J. A. Fauerbach, E. A. Jares-Erijman and T. M. Jovin, *J. Phys. Chem. Lett*, 2012, **3**, 1011–1016.

30 W. A. Morris, M. Kolpaczynska and C. L. Fraser, *J. Phys. Chem. C*, 2016, **120**, 22539–22548.

31 R. Ghosh and D. K. Palit, *J. Phys. Chem. A*, 2015, **119**, 11128–11137.

32 J. Zhao and Y. Yang, *J. Mol. Liq.*, 2016, **220**, 735–741.

33 M. A. Haidekker, T. P. Brady, D. Lichlyter and E. A. Theodorakis, *Bioorg. Chem.*, 2005, **33**, 415–425.

34   S. Sasaki, G. P. C. Drummen and G. Konishi, *J. Mater. Chem. C*, 2016, **4**, 2731–2743.

35   R. Hu, E. Lager, A. Aguilar-Aguilar, J. Liu, J. W. Y Lam, H. H. Y Sung, I. D. Williams, Y. Zhong, K. Sing Wong, E. Peñ a-Cabrera and B. Z. Tang, *J. Phys. Chem. C.*, 2009, **113**, 1845–15853.

36   M. K. Kuimova, *Phys. Chem. Chem. Phys.*, 2012, **14**, 12671–86.

37   A. P. Demchenko, Y. Mély, G. Duportail and A. S. Klymchenko, *Biophys. J.*, 2009, **96**, 3461–3470.

38   A. Marini, A. Muñoz-Losa, A. Biancardi and B. Mennucci, *J. Phys. Chem. B*, 2010, **114**, 17128–17135.

39   O. A. Kucherak, S. Oncul, Z. Darwich, D. A. Yushchenko, Y. Arntz, P. Didier, Y. Mély and A. S. Klymchenko, *J. Am. Chem. Soc.*, 2010, **132**, 4907–4916.

40   R. Kreder, K. A. Pyrshev, Z. Darwich, O. A. Kucherak, Y. Mély and A. S. Klymchenko, *ACS Chem. Biol.*, 2015, **10**, 1435–1442.

41   E. Lippert, *A Phys. Sci.*, 1955, **10**, 541–545.

42   N. Mataga, Y. Kaifu and M. Koizumi, *Bull. Chem. Soc. Jpn.*, 1956, **29**, 465–470.

43   A. P. Demchenko, K.-C. Tang and P.-T. Chou, *Chem. Soc. Rev.*, 2013, **42**, 1379–1408.

44   O. A. Kucherak, L. Richert, Y. Mély and A. S. Klymchenko, *Phys. Chem. Chem. Phys.*, 2012, **14**, 2292.

45   S. Park, J. E. Kwon and S. Y. Park, *Phys. Chem. Chem. Phys.*, 2012, **14**, 8878–8884.

46   J. E. Kwon and S. Y. Park, *Adv. Mater.*, 2011, **23**, 3615–3642.

47   A. S. Klymchenko, V. G. Pivovarenko, T. Ozturk and A. P. Demchenko, *New J. Chem.*, 2003, **27**, 1336–1343.

48   V. V. Shynkar, A. S. Klymchenko, C. Kunzelmann, G. Duportail, C. D. Muller, A. P. Demchenko, J.-M. Freyssinet and Y. Mely, *J. Am. Chem. Soc.*, 2007, **129**, 2187–2193.

49   J. Mei, Y. Hong, J. W. Y. Lam, A. Qin, Y. Tang and B. Z. Tang, *Adv. Mater.*, 2014, **26**, 5429–5479.

50   T. Han, X. Gu, J. W. Y. Lam, A. C. S. Leung, R. T. K. Kwok, T. Han, B. Tong, J. Shi, Y. Dong and B. Zhong Tang, *J. Mater. Chem. C*, **4**, 10430–10434.

51   Z. Li, Y. Q. Dong, J. W. Y. Lam, J. Sun, A. Qin, M. Häußler, Y. P. Dong, H. H. Y. Sung, I. D. Williams, H. S. Kwok and B. Z. Tang, *Adv. Funct. Mater.*, 2009, **19**, 905–917.

52   Y. Hong, J. W. Y. Lam and B. Z. Tang, *Chem. Commun.*, 2009, **0**, 4332–4353.

53   C. Dai, D. Yang, X. Fu, Q. Chen, C. Zhu, Y. Cheng and L. Wang, *Polym. Chem.*, 2015, **6**, 5070–5076.

54   S. Chen, H. Wang, Y. Hong and B. Z. Tang, *Mater. Horiz.*, 2016, **3**, 283–293.

55   X. Y. Shen, Y. J. Wang, E. Zhao, W. Z. Yuan, Y. Liu, P. Lu, A. Qin, Y. Ma, J. Z. Sun and B. Z. Tang, *J. Phys. Chem. C*, 2013, **117**, 7334–7347.

56   Y. Gong, Y. Tan, J. Liu, P. Lu, C. Feng, W. Z. Yuan, Y. Lu, J. Z. Sun, G. He and Y. Zhang, *Chem. Commun.*, 2013, **49**, 4009–4011.

57   R. Yoshii, A. Hirose, K. Tanaka and Y. Chujo, *Chem. - A Eur. J.*, 2014, **20**, 8320–8324.

58   M. Kasha, *Radiat. Res.*, 1963, **20**, 55–70.

59   D. Cheng, Y. Pan, L. Wang, Z. Zeng, L. Yuan, X. Zhang and Y.-T. Chang, *J. Am. Chem. Soc.*, 2017, **139**, 285–292.

60   S. Varghese and S. Das, *J. Phys. Chem. Lett*, 2011, **2**, 863–873.

61   X. Sun, X. Zhang, X. Li, S. Liu and G. Zhang, *J. Mater. Chem.*, 2012, **22**, 17332–17339.

62   F. Würthner, T. E. Kaiser and C. R. Saha-Möller, *Angew. Chemie*, 2011, **50**, 3376–3410.

63   M. Moßhammer, M. Strobl, M. Kühl, I. Klimant, S. M. Borisov and K. Koren, *ACS Sensors*, 2016, **1**, 681−687.

64   C. Huang, X. Peng, D. Yi, J. Qu and H. Niu, *Sensors Actuators B Chem.*, 2013, **182**, 521–529.

65   X. Wang, O. S. Wolfbeis and R. J. Meier, *Chem. Soc. Rev.*, 2013, **42**, 7834–7869.

66   S. Schreml, R. J. Meier, K. T. Weiß, J. Cattani, D. Flittner, S. Gehmert, O. S. Wolfbeis, M. Landthaler and P. Babilas, *Exp. Dermatol.*, 2012, **21**, 951–953.

67   X. Zhang, Z. Chi, Y. Zhang, S. Liu and J. Xu, *J. Mater. Chem. C*, 2013, **1**, 3376–3390.

68   K. Nagura, S. Saito, H. Yusa, H. Yamawaki, H. Fujihisa, H. Sato, Y. Shimoikeda and S. Yamaguchi, *J. Am. Chem. Soc.*, 2013, **135**, 10322–10325.

69   M. Jin, T. Seki and H. Ito, *Chem. Commun.*, 2016, **52**, 8083–8086.

70   F. Ciardelli, G. Ruggeri and A. Pucci, *Chem. Soc. Rev.*, 2013, **42**, 857–870.

71   J. Wu, Y. Cheng, J. Lan, D. Wu, S. Qian, L. Yan, Z. He, X. Li, K. Wang, B. Zou and J. You, *J. Am. Chem. Soc.*, 2016, **138**, 12803–12812.

72   X. Zhang, Z. Ma, Y. Yang, X. Zhang and Y. Wei, *J. Mater. Chem. C*, 2014, **2**, 8932–

8938.

73   P. Galer, R. C. Korošec, M. Vidmar and B. Šket, *J. Am. Chem. Soc.*, 2014, **136**, 7383–
      7394.

74   M. Li, Q. Zhang, J.-R. Wang and X. Mei, *Chem. Commun.*, 1128, **52**, 11288–11291.

75   S. J. Yoon, J. W. Chung, J. Gierschner, K. S. Kim, M. G. Choi, D. Kim and S. Y. Park, *J. Am. Chem. Soc.*, 2010, **132**, 13675–13683.

76   Y. Sagara, T. Komatsu, T. Ueno, K. Hanaoka, T. Kato and T. Nagano, *J. Am. Chem. Soc.*, 2014, **136**, 4273–4280.

77   W. A. Morris, T. Liu and C. L. Fraser, *J. Mater. Chem. C*, 2015, **3**, 352–363.

78   P. S. Hariharan, N. S. Venkataramanan, D. Moon and S. P. Anthony, *J. Phys. Chem. C*, 2015, **119**, 9460–9469.

79   K. Mizuguchi, H. Kageyama and H. Nakano, *Mater. Lett.*, 2011, **65**, 2658–2661.

80   K. Chung, M. S. Kwon, B. M. Leung, A. G. Wong-Foy, M. S. Kim, J. Kim, S. Takayama, J. Gierschner, A. J. Matzger and J. Kim, *ACS Cent. Sci.*, 2015, **1**, 94–102.

81   Y. Shirota and H. Kageyama, *Chem. Rev.*, 2007, **107**, 953–1010.

82   Y. Shirota, *J. Mater. Chem.*, 2005, **15**, 75–93.

83   G. Zogra and A. Newman, *J. Pharm. Sci.*, 2017, **106**, 5–27.

84   S. Yagai, T. Seki, H. Aonuma, K. Kawaguchi, T. Karatsu, T. Okura, A. Sakon, H. Uekusa and H. Ito, *Chem. Mater.*, 2016, **28**, 234–241.

85   T. Seki, Y. Takamatsu and H. Ito, *J. Am. Chem. Soc.*, 2016, **138**, 6252–6260.

86   G. Zhang, S. E. Kooi, J. N. Demas and C. L. Fraser, *Adv. Mater.*, 2008, **20**, 2099–2104.

87   G. Zhang, J. P. Singer, S. E. Kooi, R. E. Evans, E. L. Thomas and C. L. Fraser, *J. Mater. Chem.*, 2011, **21**, 8295–8299.

88   T. Liu, A. D. Chien, J. Lu, G. Zhang and C. L. Fraser, *J. Mater. Chem.*, 2011, **21**, 8401–8408.

89   G. Zhang, J. Lu, M. Sabat and C. L. Fraser, *J. Am. Chem. Soc.*, 2010, **132**, 2160–2162.

90   G. R. Krishna, M. S. R. N. Kiran, C. L. Fraser, U. Ramamurty and C. M. Reddy, *Adv. Funct. Mater.*, 2013, **23**, 1422–1430.

91   G. Zhang, J. Lu, M. Sabat and C. L. Fraser, *J. Am. Chem. Soc.*, 2010, **132**, 2160–2162.

92   N. D. Nguyen, G. Zhang, J. Lu, A. E. Sherman and C. L. Fraser, *J. Mater. Chem.*, 2011, **21**, 8409–8415.

93   W. A. Morris, M. Sabat, T. Butler, C. A. DeRosa and C. L. Fraser, *J. Phys. Chem. C*, 2016, **120**, 14289–14300.

94   W. A. Morris, T. Butler, M. Kolpaczynska and C. L. Fraser, *Mater. Chem. Front.*, 2017, **1**, 158–166.

Chapter 2

Mechanochromic Luminescence and Aggregation Induced Emission in Metal-Free β-Diketones
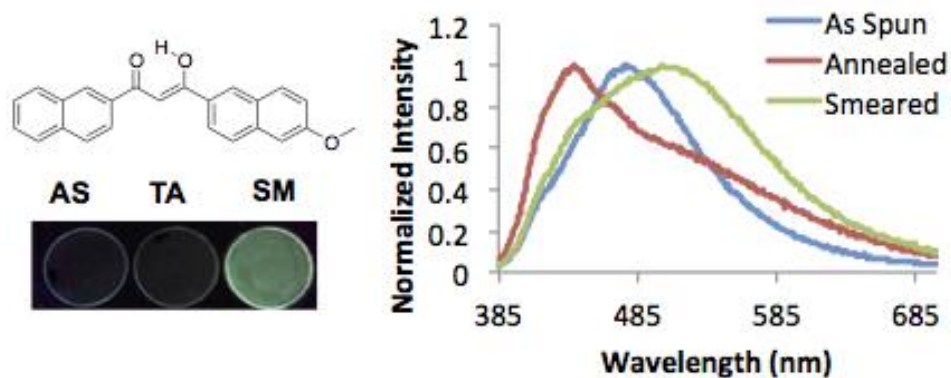
2.1 Introduction

As discussed in the introduction, compounds that show ML are of interest for numerous applications.[1,2] Previously, we described difluoroboron coordinated β-diketonates (BF$_2$bdk) with efficient solid-state emission that also exhibit ML.[3] Furthermore, these materials can self heal at room temperature and be smeared and erased multiple times without degradation.[4] The effects of arene size,[5] alkyl chain length[6] and halide substitution,[7–9] have been investigated, however ML properties of uncoordinated bdk ligands were not observed. In the course of exploring substituent and processing effects on ML properties for BF$_2$bdk complexes with dinaphthoyl methane scaffolds, it was discovered that the para-methoxy substituted derivative, dnmOMe, shows ML absent coordination to boron. High contrast blue-green emission is visible when dnmOMe thin films are exposed to a mechanical stimulus. This also dye exhibits aggregation induced emission (AIE), a phenomenon previously unobserved in bdk materials.

In order to characterize the stimuli-responsive properties of boron-free dnmOMe, its absorption and emission spectra were measured in a variety of organic solvents. Additionally, THF/H$_2$O solutions were prepared in order to evaluate AIE behavior. In the solid state, ML and room-temperature recovery properties were investigated on spin cast films. Structural and morphological characterization was done using powder x-ray diffraction and atomic force microscopy, respectively. The results of this study are presented below.
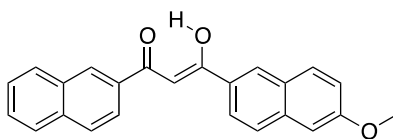
Figure 2.1. Chemical Structure of dnmOMe.

2.2 Results and Discussion

2.2.1 Synthesis

Methoxy-dinaphthoyl methane, dnmOMe, was prepared via Claisen condensation from 6-methoxy-naphthanone and methyl- 2-naphthoate (Figure 2.1). The ligand dnmOMe was isolated as a light tan-colored powder that is soluble in common organic solvents such as THF, acetone, CH2Cl2, and DMSO.

2.2.2 Optical Properties in Solution

The absorption and emission spectra emission spectra of dnmOMe were recorded in CH_2Cl_2 (Figure S2.1; Appendix A). In DCM solution, the optical properties of dnmOMe are unremarkable. An absorption peak is observed at 378 nm with a molar absorptivity of 34000 M^{-1} cm^{-1}. To the eye, dnmOMe appears non-emissive, however a peak is observed at 443 nm in the emission spectrum. The quantum yield of dnmOMe in CH2Cl2 is negligible (FB0.002). Lifetime measurements of dnmOMe solutions showed short lifetimes (t = 0.18 ns) and multi-exponential decay, which suggests that multiple emissive species are present in solution. One possible explanation for this observation is that emission from both keto and enol forms are detected. Both forms are observed in the 1H NMR spectrum, as previously reported for bdks.[10] Different naphthyl ring rotomers are also possible.

2.2.3 Computational and Solvatochromic Studies

Density functional theory (DFT) calculations of the HOMO and LUMO molecular orbitals using B3LYP/6-31G(d) point to an intramolecular charge transfer (ICT) transition from the methoxy substituted major donor ring to the rest of the molecule, suggesting solvatochromism might be present for dnmOMe (Figure. 2.2).
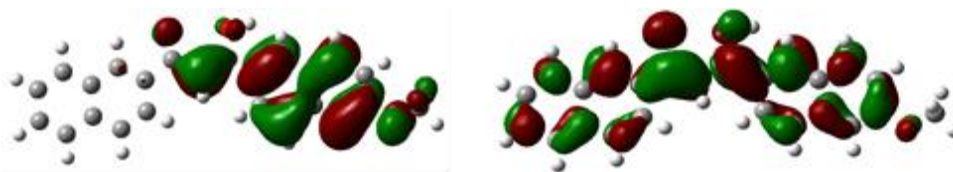
Figure 2.2. Molecular Orbitals of dnmOMe. HOMO (left) and LUMO (right) molecular orbitals of dnmOMe.

To explore this possibility, absorption and emission spectra of dnmOMe were measured in a variety of solvents with a dnmOMe concentration of 10^{-5} M (Figure 2.3). The peak absorptions of dnmOMe showed maxima between 378–379 nm and similar relative absorption intensities ranging from 1.69 in toluene to 1.91 in THF. Under UV-excitation dnmOMe showed no emission in nonpolar solvents. As the solvent polarity was increased, blue emission is evident. The emission spectra showed a bathochromic shift from 422 nm in hexanes to 466 nm in acetonitrile, and the emission intensity was larger in polar solvents. The data were fit according to Lippert–Mataga[11,12] theory in order to further evaluate the solvatochromic behavior of dnmOMe (Figure S2.2; Appendix A). The plot of Stokes shift ($\Delta\nu$) versus the solvent polarity parameter (Δf) shows a slightly positive trend with a slope of 1850 indicating moderate solvatochromism. In addition to solvatochromism, dnmOMe shows sensitivity to base due to the acidic proton in uncoordinated β-diketones (e.g. α-methylene or enol depending on the tautomer). Emission in CH_3CN is quenched upon the addition of triethylamine (TEA) and can be recovered with the addition of acetic acid (Figure S2.3, Appendix A).
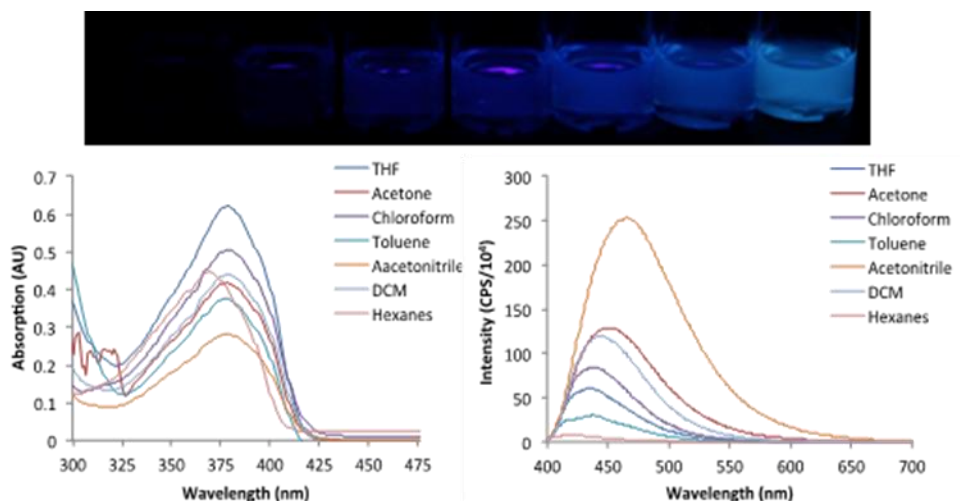
Figure 2.3. Solvatochromism of dnmOMe. Top: UV excited dnmOMe in different solvents, from left to right: hexanes, toluene, DCM, acetone, THF, chloroform, acetonitrile. Bottom: Absorption (left) and emission (right) spectra of dnmOMe (10^{-5} M) in different solvents.

2.2.4 Aggregation Induced Emission

The AIE properties of dnmOMe were investigated by measuring the absorption (Figure S2.4; Appendix A) and emission (Figure S2.5; Appendix A) spectra of THF/H2O mixtures with increasing H2O fractions (Figure 2.4).[13] As the water fraction was increased from 0–70% a gradual increase in emission intensity was observed, which demonstrates AIE behavior for dnmOMe. Over nearly the same water fraction range, a 47 nm red-shift in emission wavelength from 438 nm in pure THF (blue) to 485 nm in 80% water (blue-green) was observed. When the water fraction was increased above 70% the solution became cloudy accompanied by a dramatic decrease in emission intensity and a hypsochromic wavelength shift. At this point, it is likely that aggregates reached a critical size and dnmOMe precipitate is formed. As more aggregates precipitated out of solution the emission decreased until eventually, in 100% water, the mixture was essentially non-emissive. Though dnmOMe shows AIE, in the solid state pristine samples appeared non-emissive to the eye. This suggests that optical properties of dnmOMe solids are

41

sensitive to molecular packing and different optical properties may be accessible through mechanical perturbation.
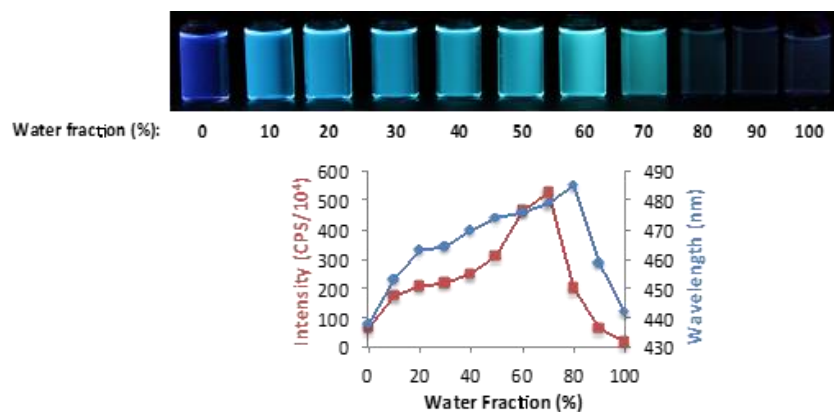
Figure 2.4. Aggregation Induced Emission of dnmOMe. Top: THF/H$_2$O dnmOMe mixtures with increasing water fractions. Bottom: Plot of emission intensity (red) and peak emission wavelength (blue) versus water fraction.

2.2.5 Mechanochromic Luminescence

The ML properties of dnmOMe were explored using spin-cast films on glass prepared from a 10^{-3} M THF solution as previously described.[3] The annealing temperature was determined experimentally by monitoring the peak wavelength as a function of temperature (Figure S2.6; Appendix A).[28] Though the dnmOMe emission maximum was largely independent of annealing temperature, the full width at half maximum (FWHM) was minimized at 140 ℃, thus samples were annealed at this temperature. Differential scanning calorimetry thermograms show that dnmOMe has a melting point (T_m) of 164 ℃ and crystallization temperature (T_c) of 126 ℃, so it is not necessary to heat dnmOMe thin films above T_m to anneal and change the optical properties, and presumably aggregation state of the sample (Figure S2.7; Appendix A). After cooling to room temperature, annealed samples were gently smeared with a cotton swab to induce a bathochromic shift in emission.

The optical properties and solid-state quantum yields of dnmOMe in as spun (AS), thermally annealed (TA) and smeared (SM) states were also measured. In the as spun state (i.e. prior to annealing), films of dnmOMe showed faint blue emission (Figure 2.5) (λ_{em} = 475 nm, FWHM = 109 nm, F = 3.3%). After the sample was annealed at 140 1C, no luminescence was observable to the eye, yet emission spectra showed a broad peak at 440nm(FWHM= 136 nm, Φ = 3.6%). Some fine structure emerged in the blue-shifted portion (385–480 nm) of the spectrum, however a shoulder was observed near 500 nm, which contributed to the increased FWHM observed in the annealed state. In contrast, the smeared state of dnmOMe was blue-green in color with a peak emission of 503 nm and FWHM of 165 nm, which was broader than observed for AS and TA states. Furthermore, the quantum yield increased to 10.6% compared to 3.3% and 3.6% in the AS and TA states, respectively. A contrast ratio of 22.8 was estimated for dnmOMe by comparing the ratio of the peak intensities in the SM and TA states (Figure S2.8; Appendix A).[14] Pre-exponential weighted lifetimes of dnmOMe were also measured for the films in different states. Decay curves for solid state emission were fit to multi-exponential functions indicating the formation of ground-state dimers or excimers which is typical for solid state luminescence.[15,16] In the AS state, dnmOMe exhibited a lifetime of 4.7 ns, which decreased to 1.2 ns after annealing. Upon smearing, the lifetime increased to 2.3 ns. Excitation spectra of dnmOMe in each state monitored at 504 nm were also collected (Figure S2.9, Appendix A). The shape of each excitation spectrum is similar, however the peak intensity for the SM sample was higher than for AS and TA samples.
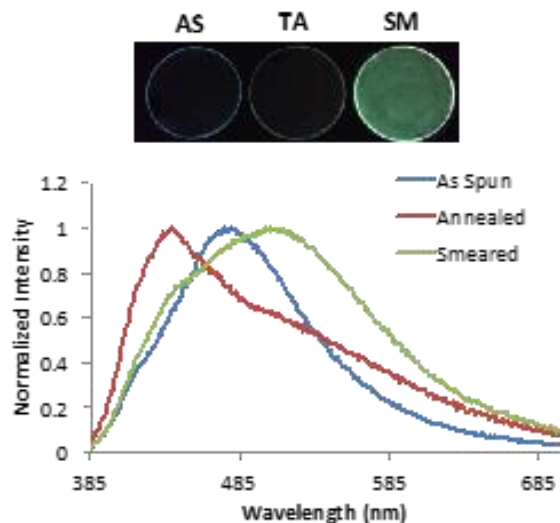
Figure 2.5. Mechanochromic Luminescence of dnmOMe. Thin films of dnmOMe (top) and emission spectra corresponding to as spun, thermally annealed, and smeared states (bottom).

Previously, certain smeared BF2bdks thin films have been shown to spontaneously recover the initial (i.e. annealed) emissive state under ambient conditions.[4] This dynamic erasing property is tunable through molecular structure and processing, making it attractive for use in certain applications. Since dnmOMe contains the same β-diketone moiety absent deprotonation and boron coordination, we were curious to see if ligand films also showed spontaneous recovery at room temperature. The recovery time of dnmOMe was measured by smearing a thin film of the dye and monitoring the emission over time (Figure 2.6). The peak emission of dnmOMe blue shifted immediately after smearing. After only ten minutes, the peak shifted from 503 nm (smeared state) to 445 nm. After one hour, the peak emission had entirely recovered to 440 nm, the peak emission in the annealed state. After a day, the FWHM of recovered dnmOMe thin films had decreased compared to the FWHM corresponding to the annealed sample (133 nm in TA vs. 106 nm in recovered). This is opposite to the trend that is typically observed in BF2bdks where the FWHM increases upon smearing and decreases upon annealing.[4] One possible explanation is that emission

44

in the annealed state is broadened by emission from certain aggregate species formed during the fabrication of the film and mechanical stimulus is required to dissociate these species. This phenomenon has been observed in other mechanochromic materials where the mechanical grinding of certain tetraphenylethene powders was required in order to produce a wavelength change upon annealing.
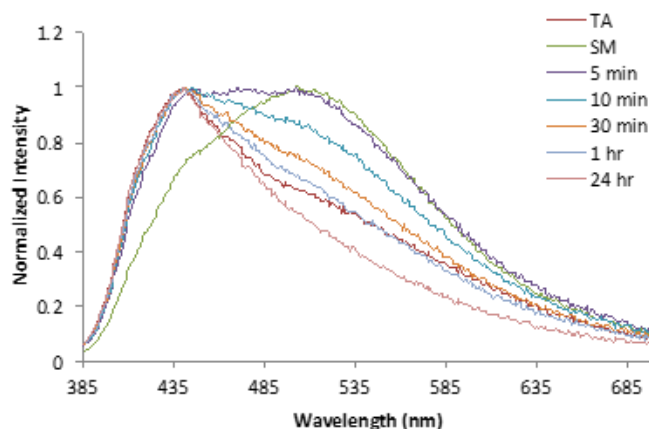
Figure 2.6. Room Temperature ML Recovery of dnmOMe. Emission spectral changes of dnmOMe thin film samples monitored over time after smearing (TA = thermally annealed; SM = smeared).

2.2.6 Solid State Characterization

Structural characterization was conducted by XRD, comparing annealed and smeared dnmOMe thin film patterns with those corresponding to the pristine powder (Figure 2.7). In the AS state, XRD patterns of dnmOMe thin films appeared amorphous. The crystallinity of dnmOMe in the annealed state was demonstrated by sharp peaks at ~13.4° and ~18.0°, which corresponded to peaks observed in the powder pattern of dnmOMe. When smeared, no peaks were observed, indicating that dnmOMe is amorphous in the smeared state.
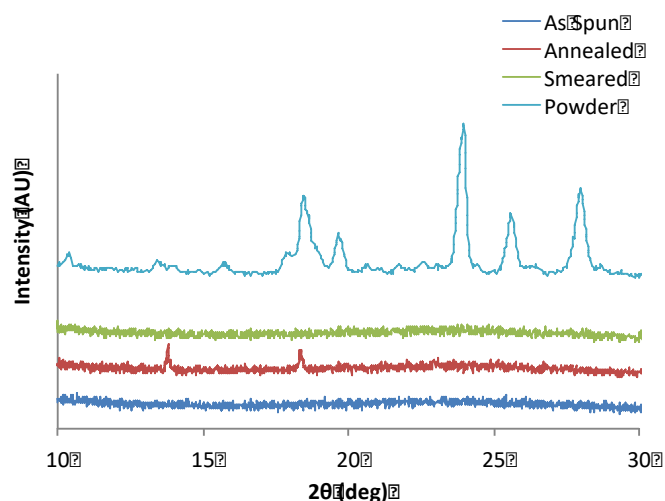
Figure 2.7. XRD Patterns of dnmOMe. Patterns of dnmOMe as a powder, and thin films in the as spun, annealed, and smeared states.

AFM images of spin cast films in as spun, thermally annealed and recovered states were recorded in order to study the morphology of dnmOMe (Figure 2.8). As spun films were used to approximate the morphology of the amorphous smeared state because quality images of smeared samples could not be obtained due to the fast rate of spontaneous recovery. The image of dnmOMe in the recovered state was obtained using a thin film one day after smearing to ensure the samples had entirely recovered prior obtaining images. In the as spun state, dnmOMe films were heterogeneous and showed plate-like features with large variation in size and shape. When annealed, dnmOMe formed both rod-like and plate-like crystallites. Compared to AS films, features are much larger with more defined shape post annealing. Images of dnmOMe after recovery showed much more disorder than both AS and TA films. Features were smaller overall, however a wider variance in particle size and shape is observed. These results are consistent with XRD patterns, which showed diffraction peaks for annealed samples but none were observed after smearing.[17]
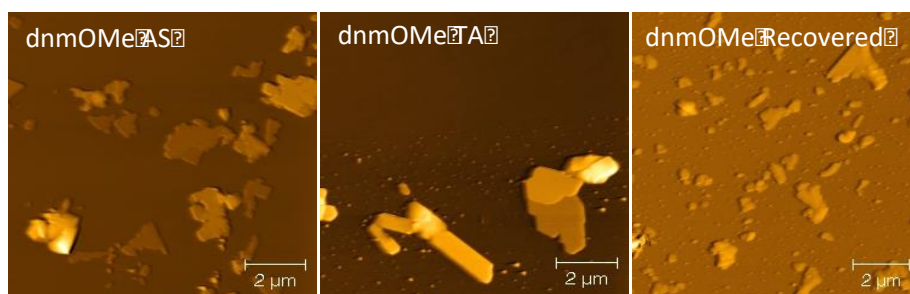
Figure 2.8. AFM Images of dnmOMe. Images of films in as spun (AS), thermally annealed (TA) and recovered states.

2.2.7 Conclusions

In summary, the β-diketone dnmOMe showed unexceptional optical properties in DCM, but a positive solvatochromic effect was observed when solvents were compared. AIE was demonstrated by measuring the emission of different THF/H2O ratios. High contrast ML with rapid recovery was observed in dnmOMe thin films and structural characterization indicates that the emissive smeared state is amorphous while the non- emissive annealed state is crystalline. Because β-diketones are readily deprotonated to form diketonates, and can coordinate to metals and main group elements, this points to additional sensing possibilities for these responsive optical materials. Substituent effects on solid-state dinaphthoyl methane properties and comparison to corresponding boron complexes serve as subjects of future reports.

2.3 Experimental Procedures

2.3.1 Materials

Solvents THF, and CH_2Cl_2, were dried by previously reported methods. Reactions were monitored using silica TLC plates. Compounds purchased from Sigma-Aldrich, and TCI were reagent grade and used without purification.

2.3.1 Methods

^{1}H NMR spectra (500 MHz) were recorded on a Varian Unity Inova spectrometer in deuterated DMSO. ^{13}C NMR spectra (600 MHz) were recorded on a Varian Unity Inova spectrometer in deuterated DMSO. Spectra were referenced to the signals for residual protio-chloroform at 7.26 ppm, and protio-DMSO at 2.50 ppm and coupling constants were reported in Hz. Mass spectra were recorded using an Applied Biosystems 4800 spectrometer with a MALDI TOF/TOF analyzer. UV-vis spectra were recorded on a Hewlett-Packard 8452A diode-array spectrophotometer. Steady-state fluorescence emission and excitation spectra were recorded on a Horiba Fluorolog-3 Model FL3-22 spectrofluorometer (double-grating excitation and double-grating emission monochromator). An excitation wavelength λ_{ex} of 369 nm was used for all emission spectra collected in solution and the solid state. Excitation spectra were monitored at 504 nm. Time-correlated single-photon counting (TCSPC) fluorescence lifetime measurements were performed with a NanoLED-370 (λ_{ex} = 369 nm) excitation source and a DataStation Hub as the SPC controller. Lifetime data were analyzed with DataStation v2.4 software from Horiba Jobin Yvon. Fluorescence quantum yields, φ_F, in CH_2Cl_2 were calculated versus anthracene as the standard using the following values: Φ_F anthracene in ethanol = 0.27, n_D ethanol = 1.36, n_D CH_2Cl_2 = 1.424. Optically dilute CH_2Cl_2 solutions of all samples were prepared in 1 cm path length quartz cuvettes with absorbances <0.1 (a.u.). Solid-state quantum yield were performed using a F-3029 Quanta-Φ Integrating Sphere from Horiba Scientific and analyzed using FluorEssence software. The sample morphologies of spin-cast films were characterized by Atomic Force Microscopy (AFM) (Digital Image, DI 3000) in tapping mode and the resulting images were processed using Gwyddion software version 2.31. Powder XRD patterns were obtained using a Panalytical X'Pert Pro MPD diffractometer operating at 40kV and 40 ma using Cu Kα radiation. Differential scanning

calorimetry (DSC) was done on the pristine powders using a TA Instruments DSC 2920 Modulated DSC and were analyzed using the Universal Analysis software V 2.3 from TA Instruments. Thermograms were recorded using the standard mode and a temperature ramp rate of 5 °C/min from 0 to 200 °C. The second scan was reported. Thermograms were analyzed using TA Instruments Universal Analysis software V 2.3 .

Fabrication of aggregates for AIE measurements. A 10^{-3} M stock solution of dnmOMe in THF was prepared. Aliquots of 100 µL of the stock solution were added to 10 mL volumetric flasks and diluted to volume with THF and H_2O in the proper ratios. Solutions were placed in a sonicator for 10 min before measuring absorption and emission spectra

Preparation of solutions for pH sensitivity measurements. A 2.25 mM solution of dnmOMe in CH_3CN was prepared and 1 mL portions of the stock solutions were added to three separate 10 mL volumetric flasks, which contained (1) no TEA or acetic acid, (2) TEA (0.457 g, 0.45 mM), (3) TEA (0.457 g, 0.45 mM) and acetic acid (0.409 g, 0.68 mM), respectively. Each solution was diluted to volume with CH_3CN and placed in the sonicator for 10 min prior to taking measurements.

Preparation of dnmOMe thin films. Thin films used for AFM, XRD, and ML characterization were prepared on 22 mm diameter glass coverslips purchased from Fisher Scientific. Solid-state quantum yield measurements were performed on films cast on glass coverslips with 12 mm diameter. With the exception of spin-cast films subjected to XRD, the films were fabricated by preparing 10^{-3} M solutions and applying ~10 drops to the coverslips rotating at 3,000 rpm. The films were dried *in vacuo* for 15 min before measurements or thermal annealing. Thin films subjected to XRD analysis were made from a saturated dnmOMe stock solution on 25 mm

diameter glass slides and were prepared by applying ~10 drops of the stock solution to the slides spinning at 1000 rpm.

2.4 Acknowledgements

2.5 References

1   Y. Q. Dong, J. W. Y. Lam and B. Z. Tang, *J. Phys. Chem. Lett.*, 2015, **6**, 3429–3436.

2   Y. Sagara, S. Yamane, M. Mitani, C. Weder and T. Kato, *Adv. Mater.*, 2016, **28**, 1073–1095.

3   G. Zhang, J. P. Singer, S. E. Kooi, R. E. Evans, E. L. Thomas and C. L. Fraser, *J. Mater. Chem.*, 2011, **21**, 8295–8299.

4   G. Zhang, J. Lu, M. Sabat and C. L. Fraser, *J. Am. Chem. Soc.*, 2010, **132**, 2160–2162.

5   T. Liu, A. D. Chien, J. Lu, G. Zhang and C. L. Fraser, *J. Mater. Chem.*, 2011, **21**, 8401–8408.

6   N. D. Nguyen, G. Zhang, J. Lu, A. E. Sherman and C. L. Fraser, *J. Mater. Chem.*, 2011, **21**, 8409–8415.

7   W. A. Morris, T. Liu and C. L. Fraser, *J. Mater. Chem. C*, 2015, **3**, 352–363.

8   G. Zhang, J. Lu and C. L. Fraser, *Inorg. Chem.*, 2010, **49**, 10747–10749.

9   W. A. Morris, M. Sabat, T. Butler, C. A. DeRosa and C. L. Fraser, *J. Phys. Chem. C*, 2016,

120, 14289–14300.

10   N. V. Belovaa, V. V. Slizneva, H. Oberhammerb and G. V. Giricheva, *J. Mol. Struct.*, 2010, **978**, 282–293.

11   E. Lippert, *A Phys. Sci.*, 1955, **10**, 541–545.

12   N. Mataga, Y. Kaifu and M. Koizumi, *Bull. Chem. Soc. Jpn.*, 1956, **29**, 465–470.

13   X. Y. Shen, Y. J. Wang, E. Zhao, W. Z. Yuan, Y. Liu, P. Lu, A. Qin, Y. Ma, J. Z. Sun and B. Z. Tang, *J. Phys. Chem. C*, 2013, **117**, 7334–7347.

14   J. Luo, L.-Y. Li, P. Y. Song and P. J. Pei, *Chem. - A Eur. J.*, 2011, **17**, 10515–10519.

15   X. Sun, X. Zhang, X. Li, S. Liu and G. Zhang, *J. Mater. Chem.*, 2012, **22**, 17332–17339.

16   A. G. Mirochnik, B. V. Bukvetskii, E. V. Fedorenko and V. E. Karasev, *Russ. Chem. Bull.*, 2004, **53**, 291–296.

17   Y. Lv, Y. Liu, X. Ye, G. Liu and X. Tao, *CrystEngComm*, 2015, **17**, 526–531.

Chapter 3

Mechanochromic Luminescence and Aggregation Induced Emission of Dinaphthoylmethane β-Diketones and their Boronated Counterparts
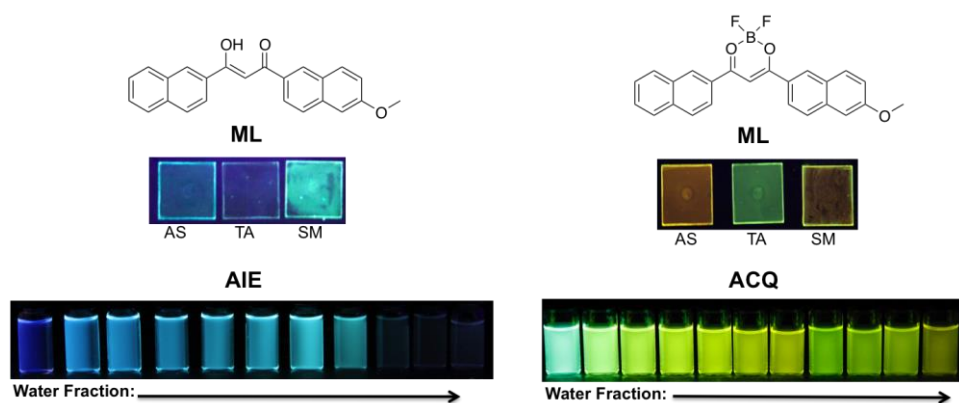
3.1. Introduction

To fabricate BF_2 coordinated β-diketonate (bdk) materials which exhibit more red-shifted mechanochromic luminescence (ML) compared to previously studied systems, a series of dinaphthoylmethane (dnm) ligands were synthesized. These derivatives possess bdk scaffolds with extended π-conjugation, and therefore could emit longer wavelength light. In the previous chapter, we reported solvatochromism, AIE, and high contrast ML with rapid room temperature recovery for a methoxy-substituted dinaphthoylmethane ligand (dnmOMe) even without boron coordination.[1] In this study, we explore how BF_2 coordination affects ML and AIE properties for this series of β-diketonate dyes. Additionally, substituent effects were probed via a series of methoxy- and bromo-substituted dnm compounds and their corresponding boronated complexes.[2]

The parent compound difluoroboron dnm (BF_2dnm) has been previously synthesized and shown to have a high extinction coefficient, in addition to two photon absorption, however the ML and AIE properties were not reported. Methoxy substitution was used as a means of assessing electron donation effects on ML; whereas, bromide, a σ withdrawing, π-donating heavy atom substituent,[3–5] allows for different kinds of ML modulation. Bromide can also disrupt molecular packing, as has been demonstrated in phenothiazine-based benzoxazole systems that show different ML mechanisms depending on bromo substitution.[6] In addition to measuring the aggregation induced emission (AIE) properties of each dye in THF/H_2O solutions and using spin-cast films to explore their ML responses, dyes were also characterized with differential scanning calorimetry (DSC), powder x-ray diffraction (XRD), and atomic force microscopy (AFM) techniques.

3.2. Results and Discussion

3.2.1 Synthesis

β-Diketones were prepared via Claisen condensation with the appropriate ketone and ester pair using a previously reported method.[7] Boron complexes were synthesized by reaction of β-diketones with boron difluoride diethyl etherate (Figure 3.2).[5] β-Diketones were soluble in most common organic solvents (THF, acetone, dichloromethane, chloroform, acetonitrile, toluene, DMSO). In general, boron derivatives were soluble at low concentrations in THF, toluene, and acetone.
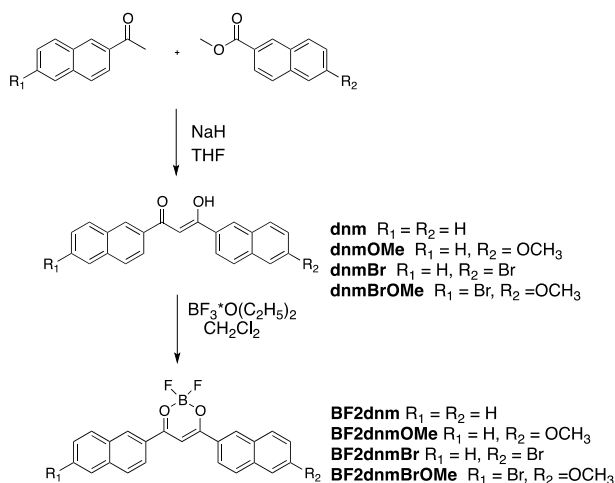
Figure 3.1. Synthesis of dnm Dyes. Synthetic pathway and nomenclature of β-diketones and their corresponding boron complexes.

3.2.2 Optical Properties in Solution

Incorporation of donor and acceptor ligands is an effective strategy for modulation of optical properties. In order to probe the effects of electron donation on optical properties in solution, UV-vis characterization, DFT calculations, and solvatochromism measurements were performed on bdk ligands and boron complexes. UV-vis spectra of β-diketonate ligands were measured in CH_2Cl_2, and showed peak absorbances (λ_{abs}) between

371-382 nm (Table 3.1, Figure S3.3; Appendix B). Upon methoxy substitution, λ_{abs} of dnmOMe (λ_{abs} = 378 nm) was red shifted compared to dnm (λ_{abs} = 371 nm). Despite bromo substitution, the absorbance of dnmBr (λ_{abs} = 372 nm) remained similar to dnm. The shift in absorbance can be explained by the difference in electron donation ability between methoxy and bromo substituents. The absorbance of dnmBrOMe (λ_{abs} = 382 nm) was further red shifted compared to dnmOMe. Boron derivatives showed broad, red shifted λ_{abs} compared to the corresponding diketones. Derivatives BF_2dnm (λ_{abs} = 421 nm) and BF_2dnmBr (λ_{abs} = 423 nm) showed nearly identical absorbances. As observed for their uncoordinated ligands, BF_2dnmOMe (λ_{abs} = 435) and BF_2dnmBrOMe (λ_{abs} = 436) exhibited red shifted absorbance indicative of increased electron donation due to methoxy substitution. Increased quantum yields and red shifted emission is typical for BF_2bdk systems versus boron-free β-diketones.[8]

Emission of β-diketones in CH_2Cl_2 solution appeared faint to the eye, yet spectra showed weak emission with peak wavelengths (λ_{em}) between 430 and 447 nm. The λ_{em} for dnm (430 nm) was significantly blue shifted compared to dnmOMe (443 nm), dnmBr (446 nm) and dnmBrOMe (447 nm). The quantum yields for dnm (Φ ~ 0.07) and dnmBr (Φ ~ 0.09) were larger than the methoxy substituted derivatives, dnmOMe and dnmBrOMe (Φ < 0.01), which were nearly non-emissive in solution. The diminutive quantum yields may be attributed to the non-radiative decay of the excited state through molecular motions, or through the formation of a less emissive charge transfer state. Particularly dnmOMe and dnmBrOMe have increased electron donation due to methoxy substitution, which could result in the appearance of an intermolecular charge transfer (ICT) state and contribute to their weak emission. The lifetimes of the ligands were all fit to double exponential decays, which indicated emission from multiple species in CH_2Cl_2 solution. Previously, β-diketone

lifetimes were fit to double exponential decays, which was attributed to emission from both keto and enol forms of each ligand. This observation could also be due to emission from different rotamers of the naphthyl ring.[1] The lifetime of dnm (τ = 0.03 ns) was shorter than for dnmOMe (τ = 0.18), dnmBr (τ = 0.23), and dnmBrOMe (τ = 0.17).

Table 3.1. Optical Properties of β-Diketones and Difluoroboron Complexes in CH_2Cl_2[a]

Compound	λ_{abs}[b] (nm)	ε ($M^{-1}cm^{-1}$)	λ_{em}[c] (nm)	Φ	τ (ns)
dnm	371	32000	430	0.07	0.03
dnmOMe	378	34000	443	< 0.01	0.18
dnmBr	372	37000	446	0.09	0.23
dnmBrOMe	382	39000	447	< 0.01	0.17
BF₂dnm	421	47000	479	0.68	1.7
BF₂dnmOMe	435	51000	514	0.70	2.5
BF₂dnmBr	423	61000	483	0.39	1.8
BF₂dnmBrOMe	436	61000	519	0.67	2.1

[a] Excited at 369 nm, room temperature, air. [b] Absorbance maximum. [c] Emission maximum

Coordination of boron difluoride resulted in intense blue-green emission in CH_2Cl_2 compared to the diketones. The complexes BF₂dnm (λ_{em} = 479 nm) and BF₂dnmBr (λ_{em} = 483 nm) showed similar peak emissions whereas the emissions of methoxy substituted BF₂dnmOMe (λ_{em} = 514 nm) and BF₂dnmBrOMe (λ_{em} = 519 nm) were red shifted. Boron coordination also increased the molar absorptivity, and vastly increased the quantum yield. The rise in quantum yield is attributed to the decrease in non-radiative decay modes, such as vibrations and rotations, due to constraints imposed by coordination to BF₂. Finally, the lifetimes of BF₂dnm and BF₂dnmOMe in solution were fit to single exponential decay, given that boron coordination prevents keto-enol tautomerization.

3.2.3 Computational Studies

Density functional theory (DFT) calculations with a Tomasi polarized continuum for dicholormethane solvent were utilized to generate HOMO and LUMO molecular orbitals (MOs) for ligands and boron complexes using B3LYP/6-31G(d) in order to better understand the nature of each transition (Figure 3.2).[9] All compounds show nearly planar conformations regardless of coordination to boron. However, it is likely that these conformations represent local minima and significant twisting in solution is still highly probable. With the exception of the symmetrical diketone, dnm (Figure S3.4; Appendix B), the HOMO of each ligand showed amplitude mostly localized on the major donor (i.e. the methoxy-substituted ring) and then delocalized throughout the molecule in the LUMO. For example, dnmOMe and dnmBrOMe showed amplitude on the methoxy substituted naphthyl ring in the HOMO; whereas, the majority of electron density is located on the unsubstituted naphthyl ring of dnmBr. Except in the case of symmetrical dnm, which undergoes a π-π* transition, these results suggest that all ligands undergo an ICT transition, regardless of bromo or methoxy substitution. This is consistent with previous reports for symmetrical and unsymmetrical systems,[10] and is further supported experimentally by the relatively large Stokes shifts of the ligands (3,698 cm^{-1} - 4,460 cm^{-1}) compared to the boronated complexes (2,876 cm^{-1} – 3,668 cm^{-1}). These larger Stokes shifts correspond to molecular geometry changes in the excited state typical of ICT processes.[10] For the HOMOs of the boron complexes, some electron density is observed on each naphthyl ring. However, electron density is much more concentrated on the methoxy-substituted naphthyl ring of BF$_2$dnmOMe and BF$_2$dnmBrOMe. For all boron complexes, electron density is distributed throughout the entire LUMO. Based on these results, it seems that BF$_2$dnm

(Figure S3.4; Appendix B) and BF$_2$dnmBr undergo predominantly π-π* transitions compared to BF$_2$dnmOMe and BF$_2$dnmBrOMe, which show greater ICT character.
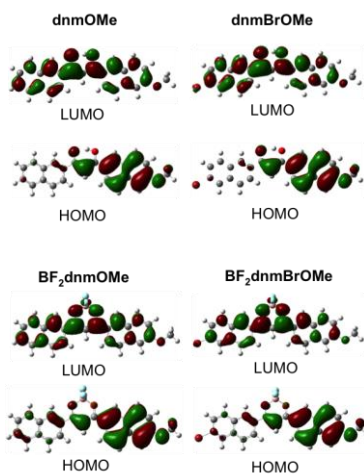
Figure. 3.2. Molecular Orbitals of dnm Dyes. Frontier molecular orbitals of selected dinaphthoyl β-diketones and corresponding boron complexes.

3.2.4 Solvatochromic Studies

Previously, it was shown that dnmOMe displayed a moderate solvatochromic effect.[1] Additionally BF$_2$ coordination has been previously shown to affect the optical properties of β-diketones when dissolved in solvents of increasing polarity.[11] In order to examine how BF$_2$ coordination affects the solvatochromic behavior of this system, the absorption and emission spectra were recorded for 10^{-5} M solutions of each compound dissolved in a series of organic solvents. Methoxy substituted systems, dnmOMe and dnmBrOMe, that showed ICT transitions according to DFT calculations, displayed solvatochromism under UV irradiation that was clearly visible to the eye (Figure 3.3). Emission was barely visible in dnmBr solutions (Figure S3.5; Appendix B) and unobservable for dnm in all solvents. All boron coordinated compounds showed solvatochromism regardless of the type of transition predicted by DFT calculations.
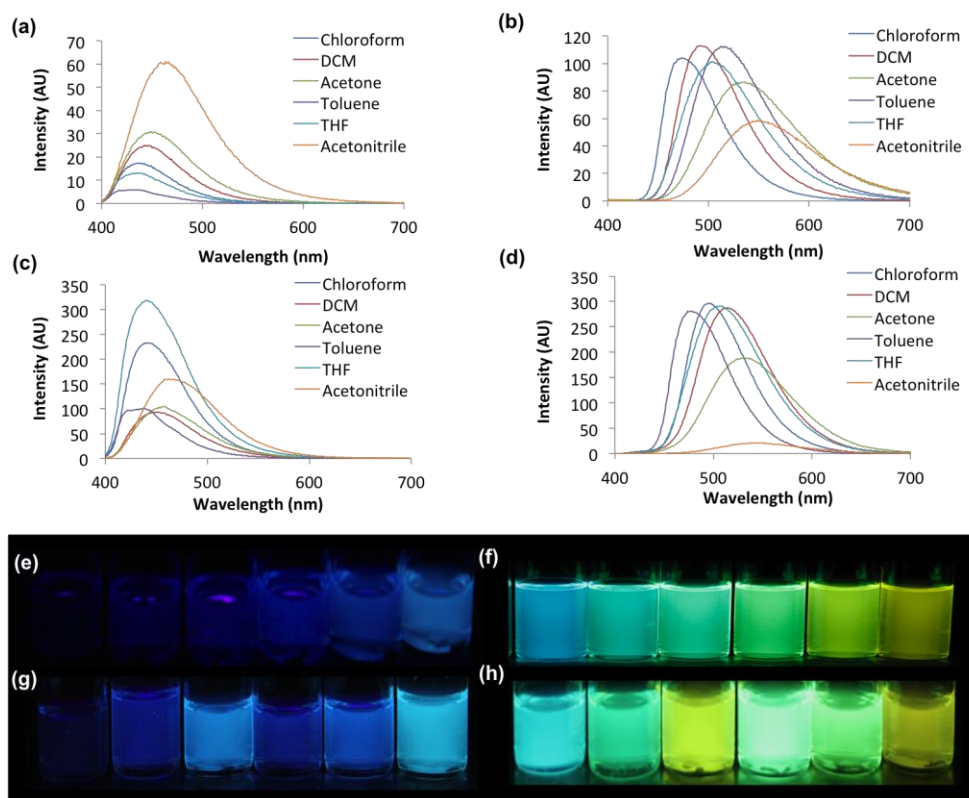
Figure. 3.3. Solvatochromism of dnm Dyes. Emission spectra of dnmOMe (a), BF$_2$dnmOMe (b), dnmBrOMe (c), and BF$_2$dnmBrOMe (d) (10^{-5} M) in the indicated solvents (λ_{ex} = 369 nm). UV excited images of dnmOMe (e), BF$_2$dnmOMe (f), dnmBrOMe (g), and BF$_2$dnmBrOMe (h) in different solvents, from left to right: toluene, dichloromethane (DCM), acetone, THF, chloroform, acetonitrile.

In toluene, both dnmOMe and dnmBrOMe showed almost no emission, however as the solvent polarity was increased, a bathochromic shift in emission was observed. The shifts in emission for dnmOMe and dnmBrOMe occur over a similar wavelength range, however the most blue shifted peak emission for dnmOMe occurred when dissolved in toluene (434 nm) compared to dnmBrOMe, which showed the most blue shifted peak emission in CHCl$_3$ solution (438 nm). In both methoxy substituted ligands, the most red shifted emissions (466 nm for dnmOMe and 462 nm for dnmBrOMe) were observed in CH$_3$CN, the most polar solvent tested. These results demonstrate slight positive solvatochromism in dnmOMe and dnmBrOMe.

Compared to dnmOMe and dnmBrOMe, which show a solvatochromic shift from blue to green, the corresponding boron compounds show a larger wavelength shift from blue to orange. Unlike their uncoordinated counterparts, BF$_2$dnmOMe, and BF$_2$dnmBrOMe are both emissive when dissolved in polar and non-polar solvents. The most blue shifted emission was observed when BF$_2$dnmOMe (475 nm) was dissolved in CHCl$_3$ compared to BF$_2$dnmBrOMe, which showed the furthest blue shifted emission in toluene (478 nm). Like the uncoordinated ligands, BF$_2$dnmOMe and BF$_2$dnmBrOMe have the most red shifted peak emission when dissolved in CH$_3$CN, at 549 nm and 545 nm, respectively. While the emissions of BF$_2$dnm (Figure S3.6; Appendix B) and BF$_2$dnmBr (Figure S3.7; Appendix B) were also solvent dependent, the changes in emission colors were less pronounced compared methoxy substituted derivatives.

The solvatochromic behavior of each compound was also examined using Lippert-Mataga theory (Figure. S3.8, Figure. S3.9; Appendix B). [12,13] The plots of Stokes shift (Δv) versus the solvent polarity parameter (Δf) showed slightly positive trends with a slope of 1850 for dnmOMe and 1110 for dnmBrOMe, indicating moderate solvatochromism. Upon boronation, the slope increased to 2200 for BF$_2$dnmOMe and 2500 for BF$_2$dnmBrOMe. Overall these results indicate that boronation of dinaphthoyl β-diketonate ligands enhances solvatochromism, however bromo substitution has very little effect on solvatochromic behavior. The increase in solvatochromic behavior ,may be attributed to a larger excited state dipole induced through BF$_2$ coordination.[14]

3.2.5 Aggregation Induced Emission

Previously, we have detected AIE in dnmOMe when dissolved in THF/H$_2$O solutions despite a mostly planar conformation according to DFT calculations.[1] Based on the calculations, other ligands and boron complexes in this study also show planar conformations. Thus we were eager to examine how boron coordination and methoxy/bromo substitution affected the AIE behavior. Ligands and corresponding boron complexes were dissolved in THF/H$_2$O solutions with increasing H$_2$O concentrations and their absorption and emission spectra were measured (Figure. 3.4, Figures. S3.10 –S315; Appendix B).
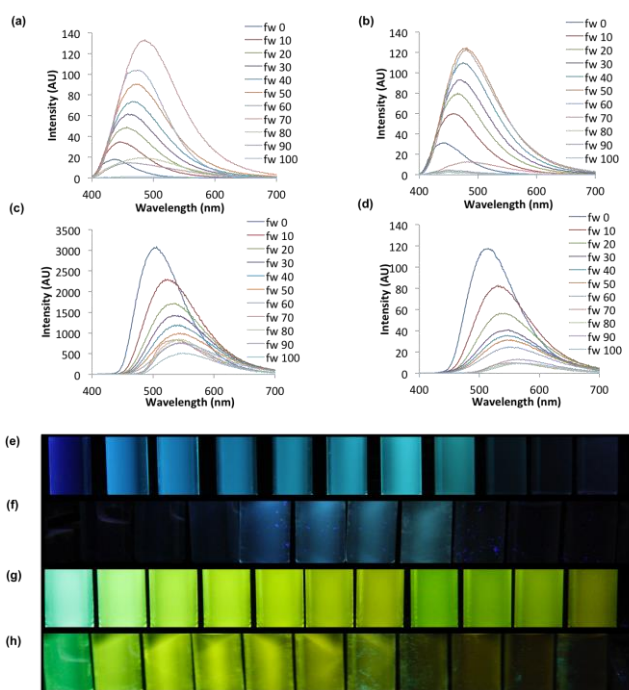
Figure 3.4. Aggregation Induced Emission of dnm Dyes. Emission spectra of THF/H$_2$O solutions containing dnmOMe (a), dnmBrOMe (b), BF$_2$dnmOMe (c), and BF$_2$dnmBrOMe (d) with increasing H$_2$O fractions (λ_{ex} = 369 nm). Images under UV illumination (λ_{ex} = 350 nm) of dnmOMe (e) dnmBrOMe (f), BF$_2$dnmOMe (g), and BF$_2$dnmBrOMe (h).

All dinaphthoyl β-diketones showed measurable AIE, however THF/H$_2$O solutions of dnm (Figure S3.10; Appendix B) and dnmBr (Figure S3.11; Appendix B) appeared nearly non-emissive to the eye for all water fractions. Methoxy substituted dnm ligands

showed more dramatic AIE (Figure 3.4). An eight-fold increase in relative intensity was observed in dnmOMe at 70% H_2O. Additionally, the peak emission of dnmOMe was red shifted 47 nm over nearly the same range of water fractions.[1] In the case of dnmBrOMe, a four-fold increase in relative emission intensity was noted at 60% H_2O. As the water fraction was increased above this point, the emission dropped precipitously. As with dnmOMe, there was a similar wavelength shift from 442 nm in THF to 482 nm in 70% H_2O. The gradual redshift in wavelength was attributed to aggregation as well as increasing solvent polarity due to the addition of H_2O. In both cases, the intensity dropped when the water fraction was increased above a certain threshold. At this point, it is believed that aggregates reached a critical size and began precipitating out of solution. As more aggregates precipitated out of solution, the emission decreased until eventually the solution was nearly non-emissive in H_2O.[1] The difference in AIE threshold is likely due to the difference in solubility between dnmOMe and dnmBrOMe as it has been observed that bromo substitution decreases the solubility of ligands.

Unlike the ligands, AIE was not observed for boron complexes. In all cases, the emission intensity decreased as the H_2O fraction was increased. For BF_2dnmOMe, a bathochromic shift was observed from 506 nm in THF to 545 nm in 100% H_2O and all THF/H_2O solutions were emissive to the eye, despite the decrease in intensity. A wavelength shift from 515 nm in THF to 576 nm in H_2O was observed for BF_2dnmBrOMe; however, emission was not observable to the eye above a H_2O fraction of 70%. This could be attributed to the limited solubility of BF_2dnmBrOMe. A decrease in emission was also observed as the water fraction was increased for BF_2dnm (Figure S12) and BF_2dnmBr (Figure S13). The lack of AIE character in boron dyes is likely due coordination of the BF_2 moiety, which constricts molecular motion from the onset and forces the diketonate into a

planar conformation. As a result, the likelihood of BF$_2$dnm derivatives to π stack is increased, resulting in the formation of non-emissive aggregates, which can promote ACQ. While the boron coordinated dyes show diminished intensity upon aggregation, it is important to note that they still show bright emission in the solid state.

The AIE observed in uncoordinated diketones is not as pronounced as some other examples in the literature, which contain more typical AIE active moieties such as triarylamine,[15] tetraphenylethene,[16] silole,[17] and cyanostilbene.[18] For example, the star shaped TPE substituted cyclohexanehexone luminogen developed by Bhosale *et al.* is non-emissive in THF solution but shows intense blue emission at increased water fractions.[19] However, a 218-fold increase was observed, compared to an 8-fold increase for dnmOMe.[1,19] The dramatic difference in AIE activity was attributed to the extended π-conjugation inherent within its star shaped structure. Additionally, some materials that incorporate more traditional AIE luminogens have shown a wide range of emission wavelengths[20] compared to uncoordinated diketones that show high-contrast blue emission upon aggregation. Boron coordination of these diketones resulted in a decrease in emission intensity upon aggregation, however AIE has been demonstrated by Chujo *et al.* in boron coordinated ketoiminate and diiminate materials due to increased steric hindrance provided by substitution of the imine unit.[21]

3.2.6 Mechanochromic Luminescence

The ML behaviors of diketones and boron complexes were studied for spin-cast films in "as spun" (AS), thermally annealed (TA), and smeared (SM) states. Typically, AS films are amorphous but become crystalline after annealing, while smeared films are amorphous.[22] However, AS films with crystalline domains have been reported.[40] Thin films of dinaphthoyl ligands and boron complexes were studied using a previously described

method (Table 3.2).[5] Annealing temperatures (T_{TA}) were determined by heating thin films of each compound for ten minutes over a range of temperatures while monitoring the peak emission. The temperature that showed the most blue shifted peak emission was used as the annealing temperature (Figure S3.1, Figure S3.2; Appendix B).

In the as spun state, methoxy substituted ligands, dnmOMe ($\lambda_{AS} = 480$ nm) and dnmBrOMe ($\lambda_{AS} = 479$ nm), were blue-green under UV illumination whereas the other dnm thin films were non-emissive (Figure 3.5). In the AS state, quantum yields were quite low for all ligands with a maximum value of $\varphi_{AS} = 0.03$ for dnmOMe thin films. Broad emission profiles, as evidenced by the full width at half-maximum (FWHM) of dnmOMe (FWHM = 147 nm), and dnmBrOMe (FWHM = 139 nm), could indicate the presence of multiple species in thin films for the AS state.

Excluding dnm, which showed no change, the peak emissions of thermally annealed thin films of dnmOMe ($\lambda_{TA} = 441$ nm), dnmBr ($\lambda_{TA} = 442$ nm), and dnmBrOMe ($\lambda_{TA} = 448$ nm) were blue shifted and could not be detected visually. Compared to as spun thin films, shorter lifetimes were observed in all ligands after heating. Previously, a decrease in FWHM had been observed for BF_2bdk systems,[5] however a low energy shoulder emerged after thermal treatment for dnmOMe ($FWHM_{TA} = 152$ nm), and dnmBrOMe ($FWHM_{TA} = 179$ nm) which resulted in an increase in FWHM. The presence of a shoulder was attributed to residual AS emission detected in TA thin films.[1] In the TA state, the quantum yield of dnmBrOMe ($\varphi_{TA} < 0.01$) decreased whereas little or no change was detected for the other ligands upon annealing.

The smearing of thermally annealed samples resulted in red shifted emission and an increase in lifetime. In the smeared state, the peak emissions of dnm ($\lambda_{SM} = 464$ nm),

dnmOMe (λ_{SM} = 494 nm), and dnmBr (λ_{SM} = 524 nm) were similar, however the peak

emission of dnmBrOMe (λ_{SM} = 530) was significantly red shifted. In addition, a small blue

shifted shoulder was observed in the smeared emission spectra of dnmBrOMe, which could

be indicative of residual TA emission. In all cases, smearing resulted in an increase

quantum yield compared to TA samples.

Table 3.2. Mechanochromic Luminescence of β-Diketones and Boron Complexes as Spin-Cast Films [a]

Compound	As Spun				Annealed				Smeared			
	λ_{AS} [e] (nm)	FWHM$_{AS}$ (nm)	τ_{AS} (ns)	φ_{AS}	λ_{TA} (nm)	τ_{TA} (ns)	FWHM$_{TA}$ (nm)	φ_{TA}	λ_{SM} (nm)	T$_{SM}$ (ns)	FWHM$_{SM}$ (nm)	φ_{SM}
dnm [d]	437	110	1.53	0.01	437	0.57	58	0.01	464	2.37	158	0.02
dnmOMe [e]	480	147	4.71	0.03	441	1.22	152	0.03	494	2.32	118	0.10
dnmBr [b]	442	139	0.86	< 0.01	440	0.85	146	< 0.01	524	1.76	151	0.02
dnmBrOMe [c]	479	139	3.76	0.02	448	0.35	179	< 0.01	530	2.28	163	0.03
BF$_2$dnm [c]	538	112	3.76	0.31	527	2.95	98	0.40	563	11.1	126	0.52
BF$_2$dnmOMe [c]	588	121	10.06	0.27	552	7.32	114	0.20	578	10.9	128	0.30
BF$_2$dnmBr [c]	565	122	2.23	0.03	544	1.71	119	0.02	563	2.67	123	0.03
BF$_2$dnmBrOMe [c]	595	127	5.7	0.14	551	2.57	107	0.08	598	6.70	130	0.10

[a] Excited at 369 nm.
Optimized annealing temperatures: 110°C,[b] 120°C,[c] 130°C,[d] and 140°C. [e]

Boronation resulted in a significant red shift of emission and increased lifetimes in

the AS state compared to emission from the corresponding ligands. BF$_2$dnm (λ_{AS} = 538

nm), BF$_2$dnmOMe (λ_{AS} = 588 nm), and BF$_2$dnmBr (λ_{AS} = 565 nm) were yellow-green

under UV illumination whereas BF$_2$dnmBrOMe (λ_{AS} = 595 nm) glowed orange. Boron

coordination also resulted in a substantial increase in quantum yield for BF$_2$dnm (φ_{AS} =

0.31) and BF$_2$dnmOMe (φ_{AS} = 0.27) compared to values for corresponding ligands. While

coordination resulted in an increase in quantum yield for BF$_2$dnmBr (φ_{AS} = 0.03) and

BF$_2$dnmBrOMe (φ_{AS} = 0.14), the effect was far less dramatic than for boron compounds without heavy atoms. The decrease in quantum yield is likely due to increased intersystem crossing to a non-emissive triplet state via the heavy atom effect.[5]
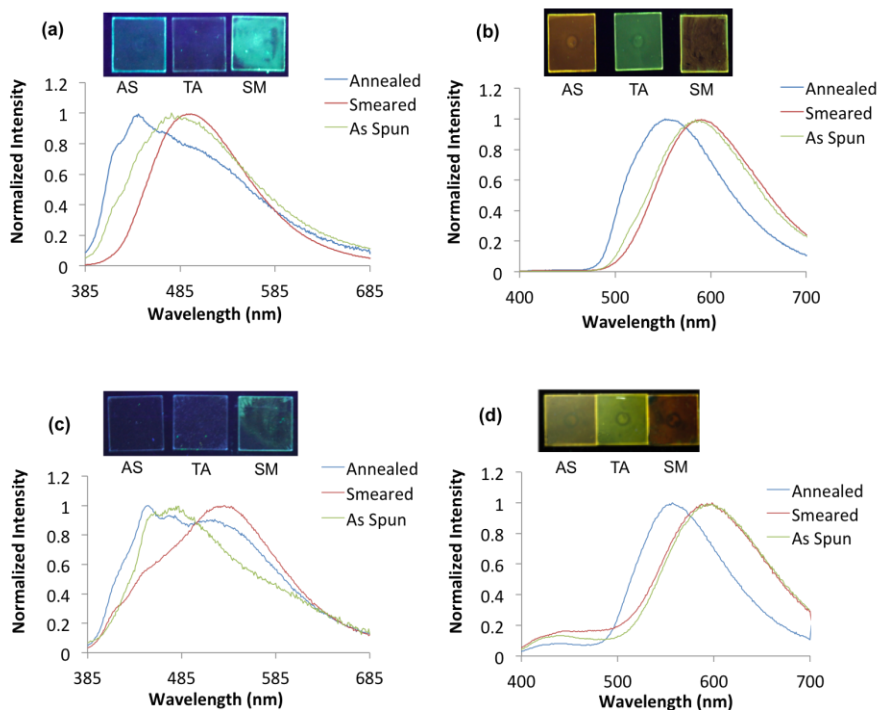
Figure 3.5. Mechanochromic Luminescence of dnm Dyes. Images and emission spectra of dnmOMe (a), BF$_2$dnmOMe (b), dnmBrOMe (c), and BF$_2$dnmBrOMe (d) thin films in as spun (AS), thermally annealed (TA), and smeared (SM) states (λ_{ex} = 369 nm).

As in ligand thin films, thermal treatment resulted in blue shifted emission and shorter lifetimes for all boronated dyes. Additionally, the FWHM in the TA state decreased slightly and no low energy shoulders were observed in the emission spectra which indicated that coordination of BF$_2$ resulted in the disappearance of any residual emission from the AS state that was observed in TA spectra of dnmOMe and dnmBrOMe. Heating BF$_2$dnm (φ_{TA} = 0.40) resulted in an increase in quantum yield, however quantum yield decreased for BF$_2$dnmOMe (φ_{TA} = 0.20), BF$_2$dnmBr (φ_{TA} = 0.02), and BF$_2$dnmBrOMe (φ_{TA} = 0.08) after thermal treatment. Upon smearing, the peak emission for BF$_2$dnm (λ_{SM} = 563), BF$_2$dnmOMe (λ_{SM} = 578 nm), BF$_2$dnmBr (λ_{SM} = 563) and BF$_2$dnmBrOMe (λ_{SM} = 598 nm)

were almost identical to the corresponding values in the AS state. Smeared lifetimes were longer for all boron complexes and the quantum yield increased compared to AS and TA thin films for BF_2dnm ($\varphi_{SM} = 0.52$), $BF_2dnmOMe$ ($\varphi_{SM} = 0.30$), and $BF_2dnmBrOMe$ ($\varphi_{SM} = 0.10$) after smearing. In the case of BF_2dnmBr ($\varphi_{SM} = 0.03$), the quantum yield increased slightly after smearing.

Since the quantum yields of ligands are very low, it is difficult to establish a conclusive trend upon smearing, however it appears that the quantum yields increase in the smeared state. A clear trend can be observed for boron complexes since the quantum yields are sufficiently high to detect. Bromo substitution results in a decrease in quantum yield for boron complexes regardless of whether they are in AS, TA or SM states. This can be explained via the heavy atom effect, which increases intersystem crossing to the non-emissive triplet state and thus decreases the amount of energy in the population of the singlet excited state, lowering the overall quantum yield.[23] Furthermore, the quantum yields of BF_2dnmBr and $BF_2dnmBrOMe$ decrease upon smearing whereas all other boron compounds (and ligands) increase. Based on previous studies examining the effect of heavy atom substitution on BF_2bdk materials,[5] smearing results in mechanochromic luminescence quenching, whereby a lower energy state is generated closer to the non-emissive triplet state, which enhances intersystem crossing and lowers the quantum yield.[3]

The spontaneous recovery at room temperature of blue shifted emission after smearing has been well established in BF_2bdk systems.[24] It has also been shown that dnmOMe shows fast room temperature recovery.[1] We were curious how the coordination of boron affects the dynamic recovery processes of dinaphthoyl β-diketonate systems, and whether it can be modulated through bromo or methoxy substitution. The room temperature

recovery was determined by smearing thin films of ligands and boron complexes and recording emission spectra over time (Figure 3.6).
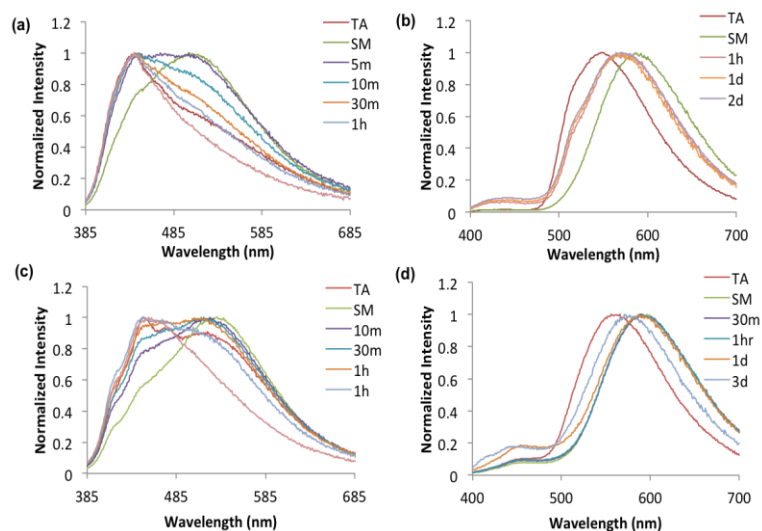
Figure 3.6. Room Temperature Recovery of dnm Dyes. Emission spectral changes over time for dnmOMe (a), BF$_2$dnmOMe (b), dnmBrOMe (c), BF$_2$dnmBrOMe (d) (λ_{ex} = 369 nm).

The recovery of dnm ligands is rapid compared to other ML active BF$_2$bdks. For example, the emission of dnmOMe is almost entirely recovered over the course of an hour.[1] Over that span, a hypsochromic shift in λ_{em} of 63 nm was observed. While no shift in emission maximum, λ_{em} was seen for dnm upon smearing, the FWHM decreased from 158 nm to 97 nm over that time interval, which demonstrates the ability of dnm to self-heal. Bromo substitued dnm derivatives showed increased recovery times compared to dnm and dnmOMe, which might be attributed to C-H$^{...}$Br interactions that hinder self-healing.[6] Over the course of an hour, the λ_{em} of dnmBr and dnmBrOMe only blue shifted 26 nm and 17 nm, respectively. Recovery of FWHM and λ_{em} was achieved after one day for dnmBr, and two days for dnmBrOMe, which demonstrates that bromo substitution dramatically slows recovery compared to dnm and dnmOMe. In addition to substitution with different molecular weight alkyl[44] and arene[40] substituents, these results suggest that incorporating

different halogens into the design of BF_2bdk ML materials may also be an effective strategy for modulating recovery.

When compared to ligands, boron complexes with naphthyl ligands showed only modest changes in emission over the course of several days. The emission wavelength for BF_2dnm only blue shifted 14 nm from its smeared emission (559 nm) after three days. Methoxy and bromo substitution had little effect on recovery time. The most rapidly recovering boron complex was BF_2dnmOMe, which showed a hypsochromic shift in λ_{em} of 21 nm over two days, whereas BF_2dnmBr and BF_2dnmBrOMe had only shifted 18 nm and 20 nm, respectively over a three-day period. The FWHM of each complex showed very little change over time. The increased recovery time observed in boron complexes could be explained by the propensity of BF_2 to form strong C-H$\cdots$F hydrogen bonds.[68] Stronger arene-arene interactions may also be playing a role, which is manifested in decreased solubility for dinaphthyl systems.[69] Thus, heating is required to overcome these strong interactions in order to access emission wavelengths associated with the crystalline state; whereas, ambient temperatures provide enough energy for the thermal back reaction population to occur in diketone ligands. These results indicate that emission wavelength and recovery time can be tuned through difluoroboron coordination.

3.2.7 Solid State Characterization

Solid-state characterization of ligands and boron complexes was performed using DSC, AFM and powder XRD. DSC was used for thermal characterization of bulk powders for each compound. Ligands show a wide range of points (T_m) between 164 °C and 247 °C for dnmOMe and dnmBrOMe, respectively (Figure S3.16; Appendix B). Boron complexes show higher melting points overall ranging from 275 °C for BF_2dnmOMe and 338 °C for BF_2dnmBrOMe (Figure S3.17; Appendix B). In general, methoxy substitution resulted in

a decrease in T_m compared to unsubstituted dnm and BF_2dnm. However, bromine substituted derivatives exhibited larger melting points than their methoxy substituted counterparts, dnmOMe and BF_2dnmOMe.

AFM images of spin cast films in as spun and annealed states were measured in order to study the morphology of ligand and boron materials (Figure 7). As spun films were used to approximate the smeared state since quality images of smeared films could not be obtained due to inhomogeneity and dynamic recovery. Based on comparison with XRD data, diketone samples generally appeared semi-crystalline with undefined features in the AS state, whereas better defined crystallites were observed after annealing, for dnm and dnmOMe, lamellar crystallites were observed even in the as spun state, and grew larger after annealing. The as spun state for bromo substituted dnm samples appeared devoid of any clearly defined features and smaller particle sizes were observed overall. Thermal treatment of dnmBrOMe films resulted in the formation of rod-like crystallites whereas a mixture of rod and plate-like crystallites were observed in thermally annealed films of dnmBr. Generally, rod-like crystallites of dnmBr showed smaller aspect ratios when compared to dnmBrOMe. Overall, AFM images showed that dnm dyes formed well-ordered morphologies when annealed and appeared largely disordered in as spun states.

As in dnm, BF_2dnm also showed plate-like crystals in the as spun state that increased in size when annealed. The AS state for BF_2dnmOMe particles were plate-like, but formed whisker-like features when annealed. BF_2dnmBr and BF_2dnmBrOMe were amorphous in the AS state and, when annealed, formed rod-like and whisker-like crystals, respectively. These results are in agreement with previous studies, which showed that substituent effects have a large effect on molecular assembly in BF_2bdk systems. In particular, different morphologies have been observed depending on the electronegativity

of the halide substituent due to the formation of different energy halogen-hydrogen, and halogen-halogen associations.[5] Similar interactions are likely playing a role in determining the different morphologies of bromide substituted samples.
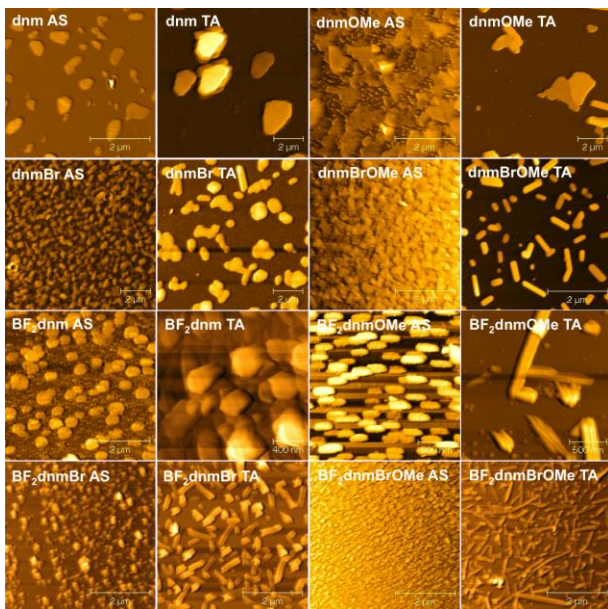
Figure 3.7. AFM Images of dnm Dyes. Images of dnm, dnmOMe, dnmBr, dnmBrOMe, BF$_2$dnm, BF$_2$dnmOMe, BF$_2$dnmBr, and BF$_2$dnmBrOMe thin films in as spun (AS) and thermally annealed (TA) states.

Structural characterization was performed by comparing XRD patterns for thin films of each compound in AS, TA, and SM states to data for pristine powders. Representative diffraction patterns for dnmOMe and BF$_2$dnmOMe are shown in Figure 3.8 while powder XRD characterization of the remaining dyes may be found in the Supporting Information (Figures S3.18-S3.19; Appendix B). Thicker films were used for X-ray analysis compared to luminescence and AFM studies in order to provide a more intense signal. Thicker films were fabricated by adding 20 drops of saturated THF solutions to microscope coverglass substrates and evaporated in air. In the AS state, most films showed small peaks that became more intense upon annealing. This indicates that samples were most crystalline in the TA state, as expected, however peaks were detected in the AS

71

samples as well indicating that they are partially crystalline. Some previous studies have also shown crystallinity in BF$_2$bdk AS thin films.[5] Furthermore, AFM images also showed visible crystallites in the AS films of dnm, dnmOMe, BF$_2$dnm, and BF$_2$dnmOMe. Smearing the thin films resulted in a phase transition to an amorphous state as evidenced by the disappearance of all peaks that were present in the TA pattern.
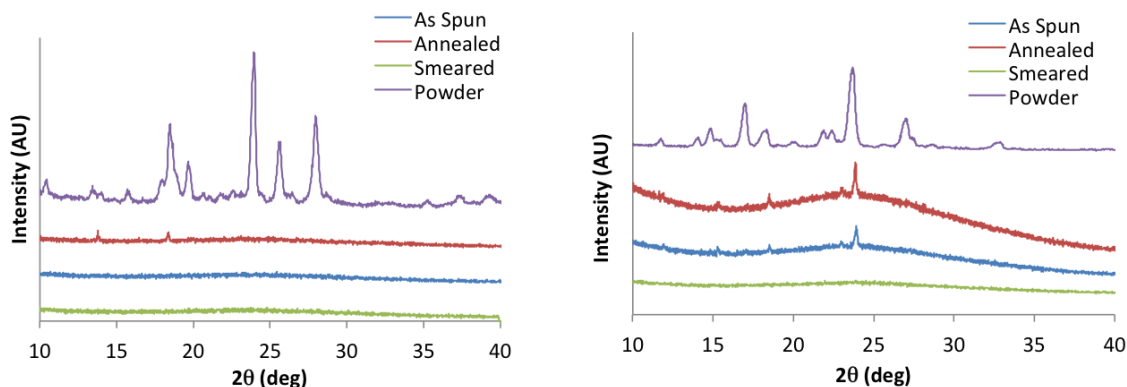
Figure 3.8. Structural Characterization of dnm Dyes. Patterns of dnmOMe and BF$_2$dnmOMe as powders and thin films in different states.

3.2.9 Conclusions

The solution and solid-state optical properties of dinaphthoylmethane β-diketones were modulated via BF$_2$ coordination, donor/acceptor effects, and bromo substitution. Methoxy substituted ligands showed moderate solvatochromism in addition to AIE, but had otherwise unremarkable optical properties in solution. Difluoroboron coordination resulted in enhanced and red shifted emission, more dramatic solvatochromism and the disappearance of AIE. Bromo substitution had very little effect on the optical properties of ligands and boron compounds in solution.

Reversible, high contrast mechanochromic luminescence was observed in dnm ligands, which showed variation in quantum yield, emission wavelength, and recovery time

via methoxy and heavy atom substitution. Boron coordination resulted in dramatically increased solid-state quantum yields compared to ligands, but unlike many dibenzoylmethane systems, room temperature recovery was not observed for complexes with dinaphthyl ligands. After smearing, both ligands and boron complexes showed increased solid-state quantum yields. Additionally, the solid-state quantum yields for bromo substituted derivatives in AS, TA, and SM states was considerably diminished. This observation was attributed to the heavy atom mechanochromic luminescence quenching effect previously observed in halide substituted BF_2bdks.[5] Bromo substitution also resulted in increased recovery times in ligands compared to dnmOMe, which showed full recovery in one hour. This indicates that halide substitution could be an effective strategy for tuning recovery time in BF_2bdks in addition to alkyl and arene substitution approaches. More in-depth understanding of ML properties including emission wavelength, intensity and recovery time allows for more rational property tuning of ML materials for applications.

3.3 Experimental

3.3.1 Materials

Solvents THF and CH_2Cl_2 were dried over molecular sieves as previously described.[50] Reactions were monitored using silica TLC plates. Compounds purchased from Sigma-Aldrich and TCI were reagent grade and used without further purification. The β-diketones and boron complexes were prepared as previously described.[8] Data for dnm[7] dnmOMe,[1] and BF_2dnm,[7] are in accord with previous reports. Characterization data for new analogues are provided in the Supporting Information.

3.3.2 Methods

^{1}H NMR (300, 500 MHz) spectra were recorded on Varian Unity Inova 300/51 and Varian Inova 500 spectrometers in deuterated DMSO. Spectra were referenced to the

signals for residual protio-DMSO at 2.50 ppm and coupling constants were reported in Hz. Mass spectra were recorded using an Applied Biosystems 4800 spectrometer with a MALDI TOF/TOF analyzer. UV-vis spectra were collected on a Hewlett-Packard 8452A diode-array spectrophotometer. Steady-state fluorescence emission spectra were obtained on a Horiba Fluorolog-3 Model FL3-22 spectrofluorometer (double-grating excitation and double-grating emission monochromator). Time-correlated single-photon counting (TCSPC) fluorescence lifetime measurements were performed with a NanoLED-370 (λ_{ex} = 369 nm) excitation source and a DataStation Hub as the SPC controller. Lifetime data were analyzed with DataStation v2.4 software from Horiba Jobin Yvon. Fluorescence quantum yields, φ_F, in CH_2Cl_2 were calculated versus a dilute anthracene solution in ethanol as a standard using a previously described method[25] and the following values: φ_F anthracene in ethanol = 0.27, n_D ethanol = 1.36, n_D CH_2Cl_2 = 1.424. Optically dilute CH_2Cl_2 solutions of all samples were prepared in 1 cm path length quartz cuvettes with absorbances <0.1 (a.u.). Solid-state quantum yield measurements were performed using a F-3029 Quanta-Φ Integrating Sphere from Horiba Scientific and analyzed using FluorEssence software. The sample morphologies of spin-cast films were characterized by Atomic Force Microscopy (AFM) (Digital Image, DI 3000) in tapping mode and the resulting images were processed using Gwyddion software version 2.31. Powder XRD patterns were obtained using a Panalytical X'Pert Pro MPD diffractometer operating at 40kV and 40ma using Cu Kα radiation. DSC was performed on the pristine powders using a TA Instruments DSC 2920 Modulated DSC and data were analyzed using the Universal Analysis software V 2.3 from TA Instruments. Thermograms were recorded using the standard mode and a temperature ramp rate of 5 °C/min. A conditioning cycle was run prior to reporting the second scan.

Preparation of Aggregates for AIE Measurements. A 10^{-3} M stock solution of dnmOMe in THF was prepared. Aliquots (100 µL) of the stock solution were added to 10 mL volumetric flasks and diluted to volume with THF and H_2O in the proper ratios. Solutions were placed in a sonicator for 10 min before measurement.[16]

Preparation of Thin Films. Thin films used for AFM, XRD, and ML characterization were prepared on 18 x 18 mm glass coverslips. Solid-state quantum yield measurements were performed on films cast on circular glass coverslips with 12 mm diameter. With the exception of spin-cast films subjected to XRD, the films were fabricated by preparing 10^{-3} M solutions and applying ~10 drops to the coverslips rotating at 3,000 rpm. The films were dried *in vacuo* for 15 min before measurements or thermal annealing. Annealing temperatures were determined experimentally by heating spin-cast films for 10 min at temperatures ranging from 110 °C to 160 °C in 10 °C increments and measuring their emission (Figure S3.1, Figure S3.2; Appendix B).[43] Annealed films were gently smeared with a cotton swab as previously described.[44] Thin films used for XRD analysis were fabricated by simple casting 20 drops of a saturated stock solution on 18 mm diameter glass coverslips.

3.4 Acknowledgements

3.5 References

1   T. Butler, W. A. Morris, J. Samonina-Kosicka and C. L. Fraser, *Chem. Commun.*, 2015, **51**, 3359–3362.

2   E. Cogné-Laage, J.-F. Allemand, O. Ruel, J.-B. Baudin, V. Croquette, M. Blanchard-Desce and L. Jullien, *Chem. - A Eur. J.*, 2004, **10**, 1445–1455.

3   G. Zhang, J. Lu and C. L. Fraser, *Inorg. Chem.*, 2010, **49**, 10747–10749.

4   W. A. Morris, M. Sabat, T. Butler, C. A. DeRosa and C. L. Fraser, *J. Phys. Chem. C*, 2016, **120**, 14289–14300.

5   W. A. Morris, T. Liu and C. L. Fraser, *J. Mater. Chem. C*, 2015, **3**, 352–363.

6   P. Xue, B. Yao, J. Sun, Q. Xu, P. Chen, Z. Zhang and R. Lu, *J. Mater. Chem. C*, 2014, **2**, 3942–3950.

7   T. Liu, A. D. Chien, J. Lu, G. Zhang and C. L. Fraser, *J. Mater. Chem.*, 2011, **21**, 8401–8408.

8   G. Zhang, R. E. Evans, K. a. Campbell and C. L. Fraser, *Macromolecules*, 2009, **42**, 8627–8633.

9   R. Tomasi, J.; Mennucci, B.; Cammi, *Chem. Rev.*, 2005, **105**, 2999–3094.

10   S. Xu, R. E. Evans, L. Tiandong, G. Zhang, J. N. Demas, C. O. Trindle and C. L. Fraser, *Inorg Chem*, 2013, **52**, 3597–3610.

11   C. Qian, M. Liu, G. Hong, P. Xue, P. Gong and R. Lu, *Org. Biomol. Chem.*, 2015, **13**, 2986–2998.

12   E. Lippert, *A Phys. Sci.*, 1955, **10**, 541–545.

13   N. Mataga, Y. Kaifu and M. Koizumi, *Bull. Chem. Soc. Jpn.*, 1956, **29**, 465–470.

14   J. R. Lakowicz, *Principles of fluorescence spectroscopy*, Springer, New York, 3rd edn., 2006.

15   Z. Ning, Z. Chen, Q. Zhang, Y. Yan, S. Qian, Y. Cao and H. Tian, *Adv. Funct.*

Mater., 2007, **17**, 3799–3807.

16   G. Zhang, F. Hu and D. Zhang, *Langmuir*, 2015, **31**, 4593–4604.

17   Z. Li, Y. Q. Dong, J. W. Y. Lam, J. Sun, A. Qin, M. Häußler, Y. P. Dong, H. H. Y. Sung, I. D. Williams, H. S. Kwok and B. Z. Tang, *Adv. Funct. Mater.*, 2009, **19**, 905–917.

18   J. Mei, Y. Hong, J. W. Y. Lam, A. Qin, Y. Tang and B. Z. Tang, *Adv. Mater.*, 2014, **26**, 5429–5479.

19   A. Rananaware, D. La Duong and S. V. Bhosale, *RSC Adv.*, 2015, **5**, 56270–56273.

20   Y. Hong, J. W. Y. Lam and B. Z. Tang, *Chem. Soc. Rev.*, 2011, **40**, 5361–5388.

21   R. Yoshii, A. Nagai, K. Tanaka and Y. Chujo, *Chem. - A Eur. J.*, 2013, **19**, 4506–4512.

22   G. Zhang, J. P. Singer, S. E. Kooi, R. E. Evans, E. L. Thomas and C. L. Fraser, *J. Mater. Chem.*, 2011, **21**, 8295–8299.

23   S. K. Lower and M. A. El-Sayed, *Chem. Rev.*, 1966, **66**, 199–241.

24   G. Zhang, J. Lu, M. Sabat and C. L. Fraser, *J. Am. Chem. Soc.*, 2010, **132**, 2160–2162.

25   E. R. Carraway, J. N. Demas and B. A. DeGraff, *Anal. Chem.*, 1991, **63**, 332–336.

Chapter 4

Camera Method for Monitoring a Mechanochromic Luminescent β-Diketone Dye with Rapid Recovery

Mechanochromic Luminescent (ML) Dye with Rapid Self-Erasing Properties

ML   Recovery Map
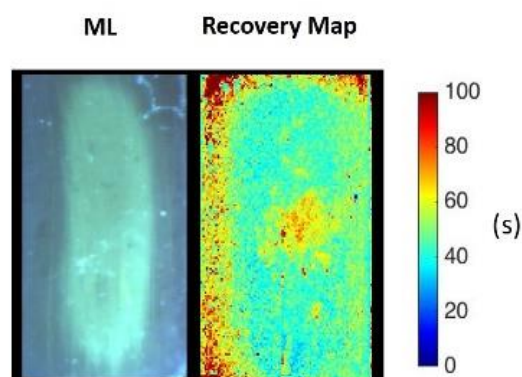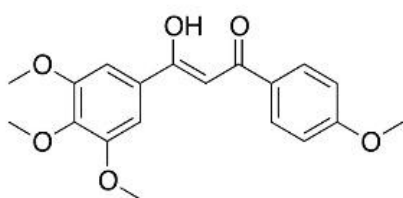
4.1 Introduction

Successful integration of bdk dyes into commercial applications requires a thorough understanding of structure-property relationships and material processing parameters (e.g. temperature, thickness, substrate). Prior reports describe the effects of alkyl chain length,[1,2] halide substitution,[3] arene size[4] and even BF_2 coordination on the optical and room temperature self-healing properties of ML materials.[5] Substitution of stimuli responsive materials with different donor and acceptor groups is also an common strategy for modulating solid state ML properties, such as emission wavelength, intensity, and spontaneous recovery.[6–9] For example, alkoxy substitution modulates solution and solid state optical properties through electronic properties and control of molecular packing.[10–13] Additionally, selective methoxy-substitution can induce intramolecular charge transfer (ICT) in certain bdk dyes, which has been correlated with the solvatochromic and phosphorescent properties.[5,14] Literature precedent combined with the abundance and variety of commercially available starting materials makes methoxy substitution a good strategy for tuning the optical and ML properties of bdk materials. Thus, in this chapter, we employ methoxy substitution to modulate the emission and self-recovery properties of a bdk dye. Though the tetramethoxy-substituted dibenzoylmethane, 3-hydroxy-3-(4-methoxyphenyl)-1-(3,4,5-trimethoxyphenyl)prop-2-en-1-one (gbmOMe) was synthesized and evaluated previously as a sunscreen additive,[15] the stimuli reponsive solid state properties of gbmOMe have yet to be reported.

gbmOMe
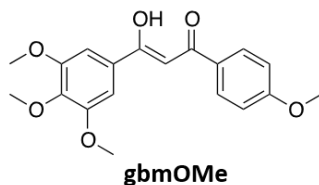
Material processing parameters such as temperature, dye-substrate interactions, film thickness and repeated smearing also influence ML properties. The thermal properties of luminophores are important both for fabrication and because the mechanically triggered changes in optical properties are often the result of temperature dependent crystalline-to-amorphous phase transitions.[3,16] For example, amorphous melt quenched thiophene and furan substituted BF_2bdk derivatives showed red shifted emission compared to their emission in the crystalline state.[17] Thus, it is possible to access the amorphous phase of these materials *via* thermal or mechanical stimululation. Similar optical properties were observed for a triphenyl amine (TPA) based material reported by Mizuguchi *et al*., which showed rapid ML recovery of a green-yellow emissive state that was produced *via* melting and cooling to room temperature in addition to smearing.[18] The identity of this emissive melted state was determined to be a supercooled liquid with red-shifted emission resulting from a twisted intramolecular charge transfer (TICT) state. Additionally, Kim *et al*., observed a high contrast change in emission for an alkylated diketopyrrolopyrrole due to shear-triggered crystallization of a thermally stable supercooled liquid state.[19] The phase transition was attributed to a small Gibbs free energy difference between the crystalline and the supercooled liquid state. Such changes in emission were even activated by small forces associated with live cell attachment. This example demonstrates an application for thermally stable amorphous solids, namely, as cell force sensors. Yet despite their potential for optical and optoelectronic uses,[20,21] and for improving the solubility of various active pharmaceutical ingredients and excipients,[22] supercooled liquids are relatively rare.

Compared to temperature, relatively little is known about how film thickness, dye-substrate interactions, and repeated smearing affect ML recovery properties. This may be due, in part, to the relative scarcity of RT self healing systems. Furthermore, certain fast recovering ML dyes such as

diketones are incompatible with standard room temperature fluorimetry, given they recover faster (s-min) than the time required to record a spectrum. On the other hand, slow self-erasing ML systems are inconvenient to monitor given intensity changes little over long time periods, and subtle substrate and film thickness effects could be inperceptible. Additionally, standard characterization often averages emission intensity over relatively large sample regions and does not account for localized differences in ML recovery. Alternatively, techniques that excite locally, do not provide good spatial resolution of ML recovery processes. To address some of these challenges and obtain 2D spatiotemporal information of ML recovery as a function of substrate, thickness and smearing, we developed a video camera method to monitor the intensity decay of individual pixels over time. Previously we employed this camera imaging technology to track photostability, oxygen dependent lifetime[23] and intensity[24] of BF$_2$bdkPLA phosphorescent materials. This method not only allows for investigation of recovery dynamics of gbmOMe thin films, averaged, as a whole. It also provides a spatially resolved means of evaluating localized recovery effects associated with the smearing process. Structural and stimuli responsive properties of gbmOMe were also investigated using powder and single crystal X-ray diffraction, differential scanning calorimetry (DSC), and through excitation and emission spectra recorded at room temperature and 77 K.

4.2 Results and Discussion

4.2.1 Optical Properties in Solution

The β-diketone gbmOMe was synthesized via Claisen condensation of ester and ketone building blocks as previously described.[25] The optical properties of gbmOMe were measured in dichloromethane solution (Figure S4.1, Table S4.1; Appendix C). UV-Vis spectra reveal an absorption peak (λ_{abs}) at 365 nm with a molar absorptivity of 64,000 M^{-1} cm^{-1}. Though the solution

appeared non-emissive to the eye due to a very low quantum yield (Φ = 0.01 %), a peak was detectable at λ_{em} = 427 nm in the steady state emission spectrum.

4.2.2 Solid State Thermal Properties

To achieve high color contrast, mechanochromic luminescent materials are typically processed by thermal annealing to produce an ordered emissive state. Smearing then generates a redshifted amorphous state. However, qualitative screening of the thermal properties of gbmOMe not only revealed differences between bulk solid and thin film samples, but also showed new phenomena. As a bulk powder, gbmOMe glowed light blue (λ_{em} = 453 nm, Φ = 5.1 %) under UV irradiation. When the powder was heated above the melting point, a melted viscous green emissive phase (MT) formed (λ_{MT} = 481 nm, Φ = 10.0 %). Crystallization of this melted phase occurred within a few minutes after the heat source was removed to yield a blue-emissive solid. However, similar crystallization was not observed for melted thin films of gbmOMe. Instead, the green emissive state persisted upon cooling. Powder XRD patterns further confirmed that bulk gbmOMe is crystalline and melted (MT) thin films are amorphous, as no peaks were observed in the diffraction pattern for the latter samples (Figure S4.2; Appendix C). This relative difference in thermal stability of the MT phase for bulk powder and thin films may indicate a thickness dependence on the crystallization rate of melted gbmOMe.

The thermal properties of gbmOMe were further investigated using differential scanning calorimetry. The sample was heated at a constant rate of 10 °C/min while the rate of cooling was varied for each cycle (Figure 4.1). Each cycle was performed in succession in order to probe the thermal history. Thermograms show that gbmOMe melts at 119 °C regardless of cooling rate. When cooled faster than 1 °C/min, crystallization was not observed for the duration of the cooling

cycle, however crystallization was observed upon subsequent heating. When the rate was slow enough (1 °C/min, 0.5 °C/min), crystallization could be seen during the cooling cycle. These results indicate that the difference in thermal stability of the green amorphous state of gbmOMe as a bulk melt compared to melted thin films could be due to differences in the cooling rates when samples are quenched (i.e. cooled) in air.
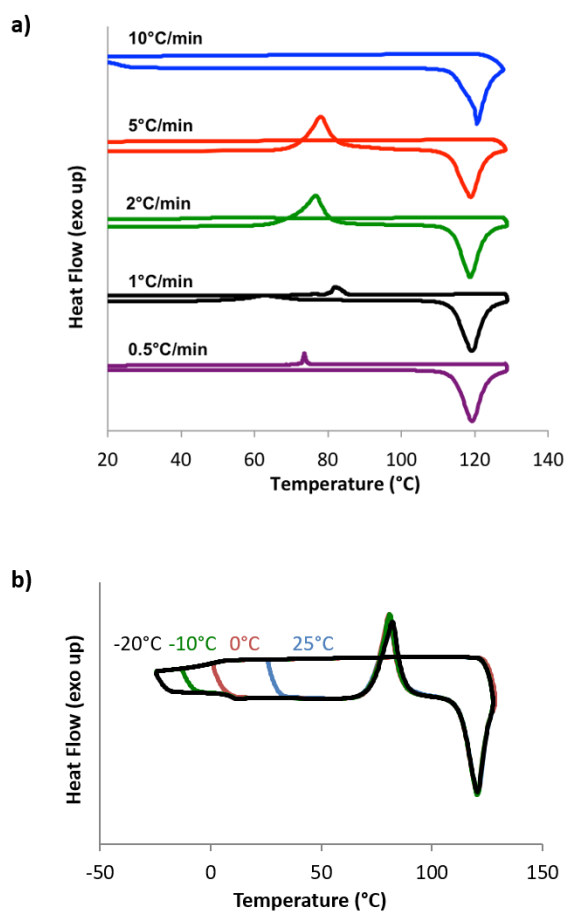
Figure 4.1. Thermal Characterization of gbmOMe. (a) Differential scanning calorimetry (DSC) thermograms of consecutive heating/cooling cycles of gbmOMe with varying cooling rates (ramp rate: 10°C/min). (b) DSC thermograms of gbmOMe cooled to different minimum temperatures (ramp rate: 10°C/min).

To gain further insight into the identity of the green emissive state, successive DSC scans of gbmOMe were run while varying the minimum cooling temperature from 25°C to -20°C (Figure 4.1b). When a relatively fast constant rate of heating/cooling (10 °C/min) was used in order to prevent crystallization of gbmOMe, all scans that were cooled to a sufficiently low temperature showed a glass transition temperature ($T_g = 2$ °C). Combined with the cooling rate dependent crystallization, the presence of a clearly defined T_g could indicate a supercooled liquid state for rapidly cooled gbmOMe above T_g that becomes a glass at lower temperatures.

4.2.3 Mechanochromic Luminescence

In addition to thermal responsiveness, changes in solid-state emission of gbmOMe thin films can also be produced mechanically. Thin films of gbmOMe were investigated on both glass (G) and weighing paper (WP) substrates (Figure 4.2, Table S4.2; Appendix C). Glass films were fabricated by spin coating dilute (0.018 M) dye/THF solutions on microscope cover slips. In the as spun (AS) state (i.e. after solvent evaporation), gbmOMe films on glass were locked into a transparent state that glowed green ($\lambda_{AS} = 499$ nm) under UV light and qualitatively resembled the melt phase. This transparency is atypical, given that as spun films are often opaque.[2,3] Typical thermal annealing of BF$_2$bdk or bdk samples involves heating below the melting temperature followed by cooling to produce a maximally blue shifted state. However, this process was insufficient to anneal gbmOMe films, which showed no change in emission and remained in the transparent green emissive state after heating and cooling. Instead, gbmOMe films on glass were heated at 75 °C (below $T_m = 119$ °C) for 10 minutes, followed by cooling to room temperature, then gentle smearing with a Kimwipe. After ~1 h, blue emissive films formed. To speed up the processing, after smearing, films were again heated at 75 °C for 10 minutes, followed by cooling to produce an opaque, blue emissive, thermally annealed (TA) state ($\lambda_{TA} = 428$ nm) (Figure 4.2d).

It is possible that perturbation of the amorphous phase *via* smearing induced gbmOMe nucleation to form the crystalline TA phase. According to their corresponding XRD pattern, TA thin films on glass were crystalline and AS films were amorphous (Figure S4.2; Appendix C). Smearing of TA films produces green emission ($\lambda_{SM} = 478$ nm) that self-recovers over the course of a few minutes (Figure 4.2, Table S4.2; Appendix C).

Mechanochromic luminescence properties of gbmOMe were also investigated on weighing paper for ready comparison with many previous studies.[3,4] Thin films were prepared by smearing a small amount of gbmOMe (~2 mg) across a piece of weighing paper. The as prepared (AP) WP film glowed blue ($\lambda_{AP} = 428$ nm) under UV exposure and smearing produced green emission that rapidly regained its original blue color (~30 s). Unlike most other ML samples, thermal annealing is not required to produce the maximally blue shifted state. Recovery happens rapidly and spontaneously. Recovery of smeared WP films was so rapid, that an emission spectrum in the SM state could not be obtained at room temperature given the green smeared emission disappeared faster than the time required to perform the measurement.
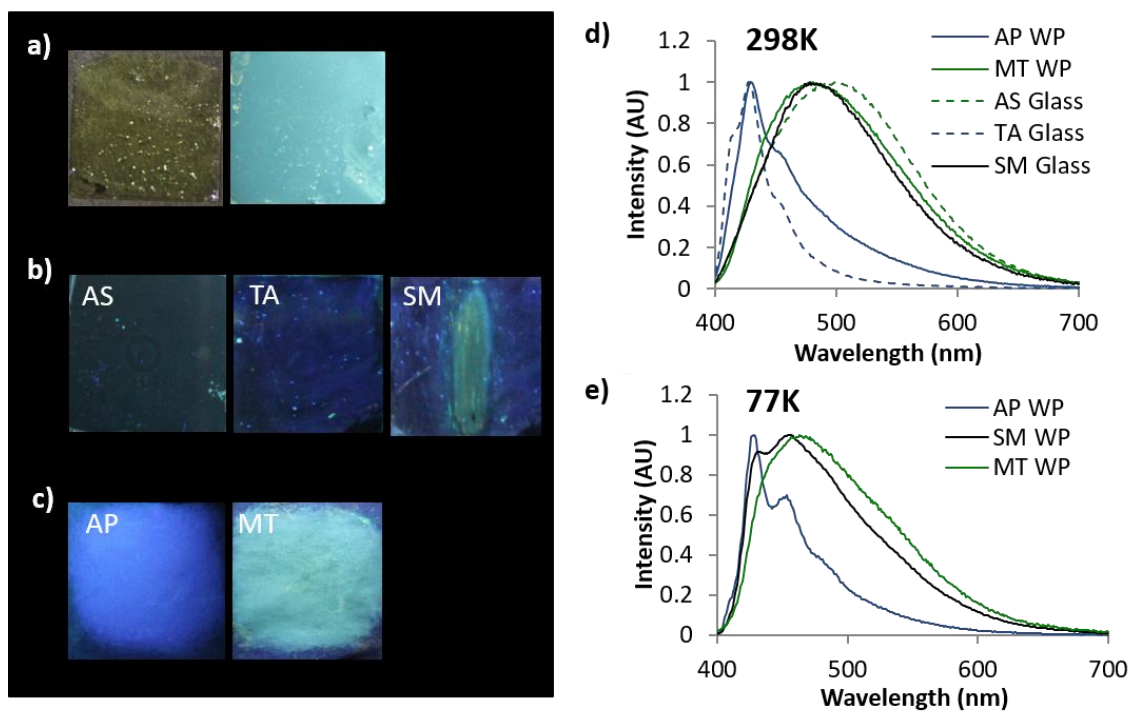
Figure 4.2. Optical Characterization of gbmOMe. Images of gbmOMe thin films (λ_{ex} = 365 nm). (a) On glass in the melted phase (MT) under ambient (left) and UV light (right) at room temperature (b) On glass in as spun (AS), thermally annealed (TA), and smeared (SM) states at room temperature. (c) On weigh paper (WP) films in as prepared (AP) and MT states. Emission spectra of gbmOMe films (λ_{ex} = 369 nm) (d) on WP and glass at room temperature and (e) on WP at 77K.

The self-healing properties of BF$_2$bdk ML materials have been previously ascribed by Ito *et al.,* to the thermal back population from the amorphous phase to the crystalline state.[26] In order to slow the rapid recovery of gbmOMe WP films and observe them in the SM state, the optical properties of WP films were measured at 77K (Figure 4.2e, Table S4.3; Appendix C). Films in the SM state were produced by rubbing the sample, followed by immediate submersion in liquid N$_2$. Excitation spectra were also recorded to probe the different emissive species that exist in AP, MT, and SM weigh paper films (Figure S4.3; Appendix C). The peak emission of smeared films (λ_{SM} = 454 nm) at 77K falls between the slightly red-shifted peak emission of melt films (λ_{MT} = 463 nm) and the blue-shifted peak emission of films in the AP state (λ_{AP} = 429 nm). The relative

proximity in peak emission and their similarly broad emission profiles indicate that the smeared and melt states of WP films contain similar emissive species. However, a shoulder corresponding with the emission of AP films is also visible in the spectrum of the smeared film. This suggests that SM gbmOMe samples are comprised of both green amorphous and blue crystalline emissive species. This is further supported by the excitation spectra monitored at the peak emission of each film. The excitation spectrum of the SM sample contains features of AP and SM films. Incomplete conversion of the sample to the amorphous state upon smearing, or rapid, partial recovery before immersion in liquid nitrogen may explain the presence of blue and green emissive states in the smeared WP film. Based on the optical characterization, it is clear that the mechanically produced color changes observed in gbmOMe films on both glass and WP substrates are produced by the same emissive species.

4.2.4 Structural Characterization

X-ray diffraction studies were performed to gain insight into crystallinity and molecular packing. As previously described, powder XRD patterns of bulk gbmOMe and thermally annealed (TA) glass films indicate that crystalline species produce blue emission and that green emission results from amorphous states (i.e. MT and AS). In order to further investigate the solid-state emission and intermolecular interactions, single crystals were grown by vapor diffusion of hexanes into a concentrated EtOAc solution of gbmOMe. The emission spectrum of the crystals is similar that of other material forms with blue emissive states, however the peak emission of the crystal ($\lambda_C = 452$ nm) is redshifted relative to emission of WP films at room temperature ($\lambda_{AP} = 429$ nm). The difference in emission profiles could indicate the presence of multiple phases in WP films (Figure S4).

According to the crystal structure, gbmOMe adopts a mostly planar conformation. However, the methoxy group in the 4-position of the trimethoxy substituted phenyl ring is out of plane, which can be attributed to steric crowding by the neighboring methoxy substituents (Figure 4.3). Despite the presence of a hydroxyl group in gbmOMe, no intermolecular hydrogen bonding is observed. In fact, the only interactions influencing the crystal packing are C-H···O-C, C-H···arene and weak C-H···H-C van der Waals interactions. For example, multiple C-O···H-Ar interactions (1) between oxygen atoms of meta (*m*-OMe) and para (*p*-OMe) methoxy groups of the tri-substituted arene ring and aryl hydrogens of an adjacent dye are observed (interaction distances: *m*-OMe: 2.711 Å, *p*-OMe: 2.416 Å) Additionally, C-H···O=C interactions (2) are also observed between hydrogen atoms of methoxy groups on the mono-substituted ring and the ketone moiety of neighboring molecules (distance: 2.667 Å) (Figure 4.3b). Examination of the unit cell shows that gbmOMe molecules are arranged in a herringbone configuration with no evidence of face-to-face or offset dimers often observed for ML active bdk-based materials.[20,47] The intermolecular distance was estimated between neighboring dyes using centroids calculated for the trimethoxy substituted rings of each molecule. As evidenced by the large intermolecular distance (5.334 Å), π-π interactions were not observed. This may be the result of out-of-plane methoxy substituents in gbmOMe preventing π-stacking and other strong associations linked with dimer formation in similar bdk systems.[48,49] These groups may also play a role in more rapid recovery.
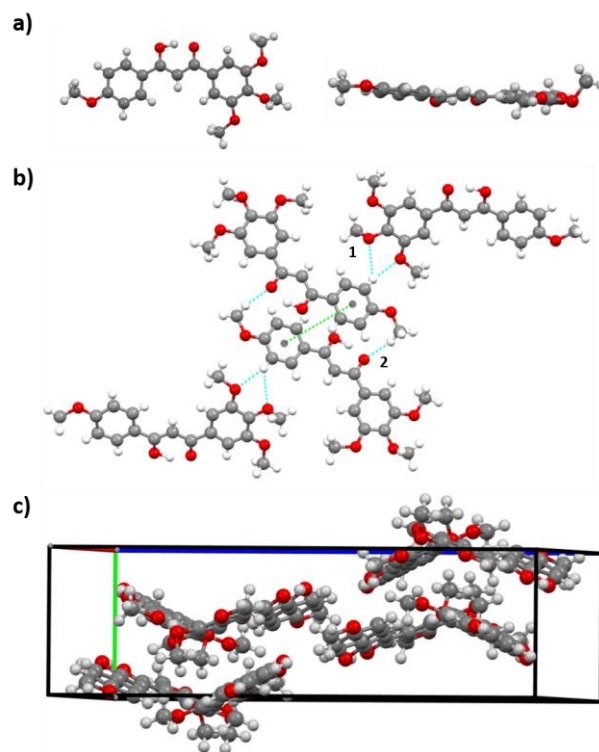
Figure 4.3. (a) Crystal structure of gbmOMe from top (left) and side (right) view. (b) View highlighting C-O⋯H-Ar and C-H⋯O=C interactions in gbmOMe crystals (interaction distances: (1) *m*-OMe: 2.711 Å, *p*-OMe: 2.416 Å; (2) 2: 2.667 Å) and intermolecular distances (green line; 5.334 Å). (c) Unit cell of gbmOMe.

4.2.5 Validation of Camera Method

The ML behavior of glass and weigh paper films is similar, however there is a large difference in their recovery times. All samples show blue to green ML, but the smeared emission of WP films vanishes much more quickly compared to smeared samples on glass. Film thickness, substrate, or other fabrication effects may be involved. In fact, the rapid recovery of gbmOMe provides a good handle for investigation, given the intensity of the SM emission changes on a convenient timescale for measurement.

A camera method was developed to monitor intensity changes during mechanochromic luminescence recovery in gbmOMe films. Specifically, a video was recorded immediately after smearing, and the intensity decay of the smearing induced color changes was monitored for each pixel. The green channel of the camera was used, given significant overlap between its quantum efficiency and the emission profile of the smeared state. Furthermore, the green channel specifically captures the smeared state, given emission from the thermally annealed state does not tail into this region (Figure S4.5: Appendix C). The smeared state decay for each pixel (i.e. recovery lifetime, τ_R) was determined using Matlab by fitting the intensity to a double exponential decay and calculating the pre-exponential weighted lifetime (Figure S4.6, Figure S4.7; Appendix C). Using the τ_R for each pixel, a spatially resolved colormap was generated for each video depicting the smeared region decay process on glass and WP substrates (Figure 4.4a). By computing the mean τ_R across a region of interest on the colormap, calculation of the average smeared state lifetime (τ_{SM}) is possible and processes on WP and glass samples may be compared.

To validate the camera method, it is important to consider other decay pathways that could affect the intensity of emission. For example, continuous UV irradiation for the duration of the video recording could result in photobleaching. In order to ensure that the photodegradation of gbmOMe does not significantly contribute to the intensity decay, a video of gbmOMe WP films was recorded under constant UV illumination. The intensity change of the green channel was measured for films in as prepared (AP) and melt (MT) states given both crystalline and amorphous species are present during the smearing process (Figure 4.4b). For the photostability control experiment, films were irradiated for over three hours which is much longer than gbmOMe recovery on both WP and glass substrates. Films typically recover (i.e. show little change in emission) within seconds (WP) or a few minutes (glass) after smearing. During the course of the

three hour photostability measurement, the intensity of crystalline AP films decreased by ~20%;

whereas, amorphous MT films only showed a slight decrease in intensity (5-10%) over the same

time period. Inspection of photostability data for shorter time frames typically used to monitor

smeared emission decay (i.e. minutes) revealed that intensity differences were imperceptible.

These results indicate that photodegradation is minimal and should not interfere with methods

utilizing intensity to calculate smeared emission decay, τ_{SM}.
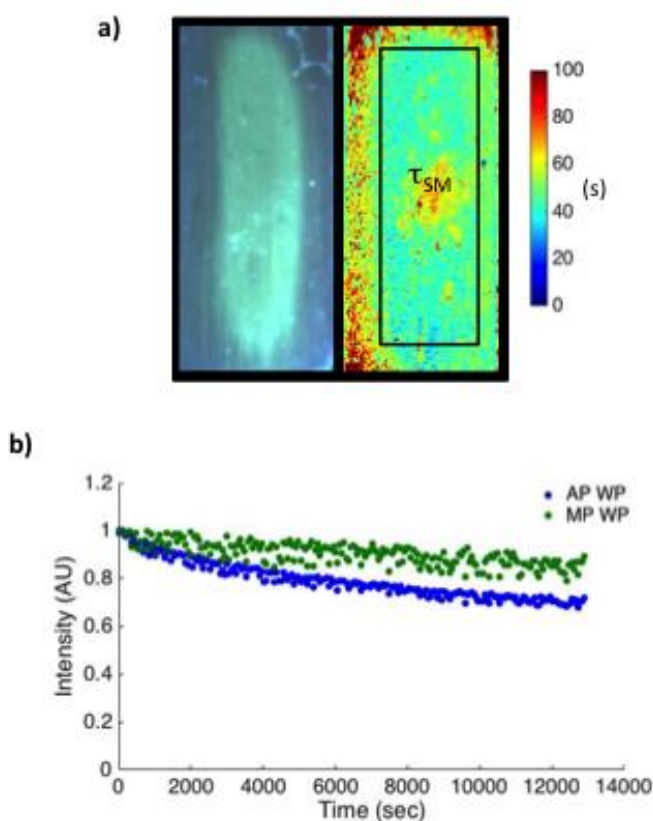
Figure 4.4. Description of Camera Detection Method. (a) Initial frame from the video of a smeared gbmOMe glass film (left) and the corresponding colormap for the smeared intensity decay process (right). The colormap was generated from the pre-exponential weighted lifetimes of the double exponential fit associated with the intensity decay of the green channel for each pixel (τ_R). A region of interest (black rectangle) was defined in order to calculate the average lifetime of the smeared state (τ_{SM}). (b) Photostability experiments showing intensity over time of a continuously illuminated weigh paper films in the "as prepared" (AP) and melted (MT) states ($\lambda_{ex} = 365$ nm).

4.2.6 Investigation of Substrate and Thickness Effects

Sample thickness effects were investigated by three different approaches. Namely, films were prepared by different common methods (i.e. surface application of the solid, drop casting, and spin casting), by varying the sample loading within a given method (e.g. spin casting from solutions of different dye concentrations), and by repeated smearing, which removes some sample with each iteration. An initial investigation was conducted to get a rough idea of how these different approaches affect smeared state decay and to screen for differences. Afterwards, a more detailed study was conducted for glass films and results are presented below.

Films for initial screening were prepared in the following ways. Glass films were prepared by two methods. Thicker glass films were made by drop casting from a concentrated gbmOMe/THF solution (0.090 M) and evaporating in air (G1). Thinner films were produced *via* spin casting from the same concentrated (G2) and more dilute (0.018 M) solutions (G3). (Note: The fabrication procedure for G3 is the same as was used to make films for ML studies on glass above.) Thicker weigh paper films were fabricated by spreading bulk gbmOMe powder (~ 2 mg) across the substrate (WP1; standard fabrication procedure for weigh paper ML films above), and thinner films were made by drop casting from the same concentrated (WP2) and dilute (WP3) solutions that were used to produce glass films. Then glass and WP gbmOMe thin films were repeatedly smeared in the same region and τ_{SM} was calculated for up to ten smearing/recovery cycles (Figure 4.5).

With the exception of G3, most films show comparable smeared state decays (τ_{SM} < 100) regardless of substrate and smearing cycle. Data for WP films shows that τ_{SM} fluctuates randomly between 32s and 52s regardless of the fabrication method (Figure 4.5a). This fluctuation may simply be due to the noise that can be expected in the fabrication and smearing process. To assess

this, the τ_{SM} values for all WP samples were averaged ($\bar{\tau}_{SM} = 41.2$ s) and the standard deviation was computed to be $\sigma_{SM} = 6.0$ s. Comparison of τ_{SM} data for G1 and G2 reveals similar smeared state decays though G2, in particular, shows a slight upward trend with each smearing cycle (G1: cycle 1 = 55 s; cycle 10 = 68 s; G2: cycle 1 = 36 s, cycle 10 = 84 s) (Figure 4.5b). For G3 however, the thinnest glass film, this effect is much more dramatic. After the first cycle, τ_{SM} is already roughly double that of G1 and G2 (e.g. G3: $\tau_{SM} = 98$ s; G1 $\tau_{SM} = 55$ s), and increases significantly with each smearing (i.e. thinning) cycle. After the fourth cycle ($\tau_{SM} = 266$ s), the signal intensity was too low for reliable camera detection, so data were no longer recorded. These results point to a film thickness effect upon smeared state decay, and a possible threshold, below which larger decay times are detected. While τ_{SM} represents an average for an entire 2D region of interest, greater resolution is achieved with colormaps, which display smeared state decays on a pixel-level scale (τ_R). Colormaps associated with both weigh paper (Figure S4.8; Appendix C) and glass films (Figure S4.9; Appendix C) show that regions with longer lifetimes are more prevalent in films that are thinner (i.e. initially, upon repeated smearing, or due to localized smearing effects at the center of the sample).
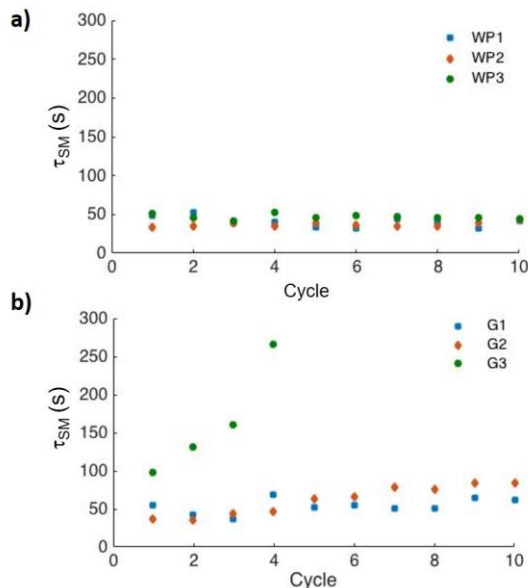
Figure 4.5. Recovery Comparison of gbmOMe on Glass and Weigh Paper Substrates. Smeared state decay (τ_{SM}) of repeatedly smeared gbmOMe thin films on (a) 3" × 1" weigh paper and (b) glass substrates. (τ_{SM} = smeared state decay (τ_R; per pixel) averaged over a region of interest.)

Differences between weigh paper and glass samples may arise from substrate or thickness effects, initially or upon repeated smearing. Though G1 and WP2 were drop cast from the same initial solution, cycle 10 smeared state lifetimes are slightly longer on glass (τ_{SM} = 68 s) than weigh paper (τ_{SM} = 48 s). Furthermore, the colormap of G1 after the tenth cycle shows well-defined regions with large τ_R that are not present in colormaps corresponding to WP2. These findings indicate that the dye likely interacts with cellulose paper fibers differently than with SiO_2 glass. Furthermore, qualitative observations suggest that more sample is removed from hard glass surfaces than from paper with each smearing cycle; additionally, smearing on paper may cause the dye to penetrate into the fibers and be somewhat more resistant to removal with mechanical perturbation. These substrate differences may help to explain why films on paper retain their reversible quality for longer, despite similar preparation and treatment as films on glass.

To test whether weigh paper films also reach a point at which τ_{SM} values begin to increase, WP films with smaller initial thicknesses than WP1-WP3 were fabricated by spin casting from a 0.018 M solution. Though spin casting is somewhat unconventional for paper substrates, it nonetheless addressed challenges associated with drop casting dilute dye solutions, which still produced relatively thick films after evaporation due to the amount of solvent needed to cover the entire sample. After spin casting and annealing at 75 °C, heterogeneous films were obtained that were thin at the centers and thicker at the edges, as confirmed by colormap histograms with bimodal distributions (Figure S4.10; Appendix C). Though a thickness gradient was observed, these films allow monitoring a distribution of smeared state decays on the same surface. After the first smearing/recovery cycle, the colormap showed regions with longer recovery lifetimes, τ_R, where the sample was thinnest compared to the thicker edges that recovered more quickly (Figure 4.6). The colormaps for subsequent smearing/recovery cycles show the erosion of the thicker regions of the sample and a general trend toward longer smeared state decays. Furthermore, the smeared state decays (i.e. calculated from recovery lifetimes τ_R for a region of interest that encompasses both thicker and thinner regions) for each of the cycles (τ_{SM} = 66 s for cycle 1; τ_{SM} = 79 s for cycle 2; τ_{SM} = 83 s for cycle 3) were significantly longer than those observed for bulk and drop cast WP1-WP3 films (35 s $< \tau_{SM} <$ 55 s). Not only does this clearly demonstrate thickness dependent recovery on weigh paper substrates, it also shows that differences in ML recovery behavior can be used to evaluate relative film thickness in a given heterogeneous sample.
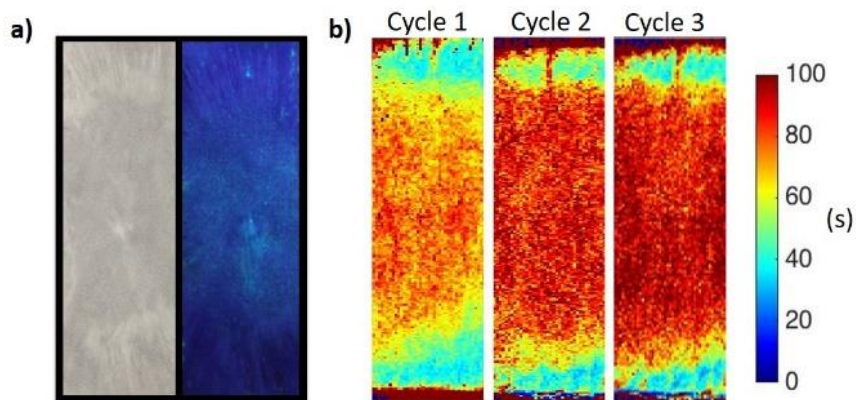
Figure 4.6. Recovery of Thin gbmOMe on Weigh Paper. (a) Images of spin cast gbmOMe films on weigh paper (WP) under ambient light (left) and UV irradiation (right). (b) Spatially resolved colormaps of repeatedly smeared spin cast gbmOMe on WP (λ_{ex} = 365 nm).

According to the initial studies, it is clear that the recovery dynamics of gbmOMe thin films are dependent on sample thickness. Smeared state decays increase with decreasing film thickness, and quite dramatically so for the thinnest samples. In order to investigate these effects more systematically using a single common film fabrication method and substrate, gbmOMe thin films of variable thickness were prepared *via* spin casting from stock solutions of different concentrations (C1 = 0.090 M, C2 = 0.072 M, C3 = 0.054 M, C4 = 0.036 M, C5 = 0.018 M) on glass. This range is bracketed by concentrations used to fabricate G1 and G3 films above. Multiple films were prepared from each solvent, and the relative film thickness was estimated by measuring the absorption spectrum of each film in the AS state, and using the peak absorption (λ_{abs} = 363 nm) and Beer's Law to calculate the corresponding path length of each film (Figure S4.11; Appendix C). Films in the AS state were used to determine relative initial thickness due to their transparency; TA films are opaque and incompatible with this measurement method given scattering effects. Approximate thicknesses were calculated relative to the thinnest film, such that the maximum thickness was over eight times greater in the initial AS state. Based on the absorption spectra, some deviations in thickness were observed when spin casting from stock solutions of the same

concentration. This was especially evident for films fabricated from solution C1. Samples spin cast from concentrated solutions produce less reproducible film thicknesses, which accounts for multiple points per concentration in Figure 4.7b. After annealing, each film was smeared in three separate locations with a cotton swab for finer control (Figure 4.7). Then τ_{SM} values for each smeared region were averaged to quantify the recovery dynamics for a given film (Figure 4.7b) (Mean $\tau_{SM} = \bar{\tau}_{SM}$). This approach provides insight into the reproducibility of smeared state decay values for regions of comparable thickness.

The representative colormaps for films of different initial thicknesses, T1-T5, produced via spin casting from different solvents, C1-C5, show a narrow distribution of smeared state decays within each smeared region (Figure 4.7). A relatively narrow range of $\bar{\tau}_{SM}$ values (26 – 41 s) was observed for all but the thinnest samples (max $\bar{\tau}_{SM}$ = 120 s), which correspond to an 87% decrease in initial thickness compared to the thickest sample. Furthermore, most samples showed very little variation in $\bar{\tau}_{SM}$ regardless of the region being sampled, however the thinnest samples showed the most significant deviation (e.g. T5, SM1). Despite the relatively large error bars associated with data for the thinnest samples, $\bar{\tau}_{SM}$ was still significantly longer compared to thicker film decays. The trend towards longer $\bar{\tau}_{SM}$ for thinner films is additional evidence of a thickness effect in gbmOMe glass films and here too, it appears that a critical thickness threshold must be reached before thickness effects are detected and smeared state decays noticeably increase.
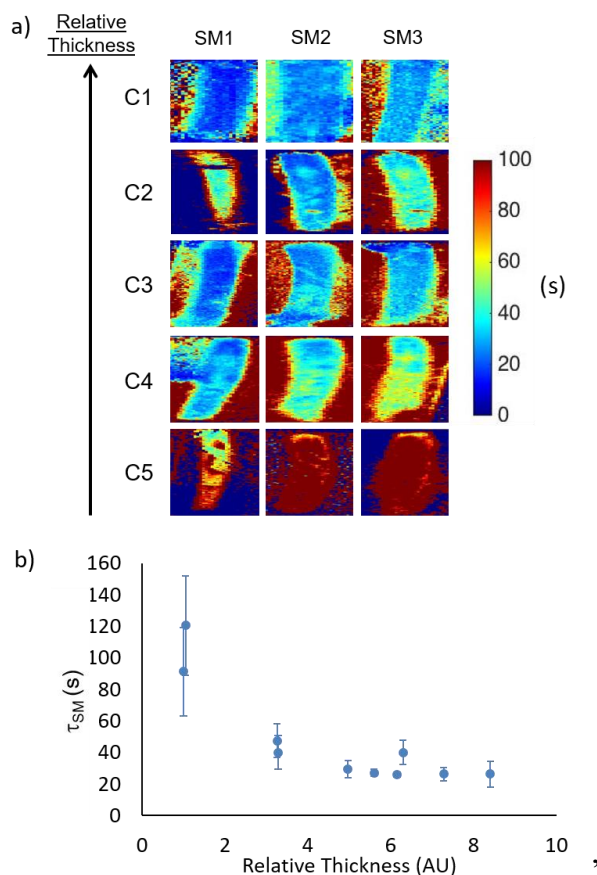
Figure 4.7. Quantitative Recovery of Glass Films with Different Thicknesses. (a) Representative recovery lifetime (τ_R) colormaps of spin cast gbmOMe thin films on glass with different initial thicknesses fabricated via spin casting from different concentration stock solutions. Relative thicknesses were calculated from absorption spectra of each film. Three different regions of each film (SM1, SM2, SM3) were smeared with a cotton swab in order to assess reproducibility of smeared state decays without changing initial thickness due to sample removal. Thicknesses T1-T5 represent films spin cast from progressively more dilute stock solutions (C1 = 0.090 M, C2 = 0.072 M, C3 = 0.054 M, C4 = 0.036 M, C5 = 0.018 M). (b) Mean smeared state decays ($\bar{\tau}_{SM}$) as a function of relative thickness. Error bars represent one standard deviation from the mean $\bar{\bar{\tau}}_{SM}$ for each sample and indicate smearing and thickness variations within a given film. Multiple films were made from each stock solution which produced films with slight variations in initial thicknesses.

To gain further insight into a possible thickness threshold, the regime where smeared state decays change most dramatically, another set of films with varying initial thicknesses, T6-T10, were prepared using the same method as described above. These films were further thinned by repeatedly smearing for five cycles (Figure 4.8). As expected, regions of longer smeared state decay ($\tau_{SM} > 100$ s) developed and grew as the sample was continuously smeared. For thinner

samples these areas became pronounced after fewer cycles. This trend is illustrated by comparing

the two extremes. For the thickest sample, T6, red colored regions with elevated recovery lifetimes

only started to develop after cycle 4. However, for T10, the thinnest sample, longer recovery

lifetimes are observed beginning with the first cycle. Additionally, as T10 was repeatedly smeared,

the size of the longer recovering red region increased such that it encompassed nearly the entire

film after the third recovery cycle. After five smearing cycles, larger τ_{SM} are observed for all

samples regardless of initial film thickness, however the increases in τ_{SM} are less significant for

the thickest sample. One potential explanation for this deviation is that the thickness of T6 has not

yet reached a critical region even after 5 smearing/recovery cycles. As observed for the first cycle,

a general upward trend was observed with decreasing initial thickness, until a maximum smeared

state decay (τ_{SM} = 104 s) was measured for T10. Coupled with the results for the colormaps, these

trends in τ_{SM} provide further evidence that the smeared state decay is highly dependent on the film

thickness of gbmOMe.
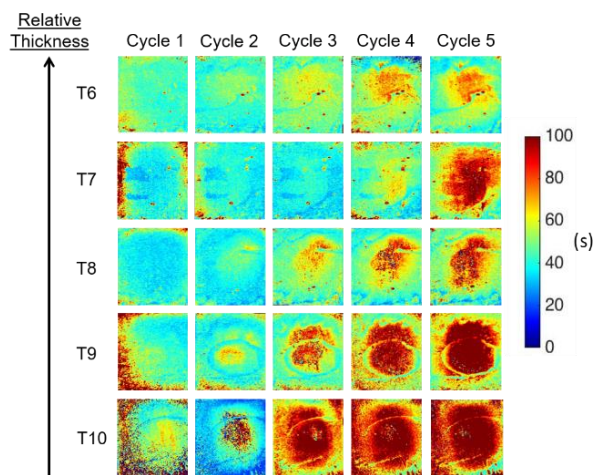
Figure 4.8. Recovery of Repeatedly Smeared Glass Films. Spatially resolved smeared state decay colormaps of repeatedly smeared spin cast gbmOMe thin films with varying thicknesses on glass substrates. Samples were smeared with a Kimwipe for 2 s to aim for consistent sample removal, for 5 smearing/recovery cycles. T6-T10 represent films spin cast from progressively more dilute stock solutions. (T6 = 0.090 M, T7 = 0.072 M, T8 = 0.054 M, T9 = 0.036 M, T10 = 0.-14 M)

Experiments indicate that τ_{SM} is relatively insensitive to thickness effects until a critical threshold is reached. This is evidenced by the small deviations in τ_{SM} that were observed until a requisite amount of gbmOMe was removed, and films with smaller initial thicknesses show longer τ_{SM} values. One potential explanation for this apparent thickness threshold is that sample-substrate interactions become more significant for thinner films and slow ML recovery. Thus, a certain amount of sample must be removed from thicker films before accessing an interfacial regime where substrate interactions can be observed. It is also possible that the material morphology changes in thinner films. Given that ML is a solid-state property, a certain particle size, and number and arrangement of molecules is likely required in the extended array to observe rapid reversibility. The thinnest of samples explored in this study may reach the limits of this regime for gbmOMe. In order to determine the origin of substrate and thickness effects, we plan to examine the smeared state decay of gbmOMe films on functionalized substrates which may alter ML recovery.
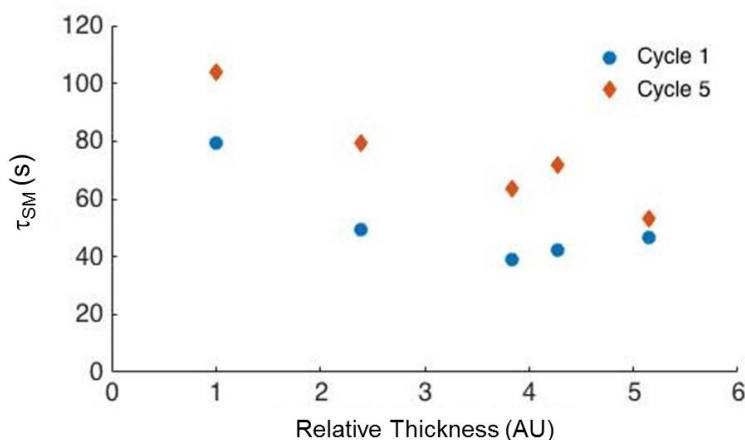
Figure 4.9. Thickness Comparison of Repeatedly Smeared Glass Films. Smeared state decay (τ_{SM}) vs relative initial thickness of smeared gbmOMe glass films after one and five smearing/recovery cycles.

4.2.7 Conclusion

Stimuli responsive gbmOMe has many interesting thermal and mechanochromic properties. As a thin film, gbmOMe forms a thermally-stable supercooled liquid phase when melted and subsequently cooled at ambient temperature. Yet when the bulk dye is cooled at room temperature, a meta-stable supercooled liquid state is formed which eventually recrystallizes after a few minutes. Mechanochromic properties include a blue to green shift in emission upon smearing, along with rapid ML recovery at room temperature. This presents a unique handle for evaluating the performance of self-recovering ML materials by a new camera method. The intensity decay of each pixel (i.e. recovery lifetime, τ_R) was used to generate a spatially resolved colormap of the recovery process. When averaged over a region of interest, smeared state decay values τ_{SM} were calculated and provided a means of comparison between different sample preparations, substrates and film thicknesses. Findings with thicker films illustrate the potential of gbmOMe as a dynamic "renewable ink," given the ability to recover even after repeated use. Thin films of gbmOMe, however, showed thickness dependent smeared state decays on both glass and WP substrates. But significant fluctuations in recovery behavior were only observed in the thinnest films investigated, indicating that a critical thickness must be reached before gbmOMe films lose full reversibility. Kim et al., have shown that quantitative force measurements yield reliable results for uniform films, but are unreliable for molecular solids with heterogeneous coverage.[19] These results show, however, that smeared state decays obtained from camera analysis are quite reproducible even with a qualitative smearing method. Particularly for fast recovering ML systems, films of similar thickness on identical substrates must be used in order to accurately compare and quantify recovery in ML materials. Additionally, threshold effects may well vary for different reversible ML dyes and substrates and should be identified in each case. For certain applications, it may be desirable

to generate films that can fully recover after many smearing/self-erasing cycles. Methods that greatly hinder or prevent sample removal and a reduction in sample thickness would be important. Other dye-substrate combinations and protective coatings that do not significantly affect ML color change and recovery behaviors are avenues worth exploring.

4.3 Experimental Section

4.3.1 Materials

Solvents THF and CH_2Cl_2 were dried over molecular sieves activated at 300 °C as previously described.[30] Reactions were monitored using silica TLC plates. Compounds purchased from Sigma-Aldrich were reagent grade and used without further purification. The β-diketone 3-hydroxy-3-(4-methoxyphenyl)-1-(3,4,5-trimethoxyphenyl)prop-2-en-1-one (gbmOMe) was synthesized as previously described.[25]

4.3.2 Methods

^{1}H NMR (600 MHz) spectra were recorded in dilute $CDCl_3$ using a Varian VRMS/600. Spectra were referenced to the signals for residual protio-$CDCl_3$ at 7.26 ppm and coupling constants were recorded in Hz. UV-vis spectra were collected on a Hewlett-Packard 8452A diode-array spectrophotometer. Steady-state fluorescence emission and excitation spectra were obtained on a Horiba Fluorolog-3 Model FL3-22 spectrofluorometer (double-grating excitation and double-grating emission monochromator). Time-correlated single-photon counting (TCSPC) fluorescence lifetime measurements were performed with a NanoLED-370 ($\lambda_{ex} = 369$ nm) excitation source and a DataStation Hub as the SPC controller. Lifetime data were analyzed with DataStation v2.4 software from Horiba Jobin Yvon. Solid-state quantum yield measurements were acquired using a F-3029 Quanta-Φ Integrating Sphere purchased from Horiba Scientific and analyzed using

FluorEssence software. Fluorescence quantum yields, φ_F, in CH_2Cl_2 were calculated versus a dilute

quinine sulfate solution in 0.1M H_2SO_4 as a standard using a previously described method[31] and

the following values: φ_F quinine sulfate in 0.1M sulfuric acid = 0.54,[32] n_D [33] 0.1M H_2SO_4 = 1.33,

n_D[34] CH_2Cl_2 = 1.424. Optically dilute CH_2Cl_2 solutions of all samples were prepared in 1 cm path

length quartz cuvettes with absorbances <0.1 (a.u.). ML emission was observed by applying a

constant, gentle pressure *via* a cotton swab or a Kimwipe against glass and weigh paper films.

Powder XRD patterns were obtained using a Panalytical X'Pert Pro MPD diffractometer operating

at 40kV and 40ma using Cu Kα radiation. DSC was performed on the pristine powders using a TA

Instruments DSC 2920 Modulated DSC and data were analyzed using the Universal Analysis

software V 2.3 from TA Instruments. Thermograms were recorded using the standard mode while

heating at a constant rate of 10 °C/min. The cooling rate was changed as indicated for different

measurements, but was held constant throughout a given heating/cooling cycle.

Crystallographic Information. Crystals for single crystal XRD were grown by vapor diffusion of

hexanes into ethyl acetate. Data collection was performed using a Bruker Kappa Duo CCD

diffractometer at -120 °C with MoKα radiation. Crystal data for gbmOMe: Orthorhombic space

group Pbca, a = 17.7840(19), b = 7.5472(8), c = 7.5472(8)Å, β = 90°, Z = 8, V = 3393.2(6) Å^3.

The structure was solved by the charge flipping method of the Bruker SHELXTL program and

refined to an R = 0.0475 using 5976 reflections with I > 2σ(I).

Preparation of Thin Films. Bulk powder films for ML characterization were fabricated on weigh

paper substrates by smearing ~2 mg of sample across the entire surface with a Kimwipe. Drop cast

films were prepared by adding 20 drops of gbmOMe/THF solutions (0.090 M and 0.018 M) to 3"

× 1" weigh paper and glass microscope slides. Spin cast films were made using a Laurel

Technologies WS-65OS spin-coater and applying 20 drops to glass microscope slides rotating at

3000 rpm. Both spin cast and drop cast samples were dried under vacuum for 20 min prior to annealing at 75 °C for 10 min. Green emission remained after annealing, so films were gently smeared with a Kimwipe, followed by annealing at 75 °C for another 10 min to produce uniform blue emission.

Smeared State Decay Measurements. Spontaneous smeared emission decay measurements were performed at room temperature using a PGR GS3-U3-41C6C-C video camera with a complementary metal oxide semiconductor CMOS chip capable of 90 frames per second (FPS) at a maximum resolution of 2048x2048 pixels. The camera was also equipped with a Spacecom f/0.95 50 mm lens and an Edmund Optics 425 nm long pass filter to minimize excitation background. The camera was operated with a Lenovo W530 laptop connected *via* a USB 3.0 cable. Point Grey FlyCap2 software was used to record videos of smeared glass and weigh paper films and the data was analyzed using a custom MATLAB 2014b program. The camera was placed approximately 0.5 m above the sample, which was illuminated with a 100W Black-Ray B-100AP/R lamp at 365 nm located ~10 cm above the sample. Videos of recovering samples were recorded using a frame rate of 1 frame per second (fps) and the intensity of the green channel was monitored over time. The initial intensity of the green channel due to sample emission prior to smearing was subtracted from each pixel before fitting data to a double exponential decay and the pre-exponential weighted lifetime was reported. Photostability measurements were performed using the same experimental setup as recovery measurements and irradiating the sample continuously for 4 h while monitoring the pixel intensity every 5 min.

4.4 Acknowledgments

4.5 References

1   W. A. Morris, M. Sabat, T. Butler, C. A. DeRosa and C. L. Fraser, *J. Phys. Chem. C*, 2016, **120**, 14289–14300.

2   N. D. Nguyen, G. Zhang, J. Lu, A. E. Sherman and C. L. Fraser, *J. Mater. Chem.*, 2011, **21**, 8409–8415.

3   W. A. Morris, T. Liu and C. L. Fraser, *J. Mater. Chem. C*, 2015, **3**, 352–363.

4   T. Liu, A. D. Chien, J. Lu, G. Zhang and C. L. Fraser, *J. Mater. Chem.*, 2011, **21**, 8401–8408.

5   T. Butler, W. A. Morris, J. Samonina-Kosicka and C. L. Fraser, *ACS Appl. Mater. Interfaces*, 2016, **8**, 1242–1251.

6   X. Y. Shen, W. Z. Yuan, Y. Liu, Q. Zhao, P. Lu, Y. Ma, I. D. Williams, A. Qin, J. Z. Sun and B. Z. Tang, *J. Phys. Chem. C*, 2012, **116**, 10541–10547.

7   T. Han, X. Gu, J. W. Y. Lam, A. C. S. Leung, R. T. K. Kwok, T. Han, B. Tong, J. Shi, Y. Dong and B. Zhong Tang, .

8   C.-T. Poon, D. Wu, W. H. Lam and V. W.-W. Yam, *Angew. Chemie*, 2015, **127**, 10715–10719.

9   Y. Gong, Y. Tan, J. Liu, P. Lu, C. Feng, W. Z. Yuan, Y. Lu, J. Z. Sun, G. He and Y. Zhang, *Chem. Commun. (Camb).*, 2013, **49**, 4009–4011.

10   T. Mutai, H. Satou and K. Araki, 2005.

11   W. Liu, Y. Wang, M. Sun, D. Zhang, M. Zheng and W. Yang, *Chem. Commun.*, 2013, **49**,

6042.

12   X. Zhang, Z. Ma, Y. Yang, X. Zhang, X. Jia and Y. Wei, .

13   X. Zhang, Z. Chi, B. Xu, L. Jiang, X. Zhou, Y. Zhang, S. Liu and J. Xu, *Chem. Commun.*, 2012, **48**, 10895.

14   J. Samonina-Kosicka, C. A. DeRosa, W. A. Morris, Z. Fan and C. L. Fraser, *Macromolecules*, 2014, **47**, 3736–3746.

15   J.-C. C. Hubaud, I. Bombarda, L. Decome, J.-C. C. Wallet and E. M. Gaydou, *J. Photochem. Photobiol. B Biol.*, 2008, **92**, 103–109.

16   P. S. Hariharan, N. S. Venkataramanan, D. Moon and S. P. Anthony, .

17   W. A. Morris, T. Butler, M. Kolpaczynska and C. L. Fraser, *Mater. Chem. Front.*, 2017, **1**, 158–166.

18   K. Mizuguchi, H. Kageyama and H. Nakano, *Mater. Lett.*, 2011, **65**, 2658–2661.

19   K. Chung, M. S. Kwon, B. M. Leung, A. G. Wong-Foy, M. S. Kim, J. Kim, S. Takayama, J. Gierschner, A. J. Matzger and J. Kim, *ACS Cent. Sci.*, 2015, **1**, 94–102.

20   Y. Shirota and H. Kageyama, *Chem. Rev.*, 2007, **107**, 953–1010.

21   Y. Shirota, *J. Mater. Chem.*, 2005, **15**, 75–93.

22   G. Zogra and A. Newman, *J. Pharm. Sci.*, 2017, **106**, 5–27.

23   A. S. Mathew, C. A. DeRosa, J. N. Demas and C. L. Fraser, *Anal. Methods*, 2016, **8**, 3109–3114.

24   C. A. DeRosa, S. A. Seaman, A. S. Mathew, C. M. Gorick, Z. Fan, J. N. Demas, S. M. Peirce and C. L. Fraser, *ACS Sensors*, 2016, **1**, 1366–1373.

25   G. Zhang, J. Lu and C. L. Fraser, *Inorg. Chem.*, 2010, **49**, 10747–10749.

26   F. Ito and T. Sagawa, *RSC Adv.*, 2013, **3**, 19785.

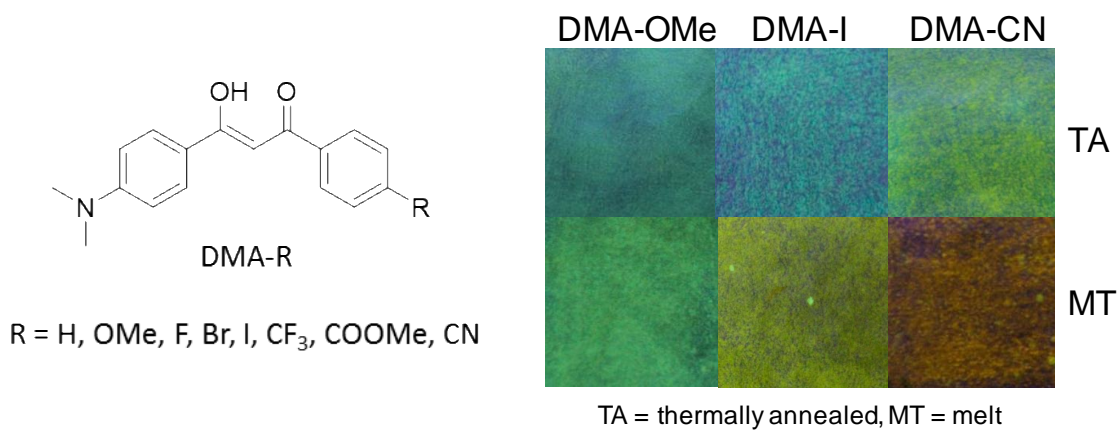27 X. Sun, X. Zhang, X. Li, S. Liu and G. Zhang, *J. Mater. Chem.*, 2012, **22**, 17332–17339.

28 W. A. Morris, M. Sabat, T. Butler, C. A. DeRosa and C. L. Fraser, *J. Phys. Chem. C*, 2016, **120**, 14289–14300.

29 E. V. Fedorenko, A. G. Mirochnik, A. Y. Beloliptsev and V. V. Isakov, *Dye. Pigment.*, 2014, **109**, 181–188.

30 D. B. G. Williams and M. Lawton, *J. Org. Chem.*, 2010, **75**, 8351–8354.

31 E. R. Carraway, J. N. Demas and B. A. DeGraff, *Anal. Chem.*, 1991, **63**, 332–336.

32 H. Zhu, X. Wang, Y. Li, Z. Wang, F. Yang and X. Yang, *Chem. Commun.*, 2009, **0**, 5118–5120.

33 Y. L. Chow, C. I. Johansson, Y.-H. Zhang, R. Gautron, L. Yang, A. Rassat and S.-Z. Yang, *J. Phys. Org. Chem.*, 1996, **9**, 7–16.

34 C. A. Heller, R. A. Henry, B. A. McLaughlin and D. E. Bliss, *J. Chem. Eng. Data*, 1974, **19**, 214–219.

Chapter 5

Dimethylamino-Substituted β-Diketones: Controlling Solid-State Optical Properties of Thermally and Mechanically Responsive Materials

OH   O

N

DMA-R

R = H, OMe, F, Br, I, CF$_3$, COOMe, CN

DMA-OMe   DMA-I   DMA-CN

TA

MT

TA = thermally annealed, MT = melt

5.1 Introduction

Emissive solids are required for many applications, however dyes that are highly emissive in solution often suffer from aggregation caused quenching (ACQ) and thus, are non-emissive in the solid state.[1] However, dyes utilizing aggregation induced emission (AIE) have been incorporated into materials ranging from bioprobes[2] to organic light emitting diodes and chemical sensors.[3,4] While AIE dyes display efficient solid state emission, many applications also require a wide range of emission wavelengths.[5,6] Substitution of luminescent dyes with donor and acceptor groups is an effective strategy for tuning emission colors of stimuli responsive fluorophores.[7–9] Depending on the position and strength of the electron donating or withdrawing substituent, the relative molecular orbital energies of a luminescent dye can be greatly affected.[10] Often this strategy leads to intramolecular charge transfer (ICT) that red shifts emission.[11] The electronic properties of a given substituent can be parameterized using their Hammett constants.[12] Comparison of the para-substituted Hammett constants of each substituent can help to explain trends in the optical properties of donor and acceptor substituted dyes.[13]

Another byproduct of donor and acceptor substitution and associated large molecular dipoles is solvent sensitive emission.[14] Known as solvatochromism, the excited states of these dyes can be stabilized by solvent molecules through dipole-dipole interactions.[15,16] Therefore, longer wavelength emission is observed when solvatochromic dyes are dissolved in more polar solvents. An analogous effect can be observed for dyes emissive in the solid state.[17] The emission of polar dyes in a polymer matrix can be modulated through the addition of polar dopant molecules such as camphoric anhydride (CA) or tris(8-hydroxyquinoline) aluminum (Alq_3).[18,19] This strategy, known as solid-state

solvation, has been used to improve the efficiency of luminescent solar concentrators.[20] Additionally, Bulovic *et al.*, recently manipulated the emission of doped organic thin films through the application of pressure, which forced dyes and dopant molecules into closer proximity and red-shifted emission.[19]

As discussed in the previous chapters, stimuli responsive behavior has been reported in dinaphthoyl-substituted bdk ligands absent boron coordination.[21,22] Compared to their boronated counterparts, bdks are even easier to synthesize and exhibit both AIE and faster rates of recovery after smearing. Additionally, bdks in the keto-enol form have hydrogen bonds in the ground state; thus, excited state intramolecular proton transfer (ESIPT) may be accessible for asymmetric bdks.[23–25] Dyes with ESIPT show particularly large Stokes shifts, of interest for bioprobes[11] and display technologies.[26,27]

R = H, OMe, F, Br, I, CF$_3$, COOMe, CN
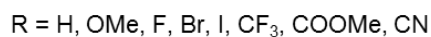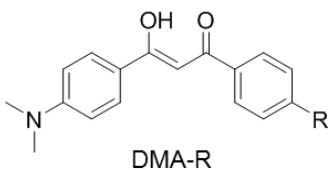
While bdks possess many characteristics promising for application, their stimuli responsive properties have been little investigated. Previously reported ML active bdk dyes showed a narrow (~420-500 nm) emission range, and their thermochromic properties were not reported.[22,28] To produce a broader wavelength range of stimuli responses, in this study, a series of dimethylamino (DMA) substituted diketones were prepared with different electron donating and withdrawing groups. The effect of donor and acceptor substitution on optical properties was tested in solution, and their mechanical and thermochromic responses were measured in the solid state. In addition, the AIE properties of DMA-I and DMA-CN were investigated in THF/H$_2$O solutions. Polystyrene (PS) thin films of these

dyes were used to examine dye loading and polar dopant effects. Structural characterization was performed using powder X-ray diffraction (XRD) and the crystal structure of DMA-I is reported. Thermal properties were investigated using differential scanning calorimetery (DSC).

5.2 Results and Discussion

5.2.1 Synthesis

In order to modulate the solution and solid state optical properties of stimuli responsive β-diketonate dyes, a series of 4-dimethylamino (DMA) substituted derivatives was prepared with various electron donating and withdrawing groups located in the 4'-para position. Substituents were chosen based on their para-substituted Hammett constants, σ_p, in order to assess the effect of donor/acceptor substitution on the optical properties of bdk dyes (OMe = -0.27, H = 0, F = 0.06, I = 0.18, Br = 0.23, CF_3 = 0.42, COOMe = 0.45, CN = 0.66, Scheme S5.1; Appendix D). Compounds were synthesized via Claisen condensation with dimethylamino substituted ketones and the corresponding para-substituted ester in the presence of NaH. All derivatives in this set show enol proton chemical shifts in their NMR spectra (~17.0 ppm) which indicates that dyes occupy a predominately keto-enol configuration in the ground state.

5.2.2 Solution and Computational Characterization

In order to gauge how these different donor/acceptor moieties affect the optical properties of DMA substituted diketones in solution, the absorption and emission spectra were measured in dichloromethane (1 x 10^{-5} M) (Table 5.1, Figure. 5.1). Two distinct peaks were observed in the UV-vis spectra of each dye. With the exception of DMA-H, where the most intense peak was highest in energy, the peak absorbance (λ_{abs}) of other dyes

corresponded to the most red-shifted band. Though bimodal absorption spectra has been attributed to absorption from different tautomeric species that exist in previous studies,[24,29] calculations indicate that that bimodal absorption profiles could arise *via* transitions to the excited state from lower energy orbitals. (See computational details in Supporting Information). Comparison of the peak absorbance (λ_{abs}) of each dye showed a general trend toward longer wavelengths (i.e. lower energy) as the electron withdrawing ability of the para substituent was increased. Only minor substituents effects were observed on the molar absorptivity; all compounds showed similar extinction coefficients ranging from 34,500 $M^{-1}cm^{-1}$ (DMA-CF$_3$) to 44,500 $M^{-1}cm^{-1}$ (DMA-OMe).
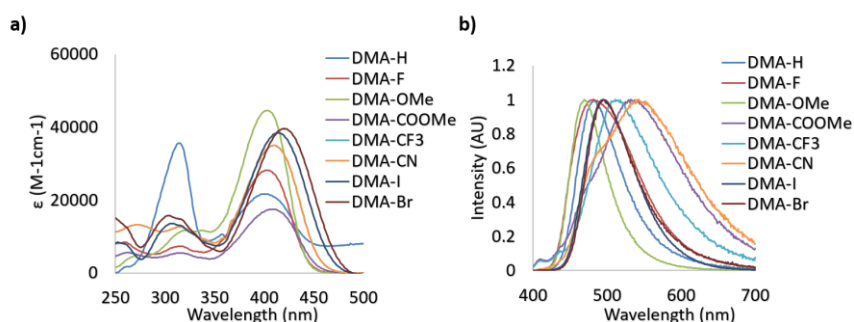
Figure 5.1. Optical Properties of DMA Dyes in Dichloromethane. Absorption (a) and emission (b) spectra of diketones in 1 x 10^{-5} M dichloromethane solution.

A clear substituent effect was observed in the emission properties for dyes in dichloromethane solution. The highest energy peak emission (λ_{em}) was observed for the methoxy substituted derivative, DMA-OMe (λ_{em} = 469 nm), which glowed blue under UV excitation. Upon substitution with stronger electron withdrawing substituents (i.e. larger Hammett constants), a gradual red-shift in λ_{em} was observed. The lowest energy emission was detected for DMA-CN (λ_{em} = 541 nm), which exhibited faint yellow-green emission when exposed to UV light. Additionally, a high-energy shoulder was present in the emission spectrum of DMA-CN, which wasn't observed in the spectra of other dyes. As bimodal emission has often been attributed to ESIPT in dyes with ground state

112

intramolecular hydrogen bonds, this blue-shifted transition could be evidence of a proton transfer process occurring for the cyano substituted diketone.[25] Comparison of the fluorescence lifetime (τ) and quantum yield (Φ) of each dye showed a similar trend. The largest quantum yield and longest lifetime was measured for DMA-OMe (τ = 1.58 ns, Φ = 51%), however both the fluorescence lifetime and quantum yield decreased considerably when substituted with progressively stronger electron withdrawing groups, such that emission is barely observable to the eye for DMA-CF$_3$ (τ = 0.56 ns, Φ = 3%), DMA-COOMe (τ = 0.30 ns, Φ = 1%), and DMA-CN (τ = 0.59 ns, Φ < 1%). Since previously reported diketones are non-emissive in dichloromethane solution,[22] these results demonstrate that donor and acceptor substitution is an effective strategy for designing bdk dyes that are emissive in solution.

Table 5.1. Optical Properties of DMA Derivatives in Dichloromethane Solution

	$\lambda_{abs}{}^b$ (nm)	ε (M^{-1}cm^{-1})	$\lambda_{em}{}^c$ (nm)	Φ^d (%)	τ^e (ns)	$\tau_{rad}{}^f$ (ns)
DMA-H	314	36000	482	30	1.32	4.4
DMA-OMe	403	44500	469	51	1.58	3.1
DMA-F	403	28000	482	37	1.42	4.0
DMA-Br	408	36000	495	16	1.00	6.3
DMA-I	409	35000	494	18	0.99	5.5
DMA-CF$_3$	410	34500	511	3	0.56	18.7
DMA-COOMe	414	38500	532	< 1	0.30	N/A
DMA-CN	420	39500	541	1	0.59	59

^{a} Excited at 385 nm, room temperature, air
^{b} Absorbance maximum
^{c} Emission maximum
^{d} Fluorescence quantum yield
^{e} Pre-exponential weighted fluorescence lifetime
^{f} Radiative lifetime = τ/Φ

According to the emission of DMA dyes in dichloromethane, there is a strong correlation between the emission properties of each dye and the electron withdrawing

ability of the para substituent. With the exception of DMA-OMe, all dyes exhibit radiative lifetimes ($\tau_{rad} > 4.0$ ns) corresponding to ICT emission.[30] The radiative lifetime observed in DMA-OMe solutions was borderline (3.1 ns). Furthermore, previous investigations show that a twisted intramolecular charge transfer transition (TICT) may result from rotation of the DMA substituent.[29] In order to further investigate these trends, density functional theory (DFT) calculations with a Tomasi polarized continuum for dichloromethane solvent were performed. The B3LYP/6-31G(d) basis set was used to produce HOMO and LUMO molecular orbitals (MOs) and simulated UV-vis spectra for all but the hydrogen substituted derivative (Figure 5.2, Figure S5.1; Appendix D), which has been investigated previously.[29] The experimental and computational UV-vis spectra are in close agreement which indicates that computations reasonably approximate optical properties in solution.

The ground state optimized geometries for the dyes are mostly planar, however slight distortions in planarity were observed. Additionally, calculations indicate that the lowest energy conformation of each dye is a keto-enol with the hydroxyl group positioned closest to the DMA substituted phenyl ring. Examination of the HOMO for each dye indicates that electron density is concentrated on the side of the molecule containing the highly electron donating DMA substituent, however a small amount of electron density can be found on the methoxy substituted phenyl ring for DMA-OMe. In the respective LUMOs, the electron density is delocalized throughout the entire molecule for each dye. Close inspection of the LUMO for DMA-CN shows a gradient in electron density throughout the molecule, where the majority is located on the cyano-substituted phenyl ring. A similar distribution in electron density was observed in the LUMO for DMA-COOMe which

114

indicates that stronger electron withdrawing groups tend to attract more electron density in the LUMO. The localized electron density observed in the HOMOs of each dye and the delocalized electron density in the LUMO, also point to ICT transitions, as expected for donor acceptor systems and based on radiative lifetime data.
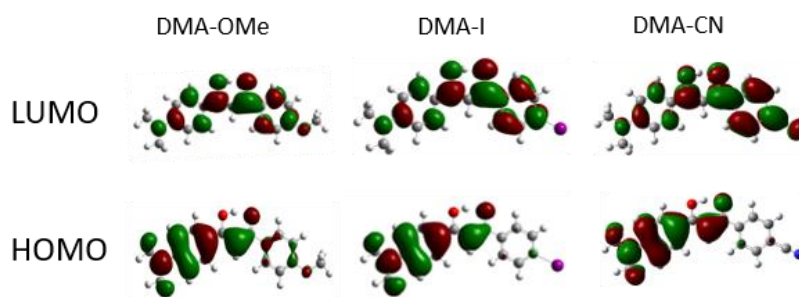
Figure 5.2. Molecular Orbitals of DMA Dyes. HOMO and LUMO molecular orbitals for methoxy (DMA-OMe), iodo (DMA-I) and cyano (DMA-CN) substituted diketones.

5.2.3 Optical Properties in Different Solvents

Relatively large Stokes shifts, long radiative lifetimes, and asymmetric distribution of electron density in molecular orbitals are observed in DMA dyes and are often associated with changes in the excited state molecular geometry as a result of TICT.[31–33] However large Stokes shifts have also been observed in systems that experience excited state intramolecular proton transfer (ESIPT). Since ESIPT has previously been observed in asymmetric diketones, it is possible that these DMA substituted derivatives also exhibit ESIPT.[27] Additionally, solvatochromism is often present in dyes that undergo ICT transitions. Solvatochromism and ESIPT emission can be observed by measuring the optical properties of a given dye in a variety of different solvents. A red-shift in emission intensity with increasing solvent polarity is typically associated with solvatochromic processes, whereas the nature of the solvent (e.g. polar, protic) determines the emission of ESIPT dyes.

Generally, polar or protic solvents disrupt the proton transfer process, which can result in a variety of spectroscopic features depending on dye structure and conformation. It is often difficult to decouple ESIPT from ICT processes since they can occur in conjunction with one another in certain dye systems. The solvent dependent emission of DMA-H was previously studied in great detail using computational and spectroscopic techniques including steady state and ultrafast transient absorption and fluorescence techniques. These studies show that solvent effects not only determine the ground state conformation of DMA-H but also govern the excited state dynamics (i.e ESIPT and/or ICT/TICT) affecting emission.[24,29] While the solvent dependent properties of DMA-H dyes are highly complex (i.e. both ESIPT and/or ICT/TICT occur depending on solvent polarity and ground state conformation) they offer insight into the optical properties of this set of dyes in different solvents.

Investigation of solvent effects on the emission of DMA diketones was performed by measuring the absorption and emission spectra of each dye dissolved in a series of organic solvents at 1 x 10^{-5} M concentration (Figure. 5.3, Figures S5.2-S5.6; Appendix D). With the exception of DMA-CN, all dyes showed a red-shift in emission as the solvent polarity was increased, which is consistent with solvatochromism. Comparison of solvatochromic dyes indicates that the degree of red-shift is dependent on the electron donating or withdrawing ability of the para substituent. To the eye, the emission of the electron donating methoxy substituted derivative, DMA-OMe, changed from blue when dissolved in toluene (λ_{em} = 437 nm) to green in acetone (λ_{em} = 478 nm). As the solvent polarity was further increased, emission was not visible and could only be detected spectroscopically. For DMA-COOMe, which is substituted with an electron withdrawing

acetate group, the emission appeared green in toluene solution ($\lambda_{em} = 483$ nm), and shifted to yellow ($\lambda_{em} = 513$ nm) in chloroform, before becoming non-emissive in more polar solvents. The quenching of emission in polar solvents is typically observed and can be attributed to increased non-radiative decay as solvent stabilization results in a smaller energy gap between ground and excited states, however it could also be due to the formation of a non-radiative TICT state.[32,34]

The slope observed in the Lippert-Mataga plots (Stokes shift, Δv, versus solvent polarity parameter, Δf) describes the sensitivity of a dye toward solvent polarity.[15,16] Aside from DMA-CF$_3$ (1750), the slope is also correlated with the electronics of the para substituent (Fig S7). The slopes of the most strongly donating and withdrawing dyes, DMA-OMe (1150) and DMA-COOMe (2800), bracket those observed for DMA-F (1500), DMA-I (2100), and DMA-Br (2200). This trend indicates that dye sensitivity towards solvent polarity can be effectively tuned through simple donor/acceptor substitutions, consistent with related studies.[14] The anomalous behavior of DMA-CF$_3$ may result from the dual emission profiles measured in chloroform, THF, and acetone, which could be due to ESIPT and/or TICT processes.[29,35] Dual emission is often observed for dyes with TICT as radiation can occur from locally excited (LE) and TICT states. Additionally, emission from both tautomeric excited state species of ESIPT dyes also produces multiple emission peaks. As previously mentioned, these processes are often intertwined so it is difficult to assign the origin of dual emission, however the relatively shallow slope observed for DMA-CF$_3$ is likely the result of dual emission.

The cyano substituted derivative, DMA-CN, shows red-shifted emission when dissolved in dioxanes ($\lambda_{em} = 519$ nm) compared to toluene ($\lambda_{em} = 492$ nm) but clear

solvatochomic trends were not observed in corresponding Lippert-Mataga plots (Figure S5.7; Appendix D). Like DMA-CF$_3$, dual emission profiles were present when dissolved in certain solvents (toluene, choloroform, dichloromethane, THF, and acetonitrile). In acetonitrile solution, the maximum emission of DMA-CN (λ_{em} = 456 nm) was blue-shifted relative to the peak emission in the non-polar solvents, toluene (λ_{em} = 492 nm), and dioxanes (λ_{em} = 519 nm). Previously, these spectroscopic features have been ascribed to the formation of a TICT state,[36] however investigation of the solvent mediated excited state dynamics of DMA-H indicate that ESIPT could also occur for DMA-CN. Despite deviating from Lippert-Mataga theory, the emission shifts observed in toluene and dioxanes solutions indicate that DMA-CN is also sensitive to polarity.

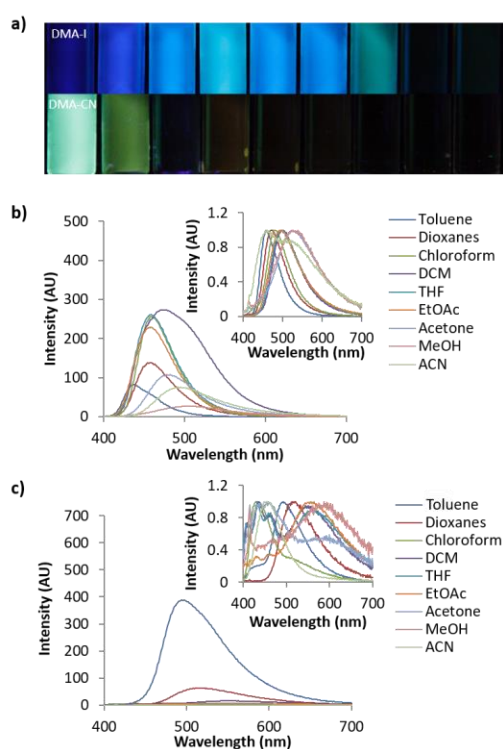**Figure 5.3**. Solvatochromism of DMA Dyes. Image under UV irradiation (from left to right: toluene, dioxanes, chloroform, dichloromethane, ethyl acetate, acetone, methanol, acetonitrile, λ_{ex} = 365 nm). (a) and emission spectra of DMA-I (b) and DMA-CN (c) dissolved in different solvents (1 x 10^{-5} M, λ_{ex} = 369 nm). Insets of (b) and (c) depict emission spectra normalized by their peak emission.

5.2.4 Aggregation Studies

Aggregation induced emission (AIE) was previously observed in dinaphthyl and tetraphenyl ethylene substituted bdk systems.[22,28] While AIE/AIEE has been detected for certain derivatives, these systems exhibit relatively small emission enhancement factors and a narrow range of emission wavelengths. To investigate potential aggregation dependent emission properties and assess donor and acceptor effects on bdk systems, the excitation and emission spectra were measured for moderately (DMA-I) and strongly (DMA-CN) withdrawing dyes (3 x 10^{-4} M) dissolved in THF/H_2O solutions of varying THF and H_2O ratios (Figure 5.4, Figure S5.8-S5.9; Appendix D). These dyes were chosen based on their relative difference in electron withdrawing substituent as well as their high solubility in THF. While H_2O acts as a non-solvent that forces these organic dyes closer together eventually forming aggregate species and enabling visualization of AIE/AIEE, it also increases the polarity of the system. Based on the positive solvatochomic shifts observed for DMA-I and DMA-CN, longer emission wavelengths should be expected as the water fraction is increased.
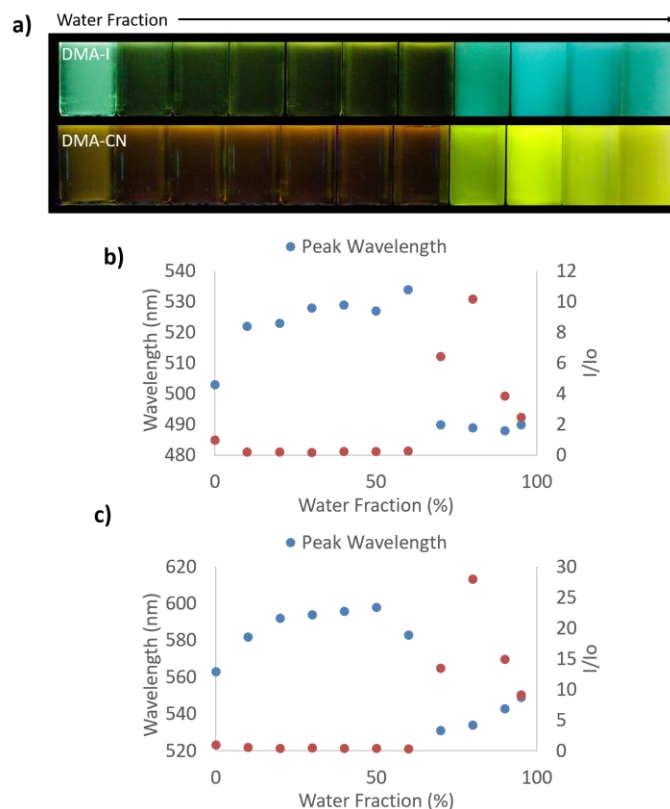
Figure 5.4. Aggregation Induced Emission of DMA Dyes. Image under UV irradiation (λ_{ex} = 365 nm) (a). Plots of peak emission wavelength and intensity relative to emission in pure THF for DMA-I (b) and DMA-CN (c) dissolved in different THF/H_2O solutions with increasing H_2O concentrations (from left to right: 0%, 10%, 20%, 30%, 40%, 50%, 60%, 70%, 80%, 90%, 95%). (3 x 10^{-4} M, λ_{ex} = 369 nm)

In pure THF, DMA-I displayed blue-green emission under UV irradiation (λ_{em} = 503 nm) that was more intense than the dim orange emission observed for DMA-CN (λ_{em} = 563 nm). These differences can be explained based on the increased electron withdrawing ability of the cyano group relative to the iodo substituent. The addition of H_2O resulted in diminished emission intensity and red-shifts in emission wavelengths for both dyes. For water fractions between 10-60%, the emission intensity remained relatively constant however a continual shift towards longer wavelengths was detected before reaching a maximum at 50% H_2O for DMA-CN (λ_{em} = 598 nm) and 60% for DMA-I (λ_{em} = 534 nm). At higher water concentrations (i.e. > 60%), both dyes exhibited sharp intensity increases

along with blue-shifted wavelengths relative to emission in pure THF, which is indicative of AIEE. Furthermore, these solutions are highly turbid which indicates that aggregate species are formed in solutions with sufficiently large H_2O concentrations.

For solutions between 70-95% H_2O, DMA-I showed very little deviation in wavelength (λ_{em} = 488 - 490 nm) and a maximal 10x increase in emission intensity compared to pure THF. Over the same concentration range, DMA-CN showed a further red-shift in emission (λ_{em} = 531 - 549 nm) and a maximal intensity enhancement of 28x. The difference in emission enhancement between iodo and cyano substituted diketones can be explained by the greater initial intensity of DMA-I in pure THF, however it is also possible that aggregate species of DMA-CN exhibit larger quantum yields. This is expected given iodo-substituted dyes show faster rates of intersystem crossing to non-radiative triplet states via the heavy atom effect, which leads to quenching under ambient conditions and therefore lower quantum yields.[37] Both dyes also exhibit trends toward longer wavelengths upon the addition of H_2O which is likely due to stabilization of the polar excited states in more polar THF/H_2O mixtures.

One of the largest differences in AIEE behavior between the iodo and cyano dyes is that the emission wavelength of DMA-CN gradually red-shifted even after aggregation whereas the wavelength of DMA-I was constant. Examination of the emission spectra for solutions that show evidence of aggregate formation (70-95% H_2O) reveals that both DMA-I and DMA-CN initially exhibit highly structured emission. However, broad emission profiles that were devoid of structure were detected for the cyano substituted dye at 90 and 95% H_2O (Figure S5.8; Appendix D). Comparatively, structured emission was noted for DMA-I even in solutions with the largest H_2O concentrations. Previous

investigation of the phase and morphology of AIE dyes suggests that this can be attributed to the formation of different emissive species (i.e. multiple crystalline or amorphous phases) depending on the THF/H_2O ratio.[38]

To better understand AIE properties of DMA-CN and DMA-I, the excitation spectra, monitored at peak emission wavelength, were measured for all THF/H_2O solutions (Figure S5.9; Appendix D). Low energy peaks attributed to ICT transitions were observed for both DMA-I and DMA-CN when dissolved in pure THF. These peaks were ascribed to ICT emission based on computational evidence and literature precedent (i.e. TICT in DMA-H).[29] As the H_2O fraction was increased, the ICT transitions were still clearly visible but with decreased intensity. Upon dye aggregation, a sharp decrease in intensity of ICT transitions was observed in the excitation spectra. For both derivatives, a hypsochromic shift in emission was observed in solutions with large H_2O fractions, which is correlated with dye aggregation. It is possible that this wavelength shift is due to the minimization of the ICT transition for both dyes. Similar behavior was observed for α-substituted BF_2 coordinated bdks dyes, which was attributed to the prevention of TICT upon aggregation.[33] Despite the absence of boron coordination, the trends in emission wavelength of DMA-I and DMA-CN could be explained by an analogous mechanism.

5.2.5 Polystyrene Films

Solvatochromism and AIE measurements indicate that DMA dyes are sensitive to the polarity of their surrounding environments. Furthermore, the degree of sensitivity appears to be correlated with the electron donating/withdrawing ability of the para substituent for a given derivative. Manipulation of the surrounding environment and donor/acceptor substitution are general strategies to tune dye emission in solution, however

the roles that they play in determining the solid-state emission of ML active diketones are less clear. For example, previously reported luminescent bdk materials have a rather narrow color palette compared to emissive boron complex materials.[22] In addition, the solid-state emission intensity of bdk materials is relatively weak compared to similar boron systems. Therefore, design strategies for tuning solid state emission color and intensity are important to improve the performance of stimuli responsive bdk materials.

The effect of matrix polarity on the solid-state emission of DMA dyes was explored by fabricating polystyrene (PS) thin films of iodo (moderately withdrawing) and cyano (strongly withdrawing) substituents. Polystyrene was used for these experiments, because it provides a non-polar medium in which both diketones are soluble. Because these dyes have large ground-state dipoles (>10 D), the polarity of the surrounding medium increases at high dye loadings. However, increased concentration can also lead to aggregation and in many cases, red-shifted emission. Both aggregation and polarity effects were explored by measuring the emission of DMA-I and DMA-CN doped PS films with increasing dye concentration. In an attempt to decouple the magnitude of these competing processes, the excitation and emission properties were also measured for PS films containing dye and camphoric anhydride (CA), a non-emissive polar molecule. For these studies, the dye concentration was held constant while the concentration of CA was increased. This experiment was conducted using dilute (3×10^{-7} mol) and concentrated (4.5×10^{-6} mol) dye loadings. Films were fabricated via spin coating from dichloromethane solutions containing dye/PS or dye/CA/PS in varying ratios.

The emission of PS films was highly sensitive to dye loading (Figure 5.5, Fig S5.10; Appendix D). At the lowest dye concentration (0.019 mol % dye), films were faintly

123

emissive to the eye, however via fluorescence spectroscopy, blue emission was detected for DMA-I/PS films ($\lambda_{em} = 448$ nm) compared to the blue-green emission ($\lambda_{em} = 464$ nm) observed in films containing DMA-CN. Both DMA-I and DMA-CN films exhibited a red-shift in emission even after relatively small changes in dye concentration (0.019 ⁻ 5.0 mol%). At higher dye loadings (>7.0 mol%), the emission wavelength was less sensitive to concentration as only modest changes in emission were detected. While maximally red-shifted emission (DMA-I: $\lambda_{em} = 511$ nm, DMA-CN: $\lambda_{em} = 543$ nm) was observed for both sets of films at the highest dye concentration measured (28 mol% dye), the trend in emission wavelengths suggests that further increases in the concentration would have little effect on the energy of emission.
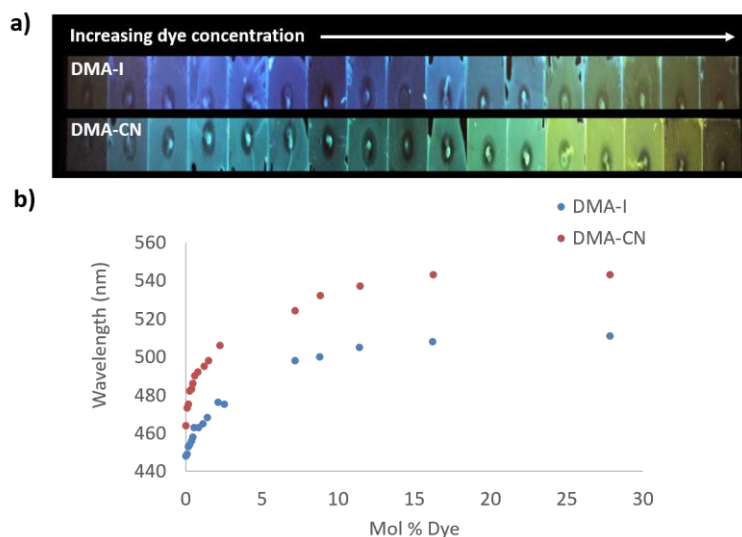
Figure 5.5. Dye Loading in Polystyrene Films. Image under UV irradiation of dye/polystyrene (PS) films with increasing dye concentration ($\lambda_{ex} = 369$) (a). Plots of peak emission (λ_{max}) versus mol% of DMA-I and DMA-CN in PS ($\lambda_{ex} = 369$ nm) (b).

One potential explanation for the emission trends of dye/PS films is that the polarity of the matrix is higher due to the presence of dye molecules. Emission can be red-shifted due to stabilization of localized excited states by surrounding dye molecules which results in a phenomenon known as the solid-state solvation effect (SSSE). Evidence for SSSE

dye/PS films can be seen in their red wavelength shifts ($\Delta\lambda_{em}$) with increasing dye concentration. The wavelength shift was greater for DMA-CN ($\Delta\lambda_{em}$ = 79 nm, μ = 12.6 D) compared to DMA-I ($\Delta\lambda_{em}$ = 63, μ = 10.4 D), which may be attributable to variances in matrix polarity given a larger dipole moment (μ) for the cyano substituted dye. (Estimates of μ were obtained *via* DFT calculations.) However, it is also possible that the red-shift is due, in part, to aggregation of DMA-I and DMA-CN dyes at higher concentrations.

In order to probe potential aggregation effects, the excitation spectra monitored at peak emission wavelength were measured for each film (Figure S5.11; Appendix D). The excitation spectra for all DMA-CN films were similar, which indicated that emission was produced by the same emissive species regardless of dye concentration. Examination of the excitation spectra for DMA-I films shows different behavior. Films with low dye concentration show broad peaks in the excitation spectra, however a blue shift in peak wavelength as well as the emergence of structure was observed at higher dye concentrations. This indicates that different emissive species formed as the concentration of DMA-I was increased, and could be indicative of aggregation. The difference in excitation spectra may be attributed to lower solubility of the iodo-substituted dye in the PS matrix.
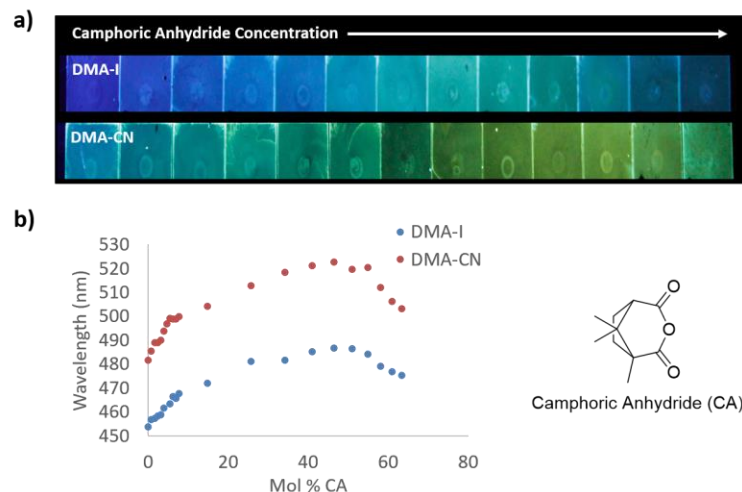
Figure 5.6. Camphoric Anhydride Doped Films with Dilute Dye Concentrations. Image under UV irradiation of dye/camphoric anhydride/polystyrene (dye/CA/PS) films with increasing camphoric anhydride (CA) concentration and dilute (3×10^{-7} mol) dye concentration ($\lambda_{ex} = 365$ nm) (a). Plots of peak emission (λ_{max}) vs mol% of CA in DMA-I and DMA-CN dye/CA/PS films ($\lambda_{ex} = 369$ nm) (b).

To decouple the wavelength trends induced by SSSE from those produced by aggregation, dye/PS films were doped with increasing amounts of camphoric anhydride ($\mu \sim 6$ D)[18] (Figure 5.7, Figure S5.12; Appendix D). When no CA dopant was added, films of DMA-I ($\lambda_{em} = 454$ nm) and DMA-CN ($\lambda_{em} = 482$ nm) glowed blue and blue-green, respectively. Similar to the dye loading experiments, a red-shift in emission was observed at low CA loadings (< 10 mol% CA) followed by a more gradual change as the concentration of CA was increased. When the mole fraction of CA was increased to 46%, green emission was observed for DMA-I films ($\lambda_{em} = 487$ nm), that was significantly higher in energy compared to films of DMA-CN ($\lambda_{em} = 523$ nm), which glowed yellow. As the concentration of CA was further increased, a hypsochromic shift in emission was observed, which can be attributed to phase separation of CA molecules within PS films. Phase separation was confirmed through examination of the XRD patterns for dye/PS/films, which showed crystalline peaks at high CA loadings (63 mol% CA), but

were amorphous for maximally red-shifted dye/CA/PS films (46 mol% CA) (Figure S5.13; Appendix D). Comparison of the wavelength shifts in CA doped films showed that DMA-CN ($\Delta\lambda_{em} = 41$ nm) was more sensitive to matrix polarity effects than DMA-I ($\Delta\lambda_{em} = 33$). This result is consistent with dye loading studies which also showed larger wavelength shifts for DMA-CN.
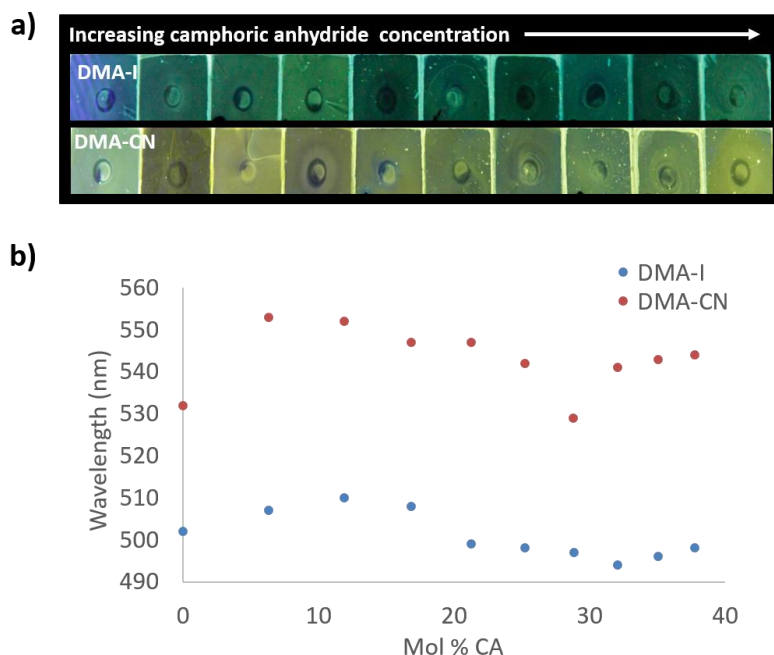

Figure 5.7. Camphoric Anhydride Doped Films with Concentrated Amounts of Dyes. Image under UV irradiation of dye/camphoric anhydride/polystyrene (dye/CA/PS) films with increasing CA concentration and concentrated (4.5×10^{-6} mol) amounts of dye ($\lambda_{ex} = 369$ nm) (a). Plots of peak emission (λ_{max}) vs mol % of CA in DMA-I and DMA-CN dye/CA/PS films ($\lambda_{ex} = 369$ nm) (b).

To investigate dopant effects on films with initially red-shifted emission, films with higher dye loadings and increasing CA concentration were produced (Figure 5.7). The emission without the CA dopant was much more red shifted for both DMA-I ($\lambda_{em} = 502$ nm) and DMA-CN ($\lambda_{em} = 532$ nm) compared to the results discussed above, presumably due to increased dye-dye interactions. Upon the addition of CA, a red shift in emission was observed for both dyes. The maximally red-shifted emissions for DMA-I ($\lambda_{em} = 510$ nm)

and DMA-CN (λ_{em} = 553 nm) were observed at CA mole fractions of 12% and 6%, respectively. Further increase of CA concentration resulted in a blue shift in peak wavelength due to phase separation. Compared to dye loading experiments, the maximally red shifted emission observed for DMA-I/CA/PS films with high initial dye concentrations was nearly identical. However, the emission of corresponding DMA-CN/CA/PS films was lower in energy than maximally red-shifted DMA-CN/PS films. This indicates that increasing matrix polarity with external dopants can further reduce the energy of emission in films with high dye-dye interactions.

Excitation spectra of dye/CA/PS films were measured in order to monitor potential dopant effects on emissive species in these films (Figure S5.14; Appendix D). Spectra showed almost no change as the amount of CA was increased, which indicated that additional ground-state species were not formed in dye/CA/PS films with high CA concentration. Therefore, the shift in emission as the matrix polarity of DMA-I and DMA-CN films was increased may be attributable to stabilization of their respective excited states by neighboring polar molecules. Though emission can be modulated through the addition of a non-polar dopant, the wavelength shift was much smaller compared to the corresponding films with increased dye loading. Additionally, greater concentrations of CA were required to produce red-shifted emission in comparison to dye/PS films, which required smaller amounts of dye to elicit a red-shifted response. This can be explained by the relative polarity of the dopant, as DMA-I and DMA-CN both have larger ground state dipoles than CA.

Dye loading and CA doping experiments suggest that SSSE is a contributing factor toward the red-shift emission observed for these films. However, evidence of aggregation

was also observed in DMA-I/PS films; thus, it is impossible to decouple aggregation from SSSE in these films. Yet, no evidence of aggregation was observed for PS films with increasing DMA-CN concentration, which indicates that the spectral shifts for those films is likely due to higher matrix polarity as opposed to aggregation effects. While it is clear that these dyes behave differently in PS films, the emissions of these dyes are sensitive to polarity effects through the addition of external dopants as well as the dyes themselves. Therefore, the relative polarity of dye molecules could also impact the emission of their corresponding stimuli-responsive solids.

5.2.6 Solid-State Optical Properties

In order to probe donor and acceptor effects on the response of DMA substituted diketones to thermal and mechanical stimuli, thin films were made by smearing a small amount of dye (~2 mg) across 5 cm x 5 cm squares of weigh paper. Films were thermally annealed at 110 ℃ (TA), then were subsequently smeared with a cotton swab to generate the smeared state (SM). The effect of melt quenching was also investigated by heating films above the melting point and cooling in air to produce the melted (MT) state. After melt quenching, the TA state could be regenerated *via* subsequent heating at 110 ℃. Emission spectra were measured for films in the TA, SM and MT states (Table 5.2, Figure 5.8, Figure S5.15; Appendix D).
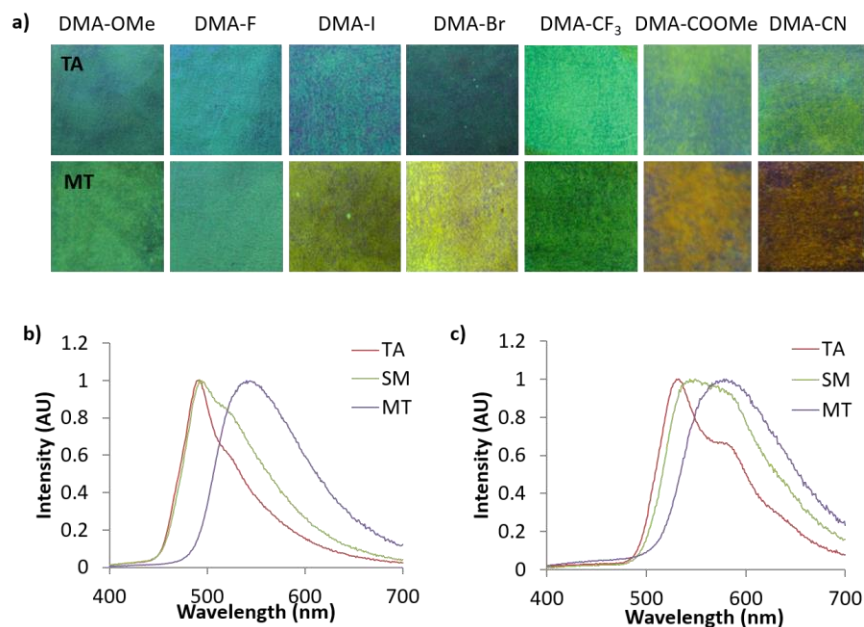
Figure 5.8. Stimuli Responsive Properties of DMA Dyes. Images under UV irradiation of diketones on weigh paper (WP) films in the thermally annealed (TA) and melted (MT) states (a). Emission spectra of DMA-I (b) and DMA-CN WP films in TA, smeared (SM), and MT states.

Since similar behavior was observed for all DMA dyes, exemplary emission spectra for DMA-I and DMA-CN are shown in Figure 5.8. While all dyes show visible solid-state emission in the TA state ranging from blue (DMA-H, DMA-OMe, DMA-F, DMA-Br, DMA-I) to green (DMA-CF$_3$, DMA-COOMe, DMA-CN), the emission of DMA-H is only faintly visible to the eye and is therefore not pictured. The emission of all films in the TA state was red-shifted compared to their emission in dichloromethane solution, however a similar trend toward longer emission wavelengths was observed as the electron withdrawing ability of the para-substituent was increased (Table 5.2). For example, the highest energy emission was observed in both methoxy and fluoro substituted derivatives ($\lambda_{em} = 488$ nm), and DMA-COOMe, a strongly withdrawing dye, exhibited the most red-shifted emission ($\lambda_{TA} = 542$ nm). In addition, both solution and TA measurements indicated that the lowest quantum yield and shortest lifetime was observed for iodo substituted

derivatives. This is likely due to increased intersystem crossing (ISC) to a non-emissive triplet state via the heavy atom effect.

Though comparable trends were observed for emission in dichloromethane solution and the annealed state, some aberrations were detected in TA emission trends. For example, only a small deviation in TA emission ($\Delta\lambda_{TA} = 4$ nm) was observed for DMA-OMe, DMA-F, DMA-Br, and DMA-I despite large changes in electron withdrawing strength. Also, the emission of DMA-COOMe was more redshifted compared to DMA-CN ($\lambda_{TA} = 532$ nm) despite being substituted with a weaker withdrawing substituent. The DMA-H dye was a further exception to this trend because the emission of annealed DMA-H films ($\lambda_{TA} = 514$ nm) was significantly higher in energy when compared to substituents with greater electron withdrawing ability (i.e. F, Br, and I). While evidence of a trend between the electron donation and withdrawing ability and the emission of TA thin films can be established, there is much more deviation compared to dichloromethane solution. This difference in behavior likely results from the more complex optical properties of emissive solids which are often determined by molecular packing effects and often form multiple emissive species.[21,39]

With the exception of dim DMA-H, the emission of all DMA substituted bdks were modulated *via* smearing. Despite visual conformation of mechanically produced color changes, narrow ML shifts ($\Delta\lambda_{ML} < 10$ nm) were measured for several DMA derivatives (DMA-OMe, DMA-F, DMA-I, DMA-CF$_3$, DMA-COOMe). The emission change for many of these analogues can be attributed to spectral broadening as increases in full width at half maximum (FWHM) were detected for each compound. Larger mechanical responses were observed for cyano ($\Delta\lambda_{ML} = 17$ nm) and bromo ($\Delta\lambda_{ML} = 30$ nm) derivatives,

however they were still significantly smaller when compared to other previously studied bromo and methoxy substituted dinaphthoyl diketones ($\Delta\lambda_{ML} > 50$ nm).[22] The absence of a mechanical response for DMA-H could indicate that thermal treatment of films at 110 ℃ was insufficient to fully anneal weigh paper films. However, no change in emission could be produced upon subsequent heating, despite annealing at a variety of different temperatures (80 ℃, 90 ℃ 100 ℃, 120 ℃, 130 ℃).

Table 5.2. Optical Properties of DMA Dyes on Weigh Paper Substrates.[a]

Compound	Annealed				Smeared		Melt			
	λ_{TA}[b] (nm)	τ_{TA}[c] (ns)	FWHM$_{TA}$[d] (nm)	Φ_{TA}[e]	λ_{SM}[b] (nm)	FWHM$_{SM}$[d] (nm)	λ_{MT}[b] (nm)	τ_{MT}[c] (ns)	FWHM$_{MT}$[d] (nm)	Φ_{MT}[e]
DMA-H	519	1.47	114	18.8	518	109	538	-	112	14.8
DMA-OMe	488	0.91	82	53.4	496	90	514	1.74	100	51.2
DMA-F	488	0.69	57	33.5	497	93	522	1.57	101	26.4
DMA-Br	492	0.44	68	25.2	517	109	522	1.48	121	30.1
DMA-I	492	0.13	63	14.1	494	90	540	0.85	106	18.6
DMA-CF$_3$	522	1.77	75	59.3	525	96	528	1.33	86	29.9
DMA-COOMe	542	1.23	103	29.9	550	111	576	1.96	117	21.7
DMA-CN	532	1.47	91	20.4	549	112	578	2.54	118	10.3

[a] Samples were annealed at 110℃ and $\lambda_{es} = 385$ nm
[b] Peak emission wavelength in thermally annealed (TA) smeared (SM) and Melted (MT) states
[c] Pre-exponential weighted lifetime in TA and MT states
[d] Full width at half maximum in TA, SM and MT states
[e] Quantum yield in TA and MT states

Although ML was detectable for all dyes, it was less vibrant when compared to other bdk systems with dinaphthoyl methane scaffolds.[22] However, emission changes could be detected for all DMA analogues after melting and cooling in air (i.e. melt quenching).

132

The degree of wavelength shift after melt quenching ($\Delta\lambda_{MT}$) varied depending on the electron withdrawing substituent. Large shifts were observed for DMA-I ($\Delta\lambda_{MT}$ = 48 nm) and DMA-CN ($\Delta\lambda_{MT}$ = 46 nm) whereas melt quenching of DMA-CF$_3$ only resulted in a 6 nm shift. As observed for samples in dichloromethane solution and the TA state, a general trend toward longer wavelengths is observed with greater electron withdrawing ability of the para substituted groups. The emissions of dyes with strongly withdrawing substituents, such as DMA-COOMe (λ_{MT} = 576 nm) and DMA-CN (λ_{MT} = 578 nm), were much lower in energy compared to the other para-substituted dyes. The peak emission in the MT state of the remaining derivatives fluctuated between a minimum for DMA-OMe (λ_{MT} = 515 nm) and maximum for DMA-I (λ_{MT} = 540 nm). While melt quenching resulted in an increase in fluorescence lifetimes (τ_{MT}) compared to τ_{TA}, quantum yields (Φ_{MT}) changed very little. An increase in lifetime has previously been correlated with the formation of a longer lived amorphous state upon smearing for other ML active bdk materials.[21,40] Because similar behavior was observed in MT films, it is possible that the emission change is also due to the formation of an amorphous state.

Comparison of the solid-state optical properties of DMA-I and DMA-CN with the trends observed in their corresponding PS thin films indicates that the emission of DMA-substituted diketones could be due to changes in the matrix polarity in addition to dye aggregation. To summarize, both the emission of DMA-I/PS and DMA-CN/PS films showed sensitivity toward matrix polarity which was increased through increasing dye loading as well as the addition of the polar, non-emissive dopant, camphoric anhydride. As solid films, the emissions of iodo and cyano substituted derivatives in the TA state were blue-shifted compared to their maximally red shifted dye/PS counterparts (DMA-I: λ_{em} =

511 nm; DMA-CN: $\lambda_{em} = 543$) despite closer proximity to neighboring dyes. Since dyes are typically crystalline after annealing, these results may indicate that the packing arrangement of molecular dipoles leads to diminished matrix polarity compared to the randomly oriented dyes in amorphous dye/PS films. Yet melt quenched thin films of pure dye exhibited more red-shifted emission compared to dye/PS films. Because MT films are typically amorphous, dyes are isotropic which could lead to larger matrix polarities. Therefore, the longer wavelengths observed for these films could be due, in part, to stabilization of localized excited states by randomly oriented neighboring dye molecules. While the emission wavelength of bdk dyes is likely a combination of SSSE and aggregation effects, these data nonetheless indicate that designing solid-state emissive molecules with large molecular dipoles is an effect strategy for modulating the color of stimuli responsive bdk materials.

5.2.7 Thermal Properties

Previously reported bdk and BF_2bdk materials have shown thermochromic properties. Specifically, some methoxy substituted ligands formed transparent supercooled liquid states upon rapid cooling.[41] Alternatively, certain furan substituted BF_2bdks formed opaque amorphous solids after melt quenching.[42] Differential scanning calorimetry (DSC) was used to distinguish these distinct behaviors and here, to probe the thermal properties of DMA diketones (Figure S5.16; Appendix D). All compounds were subjected to two heating/cooling cycles. While the heating rate was held constant between scans (5 ºC/min), the rate of cooling was varied from Cycle 1 (10 ºC/min) to Cycle 2 (1 ºC/min). A fast cooling rate was used to simulate the melt quenching process, whereas slower cooling scans were utilized to promote crystallization.

The thermal properties of all dyes are described in Table 3. All samples showed almost no change in melting temperature (T_m) from Cycle 1 to Cycle 2 and very little deviation in crystallization temperature (T_c) despite the change in cooling rate. The presence of T_c transitions in both cycles indicates that supercooled liquid phases are not formed even at faster cooling rates. The melting temperatures of dyes can give insight into the strength of the intermolecular interactions that determine packing. The lowest melting temperatures were observed when dyes were substituted with electron withdrawing fluoro (T_m = 131.5 °C) and electron donating methoxy (T_m = 132.1 °C) substituents. Comparatively, the other halogenated derivatives DMA-Br (T_m = 188.3 °C) and DMA-I (T_m = 204.9 °C) showed relatively high melting points. Strongly withdrawing derivatives DMA-CN (T_m = 209.5 °C) and DMA-COOMe (T_m = 198.0 °C) exhibited high melting points, however the melting point of DMA-CF$_3$ (T_m = 147.4 °C) was considerably lower. With the exception of DMA-CF$_3$, there is a trend toward higher melting points as the electron withdrawing ability of the substituent increases. Thus, the introduction of donor/acceptor effects can be used to tune T_m of DMA dyes. The anomalous behavior of DMA-CF$_3$ can be rationalized by the increased steric interactions of the CF$_3$ moiety which could disrupt crystal packing and lead to weaker intermolecular associations.

Table 5.3. Differential Scanning Calorimetery Data for Pristine DMA Dyes.[a]

Compound	T_m[b]	T_c[c]
DMA-H	140.4	80.1
DMA-OMe	132.1	99.4
DMA-F	131.5	89.2
DMA-Br	188.3	134.4
DMA-I	204.9	138.9
DMA- CF$_3$	147.4	137.0
DMA-COOMe	198.0	170.0
DMA-CN	209.5	164.2

[a] All data was taken from the 2nd cycle.
[b] Melting point given in ºC as the peak of the major endothermic transition.
[c] Crystallization point given in ºC as the peak of the major exothermic transition.

5.2.8 Structural Characterization

To gain insight into the different phases that determine the stimuli responsive properties of DMA substituted dyes, powder x-ray diffraction (XRD) patterns were measured for the bulk dyes, and films on glass in TA and MT states. Due to sample removal upon smearing, patterns were not obtained for glass films in the SM state. Films for XRD were fabricated by drop casting from a dye/DCM solution (1 x 10^{-5}M) with evaporation in air, followed by drying under vacuum, before annealing and melting each film to access the TA and MT states, respectively. Powder XRD patterns for DMA-I and DMA-CN are shown in Figure 5.9, and the data for the remaining diketones can be found in the supporting information (Figure S5.17; Appendix D). Single crystal XRD analysis of DMA-I was also performed to investigate potential packing effects. Crystals were grown via slow evaporation of a concentrated DMA-I/DCM solution. Though we attempted to grow

crystals of all previously unexplored DMA dyes, only DMA-I formed crystals suitable for diffraction.

The sharp diffraction peaks found in the powder XRD patterns indicate that all compounds were crystalline as bulk powders. Also, all samples showed diffraction peaks as films on glass in the TA states which corresponded to peaks in the bulk powder. Comparison of TA patterns for all dyes indicated that the relative peak intensity and number of peaks was substituent dependent, however the observation of peak patterns of TA glass films indicated the emission was produced by crystalline species. Data taken for melted films were largely devoid of peaks suggesting that they were amorphous, however small peaks were observed in bromo and iodo heavy atom substituted MT films. For example, small diffraction peaks are evident for DMA-I samples, indicating this dye has a greater propensity to crystallize, similar to previously reported iodo substituted BF$_2$bdk derivatives.
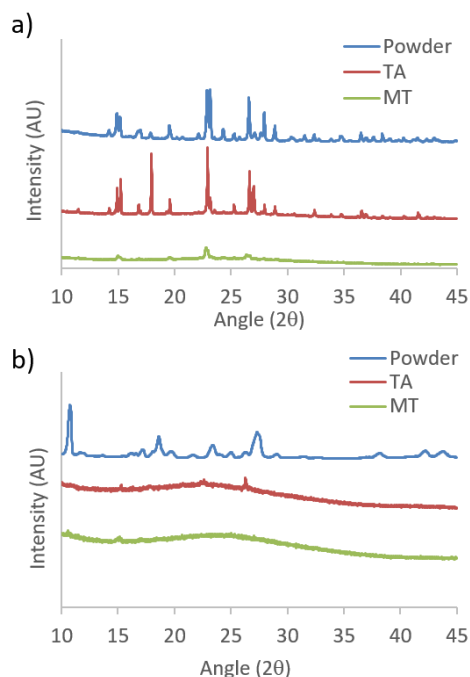

Figure 5.9. Powder X-ray of DMA dyes. Patterns of (a) DMA-I and (b) DMA-CN bulk powders and films on glass in thermally annealed (TA) and melted (MT) states.

Single crystal analysis of DMA-I revealed that dyes adopt a nearly planar conformation with the DMA substituent and phenyl rings in roughly the same plane (Figure 10a). A slight deviation from planarity is observed in the twisting of the phenyl rings about the diketone core. Examination of the unit cell shows that DMA-I packs in a herringbone motif with C-H···I, and C-H···arene interactions (Figure 5.10b). Iodine-iodine interactions, which were previously observed in crystal structures of iodo-substituted BF$_2$bdks, were not detected in the crystal packing of DMA-I.[37] Additionally, there is no evidence of dimer formation, as neighboring dyes are stacked at slight angles relative to each other. While DMA-I does show a visible ML shift upon smearing, it is less dramatic compared to previously studied dinapthoyl substituted bdks.[37] The emission spectrum of DMA-I shows that the color change is mostly due to a broadening of the emission profile rather than a shift in peak emission.
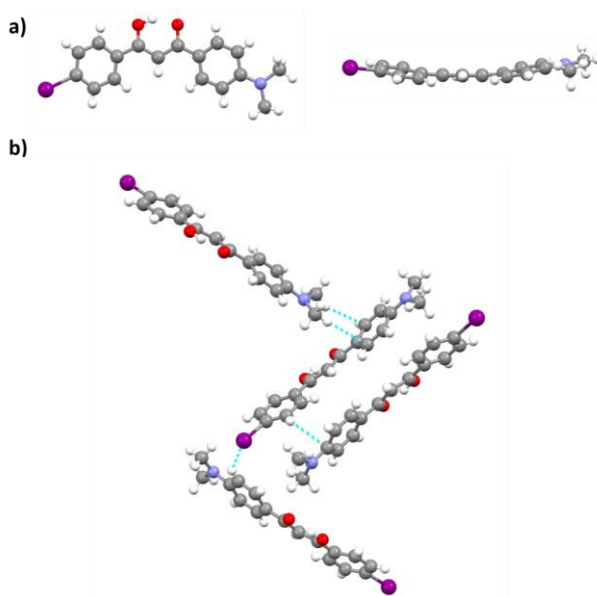

Figure 5.10. Crystal Packing of DMA-I. Crystal structure of DMA-I from two perspectives (a). Unit cell of DMA-I showing packing interactions (b).

5.2.9 Conclusion

In summary, the electron withdrawing ability of dye substituents had a large effect on the solution and solid-state optical properties of DMA dyes. According to DFT calculations, all dyes showed evidence of ICT in their HOMO and LUMO molecular orbitals which correlated with a positive solvatochromic shift. Dye sensitivity toward solvent polarity depended on the electron withdrawing strength of the para substituent, however the cyano substituted dye, DMA-CN, exhibited evidence of ESIPT. The AIE properties of DMA-I and DMA-CN were tested in THF/H_2O solutions with increasing H_2O fractions. Both dyes showed AIE, however longer wavelength emission and a larger intensity increase was observed for DMA-CN. Polystyrene thin films of DMA-I and DMA-CN with increasing concentrations of dye and camphoric anhydride, an external polar dopant exhibited red-shifted emission, which indicated that they are sensitive to matrix polarity in addition to exhibiting solvatochromism. Both smearing and melting dye films on weigh paper resulted in emission responses, however the maximally red-shifted emission was observed after melt quenching. Like other ML active BF$_2$bdk and bdk systems, powder XRD patterns indicate that the change in emission is linked with a phase change from crystalline in the TA state, to amorphous for SM and MT films. As with their emission in solution, a strong correlation between the strength of the electron withdrawing group and the wavelength of solid-state emission, especially in the amorphous MT phase. Based on the sensitivity of DMA-I and DMA-CN emission toward matrix polarity in PS films, it is possible that neighboring dye molecules stabilize the excited state of homogenous dye films as well, leading to red shifted emission. While there are likely many effects that determine emission in stimuli responsive materials (e.g. aggregation),

engineering dyes with large molecular dipoles in order to utilize matrix polarity effects is a design strategy for future stimuli responsive luminescent materials. Furthermore, this work represents an important step forward in the design of boron-free bdk materials as compounds with wide ranging colors and thermochromic properties were achieved.

5.3 Experimental Details

5.3.1 Materials

THF was dried over molecular sieves activated at 300 ºC as previously described. Reactions were monitored using silica TLC plates. Compounds purchased from Sigma-Aldrich and TCI were reagent grade and used without further purification. The dimethylamino-substituted β-diketones were synthesized *via* Claisen condensation using a previously described method.[43] Data for DMA-H,[24,29] DMA-OMe,[44] and DMA-CN,[36] are in accord with previous reports. Characterization data for new derivatives are provided in the Supporting Information.

5.3.2 Methods

^{1}H NMR (600 MHz) spectra were recorded on a Varian VRMS/600 spectrometer in deuterated DMSO and CDCl$_3$. Spectra were referenced to the signals for residual protio-DMSO at 2.50 ppm and protio-CDCl$_3$ at 7.27 ppm. Coupling constants were reported in Hz. Mass spectra were recorded using a Micromass Q- TOF Ultima spectrometer, using electrospray ionization (ESI) MS/MS techniques. Absorption spectra were collected on a Hewlett-Packard 8452A diode-array UV-vis spectrophotometer. A Horiba Fluorolog-3 Model FL3-22 spectrofluorometer (double-grating excitation and double-grating emission monochromator) was used to measure steady-state emission spectra. Time-correlated single-photon counting (TCSPC) fluorescence lifetime measurements were performed with

a NanoLED-370 (λ_{ex} = 369 nm) excitation source and a DataStation Hub as the SPC controller. Lifetime analysis was done with DataStation v2.4 software from Horiba Jobin Yvon. Fluorescence quantum yields, φ_F, in CH_2Cl_2 were calculated versus a standard of dilute quinine sulfate solution in 0.1M H_2SO_4 using a previously described method[51] and the following values: φ_F quinine sulfate in 0.1M H_2SO_4 = 0.54,[45] n_D[46] 0.1M H_2SO_4 = 1.33, n_D[46] CH_2Cl_2 = 1.424. Optically dilute CH_2Cl_2 solutions of all samples were prepared in 1 cm path length quartz cuvettes with absorbances <0.1 (a.u.). A F-3029 Quanta-Φ Integrating Sphere from Horiba Scientific was used to measure solid state quantum yields and data were analyzed using FluorEssence software. A Laurel Technologies WS-65OS spin-coater was used to fabricate polystyrene (PS) films for dye loading and polarity studies. Differential scanning calorimetry (DSC) was performed on the pristine powders using a TA Instruments 2920 Modulated DSC. Data were analyzed using Universal Analysis software V 2.3 from TA Instruments. Thermograms were recorded using the standard mode and a constant heating rate of 5 ºC/min. A cooling rate of 10 ºC/min was used during the initial cycle compared to a cooling rate of 1 ºC/min for subsequent cycles. Powder x-ray diffraction (XRD) patterns were obtained using a Panalytical X'Pert Pro MPD diffractometer operating at 40 kV and 40 ma using Cu Kα radiation.

Single Crystal Analysis. Single crystals of DMA-I for XRD analysis were grown by slow evaporation from a concentrated dichloromethane solution. Data sets were obtained using a Bruker Kappa Duo CCD diffractometer at −120 ºC using Mo Kα radiation. Crystal data follow the orthorhombic space group P 2_1 2_1 2_1, a = 6.1493(13) Å, b = 12.443(3) Å, c = 19.762(4) Å, β = 90º, Z = 4, V = 1512.1(6) Å^3. The structure was solved using the charge

flipping method in Bruker SHELXTL program and refined to R = 0.0165 using 7350 reflections with $I > 2\sigma(I)$.

Preparation of Aggregates in Solution. Stock solutions (0.03 M) of DMA-I and DMA-CN were prepared in dichloromethane and aliquots of the stock solution were added to 20 mL sample vials and evaporated in air. Each vial was diluted to a total volume of 10 mL with THF and H_2O in the indicated ratios and the resulting solutions (3×10^{-4} M) were sonicated for 10 min prior to measurement of excitation and emission spectra.

Preparation of Thin Films. Films for powder XRD characterization were fabricated by preparing a 1×10^{-3} M stock solution of each dye in dichloromethane. Ten drops of the solution were added to 18 x 18 mm glass microscope coverslips and evaporated in air. Stock solutions of the same concentration were used to make thin films for solid-state quantum yield measurements. In this case, five drops of the stock solution were added to 12 mm diameter circular glass coverslips and evaporated under air. Films were dried *in vacuo* for 20 min prior to measurement.

Dye loading and dopant effects on emission properties were investigated using spin cast polystyrene (PS) films. For dye loading experiments (dye/PS films), films were comprised of PS and increasing concentrations of a single dye (DMA-I, DMA-CN). Films for dopant studies (CA/dye/PS) contained constant amounts of PS and dye with increasing quantities of camphoric anhydride (CA). Two sets of CA/dye/PS films were made for each dye, both dilute (3×10^{-7} mol) and concentrated (4.5×10^{-6} mol). Generally, PS films were fabricated by adding 10 drops of dye/PS or CA/dye/PS dichloromethane solutions to 18 x 18 mm glass microscope coverslips rotating at 3000 rpm. Solutions for spin casting dye/PS films were prepared in sample vials by mixing dichloromethane stock solutions of PS (0.01

M), DMA-I (0.03 M), or DMA-CN (0.03 M) in the proper ratios to produce dye/PS films ranging from 0.019 to 28.0 Mol %. The resulting solutions were evaporated in air before dilution with 1 mL of dichloromethane for spin casting. Films for testing the effect of matrix polarity on properties (i.e. CA/dye/PS films) were made using an analogous procedure except that different volumes of a CA stock solution (0.33 M) was added to each vial in order to fabricate CA/dye/PS films ranging from 0 to 63.5 mol% CA. Films were dried under vacuum for 20 min prior to measurement.

To investigate the thermal and mechanical responses, nitrile examination gloves were used to smear a small amount of dye (~ 2 mg) onto 5×5 cm squares of weighing paper (WP). Films were annealed at 110 ºC for 10 min prior to measuring their emission. Mechanochromic luminescence was measured after gentle smearing of annealed films with a cotton swab. Thermochromic properties were observed after melting with a heat gun and cooling in air (i.e. melt quenching).

Computational Details. Diketones were modeled using the Gaussian 09 suite of programs with density functional theory (DFT).[47] A basis set of B3LYP/6-31+G(d) was utilized for ground state optimization. For DMA-I, the basis set B3LYP/SDD was used to model iodine. A Tomasi polarized continuum for dichloromethane was used to simulate solvent interactions. The vibrational frequencies for the optimized geometries were all positive, which indicated that the geometries are at least a local minimum. Molecular orbital diagrams were generated using single point energy calculations with B3LYP/6-31G(d). Time-dependent density functional theory, TD-B3LYP/6-311+G(d), was employed for estimates of absorption spectra and the first three excited states were calculated.

5.4 Acknowledgements

5.5 References

1   W. Z. Yuan, P. Lu, S. Chen, J. W. Y. Lam, Z. Wang, Y. Liu, H. S. Kwok, M. Yuguang and B. Z. Tang, *Adv. Mater.*, 2010, **22**, 2159–2163.

2   D. Ding, K. Li, B. Liu and B. Z. Tang, *Acc. Chem. Res.*, 2013, **46**, 2441–2453.

3   Z. Li, Y. Q. Dong, J. W. Y. Lam, J. Sun, A. Qin, M. Häußler, Y. P. Dong, H. H. Y. Sung, I. D. Williams, H. S. Kwok and B. Z. Tang, *Adv. Funct. Mater.*, 2009, **19**, 905–917.

4   Y. Dong, J. W. Y. Lam, A. Qin, J. Liu, Z. Li, B. Z. Tang, J. Sun and H. S. Kwok, *Appl. Phys. Lett.*, 2007, **91**, 1–4.

5   C. Li, M. Liu, N. G. Pschirer, M. Baumgarten and K. Muellen, *Chem. Rev.*, 2010, **110**, 6817–6855.

6   P. M. Beaujuge, C. M. Amb and J. R. Reynolds, *Acc. Chem. Res.*, 2010, **43**, 1396–1407.

7   G. Zhang, S. H. Kim, R. E. Evans, B. H. Kim, J. N. Demas and C. L. Fraser, *J. Fluoresc.*, 2009, **19**, 881–889.

8   C. M. Ip and A. Troisi, *J. Phys. Chem. Lett.*, 2016, **7**, 2989–2993.

9   C.-T. Poon, D. Wu, W. H. Lam and V. W.-W. Yam, *Angew. Chemie*, 2015, **127**, 10715–10719.

10   L. Zöphel, V. Enkelmann and K. Müllen, *Org. Lett.*, 2013, **15**, 804–807.

11   A. S. Klymchenko, *Acc. Chem. Res.*, 2017, **50**, 366–375.

12   E. J. Choi, E. Kim, Y. Lee, A. Jo and S. B. Park, *Angew. Chemie Int. Ed.*, 2014, **53**, 1346–1350.

13   J. Wu, Y. Cheng, J. Lan, D. Wu, S. Qian, L. Yan, Z. He, X. Li, K. Wang, B. Zou and J. You, *J. Am. Chem. Soc.*, 2016, **138**, 12803–12812.

14   X. Y. Shen, Y. J. Wang, E. Zhao, W. Z. Yuan, Y. Liu, P. Lu, A. Qin, Y. Ma, J. Z. Sun and B. Z. Tang, *J. Phys. Chem. C*, 2013, **117**, 7334–7347.

15   E. Lippert, *A Phys. Sci.*, 1955, **10**, 541–545.

16   N. Mataga, Y. Kaifu and M. Koizumi, *Bull. Chem. Soc. Jpn.*, 1956, **29**, 465–470.

17   V. Bulović, R. Deshpande, M. E. Thompson and S. R. Forrest, *Chem. Phys. Lett.*, 1999, **308**, 317–322.

18   C. F. Madigan and V. Bulović, *Phys. Rev. Lett.*, 2003, **91**, 247403–247404.

19   W. Chang, G. M. Akselrod and V. Bulović, *ACS Nano*, 2015, **9**, 4412–4418.

20   A. P. Green, K. T. Butler and A. R. Buckley, *Appl. Phys. Lett.*, 2013, **102**, 133501–133504.

21   T. Butler, W. A. Morris, J. Samonina-Kosicka and C. L. Fraser, *Chem. Commun.*, 2015, **51**, 3359–3362.

22   T. Butler, W. A. Morris, J. Samonina-Kosicka and C. L. Fraser, *ACS Appl. Mater. Interfaces*, 2016, **8**, 1242–1251.

23   J. E. Kwon and S. Y. Park, *Adv. Mater.*, 2011, **23**, 3615–3642.

24   J. Zhao and Y. Yang, *J. Mol. Liq.*, 2016, **220**, 735–741.

25   A. P. Demchenko, K.-C. Tang and P.-T. Chou, *Chem. Soc. Rev.*, 2013, **42**, 1379–

408.

26   J. E. Kwon, S. S. Y. Park and S. S. Y. Park, *J. Am. Chem. Soc.*, 2013, **135**, 11239–11246.

27   K.-C. Tang, M.-J. Chang, T.-Y. Lin, H.-A. Pan, T.-C. Fang, K.-Y. Chen, W.-Y. Hung, Y.-H. Hsu and P.-T. Chou, *J. Am. Chem. Soc.*, 2011, **133**, 17738–17745.

28   H. Shi, R. Liu, S. Zhu, Q. Gong, H. Shi, X. Zhu and H. Zhu, *J. Fluoresc.*, 2016, **26**, 2005–2013.

29   R. Ghosh and D. K. Palit, *Photochem. Photobiol. Sci.*, 2013, **12**, 987–95.

30   S. Xu, R. E. Evans, L. Tiandong, G. Zhang, J. N. Demas, C. O. Trindle and C. L. Fraser, *Inorg Chem*, 2013, **52**, 3597–3610.

31   Y. Kubota, Y. Sakuma, K. Funabiki and M. Matsui, *J. Phys. Chem. A*, 2014, **118**, 8717–8729.

32   X. Y. Shen, W. Z. Yuan, Y. Liu, Q. Zhao, P. Lu, Y. Ma, I. D. Williams, A. Qin, J. Z. Sun and B. Z. Tang, *J. Phys. Chem. C*, 2012, **116**, 10541–10547.

33   W. A. Morris, M. Kolpaczynska and C. L. Fraser, *J. Phys. Chem. C*, 2016, **120**, 22539–22548.

34   J. R. Lakowicz, *Principles of fluorescence spectroscopy*, Springer, New York, 3rd edn., 2006.

35   Y. Kubota, Y. Ozaki, K. Funabiki and M. Matsui, *J. Org. Chem.*, 2013, **78**, 7058–7067.

36   Y. Sato, M. Morimoto, H. Segawa and T. Shimidzu, *J. Phys. Chem.*, 1995, **99**, 35–39.

37   W. A. Morris, M. Sabat, T. Butler, C. A. DeRosa and C. L. Fraser, *J. Phys. Chem.*

C, 2016, **120**, 14289–14300.

38   H. Tong, D. Yongqiang, Y. Hong, M. Häussler, J. W. Y. Lam, H. H.-Y. Sung, X. Yu, J. Sun, I. D. Williams, H. S. Kwok and B. T. Zhong, *J. Phys. Chem. C*, 2007, **111**, 2287–2294.

39   S. Varghese and S. Das, *J. Phys. Chem. Lett*, 2011, **2**, 863–873.

40   W. A. Morris, T. Liu and C. L. Fraser, *J. Mater. Chem. C*, 2015, **3**, 352–363.

41   T. Butler, M. Alexander S., S. Michal and C. L. Fraser, *ACS Appl. Mater. Interfaces*, 2017, **Submitted**.

42   W. A. Morris, T. Butler, M. Kolpaczynska and C. L. Fraser, *Mater. Chem. Front.*, 2017, **1**, 158–166.

43   G. Zhang, J. Lu, M. Sabat and C. L. Fraser, *J. Am. Chem. Soc.*, 2010, **132**, 2160–2162.

44   JP 2005035902, 2005.

45   H. Zhu, X. Wang, Y. Li, Z. Wang, F. Yang and X. Yang, *Chem. Commun.*, 2009, **0**, 5118–5120.

46   Y. L. Chow, C. I. Johansson, Y.-H. Zhang, R. Gautron, L. Yang, A. Rassat and S.-Z. Yang, *J. Phys. Org. Chem.*, 1996, **9**, 7–16.

47   M. J. Frisch, G. W. Trucks, H. B. Schlegel, G. E. Scuseria, M. A. Robb, J. R. Cheeseman, G. Scalmani, V. Barone, B. Mennucci and G. A. Petersson, *Gaussian 09 Revis. A.1; Gaussian, Inc. Wallingford, CT*, 2009.

Chapter 6

Color Tuning of High Contrast Mechanochromic β-Diketonate Materials
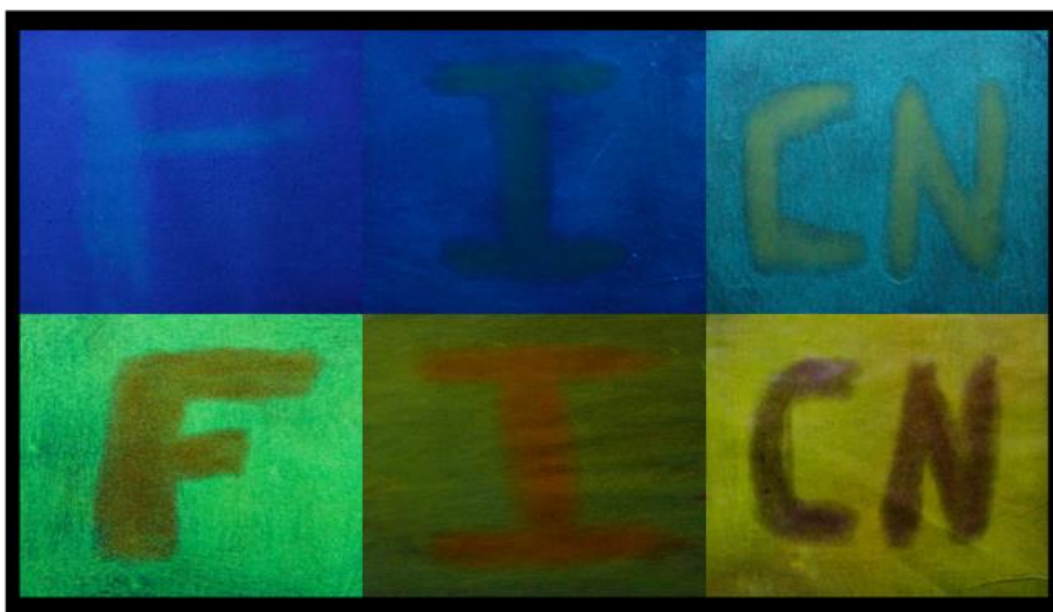
6.1 Introduction

Throughout this thesis, two main methods have been used to modulate the emission of β-diketones (bdk) in the solid state. In Chapter 3, boron coordination was used to redshift the emission of dinaphthoyl methane (dnm) derivatives.[1] While these dyes showed green-to-orange mechanochromic luminescence (ML), red emission of dyes in the smeared state was not observed. As discussed in the previous chapter, donor and acceptor effects can be utilized to tune emission in the crystalline and amorphous states of dimethylamino (DMA) substituted diketones. Though a wide range of colors was achieved after melt quenching, this method was insufficient to produce red emissive materials even after thermal and mechanical perturbation. Additionally, DMA dyes generally exhibited rather small mechanochromic shifts ($\Delta\lambda < 25$ nm) compared to other ML active bdk and BF_2bdk materials. Therefore, a different strategy is needed to produce ML active dyes that encompass the entire visible spectrum.

Recently, a correlation between loose molecular packing in emissive solids and mechanically produced optical responses has been observed.[2–4] It is believed that the weak interactions that hold crystalline phases of these materials can be easily overcome via mechanical stimulus, leading to mechanochromic luminescent (ML) emission.[5] Therefore, designing solid-state emissive materials that are sterically encumbered such as the twisted tetraphenyl ethylene derivatives developed by Tang *et al.,* has proven to be an effective strategy for inducing ML.[4] Similarly, Reddy *et al.* has shown that cyan-emissive crystals of BF_2 coordinated avobenzone form slip planes, which may assist in the formation of mechanically produced emissive species, with red-shifted emission. In Chapter 4, rapidly self-erasing ML was detected for the 3,4,5-trimethoxy substituted diketone (gbmOMe).[6] As evidenced by the single crystal of this dye, the loose packing pattern was the result of the para-methoxy group, which was forced out of plane through

unfavorable steric interactions with neighboring methoxy substituents. Therefore, incorporation of 3,4,5-trimethoxy phenyl rings may be an effective strategy for producing loosely packed solids with ML capabilities.

To achieve ML dyes with blue-to-red emission color tunability, a series of 3,4,5-trimethoxy substituted diketones were targeted (Figure 6.1). Fluoro, iodo, and cyano groups were substituted in the para position of the opposing phenyl ring and difluoroboron coordination was effected to further modulate emission via donor acceptor strategies. The emission of bdk and BF_2bdk compounds was measured in dichloromethane solution and DFT calculations were performed to generate HOMO LUMO frontier orbitals and assess electronic transitions. Due to the potential non-radiative decay pathways introduced through methoxy substitution, the aggregation induced emission properties were investigated by measuring absorption and emission in THF/H_2O solvent mixtures. The mechaochromic luminescence properties were probed using weigh paper films and the self-erasing properties of each dye were investigated on spin cast films on microscope coverglass. Finally, material structural characterization was performed using powder X-ray diffraction and differential scanning calorimetry (DSC) was used for measurement of thermal properties.
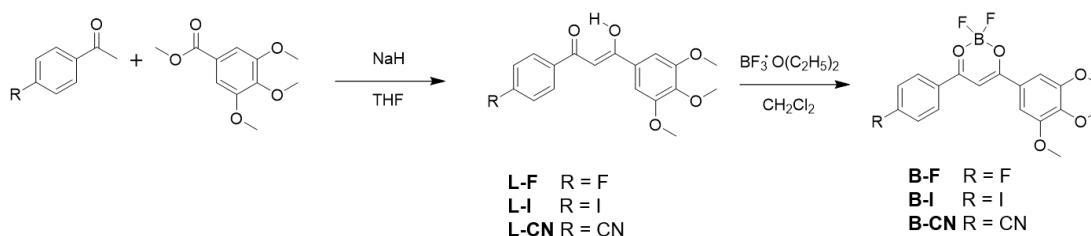

Figure 6.1. Synthesis of Trimethoxy Substituted Dyes.

6.2 Results and Discussion

6.2.1 Synthesis

In order to tune the stimuli responsive optical properties of bdk materials, fluoro (L-F), iodo (L-I), and cyano (L-CN) β-diketones were synthesized by Claisen condensation in the presence of NaH using 3,4,5-trimethoxy acetophenone, and the appropriately substituted ester. After purification, ligands were combined with boron trifluoride diethyl etherate to generate the corresponding boron complexes (B-F, B-I, B-CN) (Figure 3.1). All compounds were soluble in common organic solvents such as acetone, THF, ethyl acetate, dichloromethane, and chloroform. Peaks near 17.0 ppm were observed in the NMR spectra of each ligand which indicate dyes are in enol form when dissolved in $CDCl_3$. Upon BF_2 coordination, no enol peak was observed.

6.2.2 Optical Properties in Solution

The optical properties of all dyes were first measured in dichloromethane (1×10^{-5} M) in order to evaluate boronation and substituent effects. Comparison of absorbance spectra shows that diketones exhibit higher energy transitions compared to their respective BF_2 complexes (Figure 6.2). The absorption of both ligands and dyes shifted toward longer wavelengths when substituted with more strongly withdrawing groups (Table 1). For ligands, the fluoro-substituted dye, L-F (λ_{abs} = 360 nm), absorbed the bluest light compared to L-CN (λ_{abs} = 368 nm), which exhibited the lowest energy transition. Similarly, examination of UV-vis spectra of difluoroboron complexes revealed that the absorption of B-F (λ_{abs} = 403 nm) was blue-shifted relative to B-I and B-CN, which both showed degenerate peak wavelengths a λ_{abs} = 412 nm. The molar absorptivities of ligands and dyes

showed very little sensitivity toward substituent effects, however BF_2 coordination resulted in a slight increase, consistent with previous studies.[1]
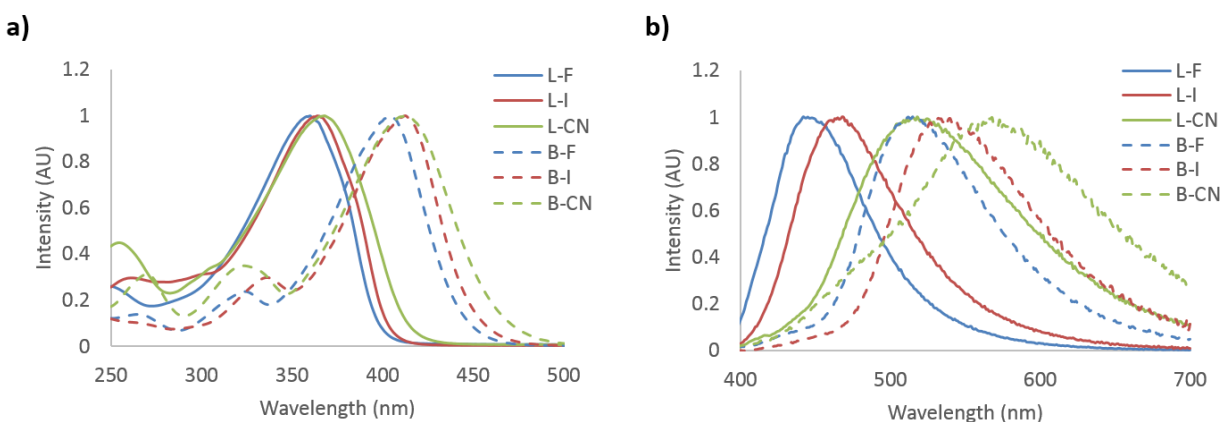
a)

b)

Figure 6.2. Optical Properties of Trimethoxy Substituted Dyes in Dichloromethane. Absorption (a) and emission (b) spectra of trimethoxy substituted ligands and boron complexes (1×10^{-5} M). (λ_{ex} = 369 nm)

As evidenced by their low quantum yields ($\phi < 8\%$), all trimethoxy-substituted compounds were nearly non-emissive in solution. Diketone emission was not detectable by eye, but faint emissions were observed for B-F ($\phi < 8\%$) and B-I ($\phi < 6\%$). Like with the absorption spectra, boronation also resulted in redshifted emission and greater emission sensitivity to substituent effects compared to the analogous trends in absorption. For both ligands and boron complexes, the fluoro-substituted derivatives L-F (λ_{em} = 442 nm) and B-F (λ_{em} = 515 nm) exhibited higher energy transitions relative to their iodo and cyano counterparts. This is attributed to differences in electron withdrawing strength of the para substituents. Compared to boron complexes, ligands were more sensitive to electron withdrawing effects, as substitution with strongly withdrawing cyano groups resulted in a redshift in peak emission wavelength of 76 nm (L-CN: λ_{em} = 518 nm) for ligands and 53 nm for BF_2 complexes (B-CN: λ_{em} = 568 nm). Examination of the fluorescence lifetimes for ligands and complexes indicates that boronation and donor/acceptor substitution have little effect as relatively short lifetimes ($\tau < 1$ ns) were observed for all compounds.

Table 6.1. Optical Properties in Dichloromethane Solution[a]

Compound	λ_{abs}[b] (nm)	ε ($M^{-1}cm^{-1}$)	λ_{em}[c] (nm)	Φ[d] (%)	τ[e] (ns)
L-F	360	25200	442	<1	0.24
L-I	364	29400	468	2	0.23
L-CN	368	25800	518	<1	0.25
B-F	403	37200	515	8	0.85
B-I	412	39200	537	6	0.22
B-CN	412	29000	568	<1	0.31

[a] Excited at 369 nm, room temperature, air
[b] Peak absorption wavelength
[c] Peak emission wavelength
[d] Quantum yield
[e] Pre-exponential weighted lifetime

6.2.3 Computational Investigation

While uncoordinated ligands are often poorly emissive in solution,[1,7] large quantum yields are typically observed in BF_2bdk dyes.[8] To investigate this discrepancy and further study the optical properties of trimethoxy-substituted compounds, density functional theory (DFT) calculations were performed with a Tomasi polarized continuum for dichloromethane solvent.[9] The HOMO and LUMO molecular orbitals (MOs) and simulated UV-vis spectra were calculated using the B3LYP/6-31G(d) basis set (Figure 6.3). The optimized ground state geometries indicate that for ligands, the trimethoxy-substituted ring was twisted with respect to the rest of the molecule (Figure S6.1; Appendix E). Furthermore, coordination of BF_2 resulted in the formation of more planar structures. For all dyes, calculations show that the para-substituted methoxy group was out of plane relative to the other methoxy substituents. In previous reports, this has been attributed to steric crowding from neighboring groups.[6] It is possible that non-radiative decay pathways are

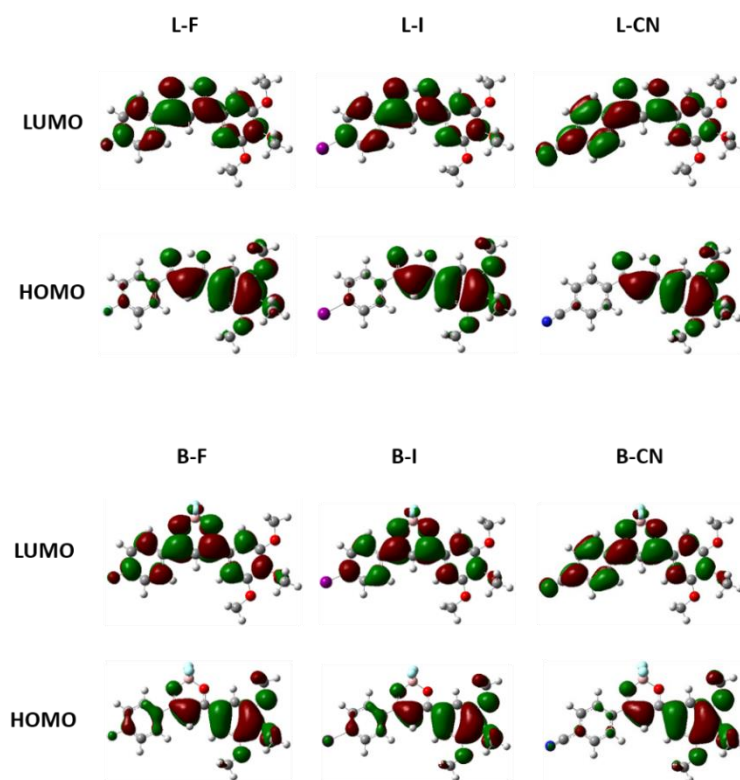increased due to disruptions in planarity, and may contribute to the low quantum yields exhibited by both sets of dyes.[10]

Figure 6.3. Molecular Orbitals of Trimethoxy-Substituted Dyes. Highest occupied molecular orbital (HOMO) and lowest unoccupied molecular orbital (LUMO) diagrams of trimethoxy ligands (top) and boron complexes (bottom).

Examination of the MOs of each dye indicates that all compounds undergo intramolecular charge transfer (ICT) transitions. For ligands, the mono-substituted arene ring in the HOMO is electron deficient, and electron density is localized on the trimethoxy-substituted ring and the diketone. Similar behavior was seen in the HOMOs for boron dyes, however, a small amount of electron density was observed on the acceptor substituted rings of B-F and B-I. Electron density was delocalized throughout the LUMOs for each dye, which taken together with HOMO results, points to ICT behavior. Since ICT transitions are typically associated with lower quantum yields, this could also `explain the diminutive quantum yields in trimethoxy-substituted dyes.[10]

6.2.4 Aggregation Induced Emission

While both ligands and dyes were nearly non-emissive in DCM solution, bright emission was observed for dyes in the solid state. The emission of B-F solid was particularly bright compared to all other compounds. Previously it was found that difluoroboron dinaphthoylmethane (dnm) derivatives showed evidence of aggregation caused quenching (ACQ) in the solid state, whereas their ligands were AIE active.[1] The difference in behavior was attributed to the planarization of dyes due to boron coordination. On the other hand, AIE was observed for α-substituted BF_2bdks that exhibited non-planar conformations as a result of steric interactions.[11] The computational results for both ligands and dyes indicate that unfavorable steric interactions force the para-substituted methoxy group out of plane. Therefore, the elimination of non-radiative decay pathways related to methoxy substitution, through aggregation, could result in AIE for both ligands and dyes.[12] Because it shows the most vibrant emission in the solid state, the AIE properties of B-F were studied by measuring the emission in a series of THF/H_2O solutions with increasing concentrations of H_2O, a non-solvent. These results were compared to those corresponding to L-F, to evaluate the effect of boron coordination (Figure 6.4).
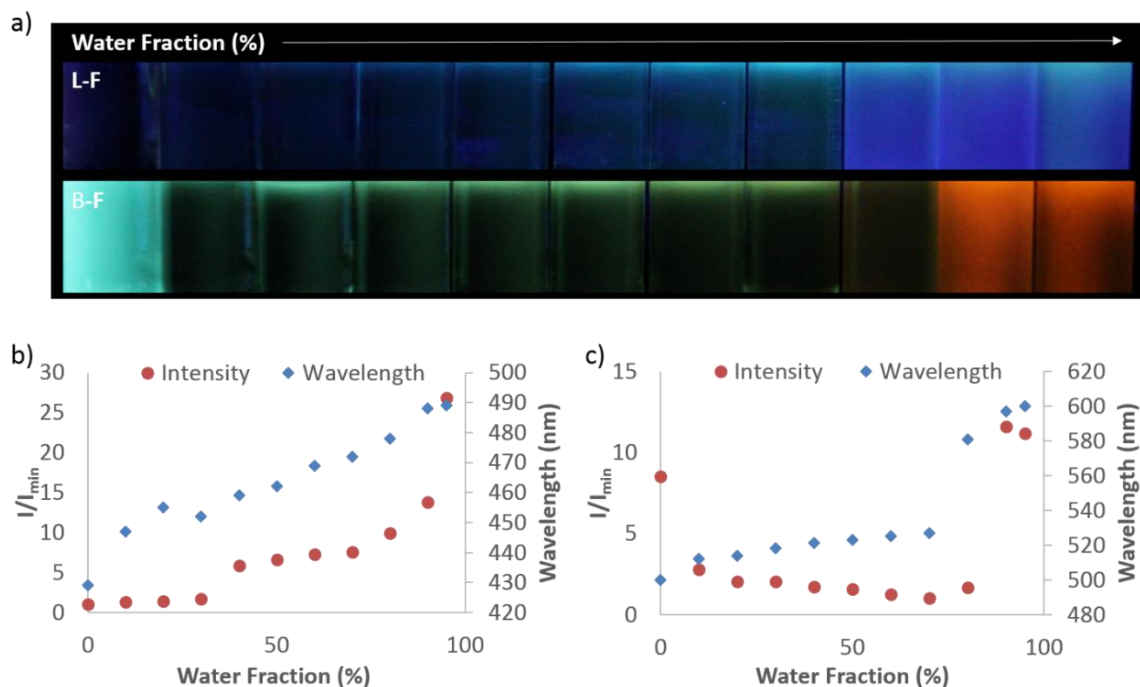
Figure 6.4. Aggregation Induced Emission of Trimethoxy Substituted Dyes. Images under UV light of L-F and B-F dissolved THF/H$_2$O solutions (a) (λ_{ex} = 369 nm). Plots of intensity and wavelength versus water fraction of L-F (b) and B-F (c) THF/H$_2$O mixtures.

When dissolved in pure THF, no emission was observed for L-F, however the corresponding boron complex glowed bright green. As stronger dye-dye interactions were induced through an increase in relative H$_2$O concentration, gradual trends toward longer emission wavelengths and greater intensities were observed for L-F (Figure S6.2; Appendix E). The maximally redshifted wavelength (489 nm) and highest intensity were detected for the 95% H$_2$O fraction, which constituted a 27 fold increase in intensity compared to the emission of L-F in THF solution. While B-F dyes were highly emissive initially, the addition of H$_2$O to THF solutions resulted in a sharp intensity decrease, even at 10% H$_2$O. Solutions of B-F between 10-70% H$_2$O showed slightly decreased intensity, and longer wavelengths compared to emission in THF. The gradual trend toward longer wavelengths for both L-F and B-F has been previously been attributed to greater solvent polarity as a result of increased H$_2$O concentration.[11] Once H$_2$O fractions were

increased beyond 70%, more dramatic intensity increases and wavelength shifts were observed. When dissolved in 95% H_2O, B-F glowed orange (600 nm) and an 11 fold intensity enhancement compared to the dimmest solution recorded.

The increase in emission intensity observed for L-F and B-F THF/H_2O solutions at higher H_2O fractions is indicative of AIE. However, more evidence of aggregation can be found in the excitation spectra of L-F and B-F solutions (Figure S6.3; Appendix E). Two distinct excitation peaks were detected for both compounds at lower H_2O fractions (0-70%). According to previous reports, the red-shifted excitation band can be ascribed to an emissive ICT state, whereas the higher energy peak corresponds to π-π* transitions.[11] At higher H_2O concentrations (>70%), a different excitation profile was observed for both compounds, which indicated that different emissive species was formed. Furthermore, the excitation spectra of these solutions also showed diminished intensity of the ICT transition. This has previously been attributed to the formation of aggregate species that hinder the formation of the ICT state.[13]

The emission of L-F and B-F dissolved in THF/H_2O solution indicate that both dyes are AIE active. Because previously reported bdk ligands showed ACQ upon boron coordination,[1] the AIE detected for L-F and B-F solutions may be due to the restriction of molecular motions which result of methoxy substitution. Despite the observation of AIE emission for both L-F and B-F dyes, several notable differences were observed. For example, L-F was non-emissive in pure THF whereas bright green emission was detected for B-F solutions absent H_2O. Additionally, the emission of B-F diminished considerably after H_2O was added, however emission could still be detected by eye for all B-F solutions. Comparatively, no emission was observable for L-F solutions until the H_2O fraction was increased above 30%. This could explain the larger emission enhancement displayed by the fluoro-substituted ligand, as the emission of L-F was quite dim prior

to aggregation. The aggregate emission of B-F was significantly red-shifted compared to L-F aggregates, therefore BF$_2$ coordination could be an effective strategy for tuning AIE properties of future bdk materials. Furthermore, the observation of AIE in both L-F and B-F indicates that incorporation of sterically crowded methoxy substituents into the structure of bdk materials could be a strategy for enhancing solid state emission.

6.2.5 Mechanochromic Luminescence

A correlation between loosely packed molecular structures and mechanochromic luminescence activity has been previously described.[4,14,15] According to previously reported crystal structures and the optimized geometry of trimethoxy substituted dyes, the out of plane para-substituted methoxy group could prevent close molecular associations and lead to high contrast ML.[6] The ML properties of ligands and dyes were investigated on weigh paper substrates and as spin cast films on microscope cover glass. Optical properties were measured for thin films in the as spun (AS), thermally annealed (TA) and smeared (SM) states. Films in the AS state were prepared by adding 20 drops of a dye stock solution in dichloromethane (1×10^{-3} M) to glass slides rotating at 3000 rpm. The annealing procedure of L-I and L-CN involved heating unperturbed AS films at 110 ºC for 10 min. However, simple heating of L-F films in the AS state was able to produce a color change. Therefore, L-F in the TA state were produced by heating corresponding AS films at 75 ºC for 10 min, followed by gentle smearing with a Kimwipe and reheating at 75ºC for another 10 min. For boronated derivatives, specific annealing temperatures were required to illicit a color change, whereas the emission shift of uncoordinated dyes was insensitive to temperature. The optimum annealing temperatures of boronated dyes were determined by incrementally heating thin films from 85-170ºC and measuring emission spectra (Figure S6.4; Appendix E). Films of these dyes in the TA state were produced *via* annealing for 10 min at the

temperature that produced maximally blue-shifted emission. According to these measurements, TA films of B-F, B-I, and B-CN were fabricated by heating at 160 ºC, 170 ºC, and 150 ºC, respectively. All TA films were smeared with a cotton swab to generate SM emission. In order to investigate film thickness and substrate effects, the ML properties were also measured for weigh paper films in TA and SM states. Films in the TA state were produced by smearing a small amount of dye (~ 2 mg) across a 5 x 5 cm sheet of weigh paper and heating at the same annealing temperatures used for glass films. The smearing procedure was the same regardless of substrate.
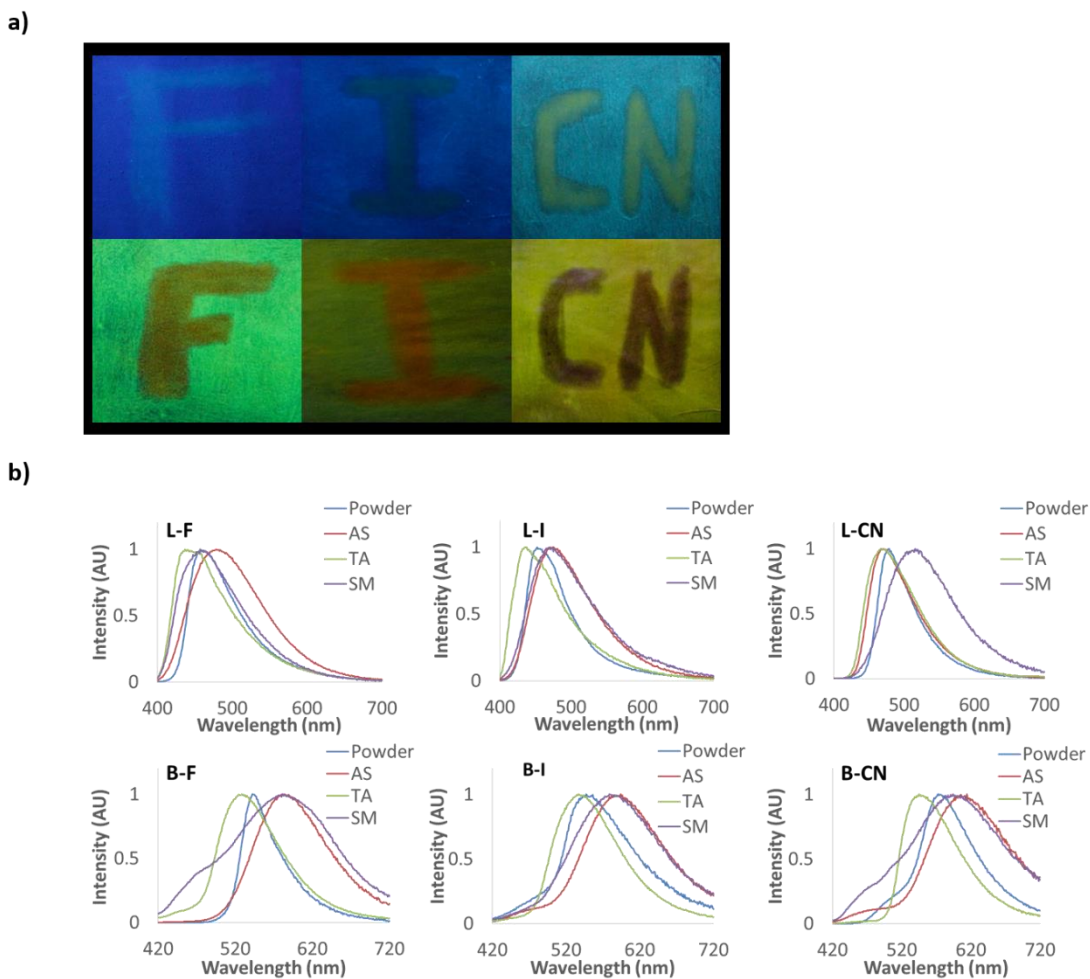
Figure 6.5. Mechanochromic Luminescence Characterization of Trimethoxy Substituted Dyes. Images under UV light of smeared weigh paper thin films if ligands (top) and boron complexes (bottom) (a). Emission spectra of dyes as bulk powders and glass thin films in as spun (AS), thermally annealed (TA), and smeared (SM) states.

Films on weigh paper were used for initial characterization of ML. Visible ML could be observed in all trimethoxy derivatives, regardless of boron coordination and electron withdrawing substituent (Figures 6.5, S6.5; Appendix E). For annealed L-F (λ_{em} = 437 nm) and L-I (λ_{em} = 467 nm) weigh paper films, dim blue emission was observed. When L-F films were smeared, transient (~ 30 s) green emission was observed before rapid self-recovery of annealed emission. Due to the changing emission of smeared L-F weigh paper films, reliable emission spectra were unobtainable in the SM state. Emission spectra of L-I (λ_{em} = 482 nm) weigh paper films showed only a slight change in peak emission upon smearing, however both emission wavelength and intensity responses were visible to the eye. Substitution with a cyano group resulted in more intense blue emission (λ_{em} = 470 nm) compared to weigh paper films of other ligands. Mechanical perturbation of L-CN films generated long lasting yellow-green emission (λ_{em} = 500 nm).

Examination of the ML trends for the boron complexes on weigh paper films indicates that a wider range of emission wavelengths can be accessed by these dyes. While ligands exhibited mostly blue emission when annealed, UV irradiation of BF_2 complexes produced green (B-F: 517 nm), yellow-green (B-I: 539 nm), and orange (B-CN: 558 nm) emission in the TA state. There was also a significant variation of emission wavelength within the SM state of boronated dyes. Smearing B-F films resulted in orange emission (λ_{em} = 578 nm), whereas B-CN (λ_{em} = 580) films glowed red-orange after mechanical stimulation. Furthermore, additional heating resulted in the erasure of the smeared marks, and regeneration of the annealed emissive state for all dyes, which demonstrates reversible ML for these materials. Comparison of the emission wavelengths for TA and SM films indicates that emission is dependent on the electron withdrawing ability of the para-substituent. For example, B-CN emits redder emission in both TA and SM states. These wavelength trends are consistent with those discussed in the previous chapter, and are likely

attributable to stabilization from neighboring dyes through dipole-dipole interactions in combination with aggregation effects.

Table 6.2. Solid-State Optical Properties.[a]

Compound	Powder		As Spun			Thermally Annealed				Smeared			
	λ_{em}[b] [nm]	FWHM[c] [nm]	λ_{em} [nm]	FWHM [nm]	τ_{pw0} [ns]	λ_{em} [nm]	τ_{pw0}[d] [ns]	FWHM [nm]	Φ[e] [%]	λ_{em} [nm]	τ_{pw0} [ns]	FWHM [nm]	Φ [%]
L-F	457	73	479	113	3.4	437	0.30	85	6.0	458	N/A	98	12[f]
L-I	452	65	474	97	0.74	437	0.13	82	7.0	470	N/A	104	17
L-CN	479	57	471	75	2.18	469	1.49	85	10	516	3.04	112	29
B-F	543	56	584	114	N/A	529	5.14	93	65	582	6.06	164	24
B-I	547	107	594	127	1.08	537	0.90	104	3.0	579	1.13	142	5.0
B-CN	573	90	614	136	1.18	545	2.02	94	2.0	594	1.17	166	2.0

[a] Excited at 369 nm, room temperature, air
[b] Emission maximum
[c] Full width at half maximum
[d] Pre-exponential weighted lifetime
[e] Quantum yield
[f] Quantum yield was estimated using as spun state due to rapid recovery

Previously studied bdk materials have exhibited substrate and processing effects. For example, the rapid self-recovery of the tetramethoxy substituted diketone, gbmOMe, was slowed by producing spin cast films with smaller initial thicknesses.[6] Similarly, the processing of diketopyrrolopyrrole materials from alcohol and water led to emission changes on silica gel substrates.[16] Based on these findings, the ML properties of trimethoxy-substituted bdk dyes were further investigated using spin-cast glass films. The emission of spin-cast films was compared to bulk powders and weigh paper films in order to probe potential substrate and processing effects (Table 6.2). In the AS state, glass films of L-F and L-I exhibited broad peaks that were significantly red-shifted in comparison to their emission as bulk powders. However, bulk L-CN solid exhibited lower energy emission compared to corresponding AS films. For all BF_2 complexes, broad emission profiles were observed in AS films which were red-shifted compared to their

corresponding bulk powders. This suggests that the emissive species that comprise L-CN films in the AS state are similar to those in the bulk solid, whereas AS films for other dyes are populated with different emissive species compared to their corresponding bulk powders.

Heating AS films induced a hypsochromic wavelength shift and more narrow emission profiles for all TA films. In fact, higher energy emission was observed in comparison to bulk powders and weigh paper films in the TA state. While this effect was muted for L-CN films, which showed similar emission for all non-smeared states regardless of substrate, large deviations were observed for all other samples. This trend can be illustrated by B-CN, which exhibits orange emission as a bulk powder ($\lambda_{em} = 574$ nm) and glows red ($\lambda_{em} = 616$ nm) as a glass film in the AS state. After annealing, TA glass films exhibit yellow-orange emission ($\lambda_{em} = 545$ nm) which was more blue-shifted compared to annealed B-CN ($\lambda_{em} = 558$ nm) weigh paper films. Because bulk powders were red-shifted relative to both glass and weigh paper films, it is possible that stronger dye-dye interactions were present compared to annealed films. Furthermore, it is likely that annealing thicker weigh paper films results in an incomplete phase transformation as thinner TA glass films exhibit more blue-shifted emission. With the exception of B-F, which was highly emissive ($\phi = 65\%$) in the solid state, very little deviation in the quantum yield of annealed ligand and dye films was observed ($\phi < 10\%$).

As with weigh paper films, mechanical perturbation of TA glass films produced red-shifted emission. Due to slower room temperature recovery on glass, green emission was observed after smearing for L-F ($\lambda_{em} = 458$ nm). Based on emission of L-F films in the AS state ($\lambda_{em} = 478$ nm) and its rapid self-recovery, the peak wavelength of smeared films is likely underestimated. Compared to their corresponding weigh paper films, similar emission was observed when glass films were smeared. However, glass films of both cyano substituted derivatives (L-CN: $\lambda_{em} = 516$

nm. B-CN: 594 nm) showed longer wavelengths in the smeared state compared to their films on weigh paper (L-CN: λ_{em} = 500 nm. B-CN: 580 nm). This could indicate that weigh paper films of L-CN and B-CN are harder to smear, however it could also be the result of a thickness or substrate effect on the recovery rate of these dyes.

All trimethoxy-substituted derivatives showed emission responses as a result of mechanical perturbation regardless of substrate. Depending on the electron withdrawing effects and boron coordination, ML active materials with emission ranging from blue to red can be achieved. These trends are correlated with the electron withdrawing strength of the para-substituent, as both cyano substituted ligands and dyes in TA and SM states exhibited red-shifted emission compared to other dyes in this series. Furthermore, the longer wavelengths emitted by boron complexes indicates that BF_2 coordination is an effective strategy for red-shifting the emission of stimuli responsive bdk dyes. While para-substitution of donor and acceptor groups has previously yielded predictable emission colors for bdk ligands, their ML responses were much smaller in comparison to these trimethoxy substituted derivatives. Therefore, substitution of bdk dyes with sterically crowded methoxy substituents may introduce a more loosely packed structure and represents an effective strategy for enhancing ML shifts in bdk ligands and BF_2 complexes.

6.2.6 Mechanochromic Luminescence Recovery

Spontaneous recovery of thermally annealed emission has been well studied in other bdk systems. In general, it has been shown that bdk ligands exhibit fast recovery times compared to boron complexes. Additionally, the self-erasing of a trimethoxy substituted derivative (gbmOMe) was even more rapid compared to other bdk ligands. Like the AIE and ML properties investigated here, the rapid recovery of gbmOMe was attributed to steric effects derived from the out-of-plane methoxy substituent. Furthermore, qualitative analysis of the room temperature recovery of L-F

163

and L-CN indicates that the fluoro-substituted derivative self-erases over similar time scales to this previously reported dye, however it takes much longer for the smeared emission of L-CN to fade. In order to investigate recovery trends, spin cast films of all derivatives were prepared in the same manner as previously described, however emission spectra were gathered at different time intervals over the course of two days. The effect of donor/acceptor substitution and BF_2 coordination on the recovery of these dyes was investigated and the results were compared to other self-recovering bdk dyes (Figure 6.6).

As expected based on ML studies, L-F films showed rapid recovery such that the emission spectrum taken 1 min after smearing was nearly identical to its TA profile. According to the full width at half-maximum (FWHM) the emission profile obtained after 30 min (77 nm) was slightly narrower even compared to TA emission (85 nm) indicating complete recovery. While the recovery time of a dye is highly dependent on substrate and processing effects, these data indicate that L-F is among the fastest recovering bdk dyes. The iodo and cyano dyes show much different room temperature recovery behavior. No recovery was observed for L-I which showed very little change in emission two days after smearing. Examination of the spectra for smeared L-CN indicates that partial recovery occurs. After 10 min the peak emission had shifted from 516 nm in the SM state to 500 nm, however no further changes in emission were observed in subsequent emission scans. One potential explanation for this behavior is that L-CN forms an emissive species that reaches a local minimum as it self recovers to the annealed state. Since the emission of partially recovered L-CN films is similar to the emission observed for weigh paper films in the SM state, it may be produced by the same emissive species. Since all ligands possess the same the trimethoxy motif, the difference in self-recovery is likely the result of increased intramolecular interactions

induced by different substituents. For example, the introduction of an iodo group could prompt formation of C-I$\cdots$I-C interactions that potentially slow recovery.[17]
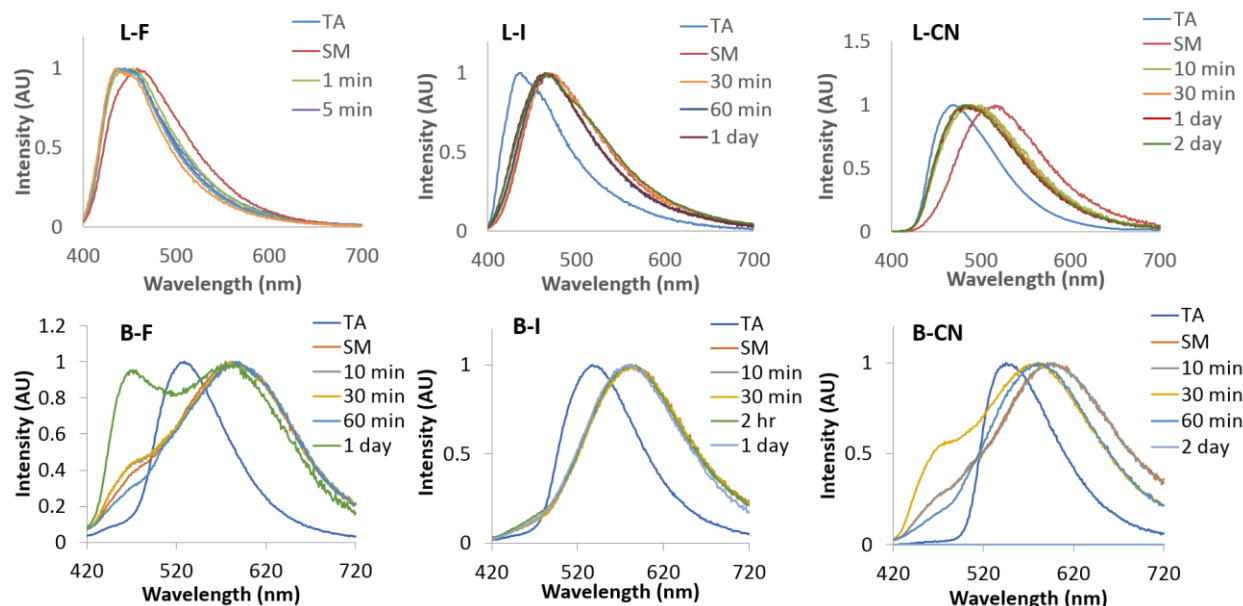
Figure 6.6. ML Recovery of Trimethoxy Substituted Dyes. Emission spectra of smeared glass thin films in the thermally annealed (TA) and smeared (SM) states and at different time intervals after smearing.

For boron dyes, recovery complete recovery of annealed emission was not observed even two days after smearing. In the case of B-I films, almost no emission change was observed over this time frame. However, the emergence of a blue-shifted shoulder occurred for both B-F and B-CN that was higher in energy then the respective emission of the TA films. This shoulder appears to overlap with the emission profile of the corresponding ligand, therefore removal of the BF_2 moiety could be a byproduct of the smearing or annealing procedures for glass films. It should be noted that similar behavior was not observed for weigh paper films. The peak emission of smeared B-CN (λ_{em} = 595 nm) showed partial recovery of annealed emission (λ_{em} = 580 nm) 30 min after smearing, but no further shifts in peak wavelength were detected during the duration of the experiment. Like its ligand counterpart, partial recovery was observed for B-CN weigh paper films. In previous reports, the difference in recovery times between bdk ligands and boron

complexes was attributed to the introduction of C-H⋯F interactions as a result of boron coordination.[1] While L-I and L-CN exhibited partial recovery at best, BF$_2$ coordination had little effect on their recovery dynamics. However, rapid recovery was observed for L-F but no self-recovery was exhibited by B-F samples. Therefore, it is possible that increased C-H⋯F interactions prevent recovery of B-F films.

6.2.7 Thermal Characterization

Previously, bdk dyes have shown emission changes in response to thermal stimuli. In some cases, melted bdk ligands have formed super cooled liquid phases that were stable for over an hour before crystallization occurred.[6] Furthermore, thermal switching between different emissive states was achieved for a furyl substituted BF$_2$bdk dye.[18] Qualitative screening of the thermal responses of trimethoxy-substituted dyes revealed that only L-F showed emission changes in response to thermal treatment, whereas no change in emission was detected for all other derivatives after melting glass films and rapid cooling in air. After L-F was melt quenched, a transparent green emissive phase was formed that persisted for an hour before an opaque phase with blue emission was observed. Qualitative screening of the responsive properties for melted L-F thin films revealed that the appearance of the blue phase could be expedited through mechanical perturbation.

Table 6.3. Differential Scanning Calorimetry Data for Trimethoxy Dyes.

| | Cycle 1 | | Cycle 2 | |
	T_m [a]	T_c [b]	T_m [a]	T_c [b]
L-F	120.5 (106.2)	N/A	107.5 (102.2)	85.0
L-I	142.6	99.0	131.6 (140.0)	121.7
L-CN	215.8	179.8	216.3	182.4
B-F	197.9	169.9	197.8 (193.6)	166.4
B-I	243.3	195.2	242.0	197.5
B-CN	233.4	218.5	231.7	214.8

[a] Melting point given in ºC as the peak of the major endothermic transition. Secondary transitions are given in parentheses.
[b] Crystallization point given in ºC as the peak of the major exothermic transition.

In order to further investigate the thermal properties of L-F and other trimethoxy-substituted dyes, successive differential scanning calorimeter (DSC) scans were performed (Figure 6.7, Table 6.3). The heating rate of both cycles were the same (5ºC/min), however a faster cooling rate (10ºC/min) was used for the first cycle compared to the second cycle (1ºC/min). During the first heating cycle of L-F, a small endothermic transition was observed (T_m = 106.2ºC) before melting at 120.5ºC. Upon rapid cooling, a broad exothermic peak was noted, however it was only slightly above the baseline so a definitive crystallization temperature could not be assigned. Examination of the subsequent heating cycle shows a broad exothermic transition (~60ºC) which could be ascribed to crystallization. As in the first cycle, an endothermic transition was observed (T_m = 107.5ºC), however the additional peak near 120ºC was absent. One potential explanation for the melting differences in thermograms of each cycle could be that multiple phases are present after recrystallization of L-F. When L-F was cooled slowly, a crystallization peak (T_c = 85.0ºC)

was observed which indicates that the rate of cooling has a large influence on the crystallization dynamics of L-F powders. In conjunction with qualitative observations and previously studies into the thermal properties of bdk dyes,[6] DSC data for L-F suggest that a super cooled liquid phase is formed when cooled rapidly.
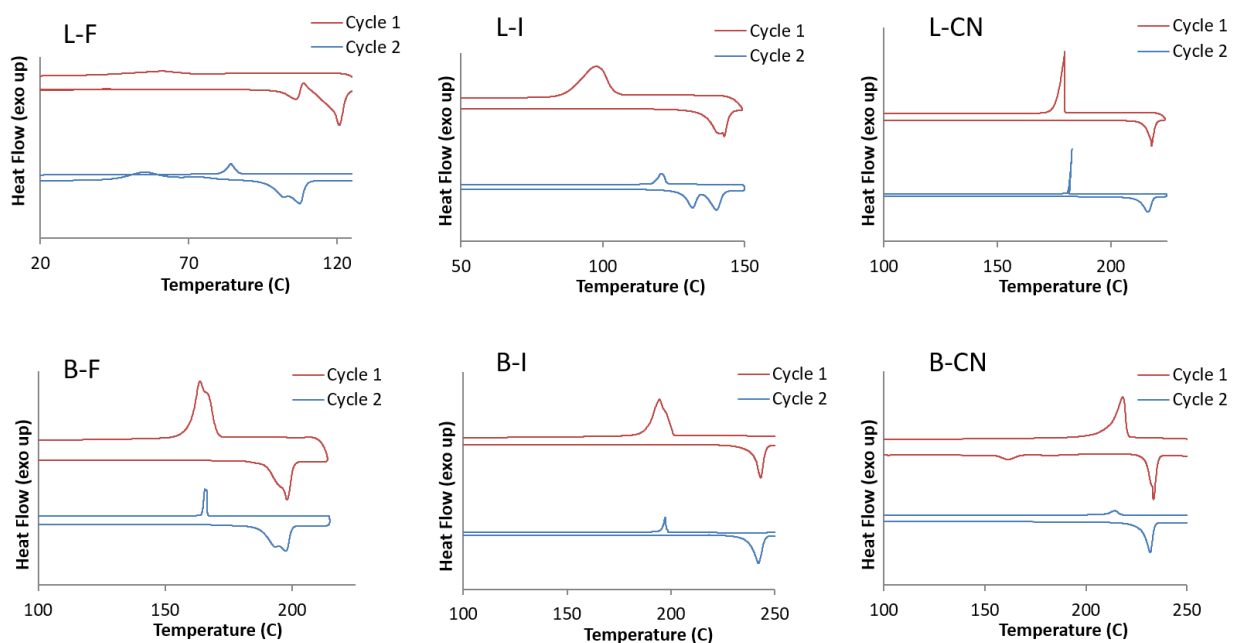
Figure 6.7. Thermal Characterization of Trimethoxy-Substituted Dyes. Differential scanning calorimetry thermograms of dyes (Cycle 1: ramp rate = 10°C/min, cooling rate = 10°C/min; Cycle 2: ramp rate = 10°C/min, cooling rate = 1°C/min).

Exothermic peaks were observed in the cooling cycles for all other dyes regardless of cooling rate. Despite structural similarities, thermograms of the first heat cycle for other ligands show wide ranging melting points. While the L-F (T_m = 120.5 °C) and L-I (T_m= 142.6 °C) exhibit similar melting temperatures, the temperature required to melt the cyano (T_m= 215.8 °C) substituted ligand was substantially higher. Little difference was observed between the first and second cycles for L-CN, however significant deviations were observed for L-I. For example, a single endothermic peak was present during the first cycle, but the second cycle of L-I displayed two similar endothermic transitions. Coupled with the broad crystallization peak (T_c = 99.0°C), this

168

could indicate that rapid cooling of L-I results in the formation of multiple phases. Since thermograms of boron complexes show few differences between cycles, the rate of cooling seems to have little effect on their crystallization. Their bulk powders may be comprised of a relatively uniform phase. Coordination of BF_2 resulted in higher melting points compared to corresponding ligands, however not all boron complexes exhibited higher melting temperatures compared to diketones as L-CN melted at a higher temperature than B-F.

6.2.8 Structural Properties

The different emissive phases of trimethoxy-substituted dyes were investigated by measuring the powder XRD patterns of glass films in the AS, TA, and SM states. For L-F, films in the SM state were unobtainable due to rapid self-recovery, however an XRD pattern was measured for gently smeared AS films in order to investigate shear induced crystallization. According to the XRD pattern for L-F in the AS state, an amorphous phase is formed. Application of mechanical stimulus induces crystallization to a blue-emissive state according to the pattern for sheared films. The XRD pattern after thermal annealing of L-F films shows very little difference from that of sheared films, which indicates that the same crystalline phase is present in both samples.
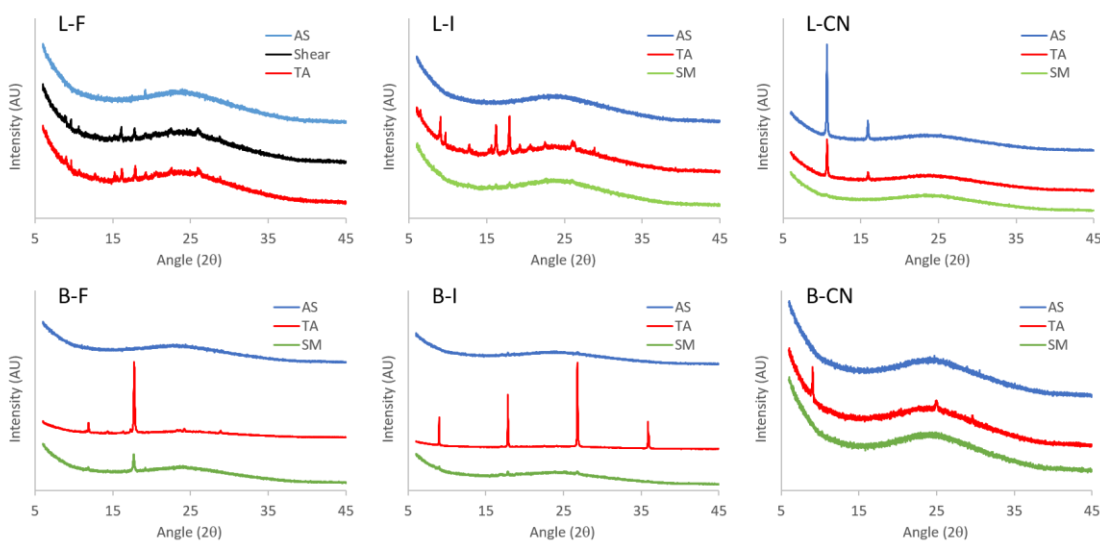
Figure 6.8. Structural Characterization of Trimethoxy-Substituted Dyes. Powder X-ray diffraction (XRD) patterns of films in the as spun (AS), thermally annealed (TA) and smeared (SM) states. For L-F, patterns were gathered for mechanically sheared AS films.

With the exception of L-CN, no peaks were observed in the powder patterns for AS films. After annealing, peaks were observed for all films indicated that crystallization occurs during the annealing process. For L-CN, the same set of peaks were observed in the AS and TA states indicating that crystalline species are present in both films, before and after heating. This is consistent with trends in solid-state optical properties as very similar peak wavelengths were observed in their corresponding emission spectra. Examination of XRD patterns in the SM state shows that mechanical perturbation results in formation of an amorphous phase. While peaks are also observed for B-F in the SM state, the change in emission and the diminished peak intensity relative to TA films suggests that some crystalline species are still present despite smearing.

6.2.9 Conclusion

With the exception of B-CN, which was non-emissive, boron dyes were faintly emissive in dichloromethane solution whereas diketone dyes were non-emissive. These solution optical properties were attributed to increased non-radiative decay pathways which likely result from the trimethoxy substituted ring and ICT transitions confirmed by DFT calculations. The emissions of

L-F and B-F in THF/H$_2$O solutions both show increases in emission intensity upon aggregation which is indicative of AIE behavior. Furthermore, this suggests that the introduction of non-radiative decay through trimethoxy substitution is an effective strategy for developing AIE active bdk materials.

All dyes show solid-state emission under UV irradiation and mechanically induced color changes. Powder XRD patterns confirm that the ML response of these materials was the result of crystalline-to-amorphous phase transitions. With the exception of L-I, larger ML shifts were observed compared to DMA-substituted ligands. Additionally, red emission was observed when B-CN films were smeared, which demonstrates that this set of bdk materials encompasses wavelengths from the entire visible spectrum. The room temperature recovery of all dyes was investigated using glass substrates. Like the previously investigated trimethoxy derivative gbmOMe, rapid self-erasing was observed when L-F films were smeared, however full recovery was not observed for all other trimethoxy-substituted derivatives. Partial recovery was observed for L-CN which indicated that a local energy minimum was formed during room temperature recovery. While thermal characterization of the dyes revealed that most dyes crystallized after melting regardless of cooling rate, the thermograms of L-F indicate that a supercooled liquid phase is formed when L-F melts are cooled rapidly. These results demonstrate that incorporation of 3,4,5-trimethoxy substituted phenyl rings into the design of bdk materials is an effective strategy for producing ML active materials. Furthermore, color tuning of this system can be achieved through a combination of boron coordination and donor/acceptor substitution.

6.3 Experimental Section

6.3.1 Materials

THF was dried over molecular sieves activated at 300 ºC as previously described.[19] Reactions were monitored using silica TLC plates. Compounds purchased from Sigma-Aldrich and TCI were reagent grade and used without further purification. The trimethoxy-substituted β-diketones were synthesized *via* Clasien condensation using a previously described method.[20] Characterization data for all previously unreported compounds are provided in Appendix E.

6.3.2. Methods

^{1}H NMR (600 MHz) spectra were recorded using a Varian VRMS/600 spectrometer in deuterated DMSO and CDCL$_3$. Residual peaks of protio-DMSO at 2.50 ppm and protio-CDCl$_3$ at 7.27 ppm were used to reference spectra, and coupling constants were reported in Hz. Mass spectra were recorded with a Micromass Q- TOF Ultima spectrometer, using electrospray ionization (ESI) MS/MS techniques. A Hewlett-Packard 8452A diode-array UV-vis spectrophotometer was used to collect absorption spectra. Steady-state emission spectra were measured using a Horiba Fluorolog-3 Model FL3-22 spectrofluorometer (double-grating excitation and double-grating emission monochromator). Fluorescence quantum yields, φ_F, in CH$_2$Cl$_2$ were calculated versus a standard of dilute quinine sulfate solution in 0.1M H$_2$SO$_4$ using a previously described method[21] and the following values: φ_F quinine sulfate in 0.1M H$_2$SO$_4$ = 0.54,[22] n_D^{23} 0.1M H$_2$SO$_4$ = 1.33, n_D^{23} CH$_2$Cl$_2$ = 1.424. Optically dilute CH$_2$Cl$_2$ solutions of all samples were prepared in 1 cm path length quartz cuvettes with absorbances <0.1 (a.u.). A F-3029 Quanta-Φ Integrating Sphere from Horiba Scientific was used to measure solid state quantum yields and data were analyzed using FluorEssence software. Time-correlated single-photon counting (TCSPC) fluorescence lifetime measurements were performed with a NanoLED-370 (λ_{ex} = 369 nm) excitation source and a

DataStation Hub as the SPC controller. Lifetime analysis was done with DataStation v2.4 software from Horiba Jobin Yvon. A Laurel Technologies WS-65OS spin-coater was used to fabricate glass thin films. Powder x-ray diffraction (XRD) patterns were obtained using a Panalytical X'Pert Pro MPD diffractometer operating at 40kV and 40ma using Cu Kα radiation. Differential scanning calorimetry (DSC) thermograms were measured using a TA Instruments 2920 Modulated DSC, and data were analyzed using the Universal Analysis software V 2.3 from TA Instruments. Thermograms were recorded using the standard mode and a constant heating rate of 5 ℃/min. A cooling rate of 10 ℃/min was used during the initial cycle compared to a cooling rate of 1 ℃/min for subsequent cycles.

Preparation of Aggregates in Solution. Stock solutions of L-F and B-F (0.10 M) were prepared in dichloromethane. Aggregate solutions of each dye (1×10^{-4} M) were prepared by adding aliquots of the corresponding stock solution to 20 mL sample vials and evaporating in air. The solutions diluted with 10 mL of THF/H_2O in the proper ratio and sonicated for 10 min prior to measurement of their excitation and emission spectra.

Preparation of Thin Films. Films for powder XRD characterization were fabricated by preparing a 1×10^{-3} M stock solution of each dye in dichloromethane and adding 10 drops to 18×18 mm glass microscope coverslips and evaporating in air. Stock solutions of the same concentration were used to make thin films for solid-state quantum yield and ML characterization measurements by adding 10 drops of the corresponding stock solution to 12 mm diameter and 18×18 mm glass coverslips, respectively. All films were dried under vacuum for 10 min prior to measurement. Weigh paper films were fabricated using a nitrile examination glove to smear a small amount of dye (~2 mg) across a 5×5 cm sheet of weigh paper.

Mechanochromic Luminescence. Emission spectra of glass films were collected for dyes in the as spun (AS), thermally annealed (TA) and smeared (SM) states. With the exception of L-F, the annealed films were produced by heating for 10 min at a constant temperature. Films of L-CN and L-I derivatives were heated at 110ºC and B-F, B-I and B-CN films were heated at 170ºC, 160ºC, and 150ºC, respectively. Films of L-F were first heated at 75ºC for 10 min, followed by gentle smearing with a Kimwipe and subsequent heating at 75ºC for another 10 min. The same annealing and smearing procedures were used to characterize ML on weigh paper films.

Computational Details. Trimethoxy-substituted diketones and boron complexes were modeled using the Gaussian 09 suite of programs with density functional theory (DFT).[24] A basis set of B3LYP/6-31+G(d) was utilized for ground state optimization of all dyes and a Tomasi polarized continuum for dichloromethane was used to simulate solvent interactions. For iodo-substituted derivatives L-I and B-I, all other settings were the same however the basis set B3LYP/SDD was used to model iodine. The calculated vibrational frequencies for the optimized geometries were all positive, which indicated that the geometries are at least a local minimum. Molecular orbital diagrams were generated using single point energy calculations with B3LYP/6-31G(d). Time-dependent density functional theory, TD-B3LYP/6-311+G(d), was used to estimate the absorption spectra and the first three excited states for each derivative.

6.4 Acknowledgements

6.5 References

1   T. Butler, W. A. Morris, J. Samonina-Kosicka and C. L. Fraser, *ACS Appl. Mater. Interfaces*, 2016, **8**, 1242–1251.

2   H. Shi, R. Liu, S. Zhu, Q. Gong, H. Shi, X. Zhu and H. Zhu, *J. Fluoresc.*, 2016, **26**, 2005–2013.

3   J. Han, J. Sun, Y. Li, Y. Duana and T. Han, *J. Mater. Chem. C*, 2016, **4**, 9287–9293.

4   Y. Q. Dong, J. W. Y. Lam and B. Z. Tang, *J. Phys. Chem. Lett.*, 2015, **6**, 3429–3436.

5   S. Yagai, T. Seki, H. Aonuma, K. Kawaguchi, T. Karatsu, T. Okura, A. Sakon, H. Uekusa and H. Ito, *Chem. Mater.*, 2016, **28**, 234–241.

6   T. Butler, M. Alexander S., S. Michal and C. L. Fraser, *ACS Appl. Mater. Interfaces*, 2017, **Submitted**.

7   T. Butler, W. A. Morris, J. Samonina-Kosicka and C. L. Fraser, *Chem. Commun.*, 2015, **51**, 3359–3362.

8   G. Zhang, J. Lu, M. Sabat and C. L. Fraser, *J. Am. Chem. Soc.*, 2010, **132**, 2160–2162.

9   W. A. Morris, T. Liu and C. L. Fraser, *J. Mater. Chem. C*, 2015, **3**, 352–363.

10   J. R. Lakowicz, *Principles of Fluorescence Spectroscopy*, Springer, New York, 2006.

11   W. A. Morris, M. Kolpaczynska and C. L. Fraser, *J. Phys. Chem. C*, 2016, **120**, 22539–22548.

12   J. Mei, Y. Hong, J. W. Y. Lam, A. Qin, Y. Tang and B. Z. Tang, *Adv. Mater.*, 2014, **26**, 5429–5479.

13   W. A. Morris, M. Sabat, T. Butler, C. A. DeRosa and C. L. Fraser, *J. Phys. Chem. C*, 2016, **120**, 14289–14300.

14   Z. Chen, J. Zhang, M. Song, J. Yin, G.-A. Yu and L. S. Hua, *Chem. Commun.*, 2015, **51**, 326–329.

15   C. Y. K. Chan, J. W. Y. Lam, Z. Zhao, S. Chen, P. Lu, H. H. Y. Sung, H. S. Kwok, Y. Ma, I. D. Williams and B. Z. Zhong, *J. Mater. Chem. C*, 2014, **2**, 4320–4327.

16   K. Chung, D. S. Yang, J. Jung, D. Seo, M. S. Kwon and J. Kim, *ACS Appl. Mater. Interfaces*, 2016, **8**, 28124–28129.

17   W. A. Morris, M. Sabat, T. Butler, C. A. DeRosa and C. L. Fraser, *J. Phys. Chem. C*, 2016, **120**, 14289–14300.

18   W. A. Morris, T. Butler, M. Kolpaczynska and C. L. Fraser, *Mater. Chem. Front.*, 2017, **1**, 158–166.

19   D. B. G. Williams and M. Lawton, *J. Org. Chem.*, 2010, **75**, 8351–8354.

20   G. Zhang, R. E. Evans, K. A. Campbell and C. L. Fraser, *Macromolecules*, 2009, **42**, 8627–8633.

21   J. N. Demas and G. A. Crosby, *J. Phys. Chem.*, 1971, **75**, 991–1024.

22   H. Zhu, X. Wang, Y. Li, Z. Wang, F. Yang and X. Yang, *Chem. Commun.*, 2009, **0**, 5118–5120.

23   Y. L. Chow, C. I. Johansson, Y.-H. Zhang, R. Gautron, L. Yang, A. Rassat and S.-Z. Yang, *J. Phys. Org. Chem.*, 1996, **9**, 7–16.

24   M. J. Frisch, G. W. Trucks, H. B. Schlegel, G. E. Scuseria, M. A. Robb, J. R. Cheeseman,

G. Scalmani, V. Barone, B. Mennucci and G. A. Petersson, *Gaussian 09 Revis. A.1;*

Gaussian, Inc. Wallingford, CT, 2009.

Chapter 7

Substituent Effects on the Thermal Stability of Luminescent Trimethoxy β-Diketone Supercooled Liquids
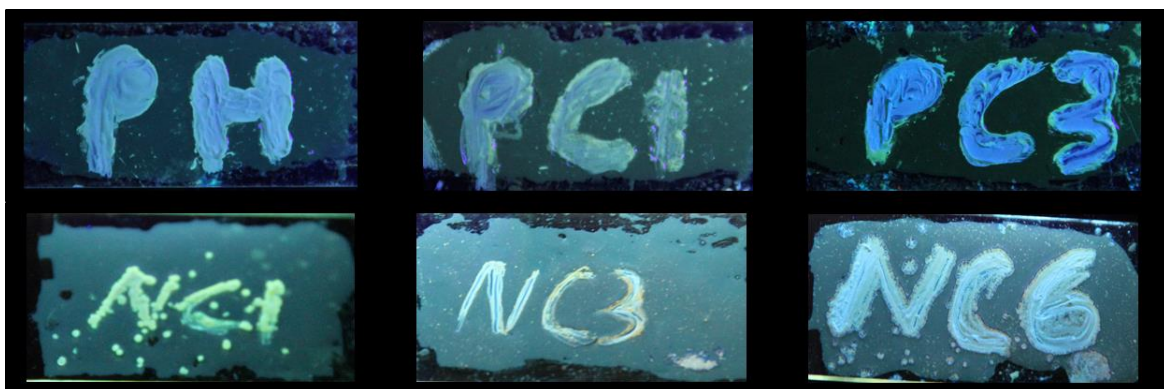
7.1 Introduction

In the absence of donor and acceptor groups and BF_2 coordination, a limited wavelength range is accessible to β-diketone (bdk) dyes. Typically, blue-to-green emission responses are produced by both thermal and mechanical stimuli.[1,2] For example, gbmOMe, the trimethoxy-substituted dye discussed in Chapter 4, shows rapidly recovering blue to green mechanochromic luminescence (ML) and forms a green-emissive supercooled liquid (SCL) phase after melting that is stable for up to 24 hours.[1] Amorphous materials, such as SCLs, are of interest for improved drug solubility, conducting materials for organic light emitting diodes (OLEDs), nanolithography, optical memory storage, and force sensors.[3–8]

Molecules that form supercooled liquids (e.g. diphenyl hydrazone, triphenyl amine (TPA), capped oligothiophenes, and π-electron starburst derivatives) tend to have bulky substituents, such that they form different non-planar conformers.[5,6,9] As these melted molecules are cooled below their crystallization temperature, different conformations are sampled in order to reach an energy minimum and crystallize.[10] Due to the steric bulk of these materials, efficient sampling is prevented, limiting intermolecular interactions. Furthermore, the viscosity of the melted phase increases considerably during cooling, further hindering the molecular motion needed for crystallization.[9–11] According to the crystal structure of gbmOMe, the out-of-plane methoxy group of the trimethoxy substituted ring seems to provide the necessary steric bulk needed for the formation of the supercooled liquid state. Therefore, designing other molecules with this motif may be an effective strategy to form supercooled liquid phases.

Kim *et al.,* recently published a study detailing the stimuli responsive properties of diketopyrrolopyrole (DPP) supercooled liquids.[7] The thermal stability, triggering force, and crystallization rate were modulated by varying alkyl chain lengths. In general, these properties

were tunable based on the balancing of alkyl chain and arene interactions. Using this design strategy, a series of trimethoxy bdks were synthesized, incorporating phenyl and naphthyl rings to probe arene effects on the thermal stability of supercooled liquid phases (Figure 7.1). Additionally, both sets of dyes (phenyl and naphthyl) were substituted with alkoxy groups of varying alkyl length (n = 0, 1, 3, 5, 6, 12) in order to induce Van der Waals interactions and drive crystallization. Previous reports of alkyl chain length and arene size effects on the mechanochromic luminescence (ML) of BF_2bdk materials indicate that the stimuli responsive optical properties of spin-cast films (thermal, ML) may be affected in addition to the thermal stability of the supercooled liquid.[12,13]

In order to estimate the thermal stability of the melted phase for this bdk dye set, videos of melt quenched films were recorded for up to three hours. If the melted phase lasted longer than 10 min, a shear force was applied to SCL films in attempt to induce crystallization. Thermal and structural characterization of dyes was performed using differential scanning calorimetry (DSC) and X-ray diffraction (XRD), respectively. When possible, single crystals were grown and assessed by XRD to provide insight into the intermolecular and packing interactions that influence the thermal stability of the melted phase. Solid-state optical properties were investigated as bulk powders and melted films. In addition, thin films of each dye were fabricated in order to investigate the ML response of each dye.
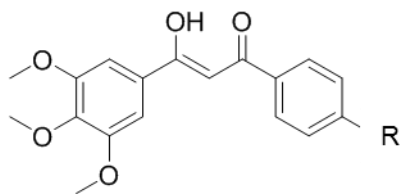
R = H (PH), OCH$_3$ (PC1), OC$_3$H$_7$ (PC3), OC$_5$H$_{11}$ (PC5), OC$_6$H$_{13}$ (PC6), OC$_{12}$H$_{25}$ (PC12)
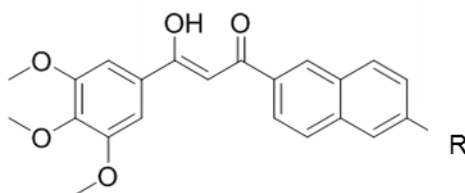
R = H (NH), OCH$_3$ (NC1), OC$_3$H$_7$ (NC3), OC$_5$H$_{11}$ (NC5), OC$_6$H$_{13}$ (NC6), OC$_{12}$H$_{25}$ (NC12)

Figure 7.1. Chemical Structures of Diketones. Dyes are named for the arene ring (P = phenyl, N = naphthyl) and the length of the alkyl chain (e.g. C1 = methyl, C3 = propyl). For example, PC1 is a phenyl dye with a methoxy substituent.

7.2 Results and Discussion

7.2.1 Synthesis

In order to investigate the stability of supercooled liquid states and ML properties of β-diketone dyes, a series of phenyl (Scheme 7.1; Appendix F) and naphthyl (Scheme 7.2; Appendix F) derivatives was synthesized via Claisen condensation with the appropriate ketone/ester pair. The ketone starting materials for both phenyl and naphthyl derivatives were synthesized *via* Williamson ether synthesis using a previously described method.[14] Diketones were soluble in common organic solvents (e.g. CH$_2$Cl$_2$, THF, CHCl$_3$), however solubility in hexanes varied depending on the length of the alkoxy chain. That is, longer chains corresponded to greater hexane solubility. Peaks near 17.0 ppm were observed in the NMR spectra for all dyes which indicates that they are in enol form when dissolved in CDCl$_3$.

7.2.2 Optical Properties in Solution

The optical properties of the dyes were measured in dilute (10^{-5} M) dichloromethane solutions (Figure S7.1, Figure S7.2, Table S1; Appendix F). As a result of increased conjugation relative to phenyl dyes, redshifted absorption and emission were observed for naphthyl derivatives. With the exception of the hydrogen-substituted derivatives that were slightly blue shifted compared to other dyes, little deviation in peak absorbance (λ_{abs}) was detected within each set of dyes (i.e. phenyl, naphthyl). As expected and previously observed, alkoxy substitution results in red-shifted emission due to increased electron donation versus H, however chain length has little effect on absorption.[13] All dyes exhibited similar molar absorptivities ranging from 55000 for NC3 to 81000 for NC5 regardless of phenyl or naphthyl substitution. Typically, increasing conjugation results in larger absorbing cross-sections and increased molar absorptivity, however no trend was observed for these trimethoxy dyes. One potential explanation could be that twisting of arene rings in the ground state limits the absorbing cross-section of both sets of dyes.[15]

Inspection of emission properties with the naked eye indicated that dyes are essentially non-emissive in solution, evidenced by low quantum yields ($\phi < 3\%$) irrespective of increased conjugation or alkoxy substitution. Similar to their absorption in solution, the emission of naphthyl dyes was redshifted compared to phenyl substituents. Phenyl derivatives PH and PC12 show redshifted emission compared to other derivatives of this kind. Similarly, no trends in emission with alkyl chain length could be established for naphthyl dyes. Relatively short lifetimes were observed (< 0.5 ns) for both sets of dyes which are consistent with other bdk derivatives (e.g. bromo and methoxy dinaphthoylmethane (dnm) dyes (< 0.23 ns)[2] and 3,4,5,-trimethoxy derivatives with fluoro, iodo, and cyano substituents (< 0.23 ns) in Chapter 6.)

7.2.3 Video Characterization of Melted Films

Qualitative screening of the thermal properties for blue-emissive bulk powders indicated that all dyes form a green-emissive melted phase, however the duration of the melted phase was dependent on the presence and length of the -OR group. In order to compare the stability of the melted states and probe mechanical shearing effects, videos were recorded of melted diketone thin films (Figure 7.2). Films of the melted state were prepared by adding a small amount of dye (~20 mg) to a microscope slide followed by placing the slide on a hotplate. Once the dye melted, it was spread evenly across the microscope slide using a wooden applicator. Videos were recorded immediately after removal from heat source, but the duration of the video depended on the stability of the melted phase. For films that exhibited phase changes (i.e. formation of blue-emissive species) without mechanical perturbation, videos were recorded until the melted phase was unobservable (i.e. the absence of green emission from the SCL/melt). If no green phase was detected after 10 min or longer, films were sheared vigorously using a wooden applicator and videos were recorded for up to three hours in order to monitor mechanically induced phase changes.
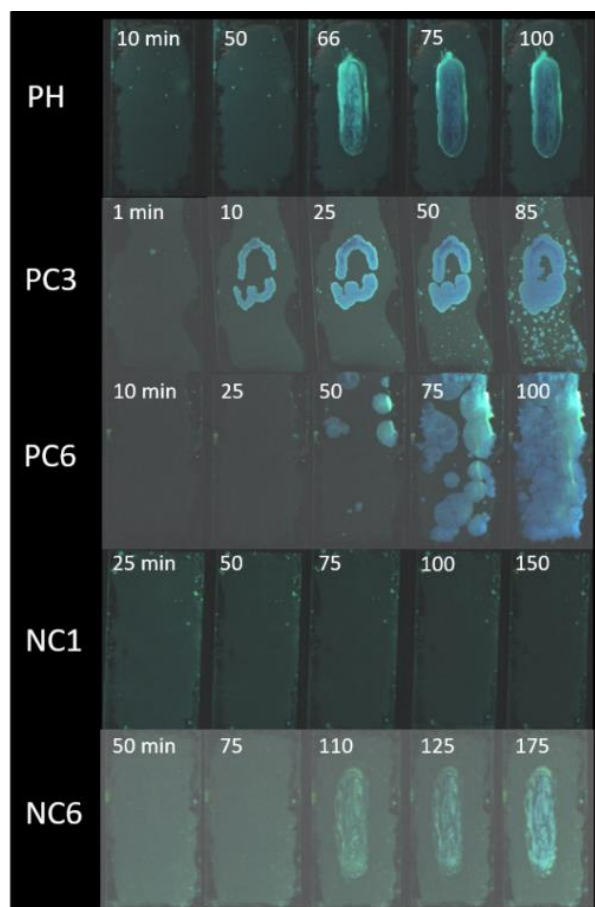
Figure 7.2. Video Characterization of Diketones. The effect of alkoxy substitution on the thermal stability and shear induced phase change of phenyl and naphthyl substituted diketone supercooled liquids/melts. Mechanical perturbation was applied to PH, PC3, NC1, and NC6 in order to induce crystallization. For PC6, crystallization was observed after melting so that sample was not smeared.

As with initial observations, videos indicated that the thermal stability of the melted phase of phenyl dyes is correlated with the length of the alkoxy chain. For PC12, the dye with the longest chain, a transiently stable (~1 min) melted phase with green emission was initially formed before rapidly turning blue. Dyes with intermediate chain lengths, PC5 and PC6, formed green emissive melted states that were stable for several minutes, however blue emissive regions eventually begin to form without mechanical stimulus (Figure 7.2, PC6). The stability of the melted phase was much greater for dyes with shorter (≤ 3 Carbon atoms) alkoxy chains. The PC3 dye formed a green phase when melted but slowly transitions to the blue phase over approximately three hours. The

emergence of the blue emissive phase in PC3 can be expedited through mechanical perturbation, as gentle smearing of the relatively fluid melted phase resulted in the rapid appearance of blue emission. As described in previous studies, melted PC1 films were thermally stable for several hours before crystallization occurred, however the effect of mechanical smearing on the melt phase was not investigated.[1] While smearing resulted in a localized phase change, compared to PC3, repeated smearing was required in order to generate blue-emissive PC1 films. Additionally, the transition was not immediate, as a significant period of time (i.e. 15 min) elapsed between mechanical smearing and the observation of blue emission. The most stable melted phase was measured for PH films which still showed green emission after 24 hours. Vigorous smearing of these films resulted in the emergence of localized blue emission. Though PH was harder to smear than PC3, it was much less viscous than PC1 films and also exhibited a more rapid phase change after smearing.

Naphthyl dyes also formed stable meted phases when melted and quenched in air. After initial cooling phase, NC3 and NH occupied thermally stable melts that were brittle and difficult to smear, whereas the melted phase of NC1 was more fluid by comparison. Like its phenyl counterpart, NC12 formed a green emissive melt that rapidly converted to a solid blue-shifted phase after a few minutes. All other naphthyl substituted dyes form melted phases that are stable for over 24 hours regardless of –OR substitution. After two days, inspection of the films showed that blue emissive phases eventually encompassed the entire film. For NC6, a localized phase transition was induced through vigorous smearing of the relatively viscous melted phase, however, for the other naphthyl films at room temperature, application of mechanical stimulation did not induce any phase changes. However, phase changes localized to smeared regions could be

produced after smeared films were gently heated. Differences in viscosity were observed depending on alkoxy substitution and chain length.

In general, the stabilities of the melted phases were longer for naphthyl versus phenyl dyes. One potential explanation for this observation is that naphthyl dyes may occupy a more twisted conformation. Like other sterically hindered dyes that form stable amorphous phases, the twisting of naphthyl diketones could prevent the dye-dye interactions necessary to form different phases.[5] It is also possible that increased arene-arene interactions result from naphthyl substitution and form species at a local energy minimum, thereby preventing transition to a different phase.[7] In support of this assertion, previously we have seen lower solubility and increased aggregation at lower concentration for naphthyl versus phenyl dyes.[16,17] Furthermore, this study indicates that the stability of melted phases for both phenyl and naphthyl derivatives was tunable based on alkoxy chain length, as the melted phases for C12 substituted dyes exhibited much lower melt stability (i.e. shorter melt lifetimes) compared to other phenyl and naphthyl diketones. Phenyl dyes were more sensitive to alkyl chain length effects, as PH, PC1, and PC3 showed progressively less stable melted phases, whereas highly stable melted phases were noted for corresponding naphthyl films. Additionally, phenyl derivatives showed greater propensity for mechanically induced phase changes since PH, PC1, and PC3 all formed blue-shifted phases after smearing, but NC6 was the only naphthyl derivative that formed a blue emissive phase at room temperature after mechanical perturbation.

7.2.4 Powder XRD Characterization of Melted Thin Films

Screening of thermal responses indicated that dyes existed as transparent green emissive melted states that, in some instances, transitioned to opaque solids with brighter and higher energy emission. To better understand the identity and structural factors associated with these phases,

powder x-ray diffraction (XRD) patterns were gathered for dyes as bulk powders and melts (Figures 7.3, 7.4).

Analysis of powder patterns for phenyl dyes indicated that derivatives with shorter alkyl chains (< C6) were crystalline as bulk powders, but mostly amorphous as melted thin films. With the exception of PC3, no diffraction peaks were observed in the powder patterns of the melted films for these dyes, which indicates that they are amorphous. For PC3, small peaks were observed in the melted phase which may be due to the formation of small crystalline regions during the course of the measurement. The XRD patterns for bulk powders and melted films of phenyl dyes with longer alkoxy chains, PC6 and PC12, indicated that both states were populated with crystalline species. Therefore, melted PC6 and PC12 films rapidly converted to a crystalline blue-emissive phase which is consistent with video characterization. Comparison of the bulk powder and melted patterns of PC6 shows that the same crystalline phase is present in both states, whereas the XRD data for PC12 shows several peaks in the bulk powder pattern that are absent when melted and crystallization occurs afterwards. This suggests that multiple crystalline phases are present in the bulk powder of PC12; some of which are not formed when PC12 was melt quenched.
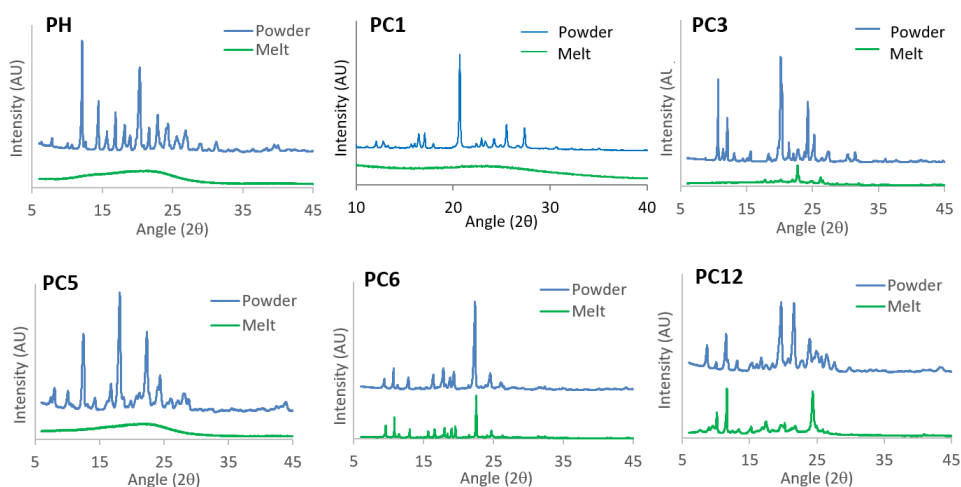
Figure 7.3. Structural Characterization of Phenyl Dyes. Powder X-ray diffraction patterns of phenyl dyes as powders and melted films.

The XRD patterns of bulk powders and melted films of naphthyl compounds showed similar behavior to their phenyl counterparts. With the exception of NC12, all dyes exhibited crystalline powder phases, and no peaks were observed after melt quenching, thereby demonstrating that the melted phases formed by naphthyl dyes are amorphous. Similar to PC12, melted NC12 films form a crystalline phase after cooling however it is comprised of the same crystalline species as the corresponding bulk powder. These results are similar to previous investigations of the thermal response of heteroarene BF$_2$bdks and dimethylamino diketones, as amorphous phases were also formed after melt quenching. However, crystallization of melted phases was not observed for naphthyl dyes even after extended periods of time.
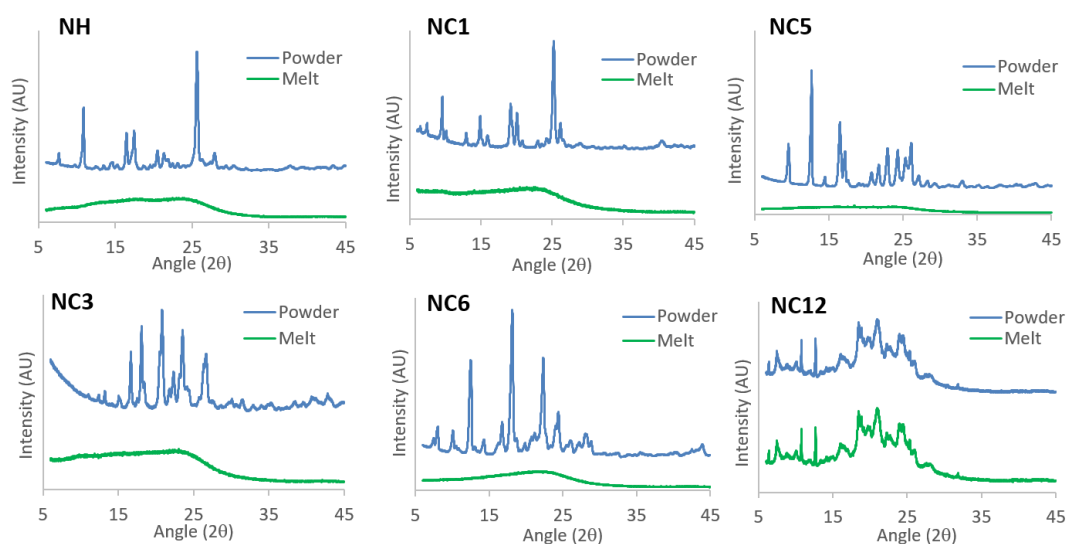
Figure 7.4. Structural Characterization of Naphthyl Dyes. Powder X-ray diffraction patterns of phenyl dyes as powders and melted films.

7.2.5 Single Crystal Analysis

As stated by homogeneous nucleation theory, the crystallization behavior of melted trimethoxy dyes can be limited by nucleation of molecules as well as propagation of crystallites.[18] These properties can be affected by intermolecular and solid-liquid interfacial interactions, in addition to the ability of molecules to sample different conformations.[10] The intermolecular interactions and dye conformations that are experienced by dyes as solids not only provide insight

into their crystallization dynamics, but also determine their optical properties. In order to analyze the intermolecular contacts that control the crystallization of trimethoxy diketones, single crystal XRD was employed. Attempts were made to grow crystals of all dyes; PH, PC3, and PC5 formed crystals suitable for diffraction. The solid-state conformations (Figure 7.5, Figure S7.3; Appendix F) and packing interactions (Figure 7.6) were investigated for these dyes and compared to PC1 which has previously been reported.[1] For clarity, different colors were used to denote dye of the same orientation (Figure 7.6). Single crystals of PH, PC3, and PC5 were grown by vapor diffusion of hexanes into concentrated THF solutions. Regardless of alkoxy substituent, all dyes crystallized into block-like formations that exhibited blue-green emission under UV irradiation. The corresponding emission spectra were similar to their bulk powders, which suggests that similar species are present in both forms (Figure S7.4; Appendix F).
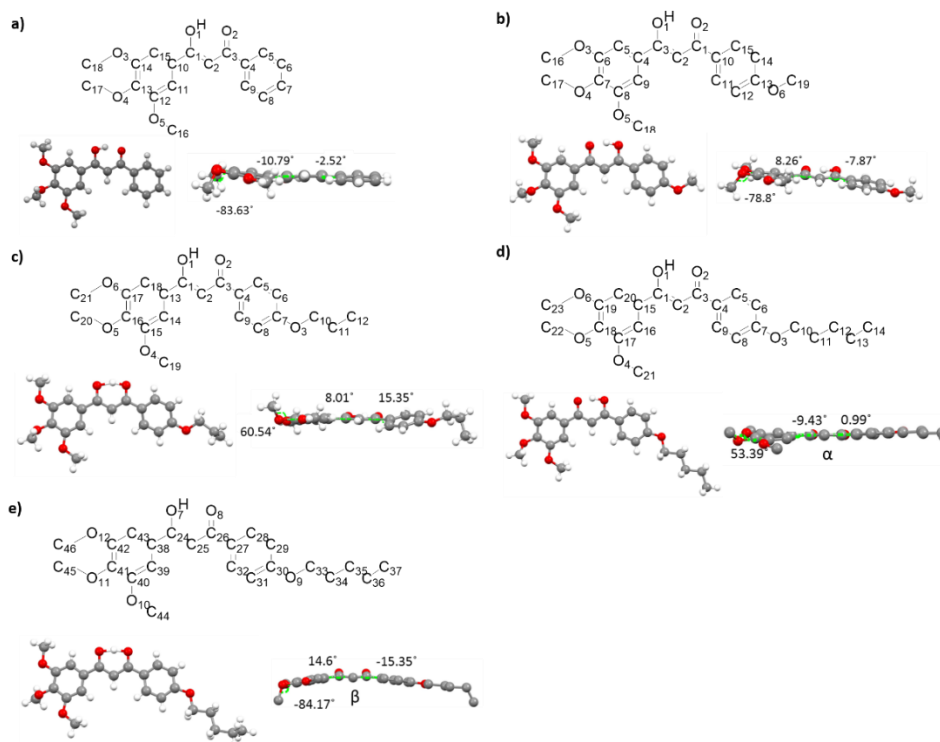
Figure 7.5. Single Crystal Structures of Phenyl Dyes. Labeled structures (top) and single crystals from head on (left) and side (right) profiles that depict selected torsion angles of PH (a), PC1 (b), PC3 (c) α-PC5 (d) and β-PC5 (e) that show selected torsion angles in PC5 crystals.

Examination of the solid-state conformation of PH shows that the para-substituted methoxy group is directed out of the plane of the molecule, which has previously been attributed to steric interactions between neighboring methoxy substituents.[1] The torsion angle between the phenyl ring and this methoxy substituent ($\angle$C12 C13 O4 C17 = -83.63º) shows that it is nearly orthogonal to the molecular plane. Additionally, the trimethoxy phenyl ring of PH was slightly twisted relative the plane of the molecule. Based on the respective torsion angles, the methoxy-substituted ring deviates from planarity more than the unsubstituted ring, which also may be attributable to steric interactions. The unit cell of PH indicates that dyes are assembled based on O-C-H···arene interactions between the para-substituted methoxy group on the trimethoxy ring of one dye and the same arene ring of an adjacent molecule. Additionally, multiple C=O···H-C interactions are noted between aryl hydrogens of the unsubstituted ring and the methane group of the ketone/enol core. Though hydrogen bonding can be observed in the enol moiety, no intermolecular hydrogen bonding interactions between PH molecules were observed. Crystal packing of PH reveals that molecules crystallized into an interlocking series comprised of dyes with the same orientation which are offset from each other. The closest arene-arene distance was estimated by measuring the distance between centroids within the trimethoxy rings of blue/red (4.979 Å) and green/yellow (5.181 Å) PH dyes. These distances are relatively long and are indicative of the lack of π-π interactions within the crystal structure One possible explanation for this is that the out of plane methoxy groups on neighboring molecules are directed towards each other which could prevent close associations of arene groups.

The crystal structure of PC1 has been previously reported and the results are summarized here.[1] Briefly, the single crystal of PC1 shows the dye is mostly planar, however the methoxy group extends out of the plane of the molecule. Relative to PH, the torsion angle ($\angle$C6 C7 O4 C17

= -78.8º) of the out-of-plane methoxy substituent of PC1 is smaller. According to its crystal packing, PC1 dyes stack in a herringbone type motif and the crystal is held together as previously described by C-H···O-C, C-H···H-Arene and C=O···H-C interactions (Figure 7.5). The intermolecular distance of PC1 was measured between centroids assigned to the trimethoxy-substituted ring of blue oriented dyes and the mono substituted arene ring of PC1 dyes in the yellow orientation (3.765 Å). These centroids were chosen in order to examine arene groups in the closest proximity. While this distance is shorter than in the PH derivative, it is still too long for π-π interactions. Compared to PH, where the out-of-plane methoxy groups of neighboring dyes were opposed each other, the methoxy groups of PC1 dimers point in the same direction, and the molecules of PC1 where slightly offset with respect to one another. The alleviation of steric interactions of opposing methoxy groups and the offset conformation of PC1 dye molecules could lead to the closer packing arrangement observed for PC1.
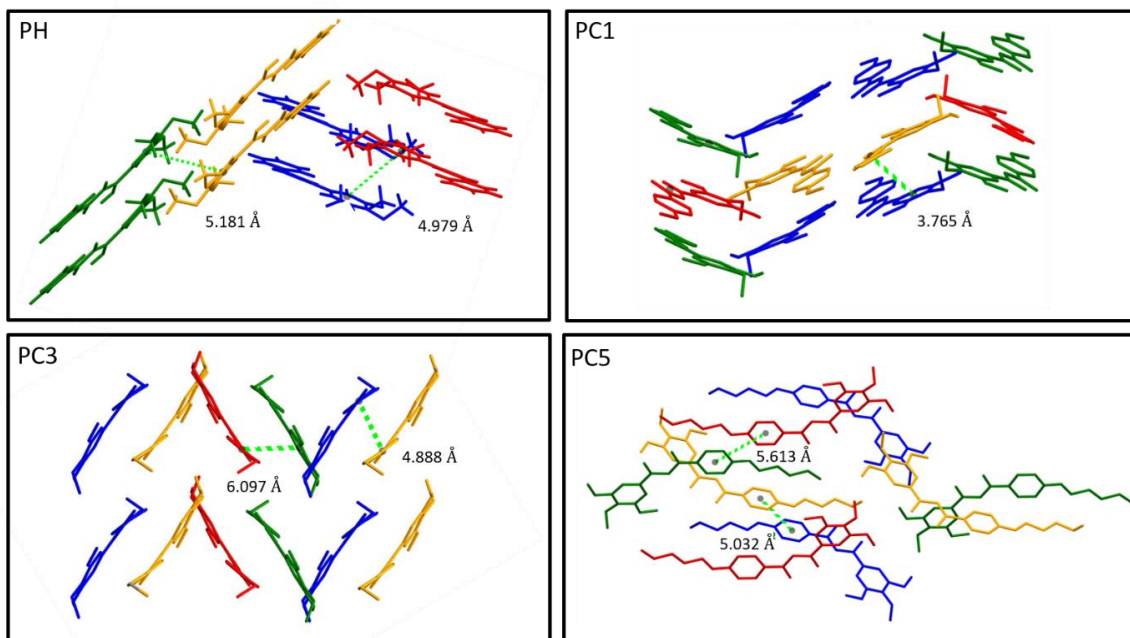
Figure 7.6. Crystal Packing of Trimethoxy Diketones. For clarity in molecular packing figures, dyes are assigned different colors depending on their orientation. Additionally, hydrogens are omitted for clarity in packing figures for PC1, PC3, and PC5. Two molecular conformations (α-PC5 and β-PC5) exist in the unit cell of PC5.

As with PH and PC1, the single crystal structure of PC3 exhibited a mostly planar conformation, but phenyl rings were slightly twisted with respect to each other. However, the C3 substituted ring was slightly more twisted ($\angle$C3 C4 C5 C9 = 15.35°) with respect to the ketone/enol core than both PH and PC1. This may be the result of unfavorable steric interactions generated by the kinked C3 chain, which points below the molecular plane. While, PC3 also shows an out-of-plane methoxy group ($\angle$C15 C16 O5 C20 = 60.54°), the torsion angle is smaller than those measured for PH and PC1 structures. Furthermore, it is directed above the plane of the molecule whereas the opposite was observed for dyes with shorter alkoxy chains. According to the unit cell of PC3, C-O···H-C interactions from trimethoxy substituted rings, and C=O···H-C contacts, which originate from separate molecules, both associate with the C3 chain of the same neighboring dye. Like the other derivatives, no hydrogen bonding or π-π interactions were observed. The herringbone-type packing arrangement of PC3 shows that dyes are arranged in an interlocking series of equivalent, but offset dimers. The inter-dimer distance was estimated by calculating the distance between centroids for trimethoxy substituted rings of dyes in blue/yellow pairs (4.888 Å), and between centroids of trimethoxy substituted and mono substituted rings of different molecules (red/green pairs, 6.097 Å). The difference between distances is further demonstration that dyes are offset and that distances are too long for π-π interaction.

Unlike the other crystals, PC5 exists as two different molecular conformations in the unit cell (α-PC5 and β-PC5). For both molecules, para-substituted methoxy substituents were out of plane with respect to the molecule, however when in the same orientation, the methoxy group of α-PC5 was directed above the plane of the molecule whereas the corresponding methoxy group of β-PC5 pointed below. The torsion angle for this group in α-PC5 ($\angle$C46 C41 O11 C45 = 53.39°) was smaller than β-PC5 ($\angle$C11 C18 O5 C22 = 84.17°) and other trimethoxy derivatives. In addition

192

to differences in the para-substituted methoxy group, the alkoxy chain for α-PC5 was planar compared to β-PC5, which showed a kinked chain with the terminal carbon extended below the molecular plane. While the trimethoxy-substituted ring was out of plane for both α-PC5 and β-PC5, the mono substituted ring of α-PC5 was mostly planar (∠C25 C26 C27 C32 = 0.99°), similar to the corresponding alkoxy chain, and β was twisted out of the plane of the molecule (∠C2 C3 C4 C9 = -15.35°).

The unit cell of PC5 shows that C=O···H-Ar interactions between the ketone/enol core of α-PC5 and arene groups of β-PC5 dyes. Additionally, α-PC5 dyes show O-C-H···H-C contacts between the trimethoxy substituted ring of β-PC5 and the alkoxy chain of α-PC5, however no intermolecular associations were noted for the alkoxy group of β-PC5. The lack of interaction with the alkoxy chain of β-PC5 may explain its kinked structure. Molecular packing of PC5 shows herringbone-type packing with dyes stacked at angles to each other, which indicates that PC5 dimers are not formed. Inter-arene distances were estimated by measuring the distances between centroids of alkoxy substituted rings in red and green (5.613 Å) molecular pairs, and for α-PC5 and for blue and yellow (5.032 Å) conformations which represent β-PC5. Large distances were observed between arene groups for both dyes and account for the absence of π-π interactions.

Comparison of crystal data shows that introduction of alkoxy groups with increasing chain lengths greatly effects dye conformation and packing of phenyl derivatives. While the packing of each dye varied significantly with the alkoxy chain, several similarities were also noted. For example, no π-π or hydrogen bonding interactions were observed for any of the dyes, and only C-O···H-C and C-H···H-C interactions were detected. Additionally, phenyl rings were twisted with respect to ketone/enol core and the para-substituted methoxy group of the trimethoxyphenyl ring

was directed out of the molecular plane for all dyes, including both conformations of PC5. These similarities can give potential insights into the thermal stability of the amorphous phase.

According to homogeneous nucleation theory, the rate of nucleation, and the rate of propagation determine crystal growth. In particular, the nucleation of dyes is governed by the intermolecular interactions which for the crystal.[8] It has been proposed previously that the out of plane methoxy substituent may prevent dye nucleation and therefore crystallization.[1] Comparison of the torsion angles of methoxy groups shows that the longer stability of the amorphous state is observed for dyes when torsion angles are closer to 90º or orthogonal to the plane of the molecule. For PH, the dye with the longest lived amorphous state, the para-substituted methoxy group was highly out of plane. Furthermore, neighboring dimers show methoxy groups directed towards each other. These interactions could prevent molecular association and likely increase stability of amorphous phase. The crystal structure of PC1 showed a large torsion angle, however out of plane methoxy groups were stacked in same direction which could ease steric interactions compared to PH. Modest torsion angles were observed for PC3, and methoxy groups were pointed in opposing directions, which allows for greater dye-dye interactions and limit stability of the melted phase.

Video characterization revealed that the thermal stability of melted PC5 films was shorter compared to other dyes with attainable crystal structures, but the different conformations of PC5 in the unit cell show different torsion angles between molecules. The α-PC5 derivative exhibits the shallowest torsion angle of all single crystals, and may allow for sterically inhibited dye-dye interactions. Conversely, torsion angle of the para-substituted methoxy group of β dyes was nearly orthogonal, and could prevent dye associations. However, unit cell of PC5 shows interactions between ketone/enol core and C5 chain which could propel nucleation, and limit stability of the amorphous state. In conjunction with qualitative screening of trimethoxy substituted dyes, these

crystal structures provide insight into the structural interactions that govern the thermal stability of amorphous state tunable *via* alkoxy substitution.

7.2.6 Thermal Properties

The ease with which dyes access different conformations in a liquid is a determining factor in the crystallization dynamics of a given material. This is related to the viscosity of the liquid phase and is therefore highly temperature dependent.[9,10,19] Additionally, substituent effects such as alkoxy and arene substitution have been shown to induce viscosity changes as well as promote van der Waals interactions, which can be used to tune stability of melted phases.[7] Previous investigations of the thermal properties of PC1 indicated that a supercooled liquid phase was formed when melted PC1 films were cooled in air. Thermal characterization of the supercooled liquid phase was performed using differential scanning calorimetry (DSC) with variable cooling rates. If cooled sufficiently slowly, an exothermic peak indicative of crystallization was observed, however no peaks were detected when PC1 was cooled rapidly. In order to probe the effect of alkoxy chain length and arene size on the phase transitions produced by heating, successive DSC thermograms were gathered for each dye with variable cooling rates. For the first cycle the dyes were cooled rapidly (10 ºC/min), followed by slow cooling (1 ºC/min) in order to facilitate crystallization when possible (Table 7.1).

Table 7.1. Thermal Properties or Trimethoxy-Substituted Diketones.

	Cycle 1		Cycle 2	
	$T_m{}^a$	$T_c{}^b$	$T_m{}^a$	$T_c{}^b$
PH	101.5	-	-	-
PC1	112.4	-	116.5	-
PC3	123.6	-	121.5	54.1, 90.8, (84.2)
PC5	105.4	(62.3)	104.3	(69.6)
PC6	98.5	(41.6)	97.4	(65.5)
PC12	95.2	(63.0)	94.7	(78.1)
NH	89.5	-	-	-
NC1	134.1	-	133.3	102.5, (107.5)
NC3	116.3	-	114.4	87.5
NC5	102.0	-	101.6	78.9
NC6	120.1	-	119.2	67.0, (94.3)
NC12	77.0	(42.9)	79.6	43.4, (44.6)

ª Melting point given in ºC as the peak of the major endothermic transition. Secondary transitions are given in parentheses
ᵇ Crystallization temperatures given in ºC as the peak of exothermic transitions. Transitions reported in parenthesis occurred during the cooling phase of each cycle.

The dependence of crystallization on cooling rate for these molecules indicates that some dyes adopt a supercooled liquid phase when rapidly cooled. Furthermore, comparison of thermograms for phenyl dyes (Figure 7.7) shows that alkyl chain length affects stability of the supercooled liquid, which is in accordance with video studies. Examination of thermal properties for the first cycle shows that most phenyl dyes melt at similar temperatures ($T_m \sim 100\,°C$), however PC1 ($T_m = 112.4\,°C$) and PC3 ($T_m = 123.6\,°C$) exhibited slightly higher melting points. Crystallization transitions were observed in the first cooling cycle for phenyl dyes with alkoxy

chains longer than three carbons. When unsubstituted or substituted with shorter alkoxy chains (PH, PC1, PC3), no exothermic transitions were noted after rapid cooling.

During the second heating cycle, exothermic transitions attributable to crystallization were observed for PC1 and PC3. Most dyes also exhibited melting points similar to those in the first cycle, but no crystallization or melting transitions were noted for PH. This indicates that nucleation/growth of crystals was not induced even after heating. Based on the crystal structure of PH, steric hindrance from opposing para-substituted methoxy groups may prevent crystallization. Two exothermic transitions were observed for PC3, which suggests that multiple phases were formed during rapid cooling of PC3. Slow cooling resulted in an exothermic crystallization transition for PC3 (T_c = 84.2 ℃), however no peaks were observed for PC1 and PH even after slow cooling. Slow cooling of dyes with longer alkyl chains (>3) resulted in higher crystallization temperatures on the second cycle.
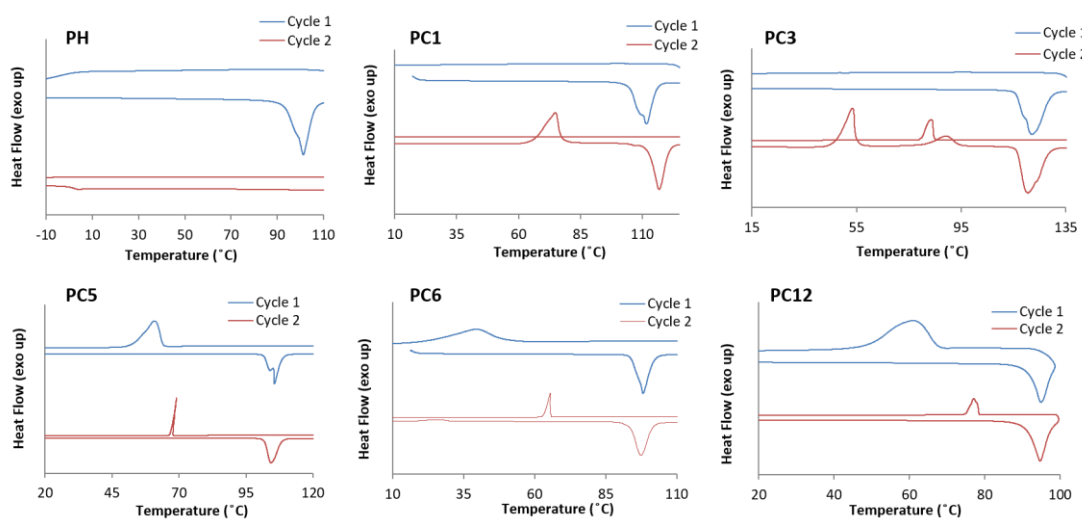
Figure 7.7. Thermal Characterization of Phenyl Dyes. Differential scanning calorimetry (DSC) thermograms of phenyl dyes (heating rate: 5 ℃/min) cooled at different rates (Cycle 1: 10 ℃/min; Cycle 2: 1 ℃/min).

Compared to phenyl dyes, a greater range of melting temperatures was observed for naphthyl dyes (Figure 7.8). The lowest melting temperature was measured for NC12 (T_m = 77.0

°C) whereas NC1 (T_c = 134.1 °C) melted at the highest temperature relative to all other dyes. Similar to their phenyl counterparts, no exothermic transitions were observed for NH, NC1, and NC3 on the first cooling cycle, however crystallization peaks were not observed upon reheating of NH. Like PH, this indicates that nucleation and crystal growth are not sufficient to promote crystallization, and further demonstrates the superior thermal stability of the SCL phases of dyes without alkoxy groups. Contrary to their phenyl analogs, NC5 and NC6 did not exhibit crystallization transitions when cooled rapidly. The slow cooling of NC5 was not sufficient to promote crystallization, but an exothermic peak was observed for NC6 during slow cooling. As with PC12, NC12 exhibits crystallization peaks when cooled rapidly or slowly.
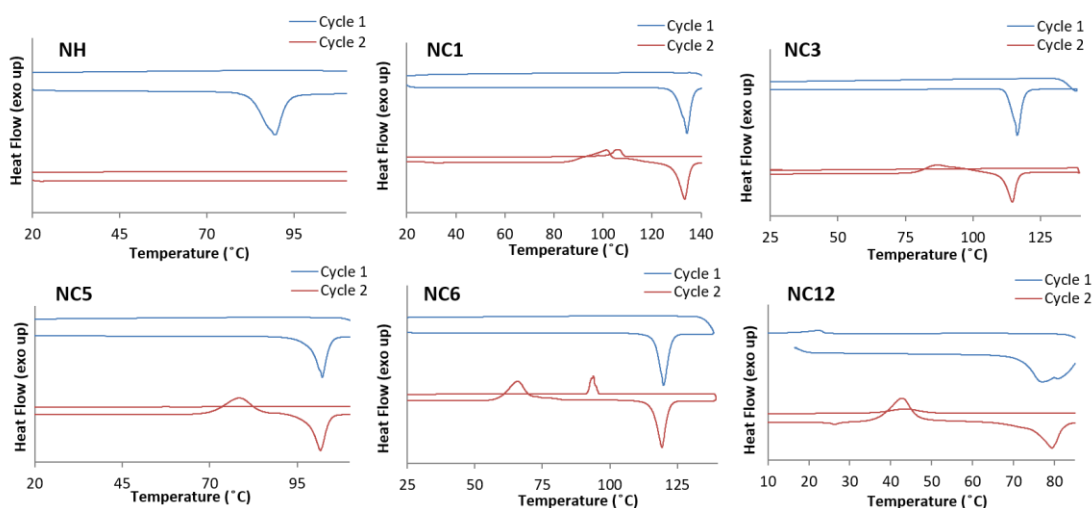
Figure 7.8. Thermal Characterization of Naphthyl Dyes. Differential scanning calorimetry (DSC) thermograms of naphthyl dyes (heating rate: 5 °C/min) cooled at different rates (Cycle 1: 10 °C/min; Cycle 2: 1 °C/min).

Differential scanning calorimetry results show that the size of the alkoxy chain affects the crystallization dynamics for both phenyl and naphthyl derivatives. As observed in video characterization, crystallization occurs for dyes with sufficiently long alkoxy chains despite rapid cooling. For phenyl derivatives, PH, PC1, PC3 formed supercooled liquid phases upon rapid cooling, whereas supercooled liquids were observed for naphthyl derivatives with longer alkyl

chains (NH, NC1, NC3, NC5, NC6) when cooled quickly. Reheating dyes resulted in evidence of crystallization for most derivatives, however no transitions were noted for PH and NH. While both sets of dyes showed melted states with tunable stability, these results further indicate that naphthyl diketones form more stable supercooled phases than corresponding phenyl dyes.

7.2.7 Solid-State Emission

It is clear that the packing interactions and other structural effects derived from alkoxy and arene substitution can affect the thermal stability of trimethoxy diketone melted states, however previous studies have shown that these factors also determine the emission of solid-state materials. The degree to which molecular packing affects the properties of solid-state emissive materials is often estimated by comparison of solid and solution emission. In general, when there are fewer dye-dye interactions, the emission of bulk powders is similar to that of their solution spectra. This has been linked to herringbone type packing structures in certain systems.[20] Prior investigation of these effects on BF$_2$bdks showed that their solid-state emission blue-shifted as alkyl chain length was increased[13] and redshifted emission was observed for BF$_2$bdk dyes with larger arene rings.[21] Given their structural similarities, the solid-state emission of uncoordinated trimethoxy-substituted diketones may exhibit similar trends.

Solid-state optical properties were initially investigated by measuring the emission of bulk properties (i.e. powder and melt phase) for all dyes. The emission of the melted phase was measured by melting dyes (~10 mg) on a piece of microscope coverglass using a hot plate. The emission of diketones as bulk powders was compared to their emission in solution in order to gauge the impact of packing on solid-state emission (Table 7.2). As bulk powders, phenyl dyes glowed blue under UV light, and a narrow range of wavelengths was detected (Figure 7.9). Higher energy emission was detected for PC3, PC5 and PC12 (λ_{em} = 449 nm) relative to PH (λ_{em} = 458

nm) and PC1 (λ_{em} = 453 nm). Compared to other phenyl dyes, the emission of PC6 (λ_{em} = 480 nm) was significantly redshifted.

Based on these results no correlation between emission energy and alkoxy chain length can be established. With the exception of PC6, all phenyl derivatives exhibited similar wavelengths between powder and solution. This indicates that most phenyl dyes are packed such that dye-dye interactions have little impact on their solid-state emission. This is consistent with crystal structures obtained for phenyl dyes which showed herringbone-type packing and no π-π interactions. However, the peak emission of PC6 is substantially red-shifted compared to solution. Therefore, it is likely that dyes occupy a different packing pattern in PC6 solids. In addition, PC6 exhibited a larger quantum yield (41.6%) compared to other phenyl dyes which also may be the result of different molecular packing.

Table 7.2. Emission Properties of Trimethoxy Substituted Diketones in Solid and Melted States

Compound	Solid				Melt			
	λ_{em} [b] (nm)	τ_{pw0} [d] (ns)	fwhm[c] (nm)	Φ_C [e] (%)	λ_{em} (nm)	τ_{pw0} (ns)	fwhm$_{MT}$ (nm)	Φ_{MT} [e] (%)
PH	458	1.14	62	5.0	505	3.38	126	8.0
PC1	453	0.15	54	5.1	481	6.31	135	10.0
PC3	449	1.25	31	24.0	481	3.76	95	-
PC5	449	1.16	38	23.0	523	5.08	135	-
PC6	480	1.67	52	41.6	481	2.78	114	-
PC12	449	< 0.1	43	24.0	526	2.43	137	-
NH	469	2.56	62	10.9	512	3.06	92	17.0
NC1	458	1.85	59	25.6	497	2.72	100	17.8
NC3	478	0.49	62	12.1	493	1.43	117	8.3
NC5	462	0.91	163	17.3	543	1.76	200	5.4
NC6	470	0.56	57	21.1	498	2.29	112	8.4
NC12	486	0.70	99	4.8	535	3.24	152	-

[a] Excited at 369 nm, room temperature, air. [b] Emission Maximum. [c] Full width at half maximum. [d] Pre-exponential weighted lifetime. [e] Quantum yield measured using crystalline (C) and melted (MT) glass films

In most cases, the emission of naphthyl derivatives as powders was red-shifted compared to their corresponding phenyl dyes (Figure 7.10). However, PC6 powders emitted lower energy photons compared to all naphthyl dyes with the exception of NC12 (λ_{em} = 486 nm). While NC12 and NC1 (λ_{em} = 458 nm) exhibited the lowest and highest energy emission detected for naphthyl dyes, respectively, the emission of NC3 was significantly red-shifted compared to derivatives with alkyl chains of intermediate length (NC5 and NC6). Like their phenyl counterparts, this demonstrates that there is no trend in solid-state emission with increasing alkoxy chain length for naphthyl dyes.
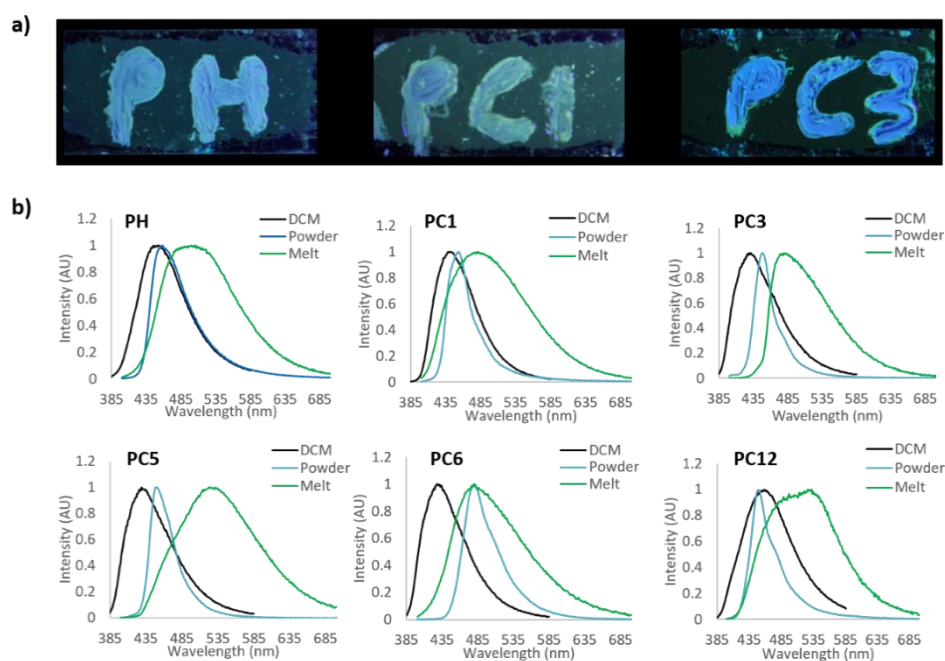
Figure 7.9. Optical Properties of Phenyl Dyes. Images under UV irradiation of mechanically perturbed melted thin films of phenyl dyes (a). Emission spectra of phenyl dyes in dichloromethane solution, as prepared powders, and as melted films (b).

All dyes in the melted phase, regardless of arene substitution, glowed green under UV irradiation, however a wider range of emission wavelengths was detected compared to their corresponding bulk powders. For phenyl dyes, the bluest emission was observed for PC1, PC3, and PC6 (λ_{em} = 481 nm) whereas PC12 exhibited the most redshifted melt (λ_{em} = 526 nm).

Naphthyl dyes exhibited different behaver, where the highest energy emission was noted for NC3 (λ_{em} = 493 nm), and NC5 (λ_{em} = 543 nm) was the most red-shifted. Additionally, broad emission profiles were observed in NC5 and NC6 samples. This could be attributed to emission from multiple emissive species.[22] As with their emission as powders, no trends in emission wavelength of the melted phase with increasing chain length were detected for both phenyl and naphthyl dyes. However, overlapping emission wavelengths were observed between phenyl and naphthyl derivatives which indicates that increasing arene size does not necessarily correspond to redshifted emission, as was the case for bulk powders. These results indicate that the emission of the melted phase cannot be rationally tuned through these methods.
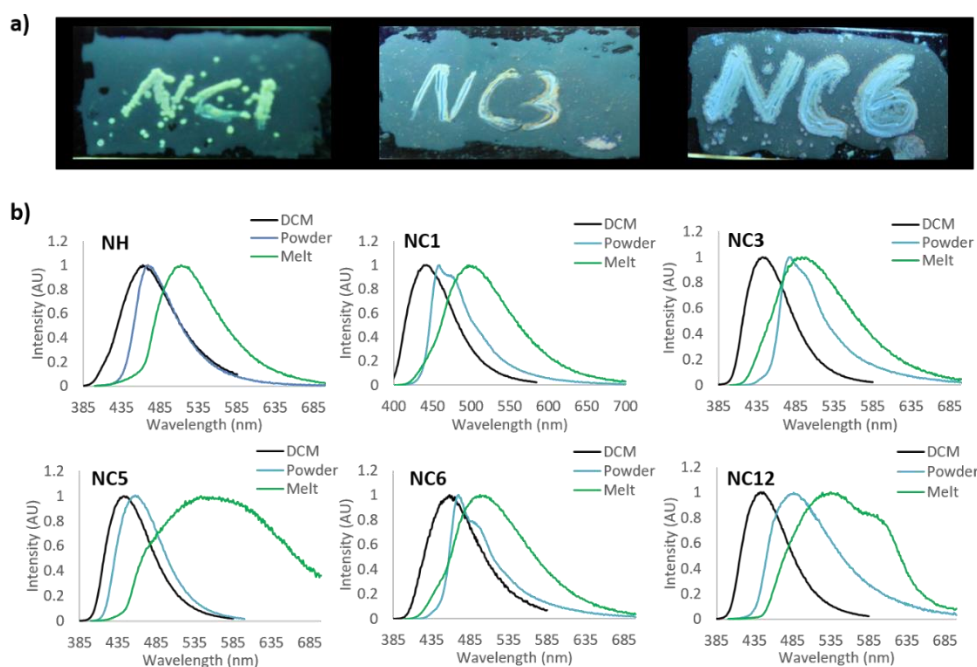
Figure 7.10. Optical Properties of Naphthyl Dyes. Images under UV irradiation of mechanically perturbed melted thin films of naphthyl dyes (a). Emission spectra of naphthyl dyes in dichloromethane solution, as prepared powders, and as melted films (b).

As depicted in the video characterization of phenyl dyes, mechanical shearing of certain phenyl dyes resulted in localized crystallization at room temperature (Figure 7.9a). With the exception of NC6, the same shearing induced crystallization at room temperature was not observed

in naphthyl dyes. However, gentle heating of mechanically perturbed melted phases of naphthyl dyes induced localized crystallization for these derivatives (Figure 7.10a). The contrast between these states can be analyzed using their quantum yields (ϕ) (Table 7.2). The quantum yields for all derivatives were measured in the crystalline phase, however obtaining quantum yields was limited by melt phase thermal stability. Therefore, quantum yields in the melted state were not measured for PC5, PC6, PC12, and NC12 due to rapid crystallization.

In the crystalline state, the quantum yield of phenyl dyes can be tuned through alkoxy substitution. The lowest quantum yields were observed for PH and PC1, but increased quantum yields were observed for dyes with longer chain lengths before reaching a maximum for PC6 (Φ_C = 41.6 %). As observed for iodo-substituted BF$_2$bdk dyes with varying length alkoxy groups in solution, this observation may be greater anchoring of the alkoxy substituted phenyl ring in dyes substituted with longer chains, which hinders rotation.[23] For naphthyl dyes, the quantum yield fluctuates as the alkoxy substituent was increased. In the melted state, little deviation in quantum yield of PH and PC1 was observed, however the quantum yield diminished for naphthyl dyes as the alkoxy chain was increased above a single carbon. Compared to the crystalline state, PH and PC1 exhibited higher quantum yields in the melted state whereas all naphthyl but NC1 exhibited larger quantum yields in the crystalline state. According to the differences in quantum yield, NC6 shows the highest contrast shearing induced crystallization.

7.2.8 Mechanochromic Luminescence

Unlike its mechanically induced crystallization properties described above, the mechanochromic luminescent (ML) properties of bdk and BF$_2$bdk dyes typically involve a red-shift in emission that is the result of a crystalline-to-amorphous phase transition. Previously, PC1 showed blue-to-green ML with rapid self-erasing (~30 s – 5 min, depending on sample). To test

the ML properties of phenyl and naphthyl derivatives, spin-cast films were prepared with dilute (0.18 M) dye solutions in dichloromethane. The emission of each film was measured in as spun (AS), thermally annealed (TA) and smeared (SM) states (Table 7.3). In general, phenyl dyes were annealed at 75 ºC for 10 minutes to produce films in the TA state. With the exception of PH and PC1, this was sufficient to produce a crystalline phase with maximally blue-shifted emission. To anneal PH and PC1, films were gently smeared with a Kimwipe before subsequent heating at 75 ºC for another 10 minutes. For all naphthyl dyes but NC12, films were heated at 85 ºC for 10 minutes, followed by gentle smearing with a Kimwipe and additional heating at 85 ºC for another 10 minutes to make TA films. The smearing and reheating step was omitted for NC12 as blue-shifted emission was observed after heating at 85 ºC for only 10 min.

Table 7.3. Optical Properties of SCLs on Glass.[a]

Compound	As Spun		Annealed		Smeared	
	λ_{em} (nm)	fwhm (nm)	λ_{em} (nm)	fwhm (nm)	λ_{em} (nm)	fwhm (nm)
PH	471	102	470	106	496	103
PC1	499	141	428	35	478	122
PC3	441	36	441	36	474	37
PC5	432	38	434	37	477	106
PC6	451	72	452	56	476	50
PC12	445	60	445	59	481	86
NH	484	111	467	72	480	105
NC1	485	114	485	114	501	111
NC3	480	111	468	80	483	107
NC5	470	138	457	71	486	134
NC6	478	108	483	114	487	111
NC12	476	99	470	101	446	83

[a] Excited at 369 nm, room temperature, air. [b] Emission Maximum. [c] Full width at half maximum. [d] Pre-exponential weighted lifetime

With the exception of PH and PC1, films glowed blue in the AS state (Figure 7.11). Green emission was observed for PH (λ_{em} = 471 nm) and PC1 (λ_{em} = 471 nm). The differences observed in PH and PC1 are in accordance with XRD and DSC studies and indicate that dyes substituted with larger alkoxy chains have a greater propensity to crystallize. No trend in emission wavelength with alkoxy chain length was observed for AS films of blue emissive dyes, as PC3 (λ_{em} = 441 nm) exhibited the maximally blue-shifted emission and the lowest energy emission was observed for PC6 (λ_{em} = 451 nm). Thermal annealing of phenyl dye films resulted in a large blue-shift for PC1, however little change in emission was observed for all other phenyl dyes, which indicates that they are likely crystalline in AS phase. The emission of PH bulk powder (λ_{em} = 458 nm), suggests that higher energy emission should be achievable, however annealing and gently smearing was insufficient to produce blue emission. For all phenyl dyes but PC6, the peak emission of annealed films is similar (< 5 nm) to the emission of monomer in dichloromethane which suggests that dye-dye interactions that modulate emission are very weak or absent for annealed films. The peak emission of PC6 is redshifted relative to emission in dichloromethane, therefore interactions between PC6 molecules are likely present in these films.

Smearing resulted in redshifted emission for all dyes, however the extent of ML shift was highly dependent on alkoxy chain length. The ML shifts ($\Delta\lambda_{ML}$) varied depending on alkoxy chain length, however no clear trend could be established. The smallest ML shifts were observed of PH and PC6 ($\Delta\lambda_{ML}$ < 26 nm) and the largest ML shifts for phenyl dyes were observed in PC1 and PC5 ($\Delta\lambda_{ML}$ > 43 nm). With the exception of PC1, no evidence of self-erasing was observed for phenyl dyes 24 hours after smearing, which indicates that room temperature recovery is hindered in derivatives with longer alkoxy chains. The same trend was observed in BF_2bdk dyes with differing alkoxy chains.
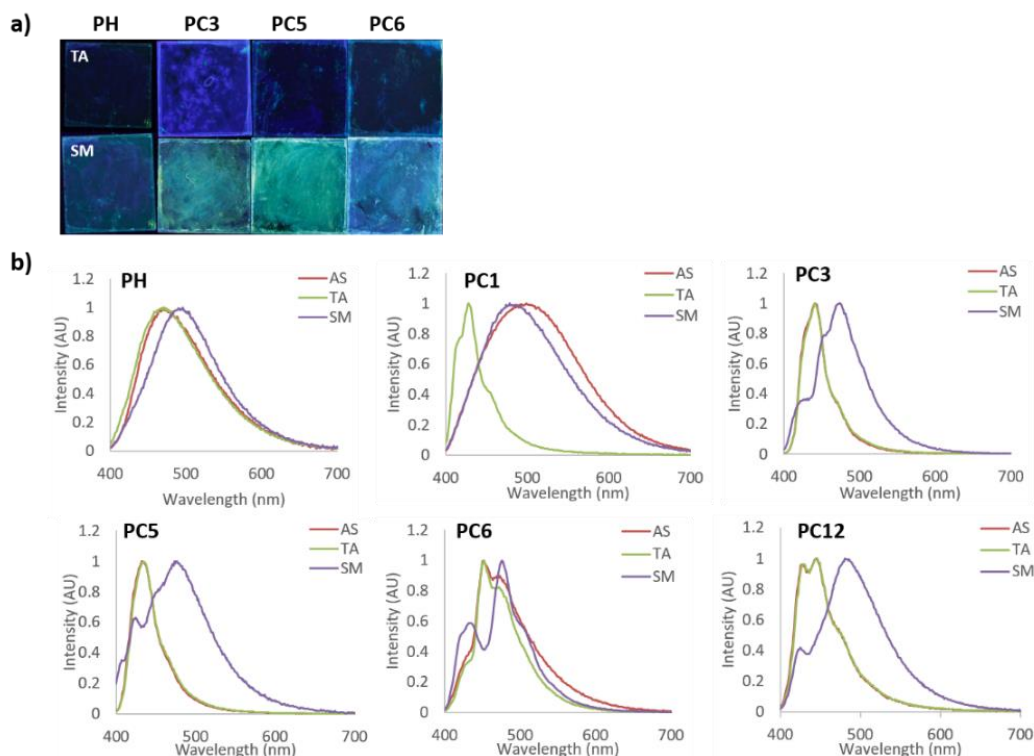
Figure 7.11. Mechanochromic Luminescence of Phenyl Dyes. Images under UV irradiation of thermally annealed (TA) and smeared (SM) thin films of phenyl dyes (a). Normalized emission spectra of phenyl dye films in as spun (AS), TA and SM states (b).

For films of naphthyl dyes, the AS state glowed green under UV irradiation. Compared to phenyl dyes, broader emission profiles were observed regardless of alkoxy chain length. Thermal annealing of naphthyl films resulted in very little change in peak emission for NC1 and NC6. Relatively small changes in peak wavelength were observed compared to phenyl dyes, however predominate change in emission was the result substantial reductions in fwhm, especially for NH, NC3, NC5 and NC12. With the exception of NH which showed similar peak emission with respect to dichloromethane solutions, large deviations in peak emission between solution and solid state spectra were observed for naphthyl dyes. This is indicative of intermolecular interactions between dyes for all alkoxy substituted naphthyl dyes. With the exception of NC5, changes in peak emission and spectral broadening were observed for naphthyl dyes indicating ML activity. No evidence of room temperature self-recovery was observed for naphthyl dyes. Much smaller ML shifts and

lower contrast mechanically generated emission changes were detected in comparison to phenyl derivatives.
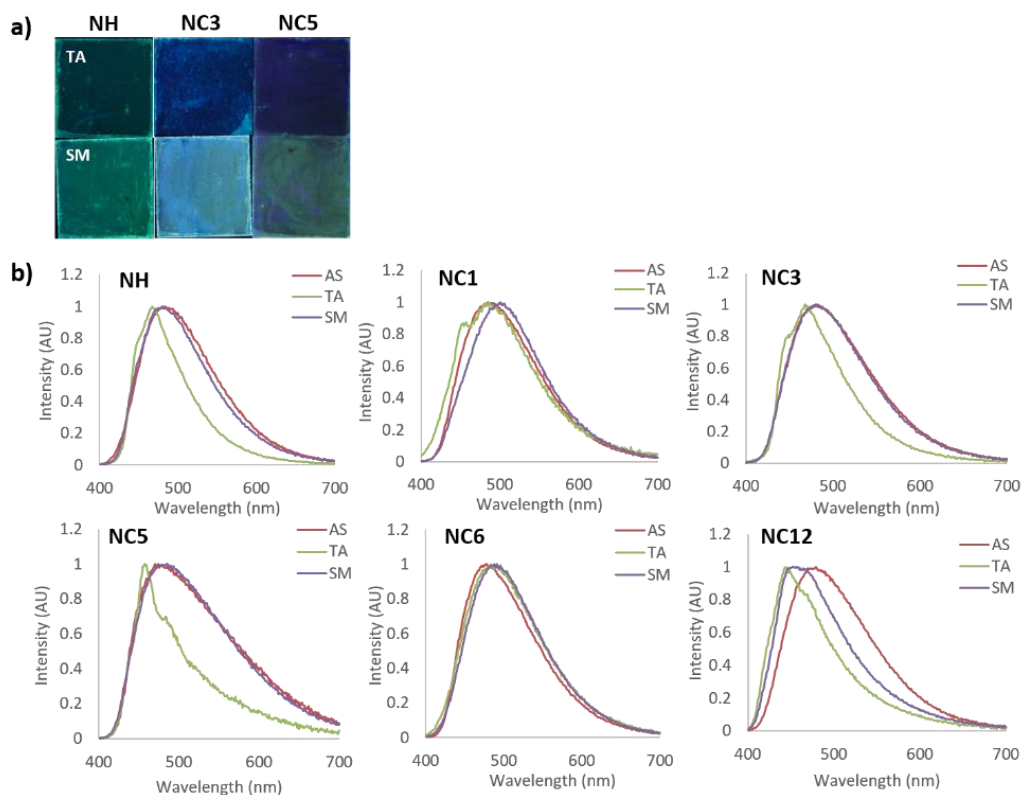
Figure 7.12. Mechanochromic Luminescence of Naphthyl Dyes. Images under UV irradiation of thermally annealed (TA) and smeared (SM) thin films of naphthyl dyes (a). Normalized emission spectra of naphthyl dye films in as spun (AS), TA and SM states (b).

7.2.9 Conclusions

Based on video characterization as well as DSC and powder XRD results, all dyes formed supercooled liquid phases when melted and cooled in air. The thermal stability of trimethoxy-substituted diketones could be tuned using a combination of alkoxy chain length and arene effects. In general, naphthyl dyes exhibited longer thermal stability than phenyl counter parts. Additionally, dyes substituted with longer alkoxy chains exhibited faster crystallization compared to unsubstituted derivatives or dyes with shorter chains. For certain derivatives, mechanically induced crystallization was observed at room temperature (PH, PC1, PC3 and NC6), and some

dyes also exhibited crystallization localized to smeared regions of the sample after gentle heat was applied. Single crystal analysis of selected phenyl derivatives indicated that the para-substituted methoxy group of the trimethoxy rings was out of the molecular plane. Furthermore, the torsion angle of this methoxy group was correlated with the thermal stability of the melted phase. For the most part, dyes that exhibited smaller torsion angles showed lower thermal stability of the melted phase (i.e. faster conversion to the crystalline state). This was attributed to diminished steric interactions that prevent crystallization.

The optical properties were also dependent on arene substitution, as the crystalline phase of naphthyl dyes was redshifted compared to phenyl derivatives. No trends with increasing alkoxy chain length could be established for either the phenyl and naphthyl sets. Mechanochromic luminescent properties were also observed for most derivatives. While dyes exhibited blue-to-green emission changes upon mechanical perturbation, the degree of wavelength shift was dependent on alkoxy chain length. These results indicate that certain trimethoxy derivatives exhibit two types of mechanochromic luminescence at room temperature; namely, (a) traditional ML, where redshifted emission occurs upon smearing and generating an amorphous state from an initially crystalline phase, and (b) shear induced crystallization, where mechanical disruption of a supercooled liquid phase results in blue-shifted emission.

7.3 Experimental Section

7.3.1 Materials

THF was dried over molecular sieves activated at 300 ℃ as previously described. Reactions were monitored using silica TLC plates. Compounds purchased from Sigma-Aldrich and TCI were reagent grade and used without further purification. The trimethoxy-substituted β-

diketones were synthesized *via* Claisen condensation using a previously described method.[14] Williamson ether synthesis was used to prepare alkoxy-substituted ketone building blocks using a previously described method.[14] Data for PH[24] and PC1[24] are in accord with previous studies. Characterization data for new derivatives are provided in Appendix F.

7.3.2 Methods

^{1}H NMR (600 MHz) spectra were recorded on a Varian VRMS/600 spectrometer in deuterated DMSO. Spectra were referenced to the signals for residual protio-DMSO at 2.50 ppm. The coupling constants for each compound were reported in Hz. Mass spectra were recorded using a Micromass Q- TOF Ultima spectrometer, using electrospray ionization (ESI) MS/MS techniques. Absorption spectra were collected on a Hewlett-Packard 8452A diode-array UV-vis spectrophotometer and a Horiba Fluorolog-3 Model FL3-22 spectrofluorometer (double-grating excitation and double-grating emission monochromator) was used to measure steady-state emission spectra. Time-correlated single-photon counting (TCSPC) fluorescence lifetime measurements were obtained with a NanoLED-370 (λ_{ex} = 369 nm) excitation source and a DataStation Hub as the SPC controller. Analysis of lifetime data was done using DataStation v2.4 software from Horiba Jobin Yvon. Fluorescence quantum yields, ϕ_F, in CH_2Cl_2 were calculated versus a standard of dilute quinine sulfate solution in 0.1M H_2SO_4 using a previously described method[25] and the following values: ϕ_F quinine sulfate in 0.1M H_2SO_4 = 0.54,[26] n_D[27] 0.1M H_2SO_4 = 1.33, n_D[27] CH_2Cl_2 = 1.424. Optically dilute CH_2Cl_2 solutions (absorbances <0.1 AU) of all samples were prepared in 1 cm path length quartz cuvettes. To measure the solid-state quantum yield, a F-3029 Quanta-Φ Integrating Sphere from Horiba Scientific was used and data were analyzed using FluorEssence software. A Laurel Technologies WS-65OS spin-coater was used to fabricate polystyrene (PS) films for dye loading and polarity studies. Differential scanning

calorimetry (DSC) was performed on the pristine powders using a TA Instruments 2920 Modulated DSC. Data were analyzed using the Universal Analysis Software V 2.3 from TA Instruments. Thermograms were recorded using the standard mode and a constant heating rate of 5 ºC/min. A cooling rate of 10 ºC/min was used during the initial cycle compared to a cooling rate of 1 ºC/min for subsequent cycles. Powder x-ray diffraction (XRD) patterns were obtained using a Panalytical X'Pert Pro MPD diffractometer operating at 40 kV and 40 ma using Cu Kα radiation.

Single Crystal Analysis. Single crystals of PH, PC3, and PC5 for XRD analysis were grown by vapor diffusion of hexanes into a concentrated THF solution. The crystallographic data for PC1 has been previously reported. Data sets were obtained using a Bruker Kappa Duo CCD diffractometer at −120 ºC using Mo Kα radiation. Data obtained from single crystal XRD was analyzed with Mercury 3.9 software from the Cambridge Crystallographic Data Centre. Crystal data of PH follow the monoclinic space group P21/c, a = 7.3484(10) Å, b = 22.855(3) Å, c = 9.6250(13) Å, β = 102.525(2) º, Z = 4, V = 1578.0(4) Å^3. The structure was solved using the charge flipping method in Bruker SHELXTL program and refined to R = 0.0523 using 6683 reflections with *I > 2σ(I)*. Crystal data of PC3 follow the monoclinic space group P21/n, a = 9.1276(6) Å, b = 15.3317(10) Å, c = 13.5716(9) Å, β = 102.751(1) º, Z = 4, V = 1852.4(2) Å^3. The structure was solved using the charge flipping method in Bruker SHELXTL program and refined to R = 0.0627 using 7538 reflections with *I > 2σ(I)*. Crystal data of PC3 follow the triclinic space group P-1, a = 10.8234(16) Å, b = 10.8522(16) Å, c = 18.235(3) Å, β = 92.755(3) º, Z = 4, V = 2087.6(6) Å^3. The structure was solved using the charge flipping method in Bruker SHELXTL program and refined to R = 0.0922 using 11053 reflections with *I > 2σ(I)*.

Preparation of Thin Films. Spin cast films for ML analysis were made by applying 20 drops of a dye stock solution in dichloromethane (0.018 M) to microscope coverglass rotating at

3000 rpm. Samples were dried under vacuum for 20 min prior to annealing phenyl and naphthyl derivatives at 75 ºC and 85 ºC for 10 min. In most cases, green emission remained after annealing, so films were gently smeared with a Kimwipe, followed by annealing at 75 ºC or 85 ºC depending on the film for another 10 min to produce uniform blue emission. Mechanical perturbation of films was done through gentle smearing with a cotton swab. Films for video analysis and emission measurements of melted and crystalline phases were fabricated by adding dye (~ 50 mg) to microscope coverglass and melting using a hot plate. Once melted films were immediately removed from heat and cooled in air. Shear induced crystallization properties were investigated by rubbing films with wooden dowel repeatedly for up to 2 min or until a color change was observed.

Video Analysis. Videos were recorded at room temperature using a PGR GS3-U3-41C6C-C video camera with a complementary metal oxide semiconductor CMOS chip capable of 90 frames per second (FPS) at a maximum resolution of 2048x2048 pixels. The camera was also equipped with a Spacecom f/0.95 50 mm lens and an Edmund Optics 425 nm long pass filter to minimize excitation background. The camera was operated with a Lenovo W530 laptop connected *via* a USB 3.0 cable. Point Grey FlyCap2 software was used to record videos of films. The camera was placed approximately 0.5 m above the sample, which was illuminated with a 100W Black-Ray B-100AP/R lamp at 365 nm located ~10 cm above the sample.

7.4 Acknowledgements

7.5 References

1   T. Butler, M. Alexander S., S. Michal and C. L. Fraser, *ACS Appl. Mater. Interfaces*, 2017, **Submitted**.

2   T. Butler, W. A. Morris, J. Samonina-Kosicka and C. L. Fraser, *ACS Appl. Mater. Interfaces*, 2016, **8**, 1242–1251.

3   B. C. Hancock and M. Parks, *Pharm. Res.*, 2000, **17**, 397–404.

4   S. Karasawa, R. Hagihara, Y. Abe, N. Harada, J. Todo and N. Koga, *Cryst. Growth Des.*, 2014, **14**, 2468–2478.

5   Y. Shirota, *J. Mater. Chem.*, 2005, **15**, 75–93.

6   Y. Shirota and H. Kageyama, *Chem. Rev.*, 2007, **107**, 953–1010.

7   K. Chung, M. S. Kwon, B. M. Leung, A. G. Wong-Foy, M. S. Kim, J. J. Kim, S. Takayama, J. Gierschner, A. J. Matzger and J. J. Kim, *ACS Cent. Sci.*, 2015, **1**, 94–102.

8   Y. Ren, J. Lee, K. M. Hutchins and J. S. Sottos, Nancy R, Moore, *Cryst. Growth Des.*, 2016, **16**, 6148–6151.

9   F. H. Stillinger, *Science*, 1995, **267**, 1935–1939.

10   P. G. Debenedetti, *Metastable Liquids: Concepts and Principles*, Princeton University Press, Princeton, N. J., 1996.

11   C. M. Whitaker and R. J. McMahon, *J. Phys. Chem.*, 1996, **100**, 1081–1090.

12   W. A. Morris, M. Sabat, T. Butler, C. A. DeRosa and C. L. Fraser, *J. Phys. Chem. C*, 2016, **120**, 14289–14300.

13   N. D. Nguyen, G. Zhang, J. Lu, A. E. Sherman and C. L. Fraser, *J. Mater. Chem.*, 2011, **21**, 8409–8415.

14   G. Zhang, R. E. Evans, K. A. Campbell and C. L. Fraser, *Macromolecules*, 2009, **42**,

8627–8633.

15   W. A. Morris, M. Kolpaczynska and C. L. Fraser, *J. Phys. Chem. C*, 2016, **120**, 22539–22548.

16   C. A. DeRosa, C. Kerr, Z. Fan, M. Kolpaczynska, A. S. Mathew, R. E. Evans, G. Zhang and C. L. Fraser, *ACS Appl. Mater. Interfaces*, 2015, **7**, 23633–23643.

17   J. Samonina-Kosicka, C. A. DeRosa, W. A. Morris, Z. Fan and C. L. Fraser, *Macromolecules*, 2014, **47**, 3736–3746.

18   M. W. Barsoum, *Fundamentals of Ceramics*, CRC Press, 2002.

19   P. G. Debenedetti and F. H. Stillinger, *Nature*, 2001, **410**, 259–267.

20   S. Varghese and S. Das, *J. Phys. Chem. Lett*, 2011, **2**, 863–873.

21   T. Liu, A. D. Chien, J. Lu, G. Zhang and C. L. Fraser, *J. Mater. Chem.*, 2011, **21**, 8401–8408.

22   W. A. Morris, T. Liu and C. L. Fraser, *J. Mater. Chem. C*, 2015, **3**, 352–363.

23   W. A. Morris, M. Sabat, T. Butler, C. A. DeRosa and C. L. Fraser, *J. Phys. Chem. C*, 2016, **120**, 14289–14300.

24   J.-C. C. Hubaud, I. Bombarda, L. Decome, J.-C. C. Wallet and E. M. Gaydou, *J. Photochem. Photobiol. B Biol.*, 2008, **92**, 103–109.

25   J. N. Demas and G. A. Crosby, *J. Phys. Chem.*, 1971, **75**, 991–1024.

26   H. Zhu, X. Wang, Y. Li, Z. Wang, F. Yang and X. Yang, *Chem. Commun.*, 2009, **0**, 5118–5120.

27   Y. L. Chow, C. I. Johansson, Y.-H. Zhang, R. Gautron, L. Yang, A. Rassat and S.-Z. Yang, *J. Phys. Org. Chem.*, 1996, **9**, 7–16.

Chapter 8

Future Directions

8.1 Color Tuning of β-Diketonate Materials

8.1.1 Summary of Color Tuning Studies

The main focus of this work has been to establish the structure property relationships and processing effects (e.g. substrate, thickness) that govern the stimuli responsive properties of β-diketone materials and their boronated counterparts. This was accomplished through a combination of computational and experimental investigations of solution (i.e. solvatochromism), aggregation induced emission (AIE) and solid-state (e.g. thermo- and mechanochromic responses) properties. Boron coordination and donor and acceptor effects were used to generate thermo and mechano responsive materials with wide ranging colors in both crystalline and amorphous states. Further studies of matrix effects (i.e. increasing polarity and dye aggregation) were performed using polystyrene films and variable dye loadings. These studies indicated that both aggregation and matrix polarity were responsible for changes in emission. Additionally, bdk and BF_2bdk dyes with 3,4,5-trimethoxy-substituted phenyl rings displayed enhanced AIE and ML responses. These findings can inform materials design and adaptation for specific applications.

8.1.2 Methoxy Substitution to Tune Emission of Oxygen Sensing Polymers

Our lab discovered that BF_2bdk dyes exhibit oxygen sensitive room temperature phosphorescence when imbedded in a poly(lactic-acid) (PLA) matrix.[1] These materials can be fabricated as nanoparticles and utilized as oxygen sensors in biological systems.[2] For example, topical application of nanoparticles enables the monitoring of wound healing in mouse models.[3] While these boron PLA materials enable oxygen sensing in biological systems, relatively short emission wavelengths lead to scattering losses and interference from tissue autofluorescence. Therefore, material performance may be enhanced by redder wavelengths.

In this work, a common strategy for tuning the optical properties of solid bdk and BF$_2$bdk materials involved substitution of dyes with electron donating methoxy groups. This allowed for energy modulation of the frontier molecular orbitals that determine the emission. In order to systematically tune the energy of BF$_2$bdk materials and produce red-shifted fluorescence and phosphorescence, a series of dyes with varying degrees of methoxy substitution were synthesized and blended into PLA matrices to investigate phosphoresce (Figure 8.1). The absorption and emission properties of each film were observed in air and nitrogen in order to probe the effects of methoxy substitution on both fluorescence and phosphorescence, respectively. Computational studies were also performed in order to gauge how the energy of participating molecular orbitals were affected by the position and degree of methoxy substitution. Initial results show that this strategy may be effective for redshifting emission in these materials, however further study is merited to optimize the emission of oxygen sensitive boron/PLA materials.
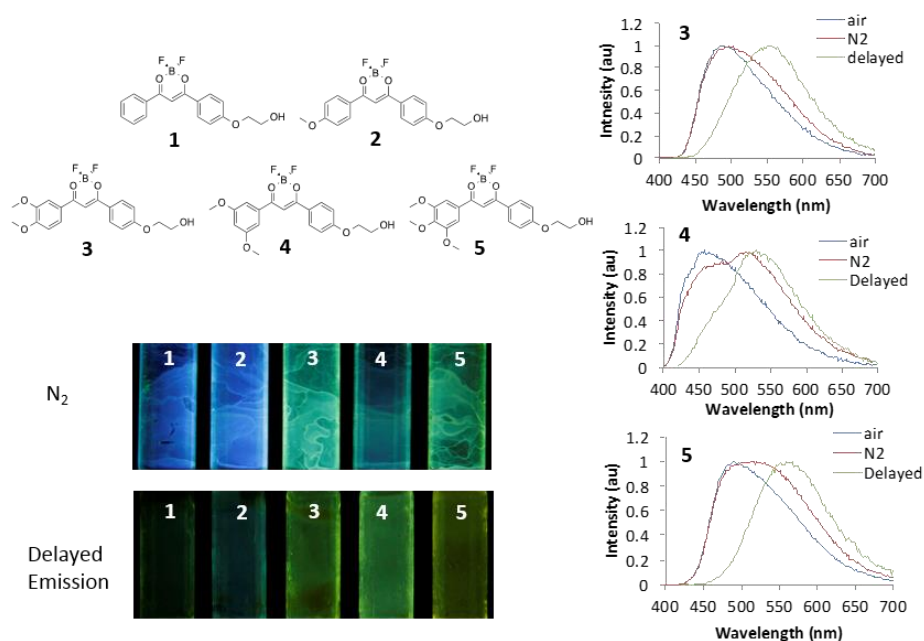
Figure 8.1. Emission properties of methoxy-substituted boron dyes imbedded in a poly(lactic-acid).

8.2 Substrate and Thickness Effects

In addition to tuning emission wavelength and enhancing mechanically responsive properties, some trimethoxy substituted derivatives exhibited rapid smeared state decay at room temperature. To measure recovery and explore substrate and thickness effects, a novel detection tool utilizing an RGB camera was developed. Using this method, heat maps of smeared films where generated to show that thick films exhibited faster recovery times compared to thinner samples regardless of substrate. However, small differences in smeared state decay were observed for films with similar thicknesses on different substrates. These preliminary studies point to a potential substrate effect on the ML recovery which could be further examined through the use of functionalized substrates. For example, films with the same thickness could be prepared on substrates functionalized with different surfactants (e.g. sodium sulfate (SDS) sodium dodecylbenzenesulfonate (SDBS), sodium dodecanoate (SDC), sodium cholate (SC) and sodium deoxy cholate (SDeC)) in order to form self-assembled monolayers which could facilitate or inhibit smeared state decay.[4] The color of these rapidly decaying materials could also be modulated using donor and acceptor effects similar to those discussed in this work.

8.3 Supercooled Liquids

8.3.1 Summary of Supercooled Liquid Investigations

Certain 3,4,5-trimethoxy derivatives formed supercooled liquid states when melted and rapidly cooled in air. The duration of these metastable amorphous states was tunable via arene substitution and alkoxy chain length effects. A correlation between the torsion angle of the para-methoxy group and the stability of the supercooled liquid was also observed for phenyl substituted derivatives. Furthermore, some of the samples showed shear induced crystallization which resulted in blue-shifted emission. These dyes could find use in various practical applications, for example

force sensing supercooled liquids developed by Kim et al. have shown the shear triggered crystallization through live cell attachment.

8.3.2 Future Investigation of Supercooled Liquid Materials

To tune the thermal stability of bdk supercooled liquids, and induce more rapid crystallization, the methoxy groups on both sides of these dyes could be replaced with alkoxy chains of varying length. Furthermore, substitution of the trimethoxy-substituted dye with –OH groups could introduce H-bonding capability and affect thermal and optixal properties in supercooled liquid phases. Additionally, aromatic groups could be replaced with other arenes (e.g. biphenyl, fluorenyl, phenanthryl, thienyl, pyridyl, oxadiazolyl) to modulate crystallization, emission and molecular rigidity. These factors have been linked to glass transition temperatures (T_g) in amorphous solids, an important parameter in determining their properties.[5] Further substitution of these dyes with donor and acceptor groups could also help to tune emission in trimethoxy-substituted supercooled liquids.

8.4 Conclusions

Throughout this work, design strategies have been presented to tune the optical properties of β-diketones and boronated complexes. It has been shown that emission can be tuned using a combination of donor and acceptor effects and BF_2 coordination. Furthermore, mechanistic investigations have shown that both aggregation and matrix polarity determine solid state emission. It has been shown that thermal and mechanical stimuli can be used to ellicit emission changes β-diketones. Using the principles described herein, the emission of dyes can be tailored depending on the requirements of a given application.

It was also discovered in this work that trimethoxy substitution can be used to imbue dyes with a variety of interesting properties. For example, thin films of certain dyes exhibited rapid self-

erasing at room temperature that was substrate and thickness dependent. Incorporation of this motif in uncoordinated dyes and boronated complexes was also used to promote aggregation induced emission and mechanochromic responses. These properties were attributed to the para-substituted methoxy group forced out of plane through steric crowding by neighboring methoxy substituent effects. Trimethoxy dyes also exhibited stable supercooled liquid phases when melted and cooled at room temperature. The stability was tunable using both arene size and alkoxy chain length. In some cases, crystallization can be observed upon the application of mechanical stimuli. This resulted in a high-energy emission shift that was previously unobserved in stimuli responsive β-diketones. The results described here, demonstrate the multipurpose optical properties of easily synthesized materials which can bet altered for specific applications from commercially available starting materials.

8.5 References

1   G. Zhang, J. Chen, S. J. Payne, S. E. Kooi, J. N. Demas and C. L. Fraser, *J. Am. Chem. Soc.*, 2007, **129**, 8942–8943.

2   G. Zhang, G. M. Palmer, M. W. Dewhirst and C. L. Fraser, *Nat. Mater.*, 2009, **8**, 747–751.

3   C. A. DeRosa, S. A. Seaman, A. S. Mathew, C. M. Gorick, Z. Fan, J. N. Demas, S. M. Peirce and C. L. Fraser, *ACS Sensors*, 2016, **1**, 1366–1373.

4   D. Kiriya, K. Chen, H. Ota, Y. Lin, P. Zhao, Z. Yu, T. J. Ha and A. Javey, *J. Am. Chem. Soc.*, 2014, **136**, 11188–11194.

5   Y. Shirota and H. Kageyama, *Chem. Rev.*, 2007, **107**, 953–1010.

Appendix A:

Chapter 2 Supporting Information

Synthesis of dnmOMe. The ligand dnmOMe was prepared by Claisen condensation of 2-acetyl-6-methoxynaphthalene (0.543 g, 2.71 mmol) and methyl-2-naphthoate (0.626 g, 3.40 mmol) in the presence of NaH. The reactants were dissolved in THF (50 mL) prior to the dropwise addition of a NaH/THF (10 mL) suspension under N_2. The reaction was heated to 60 °C and stirred for 20 h before quenching with 1 mL of a saturated $NaHCO_3$ solution (aq). Aqueous phases were extracted with CH_2Cl_2 (3 x 50 mL) and combined organic layers were washed with a dilute HCl solution (3 x 50 mL) and brine (10 mL). Organic layers were dried over Na_2SO_4 prior to the removal of solvent. The ligand dnmOMe was recrystallized twice from 1:1 hexanes/acetone mixture and recovered was recovered as a white powder (0.228 g, 24%). ^{1}H NMR (500 MHz, DMSO-d6) δ 17.36 (s, 1H, -OH) 8.87 (s, 1H, 1″-ArH) 8.82 (s, 1H, 1′-ArH) 8.25 (d, J = 9, 1H, 4″-ArH) 8.22 (d, J = 9, 1H, 4′-ArH) 8.15 (d, J = 9, 1H, 3″-ArH) 8.10-8.01 (m, 3H, 8″,5″,8′-ArH) 7.98 (d, J = 9, 1H, 3′-ArH) 7.68-7.63 (m, 3H. 7″,6″-ArH, COCHCO) 7.45 (s, 1H, 5′-ArH) 7.28 (d, J = 9, 1H, 7′-ArH); ^{13}C NMR (600 MHz, CDCl$_3$) δ 186.01, 184.80, 159.56, 135.26, 132.87, 132.78, 130.98, 130.71, 129.34, 128.44, 128.27, 128.21, 128.15, 128.06, 127.76, 127.19, 126.76, 123.99, 123.27, 119.76 105.75, 93.40, 55.42; HRMS (ESI, TOF): m/z calculated for $C_{24}H_{19}O_3$ 355.13; found 355.13 $[M+H]^+$.

Full Computational Details

The compound dnmOMe was modeled using the Gaussian 09 suite of programs[1] utilizing density functional theory (DFT). We chose B3LYP/6-31G(d) for ground state geometry optimization with a Tomasi polarized continuum for dichloromethane solvent.[2] The vibrational frequencies for the optimized geometries were calculated in an additional calculation also utilizing B3LYP/6-31G(d). All vibrational frequencies were positive, assuring that the geometries were at least a local minimum. Single point energy calculations were used to generate the molecular orbital diagrams utilizing B3LYP/6-31G(d). Time-dependent density functional theory (TD-DFT), TD-B3LYP/6-31+G(d) was used for estimates of the absorption spectra at the respective optimized geometries.[3,4] The first three excited states were computed for dnmOMe. Molecular orbitals were depicted by GaussView 5 software.[5]

Gaussian 09 Specifications for dnmOMe in CH$_2$Cl$_2$ Solvent. B3LYP/6-31G(d) optimized structure for future TD-DFT calculation in dichloromethane. Coordinates are given in Cartesian, in Angstroms.

E (HF) = -1151.09786328. μ (Debye) = 4.1691
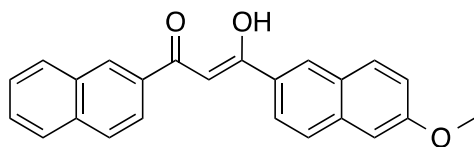
O, -2.125439, 2.230985, -0.305982
C, -2.078267, 0.96992, -0.222565
C, -0.822312, 0.273779, -0.17245
H, -0.806001, -0.79652, -0.038154
O, 0.388785, 2.292695, -0.343117
C, 0.375192, 0.965014, -0.235274
C, 1.705332, 0.337839, -0.181029
C, 2.831691, 1.136928, -0.045294
C, 1.875408, -1.078695, -0.263699
C, 4.130421, 0.579899, 0.022269
H, 2.717742, 2.21407, 0.016984
C, 3.12234, -1.645668, -0.204027

H, 1.011621, -1.721128, -0.394871
C, 4.292272, -0.843686, -0.056243
C, 5.290796, 1.384475, 0.166672
H, 3.232936, -2.72449, -0.275264
C, 5.587337, -1.398444, 0.009933
C, 6.548503, 0.826772, 0.229892
H, 5.177533, 2.463774, 0.227388
C, 6.701895, -0.584399, 0.150567
H, 5.725583, -2.474133, -0.048806
H, 7.414073, 1.469085, 0.339711
C, -3.365226, 0.213919, -0.156686
C, -3.443425, -1.197926, -0.337421
C, -4.529999, 0.924715, 0.084255
C, -4.651904, -1.849134, -0.269154
H, -2.548627, -1.770284, -0.556228
C, -5.788717, 0.282051, 0.169203
H, -4.468905, 2.000649, 0.214549
C, -5.856305, -1.139099, -0.010272
H, -4.699815, -2.924919, -0.418142
C, -6.988291, 1.003036, 0.426083
C, -7.119384, -1.783029, 0.072911
C, -8.197612, 0.34936, 0.50099
H, -6.93224, 2.080227, 0.561604
C, -8.263043, -1.056008, 0.322788
H, -7.169528, -2.860388, -0.063985
H, -9.10844, 0.907974, 0.697052
H, -9.224034, -1.559109, 0.384582
O, 7.906078, -1.215808, 0.204614
C, 9.091175, -0.434278, 0.348152
H, 9.914491, -1.149553, 0.366187
H, 9.224349, 0.25108, -0.497098
H, 9.084744, 0.135346, 1.284818
H, -0.588134, 2.571294, -0.342049

Characterization of Spectrum Computed in Solvent Dichloromethane (PCM-Tomasi as implemented in Gaussian).

Note: Max amplitude is 0.70714 for a pure one-electron excitation. The highest occupied molecular orbital (HOMO) to the lowest unoccupied molecular orbital (LUMO) transitions are in bold.
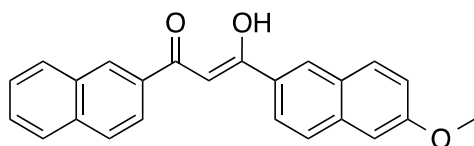
Excited State   1:   Singlet-A   3.0005 eV 413.21 nm f=0.9707 <S**2>=0.000
   93 -> 94   0.69887

Excited State 2:   Singlet-A   3.2780 eV 378.23 nm f=0.0601 <S**2>=0.000
   92 -> 94   0.69187

Excited State 3:   Singlet-A   3.5607 eV 348.20 nm f=0.3753 <S**2>=0.000
   91 -> 94   0.67509
   93 -> 96   0.12882

Gaussview traces of computed TD-B3LYP/6-31+G(d) absorption spectra for dnmOMe in CH_2Cl_2 represented by Tomasi's Polarizable Continuum Model.
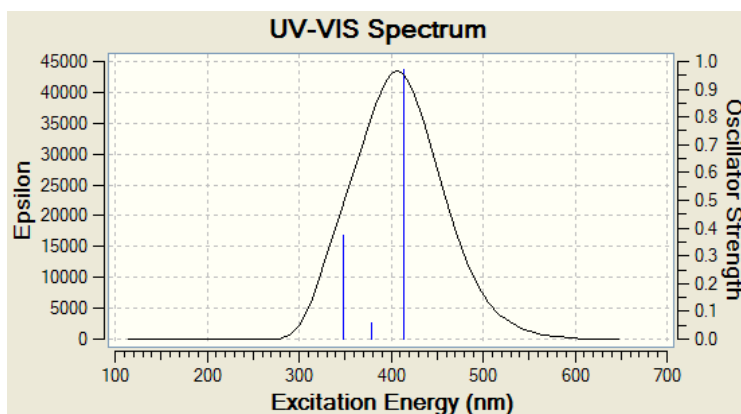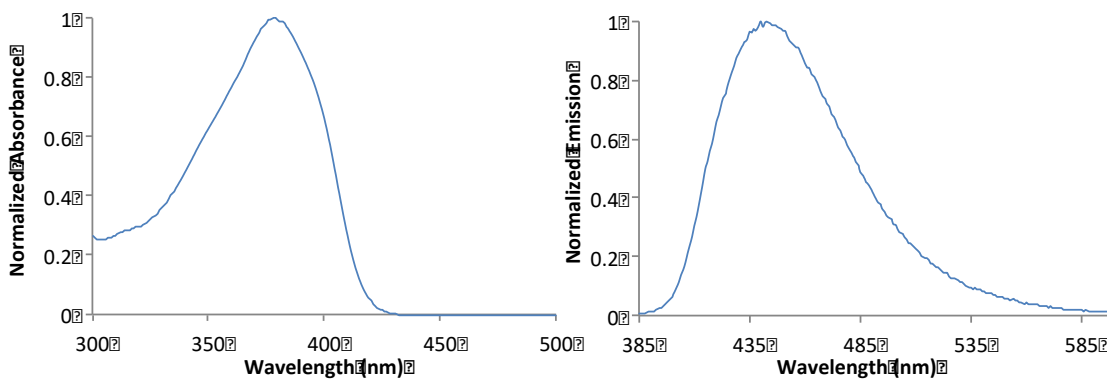
Figure S2.1. Absorption (left) and emission (right) of dnmOMe in CH_2Cl_2.
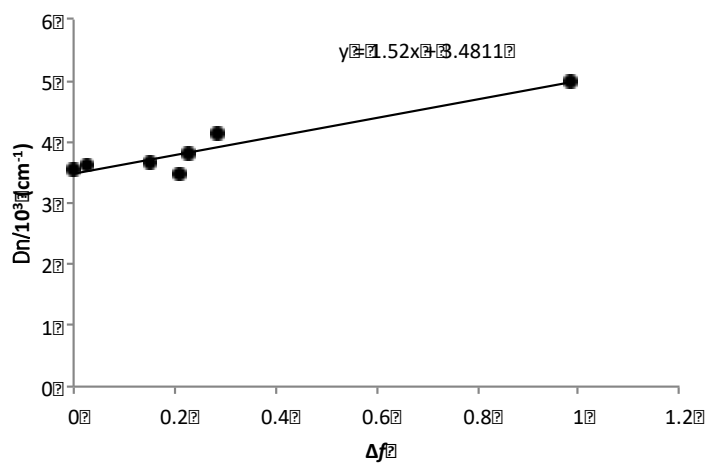
Figure S2.2. Lippert-Mataga plot of dnmOMe solvatochromism.
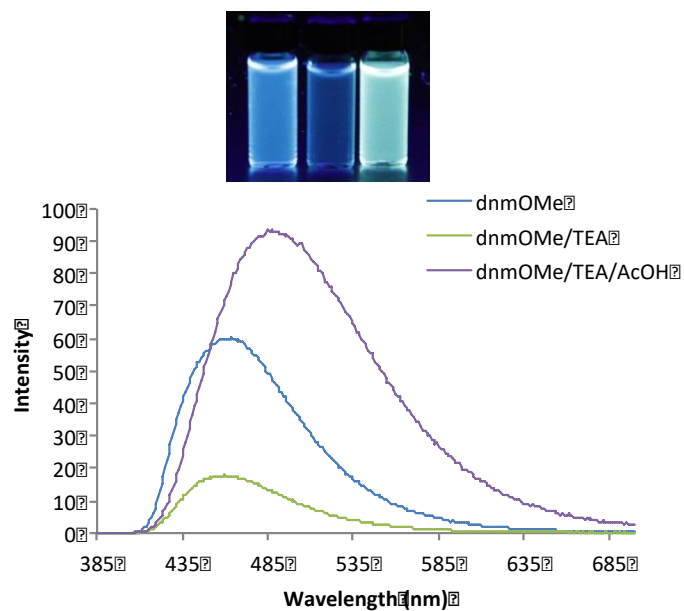
Figure S2.3. Solutions of dnmOMe in CH₃CN, CH₃CN/TEA, and CH₃CN/TEA/acetic acid, respectively (top). Emission spectra of solutions (bottom).
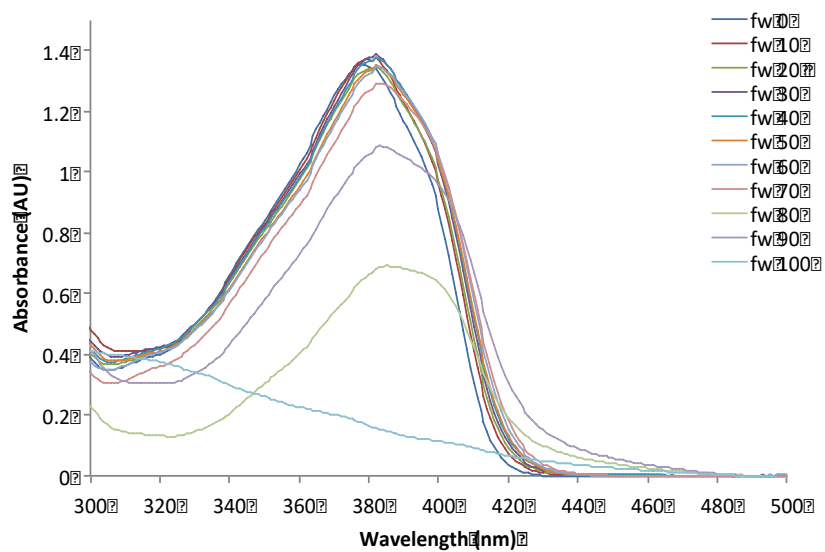
Figure S2.4. Absorption spectra of dnmOMe in THF/H₂O solutions.
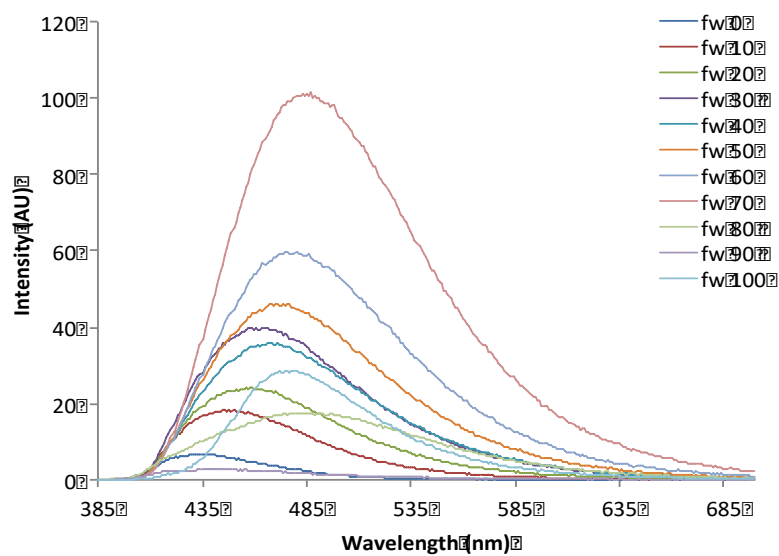
Figure S2.5. Emission spectra of dnmOMe in THF/H$_2$O solutions (λ_{ex} = 369 nm).
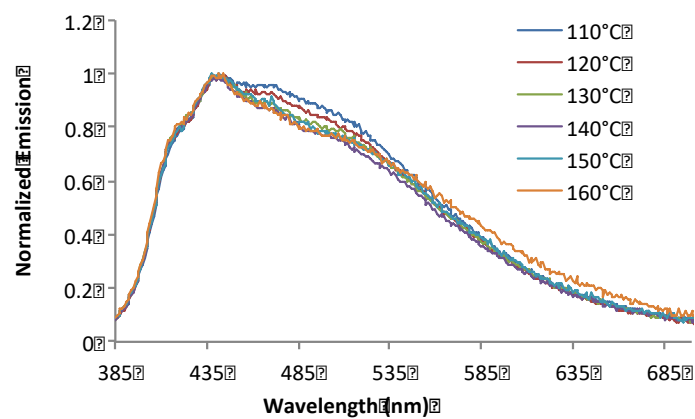
Figure S2.6. Emission spectra of dnmOMe annealed at different temperature.
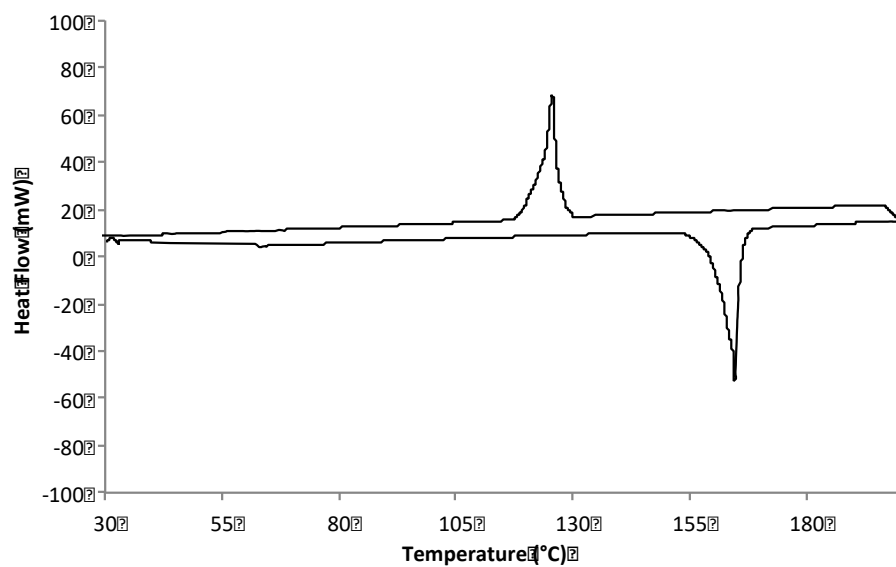
Figure S2.7. DSC thermogram of dnmOMe.
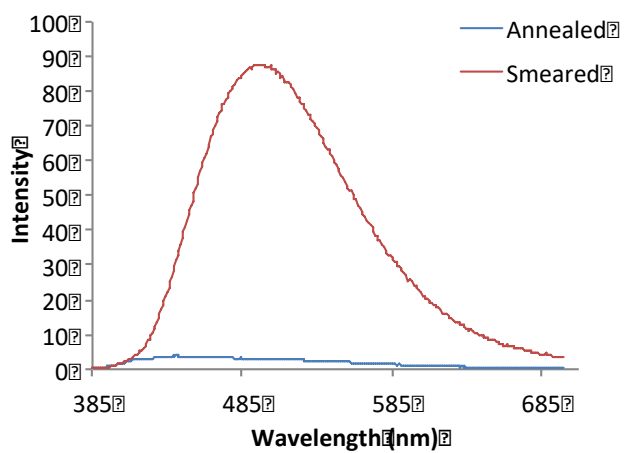
Figure. S2.8. Total emission spectra of dnmOMe thin films in smeared and annealed states.
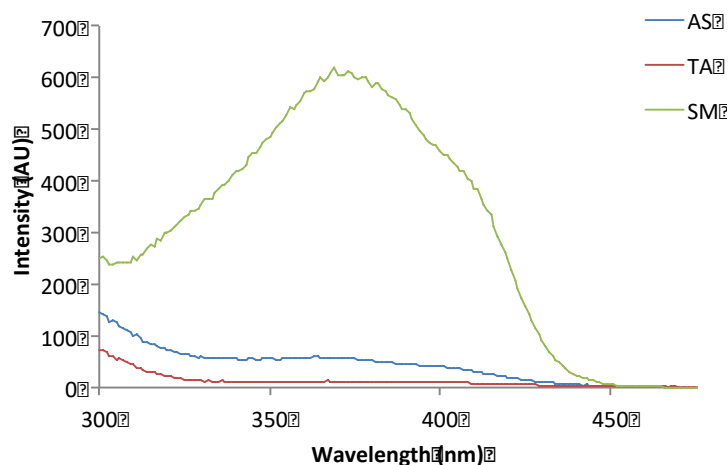
Figure S2.9. Excitation spectra of dnmOMe in AS, TA and SM states monitored at 504 nm.

References

1. M. J. Frisch, G. W Trucks, H. B. Schlegel, G. E. Scuseria, M. A. Robb, J. R. Cheeseman, G. Scalmani, V. Barone, B. Mennucci, G. A. Petersson, H. Nakatsuji, M. Caricato, X. Li, H. P Hratchian, A. F. Izmaylov, J. Bloino, G. Zheng, J. L. Sonnenberg, M. Hada, M. Ehara, K. Toyota, R. Fukuda, J. Hasegawa, M. Ishida, T. Nakajima, Y Honda, O Kitao, H. Nakai, T. Vreven, J. A. Montgomery, J. E. Peralta, F. Ogliaro, M. Bearpark, J. J. Heyd, E. Brothers, K. N. Kudin, V. N. Staroverov, R. Kobayashi, J. Normand, K. Raghavachari, A. Rendell, J. C. Burant, S. S. Iyengar, J. Tomasi, M. Cossi, N. Rega, J. M. Millam, M. Klene, R. E. Knox, J. B. Cross, V. Bakken, C. Adamo, J. Jaramillo, R. Gomperts, R. E. Stratmann, O. Yazyev, A.J. Austin, R. Cammi, C. Pomelli, J.W. Ochterski, J. J. Martin, K. Morokuma, V. G. Zakrzewski, G. A. Voth, P. Salvador, J. J Dannenberg, S. Dapprich, A. D. Daniels, A. Farkas, J. B. Foresman, J. Ortiz, J. Cioslowski, D. J. Fox, Wallingford CT, 2009.

2. J. Tomasi, B. Mennucci, R. Cammi, *Chem. Rev.* 2005, **105**, 2999.

3. A. D. Becke, *J. Chem. Phys.* 1993, **98**, 1372.

4. C. Lee, W. Yang, R. G. Parr, *Phys. Rev. B* 1988, **37**, 785.

5. R. Dennington, T. Keith, 5th Ed.; Semichem Inc.: Shawnee Mission, KS, 2009.

Appendix B

Chapter 3 Supporting Information

DnmBr. Tan powder: 0.607 g, 46%. ^{1}H NMR (300 MHz, DMSO-d6) δ 17.26 (s, 1H, ArCOH), 8.90-8.89 (m, 2H, 1″,1′-ArH), 8.35 (s, 1H, 5′-ArH), 8.31 (d, J = 9, 1H, 4″-ArH), 8.25 (d, J = 9, 1H, 4′-ArH), 8.16-8.08 (m, 4H, 8′,8″,7′-ArH, COCHCO), 8.04 (d, J = 9, 5″-ArH), 7.77 (d, J = 9, 1H, 3″-ArH) 7.71-7.62 (m, 3H, 7″,6″,3′-ArH). HRMS (ESI, TOF): m/z calculated for $C_{23}H_{16}O_2Br$ 403.0327; found 403.0334 [M+H].

DnmBrOMe. Brown powder: 0.455 g, 37%. ^{1}H NMR (300 MHz, DMSO-d6) δ 17.50 (s, 1H, ArCOH), 8.87 (s, 1H, 1″-Ar*H*), 8.81 (s, 1H, 1′-ArH), 8.33 (s, 1H, 5′-ArH), 8.29 (d, J = 9, 1H, 4″-ArH), 8.20 (s, J = 9, 1H, 4′-ArH), 8.12-8.03 (m, 3H, 8′, 8″, 5′-ArH), 7.98 (d, J = 9, 1H, 3′-ArH), 7.77 (d, J = 9, 1H, 7′-ArH), 7.62 (s, 1H, COCHCO), 7.44 (s, 1H, 5′-ArH), 7.29 (d, 1H, 7″-ArH), 3.92 (s, 3H, OCH$_3$). HRMS (ESI, TOF): m/z calculated for $C_{24}H_{18}O_3Br$ 433.0445; found 433.0439 [M+H].

BF₂dnmOMe. Yellow powder: 0.145 g, 42%. ^{1}H NMR (300 MHz, DMSO-d6) δ 9.13 (s, 1H, 1″-ArH), 9.10 (s, 1H, 1′-ArH), 8.40-8.38 (m, 2H, 4″,4′-ArH), 8.24 (d, J = 9, 1H, 3″-ArH), 8.20-8.15 (m, 4H, 7″,7′,3′-ArH, COCHCO), 8.10-8.04 (m, 2H, 8″,8′-ArH), 7.79-7.70 (m, 1H, 6′-ArH), 7.52 (s, 1H, 5″-ArH), 7.34 (d, J = 9, 1H, 5′-ArH), 3.95 (s, 3H, OCH$_3$). HRMS (ESI, TOF): m/z calculated for $C_{24}H_{17}BO_3F$ 383.1255; found 383.1255 [M-F].

BF₂dnmBr. After recrystallization (2×) from 1:1 acetone/THF, a yellow solid was obtained: 0.078 g, 17%. ^{1}H NMR (500 MHz, DMSO-d6) δ 9.18 (s, 2H, 1″,1′-ArH), 8.47 (d, J = 9, 1H, 4″-ArH),

8.42-8.39 (m, 2H, COCHCO, 4′-ArH), 8.23-8.17 (m, 5H, 8″,8′,5″,3″,3′-ArH), 8.11 (d, J = 9, 1H, 5′-ArH), 7.86 (d, J = 9, 1H, 7′-ArH), 7.79 (t, J = 5, 1H, 7″-ArH), 7.72 (t, J = 5, 1H, 6″-ArH). HRMS (ESI, TOF): m/z calculated for $C_{23}H_{14}BO_2FBr$ 431.0254; found 431.0260 [M-F].

BF₂dnmBrOMe. After recrystallization (3×) from toluene, an orange powder was obtained: 0.038 g, 11% yield. ^{1}H NMR (500 MHz, DMSO-d6) δ 9.13 (s, 1H, 1″-ArH), 9.10 (s, 1H, 1′-ArH), 8.46-8.36 (m, 3H, COCHCO, 4″,4′-ArH), 8.21-8.16 (m, 2H, 8″,5″-ArH), 8.07 (d, 1H, J = 9, 8′-ArH), 7.85 (d, J = 9, 1H, 3″-ArH) 7.52 (s, 1H, 5′-ArH), 7.36 (d, J = 9, 1H, 3″-ArH), 7.24 (d, J = 9, 1H, 7″-ArH), 7.17 (d, J = 9, 1H, 7′-ArH), 3.96 (s, 3H, OCH₃); HRMS (ESI, TOF): m/z calculated for $C_{24}H_{16}O_3BrFB$ 461.0366; found 461.0360 [M-F].

Full Computational Details

All compounds were modeled using the Gaussian 09 suite of programs[1] utilizing density functional theory (DFT). We chose B3LYP/6-31G(d) for ground state geometry optimization of the ligands with a Tomasi polarized continuum for dichloromethane solvent.[2] The vibrational frequencies for the optimized geometries were calculated in an additional calculation also utilizing B3LYP/6-31G(d). The same calculations were used for the boronated complexes except that the more flexible B3LYP/6-31+G(d) was used. Calculations performed on the ligands using B3LYP/6-31+G(d) tended to crash, possibly due to the greater degree of rotational freedom available to the ligands compared to the complexes. All vibrational frequencies were positive, assuring that the geometries were at least a local minimum. Single point energy calculations were used to generate the molecular orbital diagrams utilizing B3LYP/6-31G(d) for both the ligands and the boronated complexes. Molecular orbitals were depicted by GaussView 5 software.[3]

Gaussian 09 Specifications for all ligands and compounds in CH₂Cl₂ Solvent. B3LYP/6-31G(d) optimized structure for ligands and B3LYP/6-31+G(d) for boron compounds. Coordinates are given in Cartesian, in Angstroms. Molecular Orbitals were depicted by GaussView 5 software.[6]
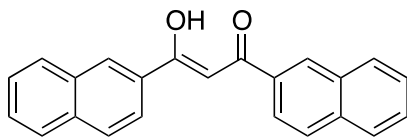
E (HF) = -1036.57373317. μ (Debye) = 4.0879

O, -2.125439, 2.230985, -0.305982
C, -2.078267, 0.96992, -0.222565
C, -0.822312, 0.273779, -0.17245
H, -0.806001, -0.79652, -0.038154
O, 0.388785, 2.292695, -0.343117
C, 0.375192, 0.965014, -0.235274
C, 1.705332, 0.337839, -0.181029
C, 2.831691, 1.136928, -0.045294
C, 1.875408, -1.078695, -0.263699
C, 4.130421, 0.579899, 0.022269
H, 2.717742, 2.21407, 0.016984
C, 3.12234, -1.645668, -0.204027
H, 1.011621, -1.721128, -0.394871
C, 4.292272, -0.843686, -0.056243
C, 5.290796, 1.384475, 0.166672
H, 3.232936, -2.72449, -0.275264
C, 5.587337, -1.398444, 0.009933
C, 6.548503, 0.826772, 0.229892
H, 5.17753, 2.463774, 0.227388
C, 6.701895, -0.584399, 0.150567
H, 5.725583, -2.474133, -0.048806
H, 7.414073, 1.469085, 0.339711
C, -3.365226, 0.213919, -0.156686
C, -3.443425, -1.197926, -0.337421
C, -4.529999, 0.924715, 0.084255
C, -4.651904, -1.849134, -0.269154
H, -2.548627, -1.770284, -0.556228
C, -5.788717, 0.282051, 0.169203
H, -4.468905, 2.000649, 0.214549
C, -5.856305, -1.139099, -0.010272
H, -4.699815, -2.924919, -0.418142

C, -6.988291, 1.003036, 0.426083
C, -7.119384, -1.783029, 0.072911
C, -8.197612, 0.34936, 0.50099
H, -6.93224, 2.080227, 0.561604
C, -8.263043, -1.056008, 0.322788
H, -7.169528, -2.860388, -0.063985
H, -9.10844, 0.907974, 0.697052
H, -9.224034, -1.559109, 0.384582
O, 7.906078, -1.215808, 0.204614
C, 9.091175, -0.434278, 0.348152
H, 9.914491, -1.149553, 0.366187
H, 9.224349, 0.25108, -0.497098
H, 9.084744, 0.135346, 1.284818
H, -0.588134, 2.571294, -0.342049

E (HF) = -1151.09785731. μ (Debye) = 4.1695

O, -2.125551, 2.231039, -0.307715
C, -2.078278, 0.969788, -0.227301
C, -0.822289, 0.273422, -0.181031
H, -0.80603, -0.797212, -0.049477
O, 0.388522, 2.292804, -0.348158
C, 0.375145, 0.96487, -0.242961
C, 1.705366, 0.337825, -0.189373
C, 2.831532, 1.136841, -0.051671
C, 1.875804, -1.078568, -0.272825
C, 4.130109, 0.579746, 0.018256
H, 2.717495, 2.213959, 0.010872
C, 3.122604, -1.645634, -0.210785
H, 1.01232, -1.720987, -0.406059
C, 4.292271, -0.843776, -0.05982
C, 5.290142, 1.384323, 0.16554
H, 3.233143, -2.724474, -0.281961
C, 5.587084, -1.398723, 0.010639
C, 6.547531, 0.82644, 0.233076
H, 5.176936, 2.463694, 0.225198
C, 6.701195, -0.584757, 0.155224

H, 5.725302, -2.474482, -0.046904
H, 7.412808, 1.468721, 0.345437
C, -3.365184, 0.213848, -0.159742
C, -3.444299, -1.197315, -0.34519
C, -4.528853, 0.924225, 0.087611
C, -4.652919, -1.848195, -0.275747
H, -2.550267, -1.769108, -0.568502
C, -5.787562, 0.281768, 0.174415
H, -4.466777, 1.99972, 0.221047
C, -5.856222, -1.138587, -0.010511
H, -4.701732, -2.923453, -0.428249
C, -6.98596, 1.00229, 0.437989
C, -7.119398, -1.782231, 0.07417
C, -8.195369, 0.348919, 0.5142
H, -6.929011, 2.07897, 0.577222
C, -8.261914, -1.055684, 0.330634
H, -7.170591, -2.859063, -0.066489
H, -9.105335, 0.907175, 0.715199
H, -9.222879, -1.55869, 0.393657
O, 7.90526, -1.215968, 0.215054
C, 9.089428, -0.433821, 0.363179
H, 9.912687, -1.148932, 0.388712
H, 9.22762, 0.248675, -0.483594
H, 9.077036, 0.139079, 1.297787
H, -0.588361, 2.571325, -0.345208
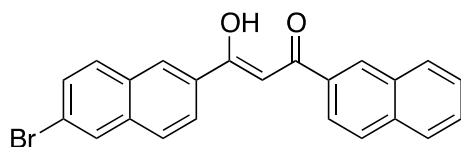
E (HF) = -3607.67847359 μ (Debye) = 4.4272

O, 0.48297, 2.459215, -0.320527
C, 0.396929, 1.2005, -0.25493
C, 1.572894, 0.375799, -0.192347
H, 1.47742, -0.692209, -0.073903
O, 2.992545, 2.259062, -0.30482
C, 2.835041, 0.940131, -0.220447
C, 4.092398, 0.173341, -0.147343
C, 5.285179, 0.84395, 0.079874
C, 4.115206, -1.245057, -0.303222

C, 6.517507, 0.151556, 0.172125
H, 5.277802, 1.922384, 0.197336
C, 5.295704, -1.940547, -0.22198
H, 3.196902, -1.783335, -0.510265
C, 6.528982, -1.273622, 0.020302
C, 7.744529, 0.830189, 0.41156
H, 5.30028, -3.019943, -0.349698
C, 7.765103, -1.965001, 0.112137
C, 8.92782, 0.130958, 0.495899
H, 7.731214, 1.911127, 0.526036
C, 8.93765, -1.278509, 0.344884
H, 7.772354, -3.045895, -0.003776
H, 9.860321, 0.657307, 0.678534
H, 9.878243, -1.817755, 0.414042
C, -0.964015, 0.583186, -0.224506
C, -1.185948, -0.812544, -0.407453
C, -2.052957, 1.414215, -0.01601
C, -2.456786, -1.334975, -0.373802
H, -0.351216, -1.477538, -0.599291
C, -3.372655, 0.906415, 0.032913
H, -1.882736, 2.478004, 0.115308
C, -3.584293, -0.499189, -0.14847
H, -2.613826, -2.399696, -0.523681
C, -4.497467, 1.748247, 0.255773
C, -4.906822, -1.0141, -0.101167
C, -5.772331, 1.233245, 0.298187
H, -4.338708, 2.81435, 0.39331
C, -5.959537, -0.157926, 0.117371
H, -5.074213, -2.077473, -0.237105
H, -6.628971, 1.875947, 0.467392
H, 2.052568, 2.641699, -0.318648
Br, -7.743838, -0.851279, 0.184318
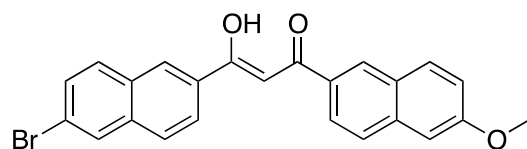
E (HF) = -3722.20263194 μ (Debye) = 5.9022

O, -0.397265, 2.575267, -0.209719
C, -0.440887, 1.311881, -0.185114

C, 0.757663, 0.523148, -0.140004
H, 0.690572, -0.550961, -0.070407
O, 2.116099, 2.451574, -0.189863
C, 2.004764, 1.125286, -0.142191
C, 3.284361, 0.400644, -0.092401
C, 4.471484, 1.117267, -0.03013
C, 3.346603, -1.027383, -0.106141
C, 5.726943, 0.467741, 0.022763
H, 4.440453, 2.201552, -0.019603
C, 4.549355, -1.683249, -0.055566
H, 2.434777, -1.611203, -0.165179
C, 5.780172, -0.966042, 0.011696
C, 6.948026, 1.188641, 0.086984
H, 4.576756, -2.769626, -0.068991
C, 7.031958, -1.613173, 0.064806
C, 8.162607, 0.541325, 0.137761
H, 6.916854, 2.275085, 0.095514
C, 8.20806, -0.879715, 0.127048
H, 7.088309, -2.697773, 0.057348
H, 9.076699, 1.121127, 0.185541
C, -1.781947, 0.650286, -0.185549
C, -1.958508, -0.741183, -0.43712
C, -2.897441, 1.434172, 0.060855
C, -3.211768, -1.305485, -0.433287
H, -1.102421, -1.368416, -0.659736
C, -4.200276, 0.882093, 0.081528
H, -2.761873, 2.495323, 0.244067
C, -4.366066, -0.518734, -0.170536
H, -3.333844, -2.365999, -0.636254
C, -5.352295, 1.674496, 0.34297
C, -5.671363, -1.077713, -0.154103
C, -6.609988, 1.117112, 0.355399
H, -5.228807, 2.736995, 0.534293
C, -6.751737, -0.268296, 0.103684
H, -5.804115, -2.137574, -0.344571
H, -7.487104, 1.722546, 0.554269
O, 9.362948, -1.597237, 0.175252
C, 10.607239, -0.901893, 0.240104
H, 11.375191, -1.675922, 0.269841
H, 10.760757, -0.272035, -0.64388
H, 10.676055, -0.287242, 1.145215
H, 1.163116, 2.801769, -0.202278
Br, -8.513068, -1.021766, 0.128535
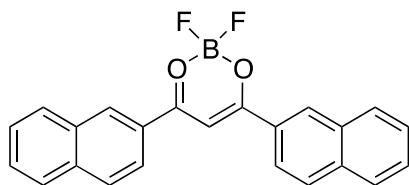
E (HF) = -1260.76184420 μ (Debye) = 10.0981

B, 0, 2.546808, -0.073425
F, -0.000001, 3.079375, 1.218378
F, 0.000001, 3.54673, -1.034357
O, -1.221052, 1.713689, -0.250755
C, -1.210912, 0.415247, -0.075817
C, 0, -0.270903, 0.067373
H, -0.000001, -1.331879, 0.257678
O, 1.221052, 1.713689, -0.250753
C, 1.210912, 0.415247, -0.075815
C, 2.526461, -0.238269, -0.060815
C, 3.67185, 0.546378, 0.018423
C, 2.658937, -1.660099, -0.121625
C, 4.962494, -0.034524, 0.049271
H, 3.578212, 1.626382, 0.066388
C, 3.900352, -2.247158, -0.097797
H, 1.780504, -2.289749, -0.208019
C, 5.086169, -1.462751, -0.008786
C, 6.140638, 0.761044, 0.137792
H, 3.989602, -3.329172, -0.152382
C, 6.382206, -2.041967, 0.021229
C, 7.385063, 0.168657, 0.165398
H, 6.041782, 1.842838, 0.181937
C, 7.505722, -1.244042, 0.106692
H, 6.477245, -3.124164, -0.023346
H, 8.279627, 0.781507, 0.232463
H, 8.49272, -1.698097, 0.12974
C, -2.526461, -0.238269, -0.060818
C, -2.658937, -1.660099, -0.121633
C, -3.67185, 0.546378, 0.018425
C, -3.900352, -2.247157, -0.097806
H, -1.780505, -2.289748, -0.208032
C, -4.962494, -0.034524, 0.049273
H, -3.578212, 1.626382, 0.066394
C, -5.086169, -1.46275, -0.008791

H, -3.989603, -3.329171, -0.152396
C, -6.140638, 0.761044, 0.137799
C, -6.382206, -2.041967, 0.021224
C, -7.385062, 0.168657, 0.165405
H, -6.041781, 1.842837, 0.181949
C, -7.505722, -1.244042, 0.106692
H, -6.477246, -3.124164, -0.023355
H, -8.279626, 0.781506, 0.232474
H, -8.49272, -1.698098, 0.12974
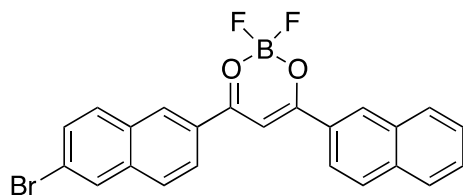
E (HF) = -3831.873676 μ (Debye) = 7.0147

Br, 1.64632, 2.709036, -0.022461
F, 1.684702, 3.130526, 1.293987
F, 1.738115, 3.723693, -0.936822
O, 0.351359, 1.968845, -0.246191
C, 0.248982, 0.685067, -0.06135
C, 1.390746, -0.110835, 0.088917
H, 1.29642, -1.166815, 0.285386
O, 2.787051, 1.748233, -0.246849
C, 2.658948, 0.467037, -0.064868
C, 3.913651, -0.305645, -0.055538
C, 5.120593, 0.37864, 0.008168
C, 3.926215, -1.732369, -0.106422
C, 6.358157, -0.308605, 0.031449
H, 5.112368, 1.463218, 0.046519
C, 5.113408, -2.422988, -0.088296
H, 2.995788, -2.285142, -0.180491
C, 6.361598, -1.741833, -0.016731
C, 7.599295, 0.384826, 0.101374
H, 5.110923, -3.509435, -0.134915
C, 7.604956, -2.426512, 0.005156
C, 8.789927, -0.308408, 0.120895
H, 7.590832, 1.4715, 0.137824
C, 8.791739, -1.725864, 0.072469
H, 7.608842, -3.513481, -0.03174

H, 9.733062, 0.228586, 0.173785
H, 9.737501, -2.261159, 0.089
C, -1.126645, 0.152924, -0.048977
C, -1.399847, -1.247812, -0.06308
C, -2.189114, 1.046629, -0.027284
C, -2.692559, -1.712148, -0.051226
H, -0.585373, -1.963192, -0.100155
C, -3.529973, 0.595763, -0.012464
H, -1.984141, 2.112185, -0.017368
H, -3.795473, -0.812337, -0.02382
H, -2.887004, -2.781641, -0.068228
C, -4.625993, 1.502423, 0.016773
C, -5.139693, -1.266633, -0.010379
C, -5.924049, 1.045037, 0.032264
H, -4.426056, 2.570916, 0.026743
C, -6.166761, -0.350205, 0.018019
H, -5.347675, -2.332133, -0.020803
H, -6.758675, 1.737599, 0.054724
Br, -7.97342, -0.955934, 0.039759
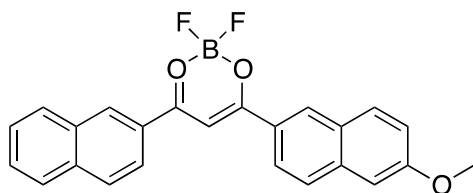
E (HF) = -1335.98816861 μ (Debye) = 8.6087

B, -0.840039, 2.617801, -0.049926
F, -0.865428, 3.142242, 1.246334
F, -0.879185, 3.626502, -1.002642
O, -2.024505, 1.738081, -0.237257
C, -1.958583, 0.438653, -0.069276
C, -0.72273, -0.196831, 0.072502
H, -0.681145, -1.258719, 0.252927
O, 0.41458, 1.839701, -0.23019
C, 0.462622, 0.539535, -0.061949
C, 1.800021, -0.05477, -0.049855
C, 2.914512, 0.779459, -0.02033
C, 1.999874, -1.47254, -0.065938
C, 4.225994, 0.256179, 0.000022
H, 2.776252, 1.855659, -0.005408
C, 3.263695, -2.00533, -0.04956
H, 1.149952, -2.14458, -0.108189

239

C, 4.42, -1.167545, -0.013497
C, 5.371644, 1.097017, 0.035693
H, 3.397993, -3.083757, -0.068451
C, 5.729927, -1.688133, 0.006151
C, 6.645611, 0.57216, 0.054692
H, 5.233718, 2.175196, 0.046763
C, 6.829295, -0.83895, 0.03978
H, 5.891999, -2.762362, -0.004516
H, 7.498593, 1.239742, 0.08082
C, -3.247726, -0.267886, -0.060583
C, -3.324294, -1.693036, -0.136204
C, -4.423037, 0.46967, 0.026223
C, -4.541753, -2.328867, -0.119196
H, -2.421695, -2.286764, -0.228772
C, -5.690174, -0.161736, 0.049922
H, -4.371942, 1.551932, 0.085135
C, -5.757655, -1.592874, -0.023158
H, -4.588308, -3.412968, -0.185176
C, -6.898586, 0.586008, 0.145568
C, -7.030161, -2.222668, -0.000704
C, -8.118994, -0.054792, 0.165559
H, -6.841997, 1.670349, 0.201305
C, -8.184216, -1.470435, 0.091733
H, -7.082732, -3.307242, -0.056649
H, -9.03687, 0.521933, 0.23818
H, -9.152668, -1.963114, 0.108766
O, 8.051056, -1.435487, 0.057315
C, 9.231107, -0.624933, 0.094148
H, 10.064704, -1.327676, 0.103112
H, 9.29907, 0.013086, -0.794064
H, 9.25939, -0.010909, 1.001212
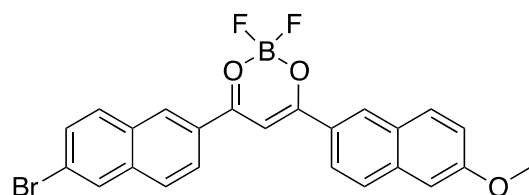
E (HF) = -3946.400079958 μ (Debye) = 7.2218

B, 0.810385, 2.889447, -0.009918
F, 0.830976, 3.30722, 1.30908
F, 0.85756, 3.913848, -0.918303
O, -0.450811, 2.096111, -0.237245

240

C, -0.494855, 0.806657, -0.061173
C, 0.679242, 0.061229, 0.08144
H, 0.63111, -0.9994, 0.26905
O, 1.992485, 1.982912, -0.239691
C, 1.923428, 0.694823, -0.066409
C, 3.206747, -0.020394, -0.061319
C, 4.385731, 0.714337, -0.018691
C, 3.285218, -1.447813, -0.094341
C, 5.648897, 0.08058, -0.000637
H, 4.332286, 1.798133, 0.006848
C, 4.49843, -2.088024, -0.080856
H, 2.379451, -2.042328, -0.149387
C, 5.721177, -1.353389, -0.03109
C, 6.860993, 0.81892, 0.04704
H, 4.54094, -3.173937, -0.113571
C, 6.982437, -1.983748, -0.014617
C, 8.086009, 0.1872, 0.061858
H, 6.814096, 1.904925, 0.070761
C, 8.148875, -1.233155, 0.030616
H, 7.05675, -3.067326, -0.037288
H, 8.992874, 0.779907, 0.097529
C, -1.846442, 0.214165, -0.049543
C, -2.05682, -1.197167, -0.071067
C, -2.948023, 1.058631, -0.023068
C, -3.327157, -1.719685, -0.060547
H, -1.211094, -1.874981, -0.113
C, -4.26753, 0.547502, -0.009063
H, -2.791345, 2.132305, -0.008145
C, -4.46945, -0.870865, -0.026916
H, -3.472941, -2.796818, -0.08316
C, -5.403602, 1.403142, 0.025568
C, -5.791798, -1.38569, -0.014986
C, -6.679715, 0.887264, 0.040203
H, -5.252516, 2.479593, 0.040607
C, -6.859372, -0.517221, 0.018882
H, -5.950994, -2.459459, -0.030449
H, -7.544653, 1.541319, 0.067298
Br, -8.637121, -1.204335, 0.040497
O, 9.315992, -1.934574, 0.042865
C, 10.554188, -1.231077, 0.089754
H, 10.637076, -0.630145, 1.003942
H, 11.327005, -2.001108, 0.091055
H, 10.681462, -0.588713, -0.790531
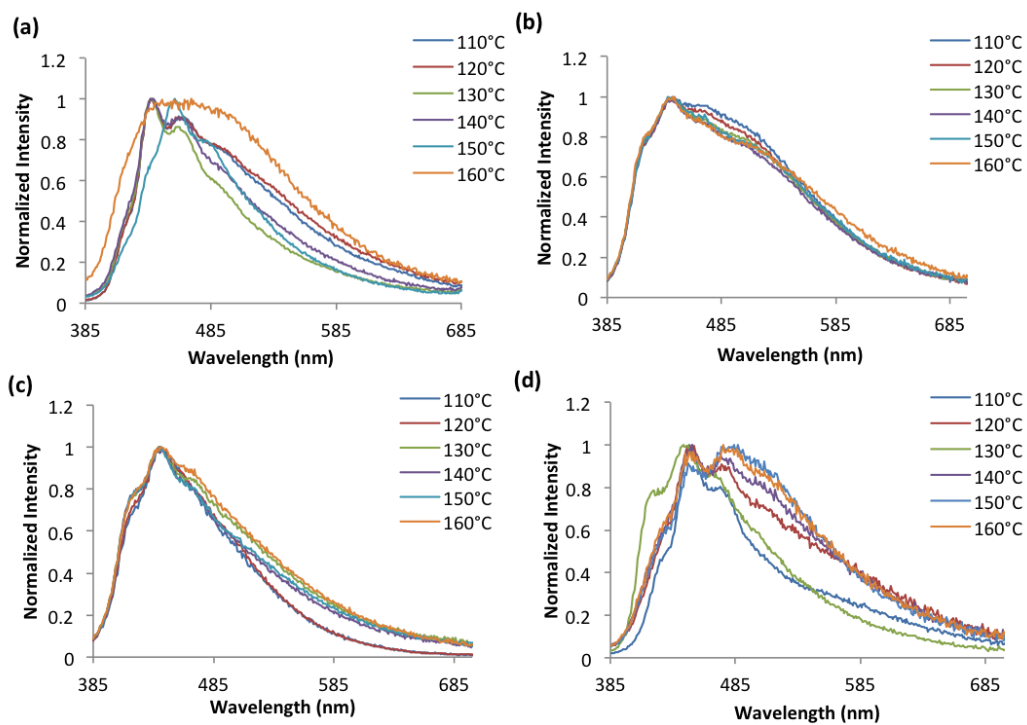
Figure S3.1. Emission spectra of dnm (a), dnmOMe (b), dnmBr (c), dnmBrOMe (d) thin films annealed at different temperatures (°C) (λ_{ex} = 369 nm).
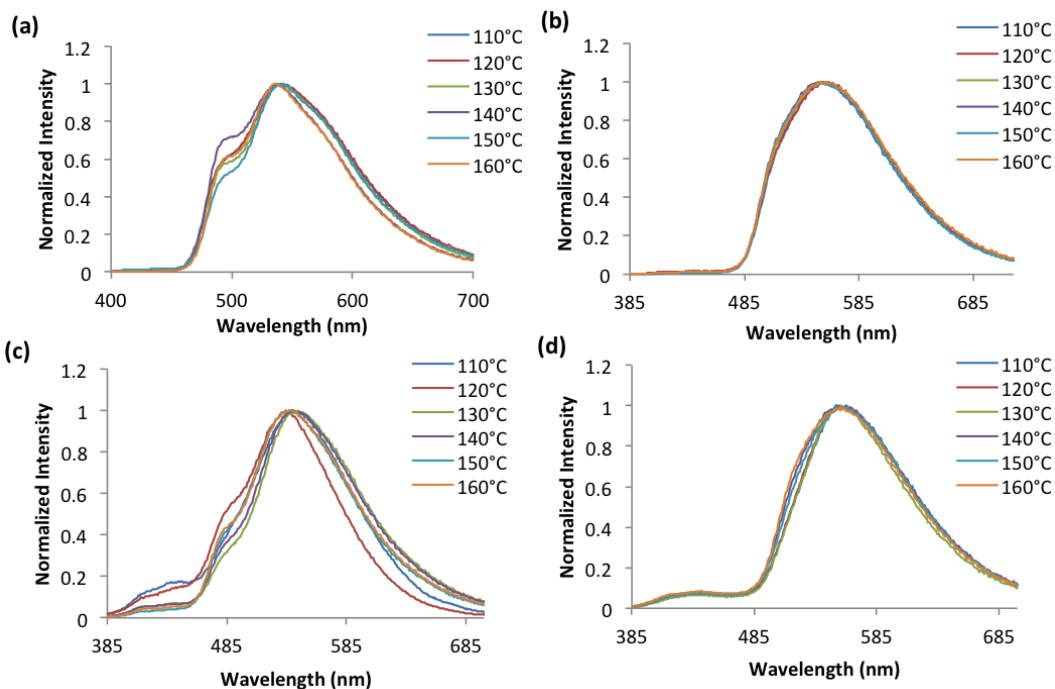
Figure S3.2. Emission spectra of BF$_2$dnm (a), BF$_2$dnmOMe (b), BF$_2$dnmBr (c), BF$_2$dnmBrOMe (d) thin films annealed at different temperatures (λ_{ex} = 369 nm).
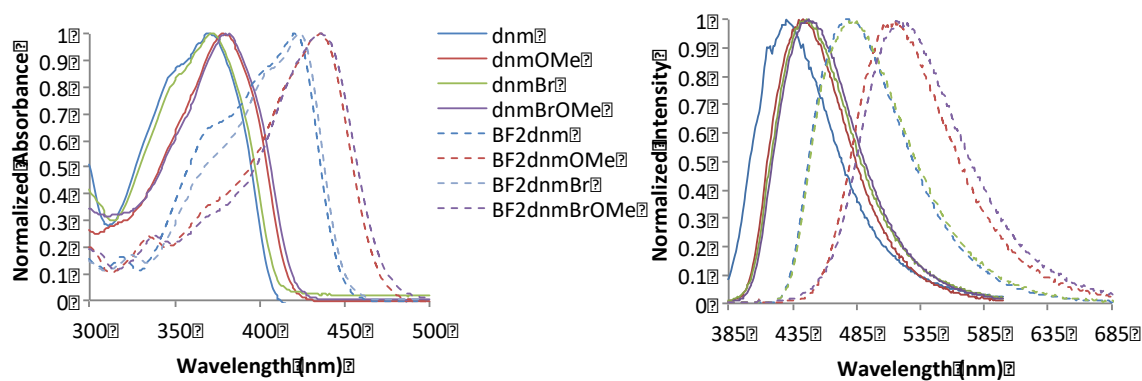
Figure S3.3. Absorption (left) and emission (right) spectra of ligands and boron compounds (λ_{ex} = 369 nm).
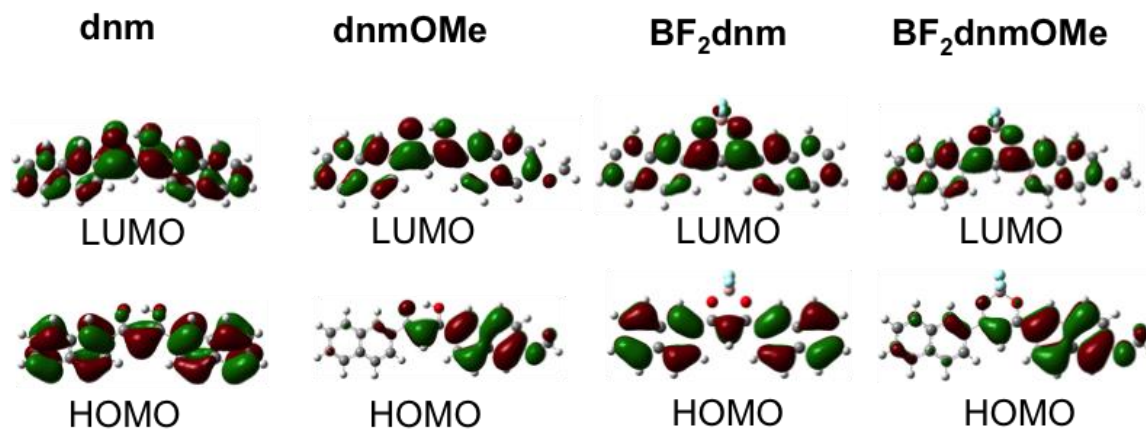
Figure S3.4. Frontier molecular orbitals of dnm, dnmOMe and boron derivatives BF$_2$dnm and BF$_2$dnmOMe.

Table S3.1. Melting Points for Ligands and Boron Complexes

Compound	Melting Temperature (°C)
dnm	162-164
dnmOMe	158-160
dnmBr	201-202
dnmBrOMe	250-255
BF$_2$dnm	326-329
BF$_2$dnmOMe	280-284
BF$_2$dnmBr	299-301
BF$_2$dnmBrOMe	343-345

244
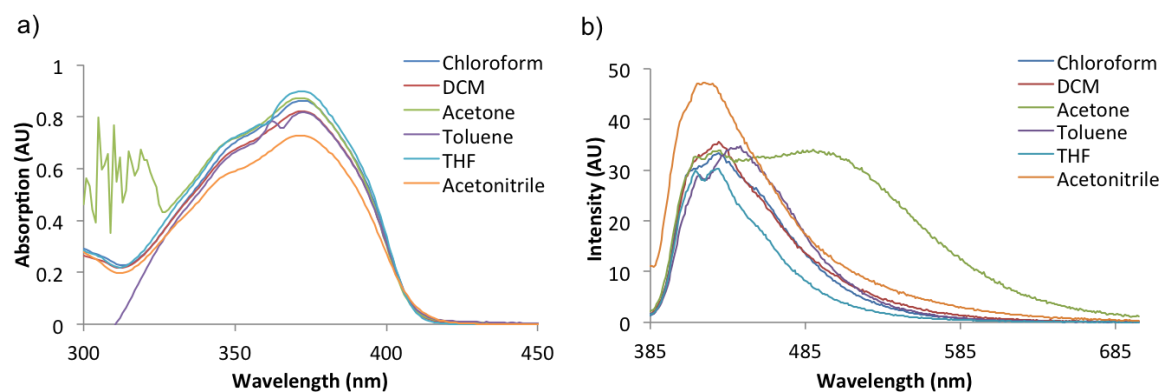
Figure S3.5. Absorption (a), and emission (b) spectra of dnmBr in varying solvents. Solvents, from left to right: chloroform, CHCl$_2$, acetone, toluene, THF, acetonitrile (λ_{ex} = 369 nm).

Fig. S3.6. Photo under UV irradiation (a), absorption (b), and emission (c) spectra of BF$_2$dnm in varying solvents. Solvents, from left to right: chloroform, CHCl$_2$, acetone, toluene, THF, acetonitrile (λ_{ex} = 369 nm).

Fig. S3.7. Photo under UV irradiation (a), absorption (b), and emission (c) spectra of BF_2dnmBr in varying solvents. Solvents, from left to right: chloroform, $CHCl_2$, acetone, toluene, THF, acetonitrile ($\lambda_{ex} = 369$ nm).
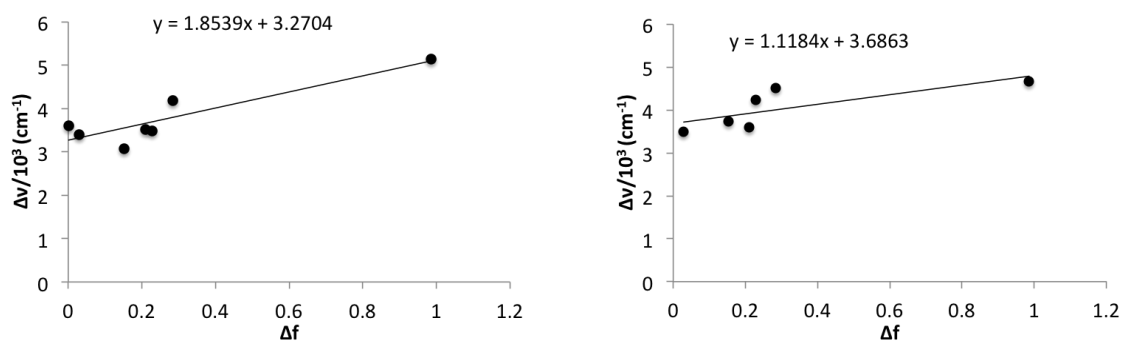
Fig S3.8. Lippert-Mataga plots of dnmOMe and dnmBrOMe solvatochromism.
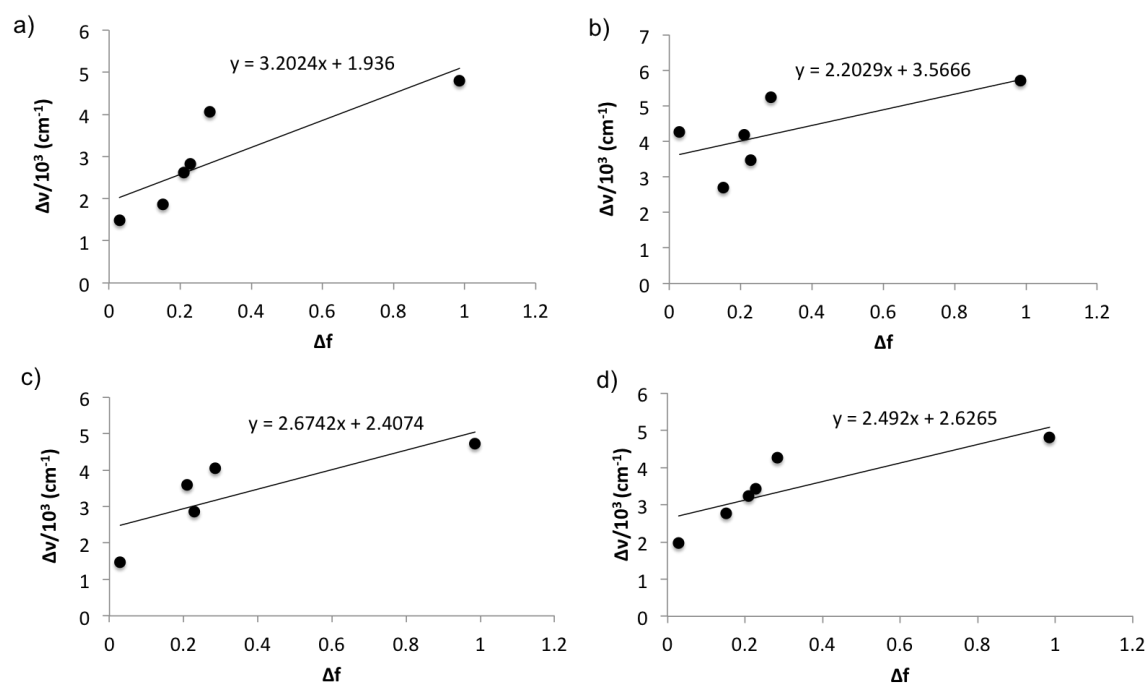
Fig. S3.9. Lippert-Mataga plots of BF$_2$dnm (a), BF$_2$dnmOMe (b), BF$_2$dnmBr (c), and BF$_2$dnmBrOMe (d) solvatochromism.
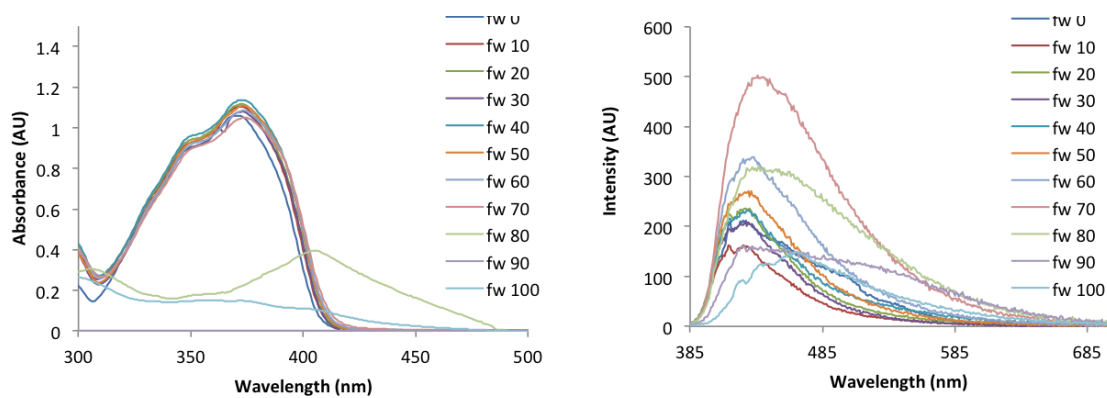
Fig S3.10. Absorption (a) and emission (b) spectra of dnm in different THF/H$_2$O mixtures (λ_{ex} = 369 nm).

Fig S3.11. Absorption (a) and emission (b) spectra of dnmBr in different THF/H$_2$O mixtures (λ_{ex} = 369 nm).

Fig. S3.12. Image under UV irradiation (a), and corresponding absorption (b) and emission (c) spectra of BF$_2$dnm in different THF/H$_2$O mixtures (λ_{ex} = 369 nm).

Fig. S3.13. Image under UV irradiation (a), and corresponding absorption (b) and emission (c) spectra of BF_2dnmBr in different THF/H_2O mixtures ($\lambda_{ex} = 369$ nm).
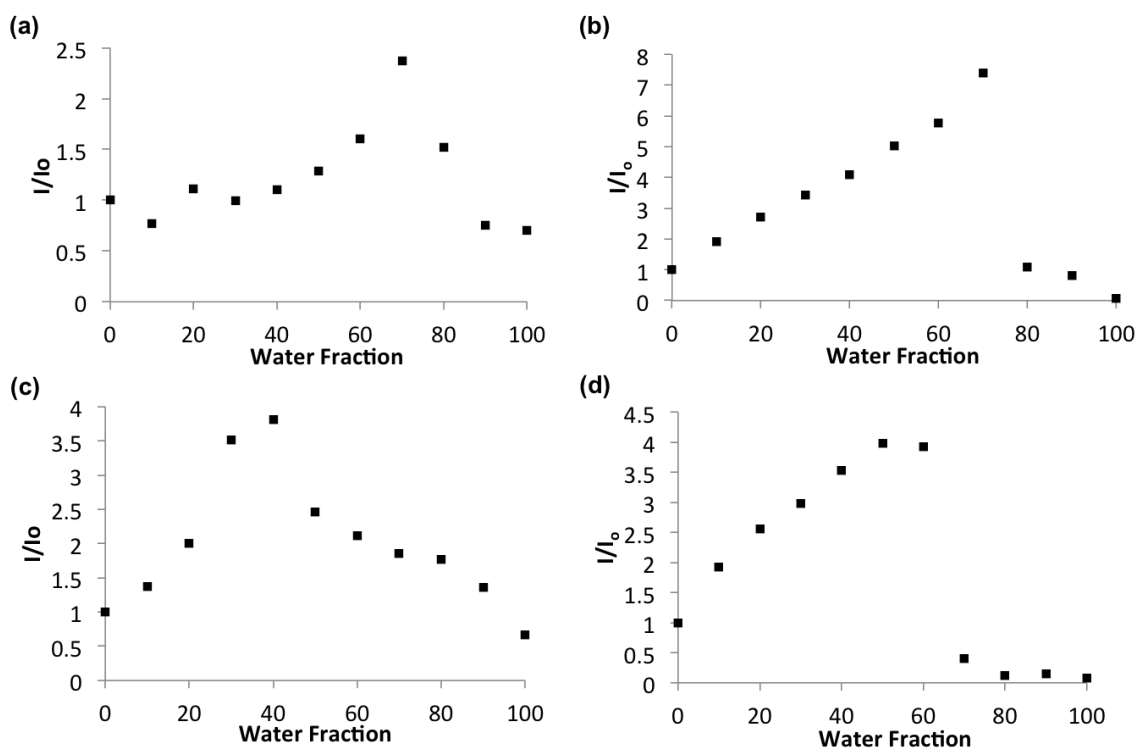
Fig. S3.14. Plots of I/I_o versus water fraction for dnm (a), dnmOMe (b), dnmBr (c), and dnmBrOMe (d).
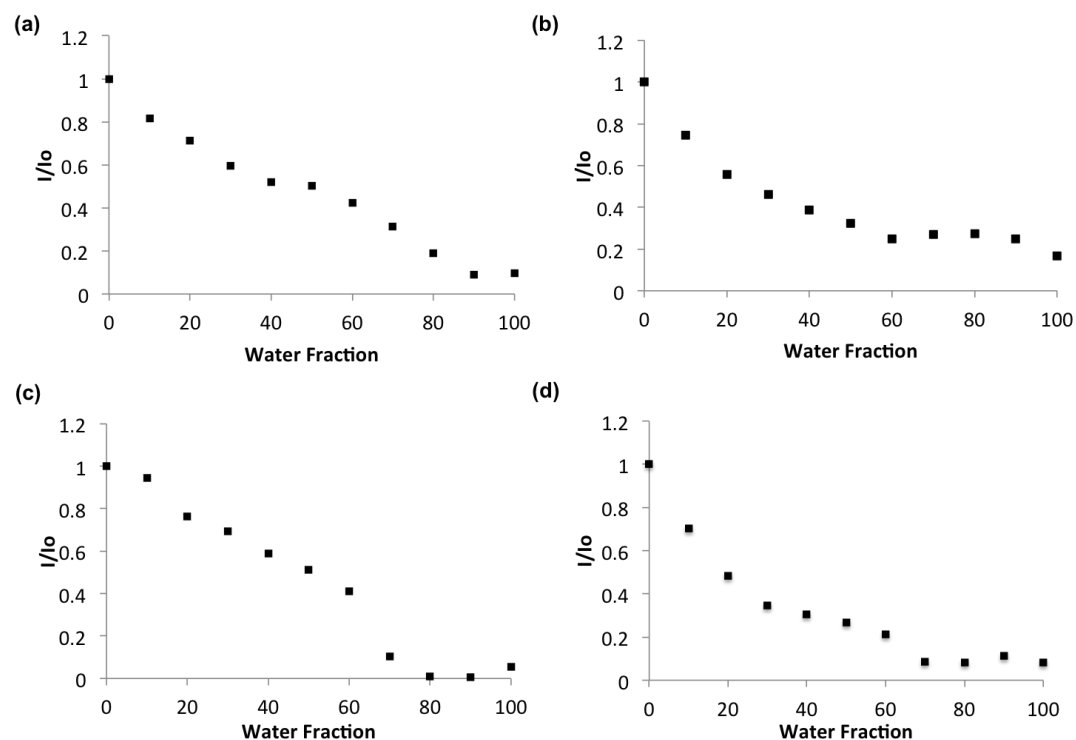
Fig. S3.15. Plots of I/I_o versus water fraction for BF_2dnm (a), $BF_2dnmOMe$ (b), BF_2dnmBr (c), and $BF_2dnmBrOMe$ (d).
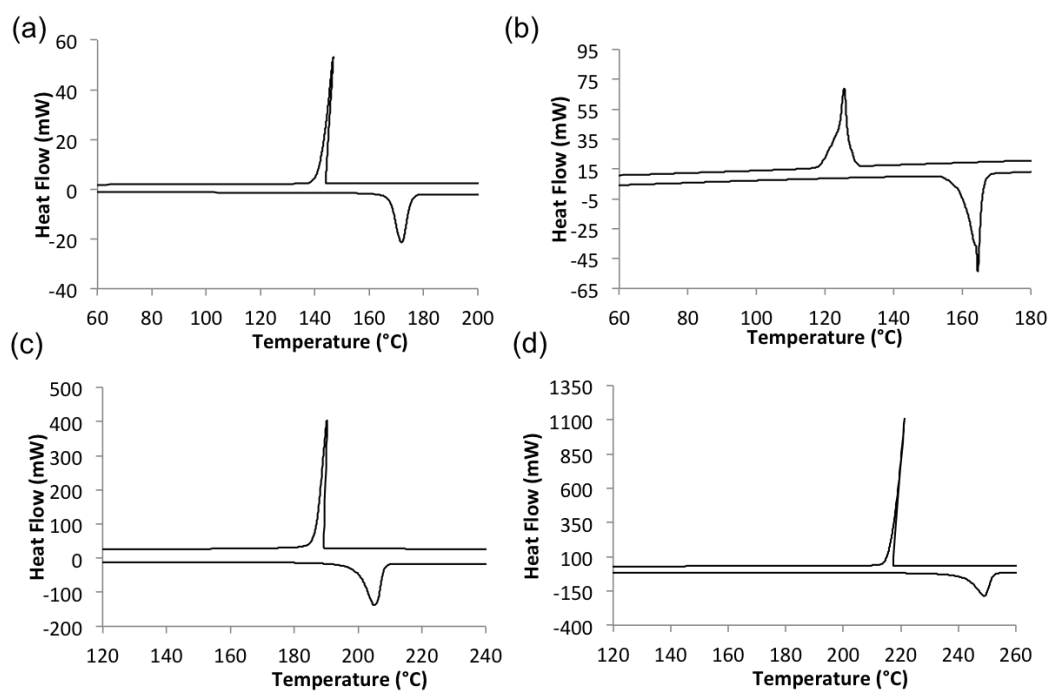
Fig. S3.16. DSC thermograms of dnm (a), dnmOMe (b), dnmBr (c), and dnmBrOMe (d).
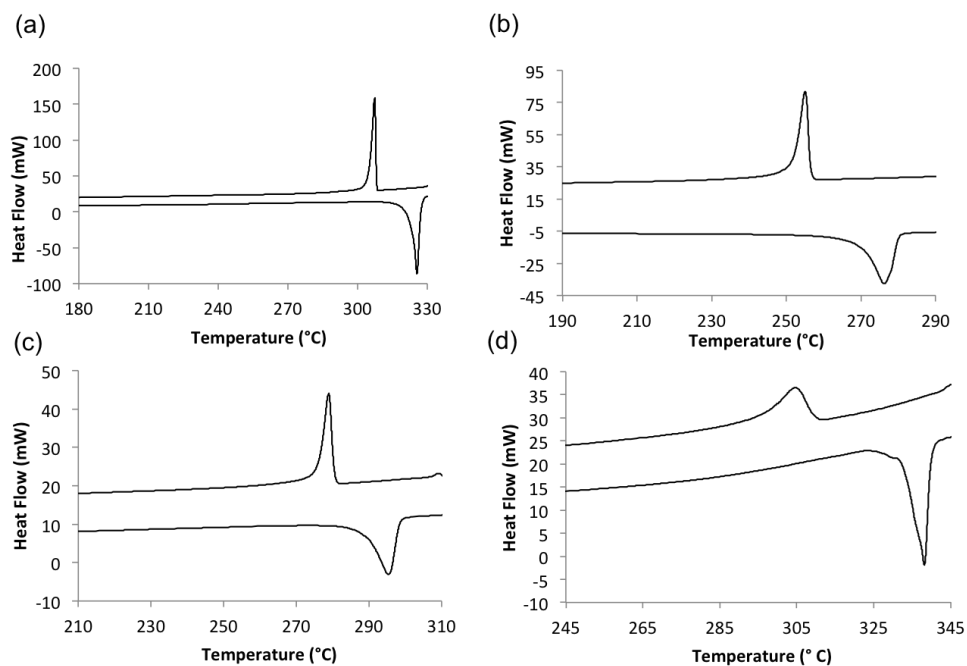
Fig. S3.17. DSC thermograms of BF$_2$dnm (a), BF$_2$dnmOMe (b), BF$_2$dnmBr (c), and BF$_2$dnmBrOMe (d).
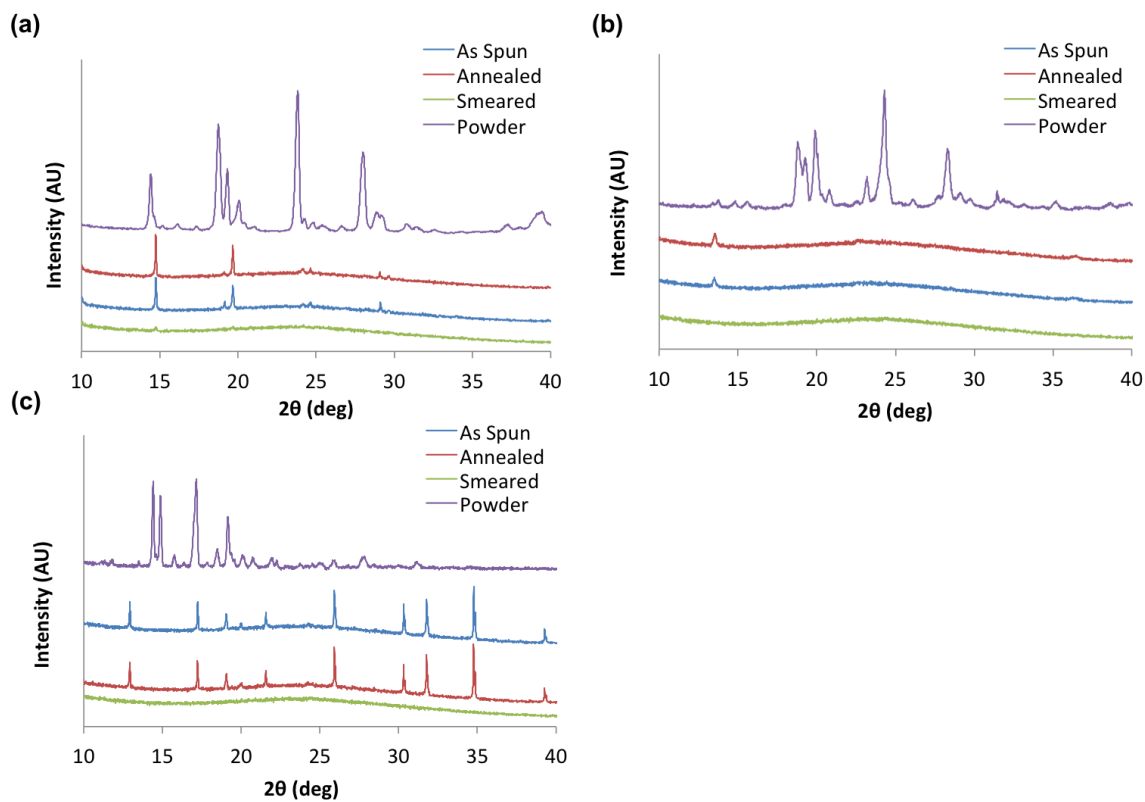
Fig. S3.18. Powder XRD patterns of dnm (a), dnmBr (b), dnmBrOMe (c) as pristine powders and AS, TA, and SM thin films.

251
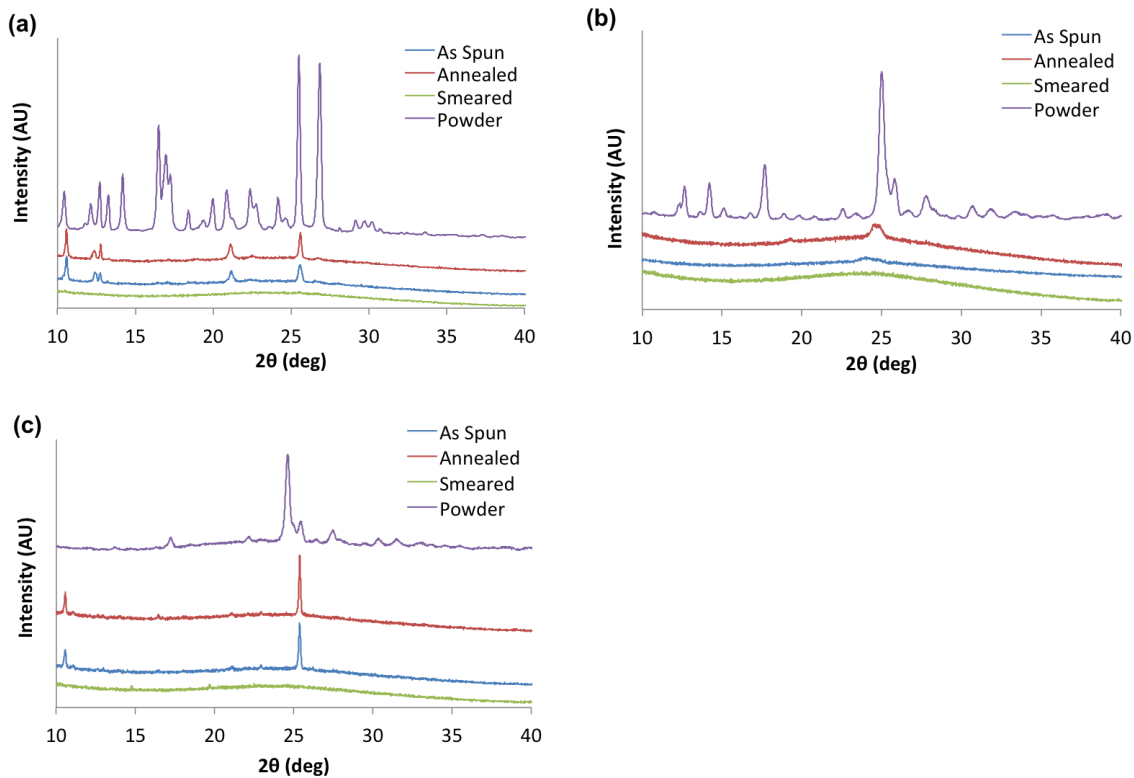
Fig S3.19. Powder XRD patterns of BF$_2$dnm (a), BF$_2$dnmBr (b), BF$_2$dnmBrOMe (c) as pristine powders and AS, TA, and SM thin-films.

References

1. Frisch, M. J.; Trucks, G. W.; Schlegel, H. B.; Scuseria, G. E.; Robb, M. A.; Cheeseman, J. R.; Scalmani, G.; Barone, V.; Mennucci, B.; Petersson, G. A.; Nakatsuji, H.; Caricato, M.; Li, X.; Hratchian, H. P.; Izmaylov, A. F.; Bloino, J.; Zheng, G.; Sonnenberg, J. L.; Hada, M.; Ehara, M.; Toyota, K.; Fukuda, R.; Hasegawa, J.; Ishida, M.; Nakajima, T.; Honda, Y.; Kitao, O.; Nakai, H.; Vreven, T.; Montgomery, J. A.; Peralta, J. E.; Ogliaro, F.; Bearpark, M.; Heyd, J. J.; Brothers, E.; Kudin, K. N.; Staroverov, V. N.; Kobayashi, R.; Normand, J.; Raghavachari, K.; Rendell, A.; Burant, J. C.; Iyengar, S. S.; Tomasi, J.; Cossi, M.; Rega, N.; Millam, J. M.; Klene, M.; Knox, J. E.; Cross, J. B.; Bakken, V.; Adamo, C.; Jaramillo, J.; Gomperts, R.; Stratmann, R. E.; Yazyev, O.; Austin, A. J.; Cammi, R.; Pomelli, C.; Ochterski, J. W.; Martin, R. L.; Morokuma, K.; Zakrzewski, V. G.; Voth, G. A.; Salvador, P.; Dannenberg, J. J.; Dapprich, S.; Daniels, A. D.; Farkas; Foresman, J. B.; Ortiz, J. V.; Cioslowski, J.; Fox, D. J. Gaussian 09, Revision B.01., Gaussian Inc., Wallingford CT, **2009**.

2. Tomasi, J.; Mennucci, B.; Cammi, R. Quantum Mechanical Continuum Solvation Models. *Chem. Rev.* **2005,** *105*, 2999-3094.

3. Dennington, R.; Keith, R.; Millam, J. GaussView, Version 5, Semichem Inc., Shawnee Mission KS, **2009**.

Appendix C

Chapter 4 Supporting Information
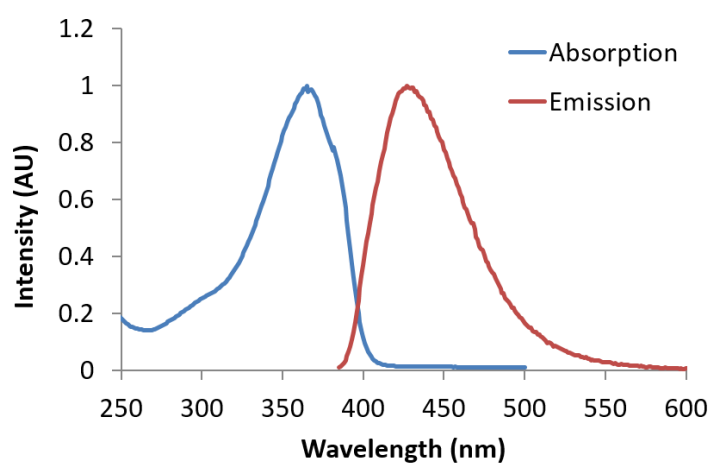
Figure S4.1. Absorption and emission spectra in CH_2Cl_2 solution ($\lambda_{ex} = 369$ nm).

Table S4.1. Optical Properties of gbmOMe in CH_2Cl_2.[a]

λ_{abs}[b] [nm]	ε [$M^{-1} cm^{-1}$]	λ_{em}[c] [nm]	Φ_F [%]	τ [ns]
365	64,000	427	0.01	0.31

[a] $\lambda_{ex} = 369$ nm; room temperature, air.
[b] Absorbance maximum.
[c] Emission maximum; fluorescence.

Table S4.2. Luminescence Properties of Dye Films on Glass and Weighing Paper Substrates[a]

Glass						Weigh Paper			
λ_{AS}[b] [nm]	τ_{AS}[g] [ns]	λ_{TA}[c] [nm]	τ_{TA}[g] [ns]	λ_{SM}[d] [nm]	τ_{SM}[g] [ns]	λ_{AP}[e] [nm]	τ_{AP}[g] [ns]	λ_{MT}[f] [nm]	τ_{MT}[g] [ns]
499	4.00	428	0.14	478	2.00	429	0.47	481	6.31

[a] $\lambda_{ex} = 369$ nm; room temperature, air.
[b] Emission maximum of as spun (AS) glass films.
[c] Emission maximum of thermally annealed (TA) glass films.
[d] Emission maximum of smeared (SM) glass films.
[e] Emission maximum of as prepared (AP) weigh paper films.
[f] Emission maximum of melted (MT) weigh papers films.
[g] Pre-exponential weighted fluorescence lifetimes.

Table S4.3. Luminescence Properties of Dye Films on Weighing Paper at 77 K.[a]

λ_{AP}[b] [nm]	λ_{MT}[b] [nm]	λ_{SM}[b] [nm]
428	463	454

[a] $\lambda_{ex} = 369$ nm; room temperature, air.
[b] Emission maximum; 77K.
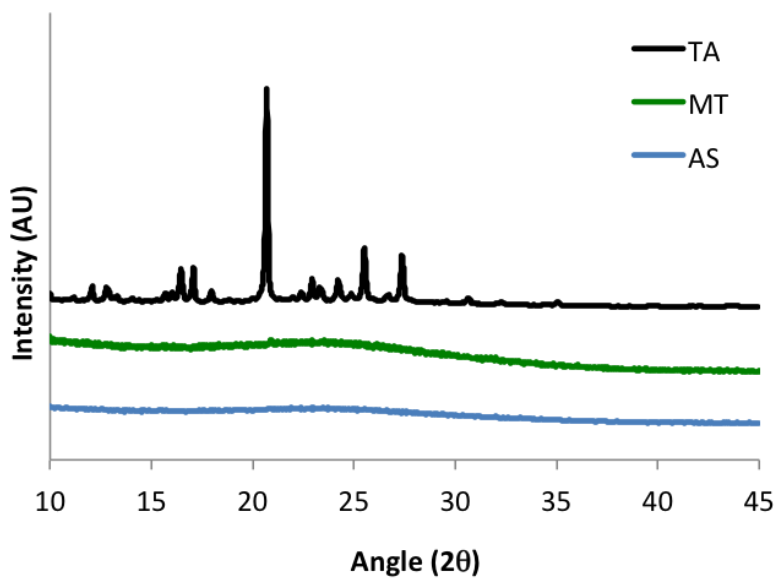
Figure S4.2. XRD patterns of thermally annealed (TA), melted (MT) and as spun (AS) gbmOMe films on glass.
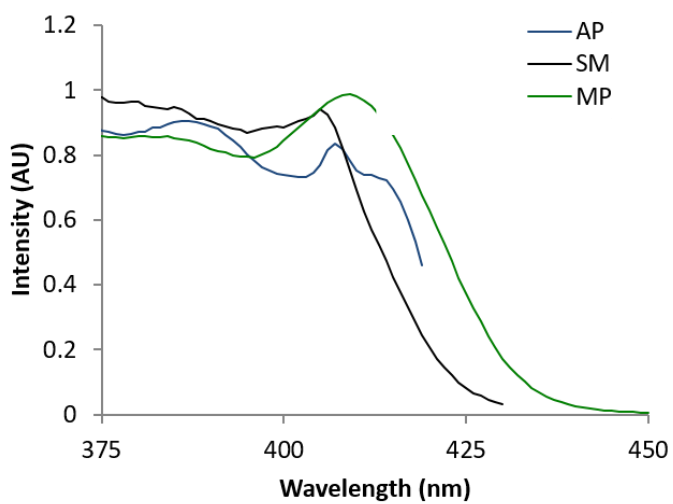
Figure S4.3. Excitation spectra of gbmOMe weigh paper films in as prepared (AP) ($\lambda_{em} = 430$ nm), melted (MT) ($\lambda_{em} = 455$ nm) and smeared (SM) ($\lambda_{em} = 455$ nm) states at 77K.
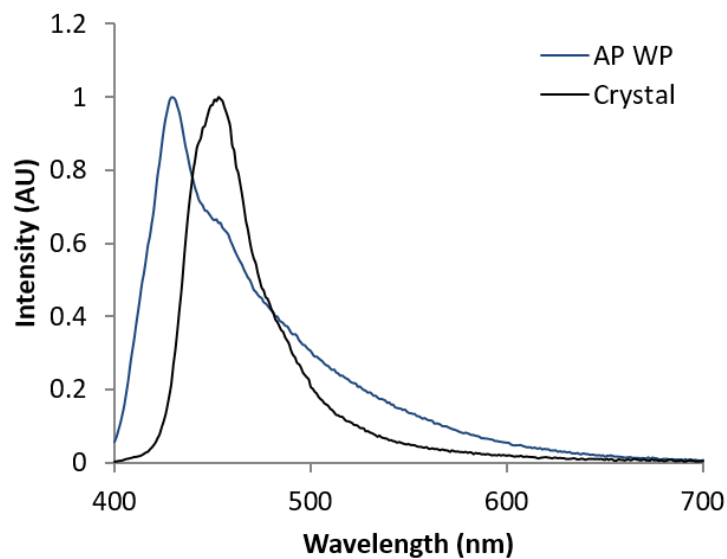
Figure S4.4. Emission spectra of gbmOMe single crystals and as prepared (AP) weigh paper films. (λ_{ex} = 369 nm)
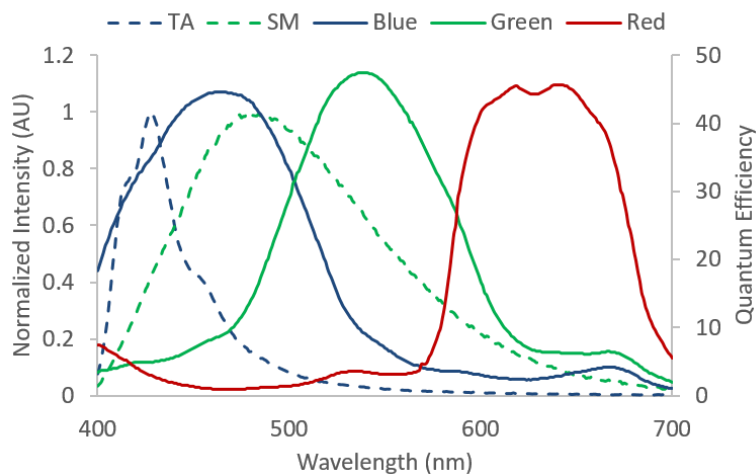

Figure S4.5. Emission spectra of gbmOMe glass films in thermally annealed (TA) and smeared (SM) phases overlaid with the quantum efficiencies of the red, green and blue channels of the camera used for detection. The green channel is used for smeared state detection. (λ_{ex} = 369 nm)

```matlab
[FileName,PathName]=uigetfile('.avi');   %Pick an .avi file
video1=read(VideoReader(strcat(PathName,FileName)));  %Read the file


%%%Crop%%%
start = 1;
imshow(video1(:,:,:,start)); %display a selected frame from the video
[x,y]=ginput(3); %ginput lets you click on a picture and returns the coordinates
close all %close the image
x=round(x); %round the x coordinate to an integer
y=round(y); %round the y coordinate to an integer


video2 = video1(y(1):y(2),x(1):x(2),:,:);
finish = size(video2,4)-2;
range = finish - start;


%%%Preallocate%%%
bin = 2;
finish = size(video2,4);
sizex = floor(size(video2,2)/bin);
sizey = floor(size(video2,1)/bin);
intensitycorr = zeros((finish-start),1);
iteration = 1;
step = 1;
xvalues = zeros(sizex*sizey,1);
yvalues = zeros(sizex*sizey,1);
binnedInt = zeros((finish-start),1);
fits = zeros(sizex*sizey,1);
time = zeros((finish-start),1);
Int0 = zeros(sizex*sizey,1);
Iteration = 1;
iteration1 = 1;




%%%Calculate Intial Intensities%%%

  for county1 = 1:sizey,
      for countx1 = 1:sizex,
       Int0(iteration) = mean2(video1((county1-1)*bin+1:county1*bin,(countx1-1)*bin+1:countx1*bin,2,1));
       iteration = iteration + 1;
      end
   end



%%%Intensity subtract%%%
for county = 1:step:sizey,
   for countx = 1:step:sizex,
      for n = start:step:finish,
         binnedInt(((n-start)/step)+1) = mean2(video2((county-1)*bin+1:county*bin,(countx-
1)*bin+1:countx*bin,2,n));
         time(((n-start)/step)+1)=(n-start+1)/15;
      end
   intensitycorr = (binnedInt - min(binnedInt))/(max(binnedInt)-min(binnedInt));
   fitdouble=fit(time,intensitycorr,'exp2');
   results2=coeffvalues(fitdouble);
```

```matlab
    lifetime1=-1/results2(2);
    lifetime2=-1/results2(4);
    weighted=(lifetime1*results2(1)+lifetime2*results2(3))/(results2(1)+results2(3));
 if weighted>0 && weighted<500000
    fits(iteration1)=weighted;

else
end
    xvalues(iteration1) = countx;
    yvalues(iteration1) = county;

    Iteration = Iteration + 1;
    iteration1 = iteration1 + 1;
  end
end

%%%Colormap%%%
z = zeros(sizey,sizex);
[x,y] = meshgrid([1:z(2)],[1:z(1)]);
warp(x,y,z,video1(:,:,:,1));
hold on
  [xq,yq] = meshgrid(min(xvalues):1:max(xvalues), min(yvalues):1:max(yvalues));
  zq=griddata(xvalues,yvalues,fits,xq,yq);
  imagesc(zq,[0 200]);
  colormap(jet(256))
```

Figure S4.6. Recovery lifetime Matlab code
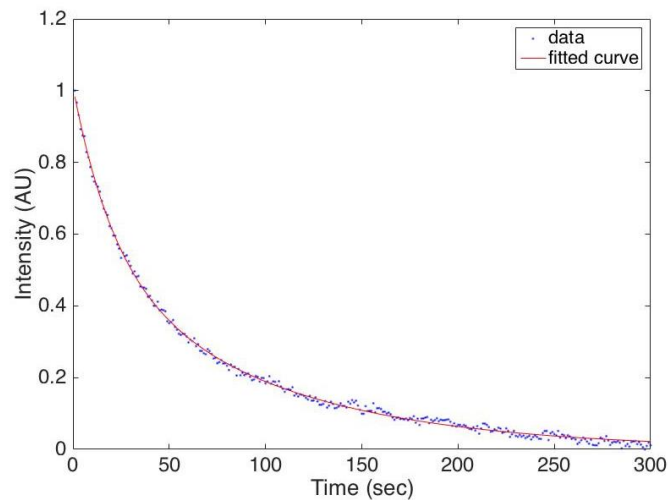
Figure S4.7. Intensity decay and double exponential fit of smeared gbmOMe film on weigh paper.
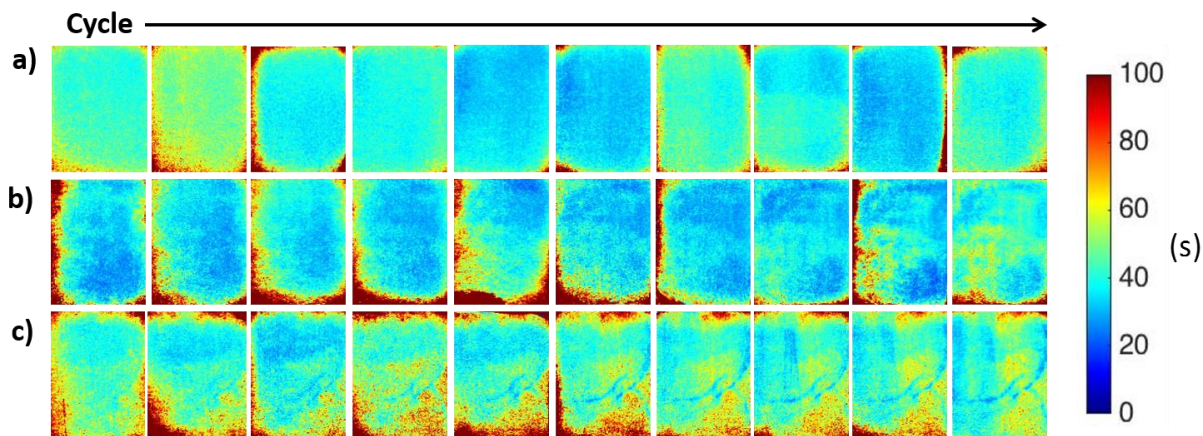
Figure S4.8. Spatially resolved smeared state decay colormaps of repeatedly smeared weigh paper films fabricated by (a) directly smearing gbmOMe powder (WP1) (b) drop casting from a concentrated gbmOMe/THF solution (0.90 M) (WP2), and (c) drop casting from a more dilute solution (0.14 M) (WP3) on 3" x 1" weigh paper.
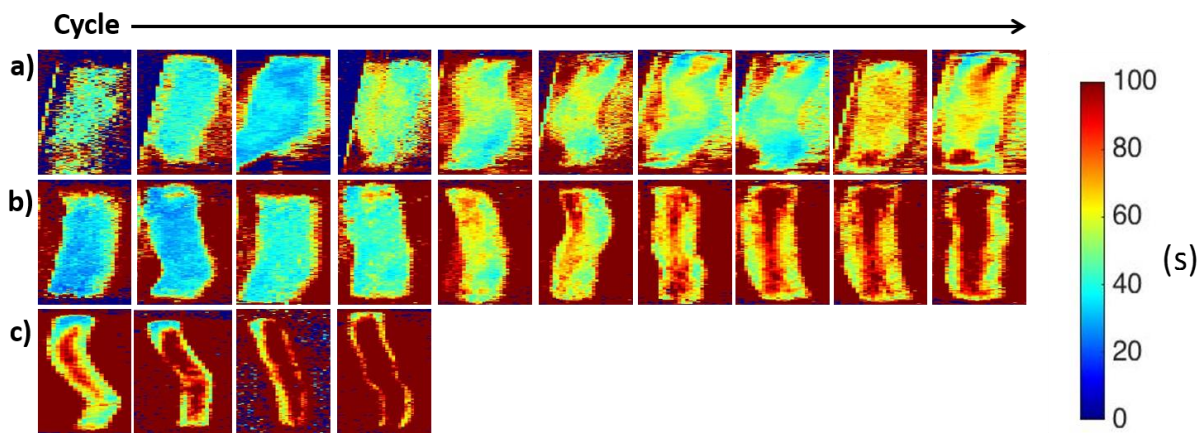
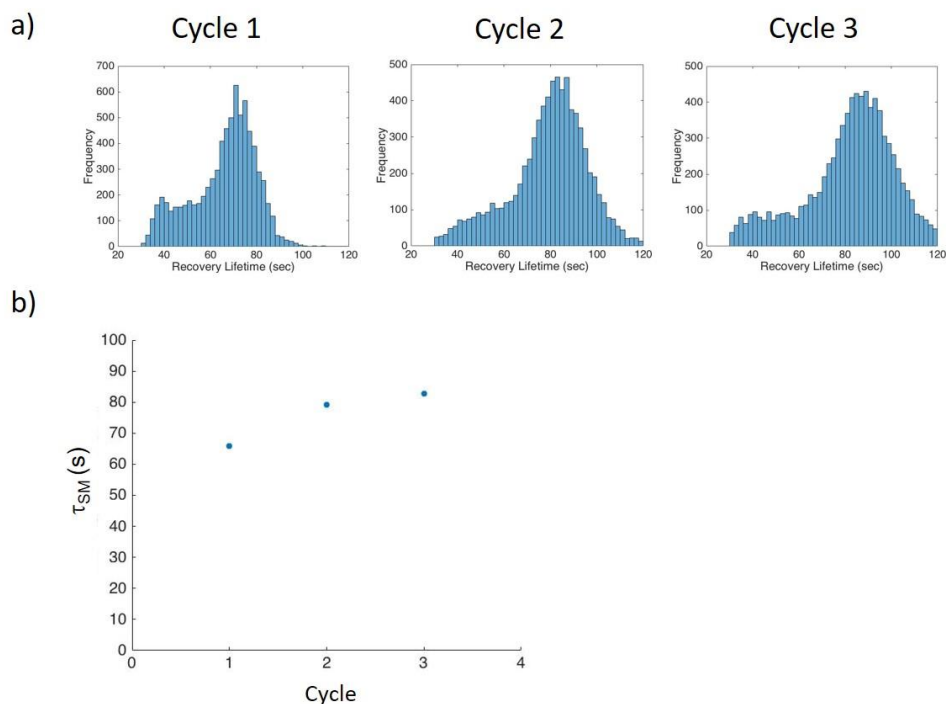
Figure S4.9. Spatially resolved smeared state decay colormaps of repeatedly smeared glass films fabricated by (a) drop casting (G1) and (b) spin casting from a concentrated gbmOMe/THF solution (0.90 M) (G2), and (c) by spin casting from a dilute solution (0.14 M) (G3) on 3" x 1" microscope slides.

Figure S4.10. (a) Distribution of recovery lifetimes τ_R for spin cast weigh paper (WP) films determined for each pixel associated with each smearing/recovery cycle. (b) Plot of smeared state decay, τ_{SM}, (i.e. average recovery lifetime) for each cycle.
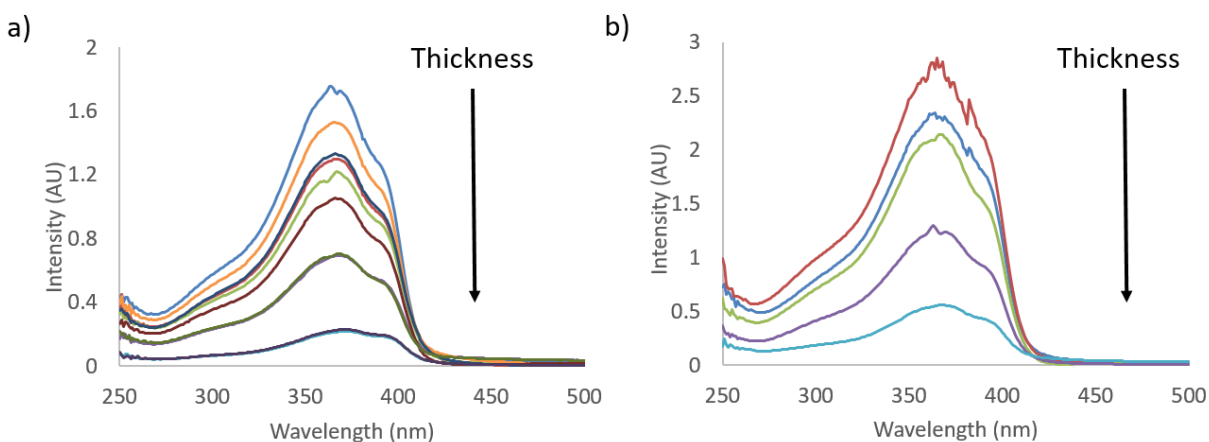

Figure S4.11. Absorption spectra of gbmOMe thin films in the amorphous phase used for the thickness testing described in Figures 4.7 (a) and 4.8 (b). Films were produced via spin casting from different concentration gbmOMe/THF solutions. Given that the path length according to Beer's Law corresponds to the sample thickness of a thin film, thicknesses relative to the thinnest sample were estimated by taking the ratio of peak absorbance for each sample to the peak absorbance of the thinnest film.

Appendix D:

Supporting Information to Chapter 5

Scheme S5.1. Synthesis of dimethylamino (DMA) substituted diketones.

R = H, OMe, F, Br, I, CF$_3$, COOMe, CN
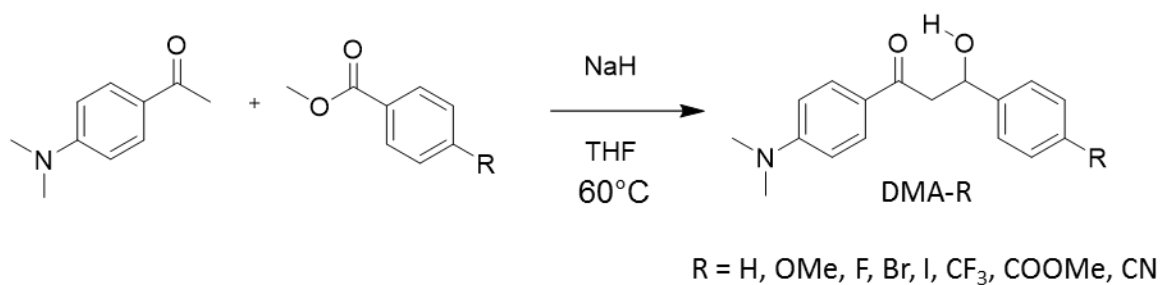
Synthesis of β-Diketones. The β-diketones were synthesized by Claisen condensation with NaH using a previously described method[1] involving 1-(4-(dimethylamino)phenyl)ethan-1-one) and the corresponding para substituted esters.

DMA-F. After recrystallization from 1:1 hexanes/EtOAc (2x), a yellow powder was obtained: 1.215g (37%). ^{1}H NMR (600 MHz, DMSO-d6) δ 17.59 (s, 1H, ArCOH) 8.17-8.15 (t, 2H, J = 12, 2″-ArH) 8.00 (d, 2H, J = 6, 2′-ArH) 7.33 (t, 2H, J = 12, 3″-ArH) 7.11 (s, 1H, COCHCO) 6.74 (d, 2H, J = 6, 3′-ArH) 2.97 (s, 6H, N(CH$_3$)$_2$) HRMS (ESI, TOF): m/z calculated for C$_{17}$H$_{17}$NO$_2$F 286.1243; found 286.1251 [M+H].

DMA-Br. After recrystallization from 1:1 hexanes/EtOAc (2x), a yellow powder was obtained: 0.420 g (34%). ^{1}H NMR (600 MHz, DMSO-d6) δ 17.53 (s, 1H, ArCOH), 8.03-7.99 (m, 4H, 2″-

ArH, 3″-ArH), 7.72 (d, 2H, J = 6, 2′-ArH) 7.14 (s, 1H, COCHCO) 6.75 (d, 2H, 3′-ArH), 3.03 (s, 6H, N(CH$_3$)$_2$) HRMS (ESI, TOF): m/z calculated for C$_{18}$H$_{17}$N$_2$O$_2$Br 346.0443; found 346.0445 [M+H].
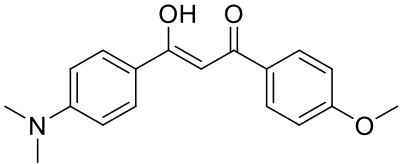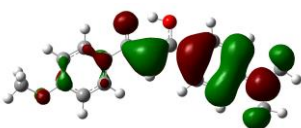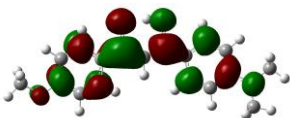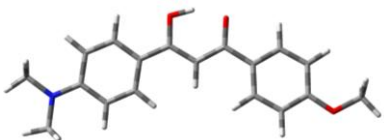
DMA-I. After recrystallization from 1:1 hexanes/EtOAc (2x), a yellow powder was obtained: 0.843g (39%). ^{1}H NMR (600 MHz, CDCl$_3$) δ 17.07 (s, 1H, ArCOH) 7.92 (d, 2H, J = 6, 3″-ArH) 7.80 (d, 2H, 2′-ArH) 7.66 (d, 2H, J = 6, 2″-ArH) 6.81 (d, 2H, J = H, 3′-ArH) 3.08 (s, 6H, N(CH$_3$)$_2$) HRMS (ESI, TOF): m/z calculated for C$_{17}$H$_{17}$NO$_2$I 394.0306; found 394.0304 [M+H].

DMA-CF$_3$. After recrystallization from 1:1 hexanes/EtOAc (2x), a yellow powder was obtained: 1.020 g, (46%). ^{1}H NMR (600 MHz, CDCl$_3$) δ 17.10 (s, 1H, ArCOH), 8.04 (d, 2H, J = 6, 2′-ArH), 7.92 (d, 2H, J = 6, 3″-ArH), 7.71 (d, 2H, J = 6, 2″-ArH), 6.75 (s, 1H, COCHCO), 6.69 (d, 2H, J = 6, 3′-ArH), 3.07 (s, 6H, N(CH$_3$)$_2$) HRMS (ESI, TOF): m/z calculated for C$_{18}$H$_{17}$F$_3$NO$_2$ 336.1211; found 336.1212 [M+H].

DMA-COOMe. This dye was passed through a silica column with 9:1 hexanes/EtOAc and recrystallized from 1:1 hexanes/EtOAc (2x). An orange powder was obtained: 0.321 g, (32%) ^{1}H NMR (600 MHz, DMSO-d6) δ 17.46 (s, 1H, ArCOH), 8.19 (d, 2H, J = 6, 2″-ArH), 8.04-8.00 (m, 4H, 2′-ArH, 3′-ArH), 7.20 (s, 1H, COCHCO), 6.75 (d, 2H, J = 9, 2″-ArH) 3.85 (s, 3H, OCH$_3$) 3.05 (s, 6H, N(CH$_3$)$_2$) HRMS (ESI, TOF): m/z calculated for C$_{19}$H$_{20}$NO$_4$Br 326.1392; found 326.1404 [M+H].

Full Computational Details

All compounds were modeled using the Gaussian 09 suite of programs[2] utilizing density functional theory (DFT). The ground state optimization of the ligands was done using the basis set B3LYP/6-311+G(d) to simulate all atoms with the exception of I, where B3LYP/SDD was used. The vibrational frequencies were calculated in an additional calculation also utilizing B3LYP/6-31G(d), and all vibrational frequencies were positive assuring that the geometries were at least a local minimum. Single point energy calculations were used to generate the molecular orbital diagrams utilizing B3LYP/6-31G(d) for all atoms except I, where B3LYP/SDD. Molecular orbitals were depicted by GaussView software. Absorption spectra at the optimized geometry were estimated using time-dependent density functional theory, TD-B3LYP/6-311+G(d) for all but I atoms, which employed B3LYP/SDD. A Tomasi polarized continuum for dichloromethane solvent was used for all calculations.[4] Cartesian Coordinates are given in Angstroms.

DMA-OMe	Occupied Orbitals	Unoccupied Orbitals
	HOMO	LUMO

E(TD-HF/TD-KS) = -977.90956420 a.u.
Dipole Moment = 7.0832 Debye

C	4.11607	1.10281	-0.17292
C	5.34217	0.43899	-0.19673
C	5.38049	-0.94766	0.01789
C	4.18334	-1.64708	0.25215
C	2.97059	-0.97193	0.26516
C	2.90941	0.42092	0.05112
H	4.08509	2.17505	-0.33569
H	2.06907	-1.54235	0.46264
C	1.63889	1.19881	0.05864
C	0.37164	0.53123	0.03221
H	0.33669	-0.54641	-0.0167
O	1.70934	2.46994	0.07421
C	-0.82459	1.23942	0.04453
C	-2.15833	0.64266	0.01924
C	-2.37082	-0.75239	0.00134
C	-3.30525	1.46488	0.01265
C	-3.64341	-1.29844	-0.02272
H	-1.52832	-1.43671	0.00817
C	-4.58627	0.93638	-0.01154
H	-3.18312	2.54265	0.02575
C	-4.80053	-0.46939	-0.0307
O	-0.80663	2.5775	0.08149
H	-3.74272	-2.37714	-0.03475
H	-5.42823	1.61809	-0.0164
H	4.22695	-2.71822	0.42597
H	6.24932	1.00304	-0.38055
N	-6.06201	-1.00286	-0.05518
C	-6.2498	-2.44922	-0.0757
H	-5.82017	-2.92497	0.81601
H	-7.31737	-2.66918	-0.09552
H	-5.79161	-2.90328	-0.96448
C	-7.23031	-0.1292	-0.06027
H	-7.24128	0.52449	-0.94267
H	-8.13211	-0.74144	-0.08055
H	-7.26589	0.50195	0.83778
H	0.17529	2.83719	0.08384
O	6.51631	-1.69668	0.02118
C	7.77247	-1.04714	-0.19666
H	8.52298	-1.83652	-0.1451
H	7.80397	-0.57328	-1.18443
H	7.9688	-0.30081	0.58163

Excitation energies and oscillator strengths:

Excited State   1:   Singlet-A   2.9913 eV 414.48 nm f=1.1302 <S**2>=0.000
   79 -> 80   0.70098

This state for optimization and/or second-order correction.
Total Energy, E(TD-HF/TD-KS) = -977.909564199
Copying the excited state density for this state as the 1-particle RhoCI density.

Excited State   2:   Singlet-A   3.8396 eV 322.91 nm f=0.1929 <S**2>=0.000
     74 -> 80   0.12152
     75 -> 80   0.24583
     78 -> 80   0.63042

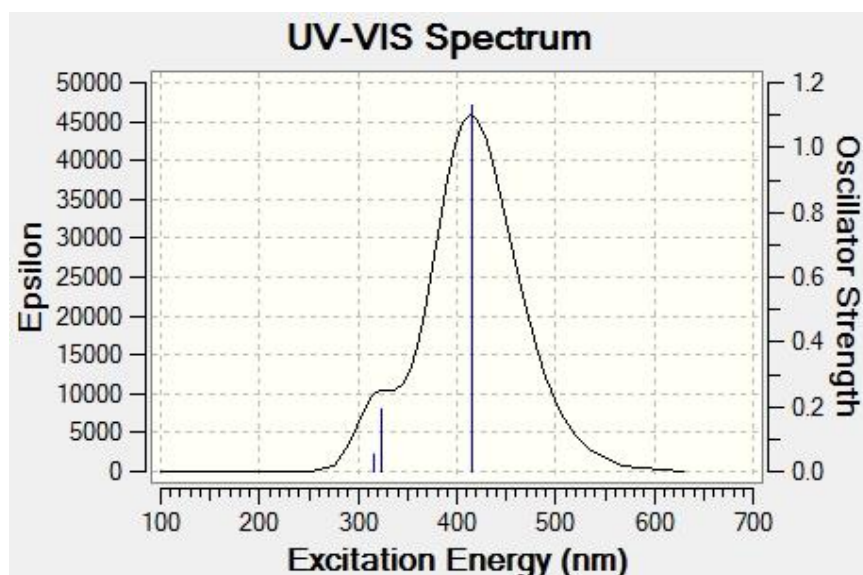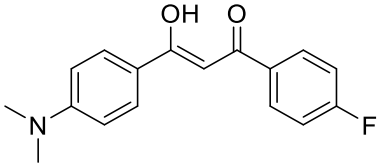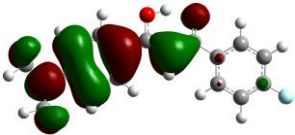Excited State   3:   Singlet-A   3.9312 eV 315.39 nm f=0.0546 <S**2>=0.000
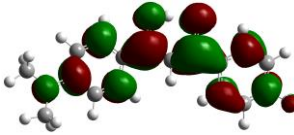   74 -> 80   0.30106
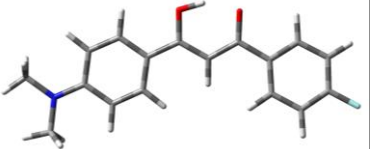   75 -> 80   0.53831
     76 -> 80   0.12634
     77 -> 80   0.11068
     78 -> 80   -0.27467

DMA-F	Occupied Orbitals	Unoccupied Orbitals
	HOMO	LUMO

E(TD-HF/TD-KS) = -962.62392731 a.u.

Dipole Moment = 10.2185 Debye

C	-4.56293	0.9175	0.26184
C	-5.7664	0.21623	0.30781
C	-5.74053	-1.1488	0.04568
C	-4.57016	-1.83339	-0.25832
C	-3.37403	-1.11562	-0.29189
C	-3.35111	0.26612	-0.03067
H	-4.54957	1.98428	0.45693
H	-2.46306	-1.64726	-0.54432
C	-2.09689	1.08219	-0.06056
C	-0.81589	0.4498	-0.03197
H	-0.75114	-0.62548	0.03649
O	-2.21116	2.348	-0.0931
C	0.36177	1.19264	-0.05886
C	1.71009	0.63524	-0.02878
C	1.96258	-0.75353	-0.00153
C	2.83292	1.49109	-0.02806
C	3.25009	-1.26182	0.02613
H	1.14024	-1.46199	-0.00434
C	4.12801	1.00049	0.00032
H	2.67935	2.56467	-0.0486
C	4.38276	-0.39897	0.02896
O	0.30388	2.52761	-0.11467
H	3.38147	-2.33691	0.04474
H	4.94998	1.70616	0.00093
H	-4.59879	-2.89795	-0.46695
H	-6.70483	0.70939	0.54047
N	5.65837	-0.89469	0.0576
C	5.88946	-2.33505	0.08596
H	5.47527	-2.82756	-0.80378
H	6.96309	-2.52258	0.10817
H	5.44393	-2.79735	0.97674
C	6.80066	0.01338	0.05741
H	6.79051	0.67322	0.93498
H	7.71997	-0.57178	0.08361
H	6.81855	0.63823	-0.8454
H	-0.683	2.76236	-0.116
F	-6.91163	-1.84407	0.08495

Excitation energies and oscillator strengths:

Excited State   1:   Singlet-A   2.9599 eV 418.87 nm f=0.9705 <S**2>=0.000
     75 -> 76   0.70368
 This state for optimization and/or second-order correction.
 Total Energy, E(TD-HF/TD-KS) = -962.623927305

Copying the excited state density for this state as the 1-particle RhoCI density.

Excited State   2:   Singlet-A   3.8853 eV 319.11 nm f=0.0044 <S**2>=0.000
         70 -> 76   0.13347
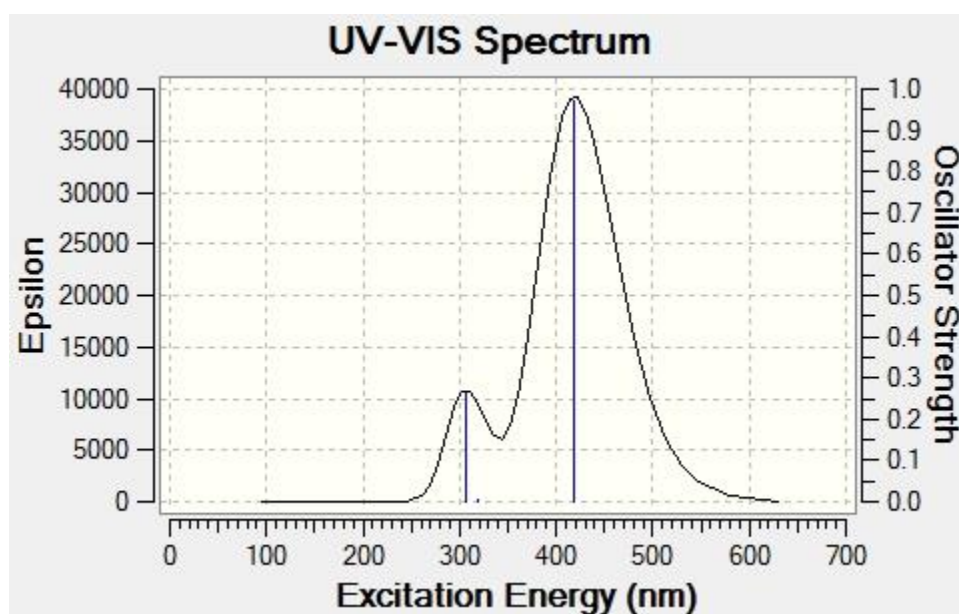   71 -> 76   0.59372
         72 -> 76   0.15155
         73 -> 76   0.30077
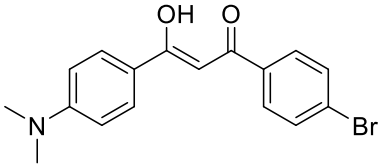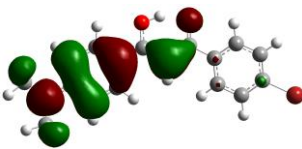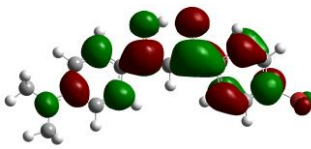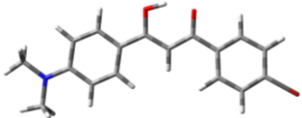
Excited State   3:   Singlet-A   4.0529 eV 305.91 nm f=0.2659 <S**2>=0.000
         74 -> 76   0.60199
         75 -> 77   -0.33480
         75 -> 78   0.11881

DMA-Br	Occupied Orbitals	Unoccupied Orbitals
	HOMO	LUMO

E(TD-HF/TD-KS) -3436.89947099 a.u.
Dipole Moment 10.3778 Debye

```
C          -3.3015   1.58916  0.24374
C          -4.57157  1.01631  0.26206
C          -4.69992 -0.34905  0.00354
C          -3.58658 -1.14343 -0.26982
C          -2.32151 -0.5556  -0.28188
C          -2.15936  0.81573 -0.02321
H          -3.1831   2.65006  0.43631
H          -1.46786 -1.1828  -0.51522
C          -0.82789  1.50129 -0.04996
C           0.38097  0.74218 -0.03193
H           0.33614 -0.33445  0.02899
O          -0.81561  2.7721  -0.07518
C           1.62839  1.36203 -0.05706
C           2.9126   0.67087 -0.02996
C           3.02283 -0.73656 -0.00885
C           4.11628  1.40881 -0.02362
C           4.25206 -1.37273  0.01932
H           2.13322 -1.35824 -0.01695
C           5.35473  0.7895   0.00486
H           4.07213  2.49247 -0.0398
C           5.4662  -0.62871  0.02845
O           1.70541  2.6962  -0.10529
H           4.27403 -2.45563  0.03363
H           6.24388  1.40823  0.00947
H          -3.70024 -2.20212 -0.47684
H          -5.44577  1.62252  0.47499
N           6.68505 -1.25042  0.05783
C           6.76953 -2.7071   0.0808
H           6.30961 -3.15199 -0.81157
H           7.81863 -3.00221  0.10393
H           6.27771 -3.12516  0.96902
C           7.91337 -0.46248  0.06176
H           7.96878  0.19239  0.94136
H           8.76886 -1.13753  0.08707
H           7.99567  0.15983 -0.83914
H           0.74778  3.03001 -0.10316
Br         -6.433   -1.14972  0.03392
```

Excitation energies and oscillator strengths:

Excited State   1:   Singlet-A   2.8961 eV 428.11 nm f=0.9895 <S**2>=0.000
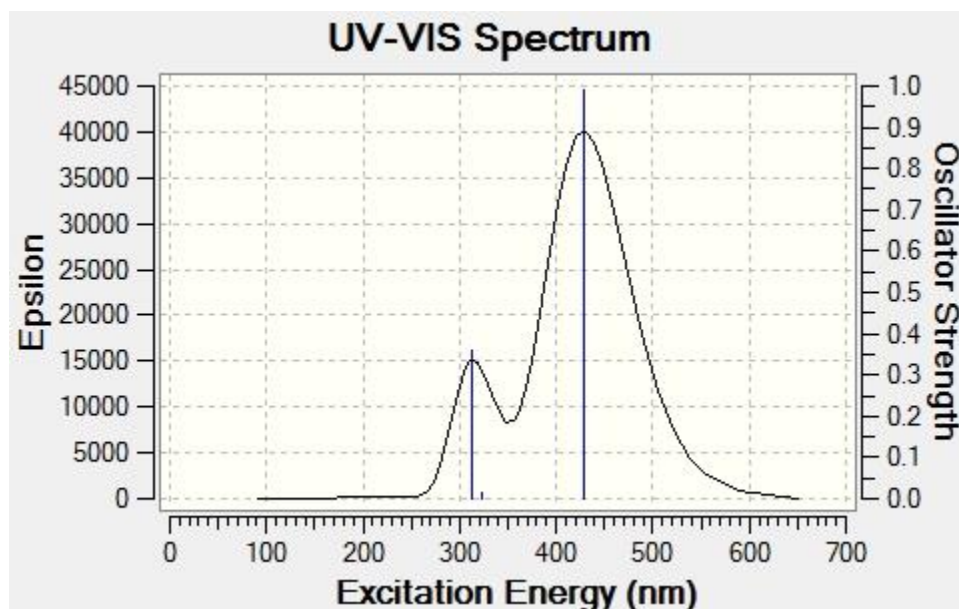   **88 -> 89   0.70315**
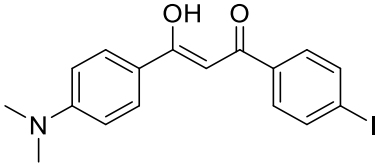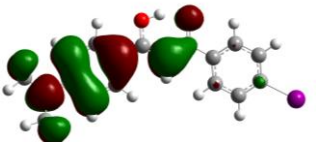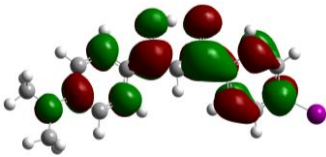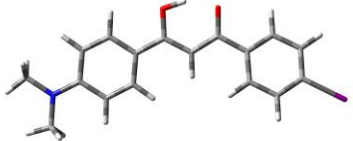This state for optimization and/or second-order correction.
Total Energy, E(TD-HF/TD-KS) = -3436.89947099
Copying the excited state density for this state as the 1-particle RhoCI density.

Excited State   2:   Singlet-A   3.8409 eV 322.80 nm f=0.0145 <S**2>=0.000
   83 -> 89   0.18778
   84 -> 89   0.63029
   86 -> 89   0.17743
   87 -> 89   0.13157

Excited State   3:   Singlet-A   3.9564 eV 313.38 nm f=0.3600 <S**2>=0.000
   84 -> 89   -0.13085
   87 -> 89   0.60094
   88 -> 90   0.33396

DMA-I	Occupied Orbitals	Unoccupied Orbitals
	HOMO	LUMO

E(TD-HF/TD-KS) = -873.93384033 a.u.
Dipole Moment = 10.2066 Debye

C	-2.58045	1.82404	0.2621
C	-3.86942	1.28975	0.28748
C	-2.96212	-0.88082	-0.32867
C	-1.67732	-0.3332	-0.33935
C	-1.46667	1.02381	-0.04287
H	-2.42684	2.87468	0.48523
H	-0.84792	-0.98077	-0.60372
C	-0.11046	1.66053	-0.051
C	1.06765	0.85403	-0.02795
H	0.97856	-0.22044	0.01978
O	-0.04928	2.93016	-0.06344
C	2.33932	1.42356	-0.04086
C	3.5941	0.67955	-0.01705
C	3.64435	-0.73089	0.03495
C	4.82849	1.36499	-0.04724
C	4.84561	-1.41903	0.05731
H	2.72891	-1.31326	0.06073
C	6.03987	0.69308	-0.02697
H	4.83059	2.44894	-0.08746
C	6.09071	-0.7282	0.02708
O	2.46961	2.75363	-0.07925
H	4.82151	-2.50117	0.09874
H	6.95481	1.27259	-0.05245
H	-3.10325	-1.92882	-0.57
H	-4.71445	1.92385	0.53463
N	7.28229	-1.40172	0.04954
C	7.30473	-2.85955	0.11459
H	6.80747	-3.30965	-0.75482
H	8.34052	-3.19926	0.12532
H	6.81424	-3.23009	1.02456
C	8.54295	-0.66704	0.02179
H	8.6412	-0.00181	0.89
H	9.3695	-1.3775	0.0432
H	8.63624	-0.06255	-0.89
H	1.52622	3.12545	-0.08055
I	-6.02264	-0.90501	0.02464
C	-4.04734	-0.06343	-0.00902

Excitation energies and oscillator strengths:

Excited State   1:   Singlet-A   2.9217 eV 424.35 nm f=0.9907 <S**2>=0.000
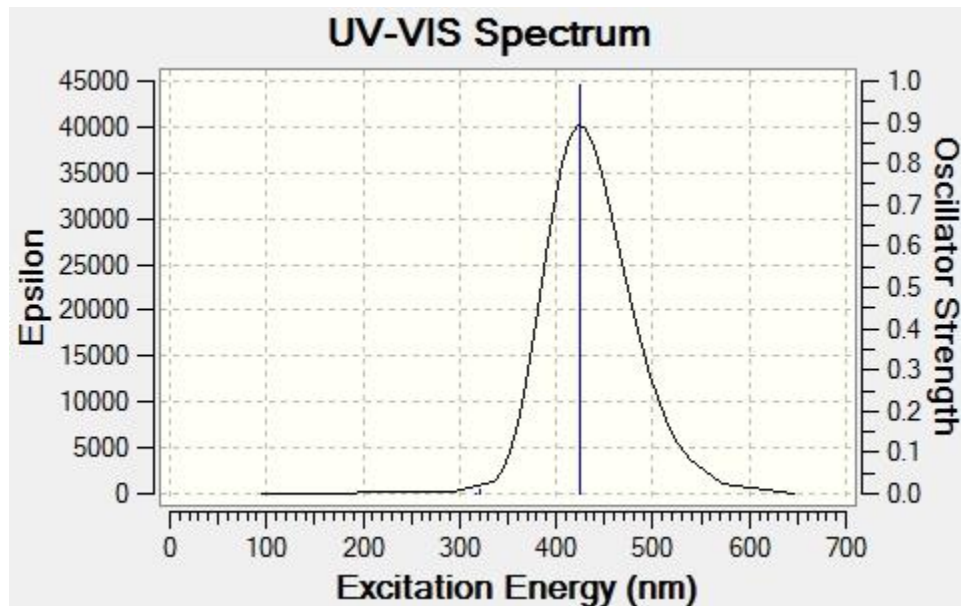   **74 -> 75   0.70296**
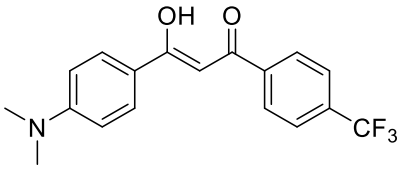 This state for optimization and/or second-order correction.
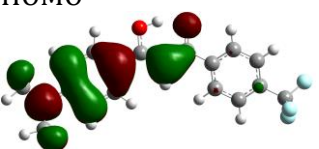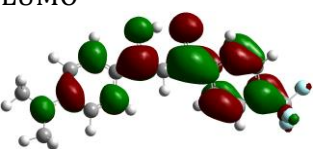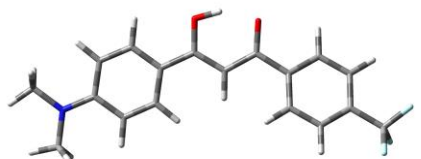 Total Energy, E(TD-HF/TD-KS) = -873.933840332
 Copying the excited state density for this state as the 1-particle RhoCI density.

Excited State   2:   Singlet-A   3.8542 eV 321.69 nm f=0.0119 <S**2>=0.000
        68 -> 75   0.17533
        70 -> 75   0.65065
        72 -> 75   -0.12827
        73 -> 75   -0.12320

Excited State   3:   Singlet-A   3.9133 eV 316.82 nm f=0.0009 <S**2>=0.000
        74 -> 76   0.70039

DMA-CF$_3$	Occupied Orbitals	Unoccupied Orbitals
	HOMO	LUMO

E(TD-HF/TD-KS) = -1200.50918528 a.u.
Dipole Moment = 11.7488 Debye

C   -3.3666   1.5491   0.3294
C   -4.62737 0.95789 0.35387

272

```
C          -4.77184  -0.38168  -0.02647
C          -3.6546   -1.1246   -0.42366
C          -2.39439  -0.52872  -0.43458
C          -2.23363   0.81433  -0.05637
H          -3.24624   2.58946   0.61115
H          -1.54484  -1.11606  -0.76606
C          -0.90301   1.50872  -0.06674
C           0.30339   0.74987  -0.03768
H           0.25453  -0.32714   0.01764
O          -0.8994    2.77886  -0.08381
C           1.55221   1.37093  -0.05099
C           2.83537   0.68069  -0.02045
C           2.94467  -0.72583   0.04601
C           4.03996   1.41713  -0.05835
C           4.17335  -1.36221   0.07417
H           2.05456  -1.34588   0.07918
C           5.27779   0.79735  -0.03269
H           3.99651   2.49972  -0.10948
C           5.3883   -0.61993   0.0353
O           1.62675   2.70456  -0.09733
H           4.19477  -2.44386   0.12735
H           6.16753   1.41435  -0.06519
H          -3.76435  -2.15931  -0.73172
H          -5.49185   1.53788   0.66051
N           6.60633  -1.24192   0.0623
C           6.69018  -2.69715   0.13665
H           6.20668  -3.17268  -0.72671
H           7.73926  -2.99303   0.14239
H           6.22144  -3.0817    1.05214
C           7.83568  -0.45588   0.02796
H           7.90484   0.22148   0.88937
H           8.69056  -1.13145   0.05775
H           7.90494   0.14233  -0.88999
H           0.67024   3.03939  -0.10128
C          -6.12264  -1.03988   0.03535
F          -6.35016  -1.62891   1.24651
F          -6.26728  -2.02002  -0.89305
F          -7.14062  -0.16308  -0.15551
```

Excitation energies and oscillator strengths:

Excited State   1:   Singlet-A   2.8238 eV 439.06 nm f=0.8475 <S**2>=0.000
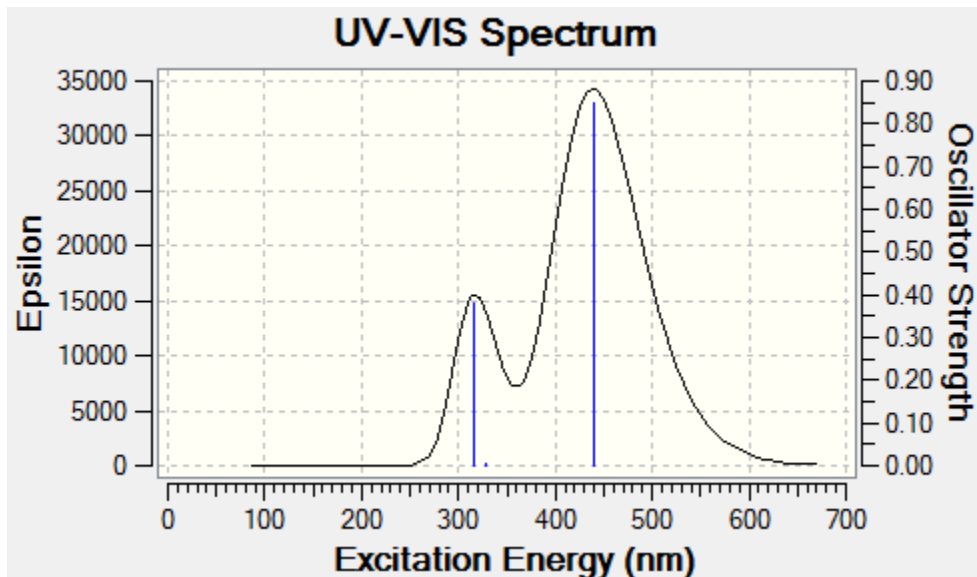 **87 -> 88   0.70466**
This state for optimization and/or second-order correction.
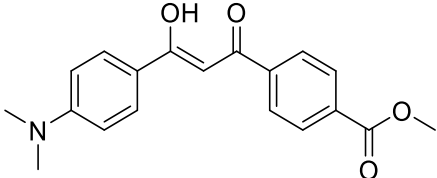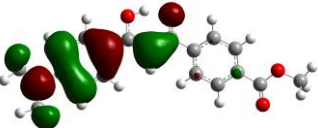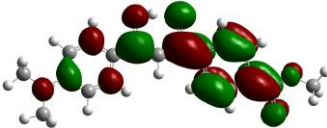Total Energy, E(TD-HF/TD-KS) = -1200.50918528
Copying the excited state density for this state as the 1-particle RhoCI density.

Excited State   2:   Singlet-A   3.7881 eV 327.30 nm f=0.0048 <S**2>=0.000
       82 -> 88   -0.14716
       83 -> 88   0.24541
       84 -> 88   0.63753

Excited State   3:   Singlet-A   3.9142 eV 316.76 nm f=0.3800 <S**2>=0.000
       86 -> 88   -0.44506
       87 -> 89   0.54068

UV-VIS Spectrum

DMA-COOMe	Occupied Orbitals	Unoccupied Orbitals
	HOMO 	LUMO

E(TD-HF/TD-KS) = -1091.30891292 a.u.
Dipole Moment = 8.4354 Debye

C	-3.34386	1.49949	0.26643
C	-4.60039	0.90095	0.29497
C	-4.74333	-0.45149	-0.05489
C	-3.61048	-1.18864	-0.43024
C	-2.35366	-0.58929	-0.4464

C	-2.20259	0.76381	-0.09572
H	-3.2302	2.54573	0.52926
H	-1.49762	-1.17903	-0.75692
C	-0.87646	1.46469	-0.1066
C	0.33511	0.71339	-0.06361
H	0.29254	-0.36339	0.00002
O	-0.87756	2.73513	-0.13578
C	1.57982	1.34203	-0.0713
C	2.8674	0.66019	-0.02474
C	2.98544	-0.74565	0.03908
C	4.06728	1.40481	-0.04357
C	4.21803	-1.37376	0.08282
H	2.09923	-1.37188	0.05608
C	5.30895	0.79343	-0.00154
H	4.01714	2.48723	-0.09236
C	5.42825	-0.62314	0.06419
O	1.64658	2.67591	-0.12599
H	4.24599	-2.45548	0.13191
H	6.19478	1.41664	-0.01952
H	-3.7246	-2.23053	-0.71104
H	-5.46995	1.47963	0.58614
N	6.65015	-1.23699	0.10744
C	6.74275	-2.69211	0.17115
H	6.27858	-3.16404	-0.70485
H	7.79358	-2.98089	0.19435
H	6.2598	-3.08727	1.07456
C	7.87452	-0.44287	0.08712
H	7.92723	0.23736	0.94735
H	8.73342	-1.11258	0.13104
H	7.95263	0.15336	-0.83155
H	0.68711	3.00372	-0.14104
C	-6.06631	-1.14059	-0.04712
O	-6.23134	-2.31337	-0.3491
O	-7.07247	-0.33139	0.33156
C	-8.39183	-0.91566	0.36967
H	-9.05154	-0.11122	0.69323
H	-8.67574	-1.27145	-0.62356
H	-8.41692	-1.7447	1.08094

Excitation energies and oscillator strengths:

Excited State   1:   Singlet-A   2.7174 eV 456.26 nm f=0.7632   <S2>=0.000**
    86 -> 87   0.70471
This state for optimization and/or second-order correction.
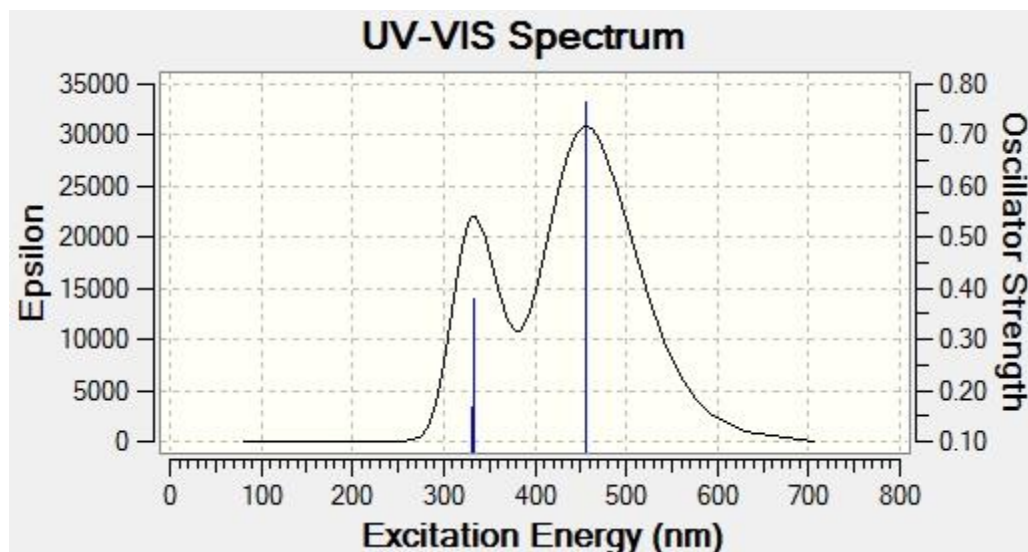Total Energy, E(TD-HF/TD-KS) = -1091.30891292
Copying the excited state density for this state as the 1-particle RhoCI density.
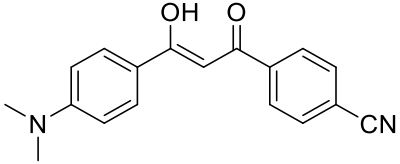
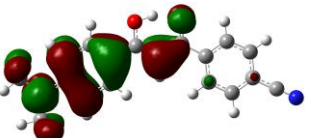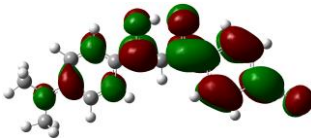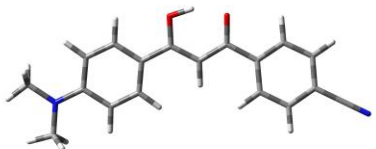Excited State   2:   Singlet-A   3.7129 eV 333.93 nm f=0.3790 <S**2>=0.000
      81 -> 87   -0.11965
      82 -> 87   0.23192
      83 -> 87   0.33320
      85 -> 87   -0.23259
      86 -> 88   0.50664

Excited State   3:   Singlet-A   3.7352 eV 331.93 nm f=0.1661 <S**2>=0.000
      81 -> 87   -0.27810
      82 -> 87   0.28456
      83 -> 87   0.38801
      85 -> 87   0.16491
      86 -> 88   -0.38745

DMA-CN	Occupied Orbitals	Unoccupied Orbitals
	HOMO	LUMO

E(TD-HF/TD-KS) = -955.40196265 a.u.
Dipole Moment = 12.5894 Debye

C	-4.27916	1.14948	0.302
C	-5.50255	0.4902	0.34689
C	-5.56523	-0.87935	0.03111
C	-4.39631	-1.57385	-0.32708
C	-3.17718	-0.90274	-0.35833
C	-3.101	0.46465	-0.04222
H	-4.22062	2.20646	0.53705
H	-2.29066	-1.45354	-0.65276
C	-1.81411	1.2383	-0.07007
C	-0.56374	0.5565	-0.0399
H	-0.54305	-0.52062	0.02583
O	-1.89003	2.50613	-0.10107
C	0.64448	1.25501	-0.06045
C	1.96733	0.64621	-0.02747
C	2.16342	-0.7521	0.0082
C	3.12431	1.45671	-0.03207
C	3.42862	-1.31159	0.03859
H	1.31335	-1.42677	0.01068
C	4.39766	0.91439	-0.0014
H	3.0143	2.53548	-0.059
C	4.59556	-0.4947	0.03549
O	0.63468	2.58986	-0.11386
H	3.51614	-2.39095	0.0642
H	5.24764	1.58585	-0.00554
H	-4.44708	-2.62768	-0.58116
H	-6.40577	1.02534	0.62223
N	5.84884	-1.04098	0.06607
C	6.02128	-2.48988	0.10065
H	5.58608	-2.96855	-0.78645
H	7.08633	-2.7207	0.12227
H	5.5586	-2.92912	0.99414
C	7.02854	-0.18119	0.05865
H	7.04661	0.48408	0.93181
H	7.92239	-0.80436	0.08816
H	7.07126	0.43579	-0.84855
H	-0.34104	2.86414	-0.11915
C	-6.82285	-1.56763	0.07007
N	-7.84401	-2.12663	0.10246

Excitation energies and oscillator strengths:

Excited State   1:   Singlet-A   2.7624 eV 448.83 nm f=0.7127   <S**2>=0.000
     77 -> 78   0.70513
This state for optimization and/or second-order correction.
Total Energy, E(TD-HF/TD-KS) = -955.401962651
Copying the excited state density for this state as the 1-particle RhoCI density.

Excited State   2:   Singlet-A   3.6828 eV   336.66 nm   f=0.0062   <S**2>=0.000
     73 -> 78   -0.22932
     74 -> 78   0.65358

Excited State   3:   Singlet-A   3.8194 eV   324.62 nm   f=0.5300   <S**2>=0.000
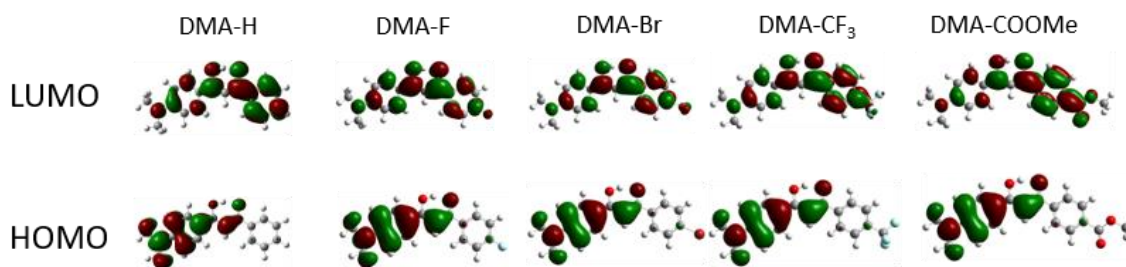   76 -> 78   0.47424
     77 -> 79   0.51477

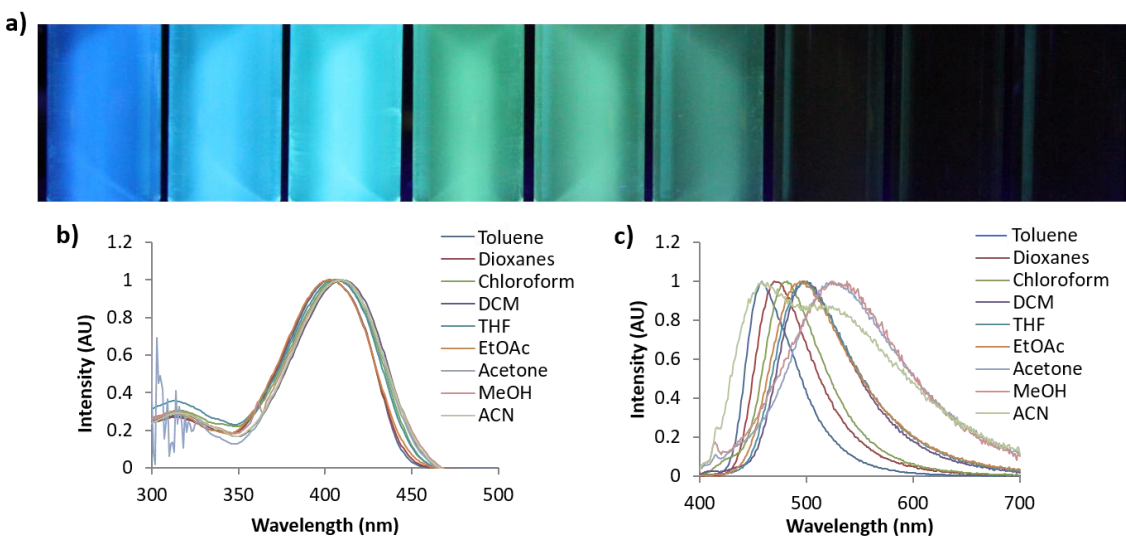**Figure S5.1.** Molecular orbitals of selected DMA substituted diketones.

Figure S5.2. Image of DMA-I dissolved (from left to right) in toluene, dioxanes, $CHCl_3$, CH_2Cl_2, THF, EtOAc, MeOH, and ACN (1×10^{-5}M) ($\lambda_{ex} = 365$ nm) (a), and corresponding absorption (b), and emission (c) spectra. ($\lambda_{ex} = 385$ nm)
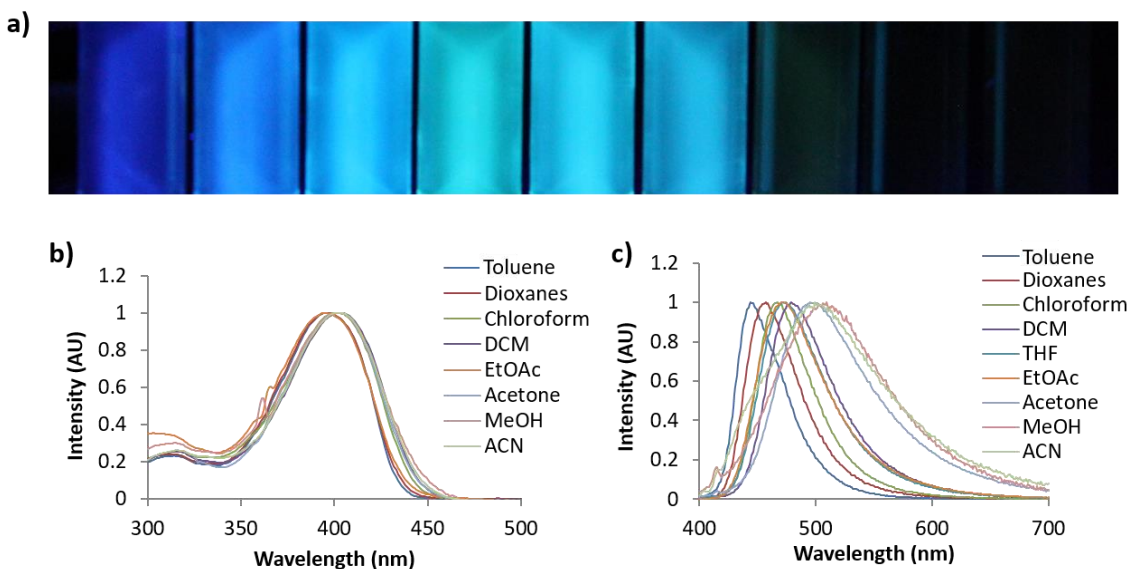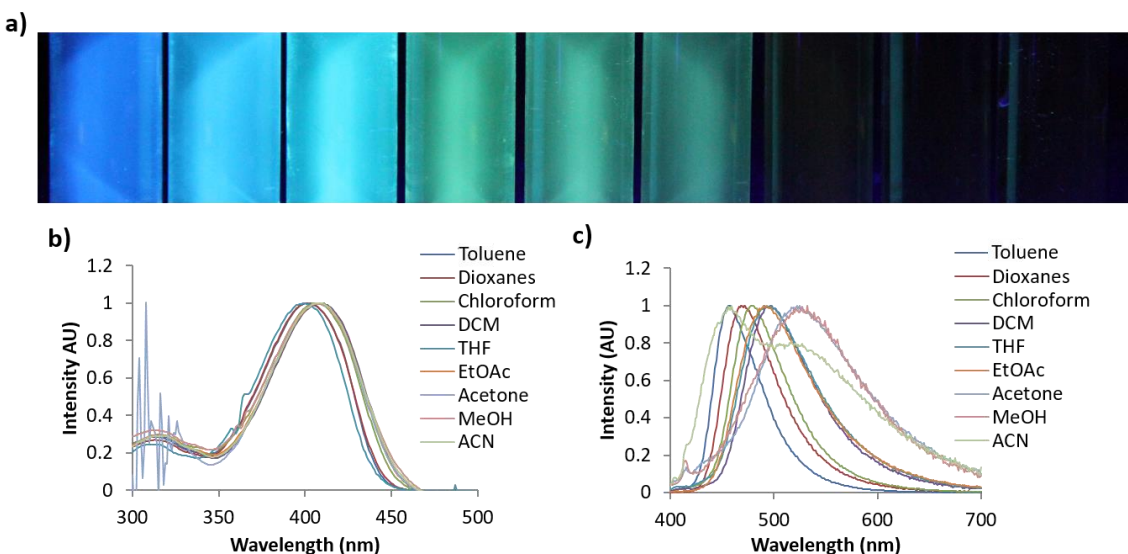
Figure S5.3. Image of DMA-F dissolved (from left to right) in toluene, dioxanes, CHCl$_3$, CH$_2$Cl$_2$, THF, EtOAc, MeOH, and ACN (1 x 10^{-5}M) (λ_{ex} = 365 nm) (a), and corresponding absorption (b), and emission (c) spectra. (λ_{ex} = 385 nm).

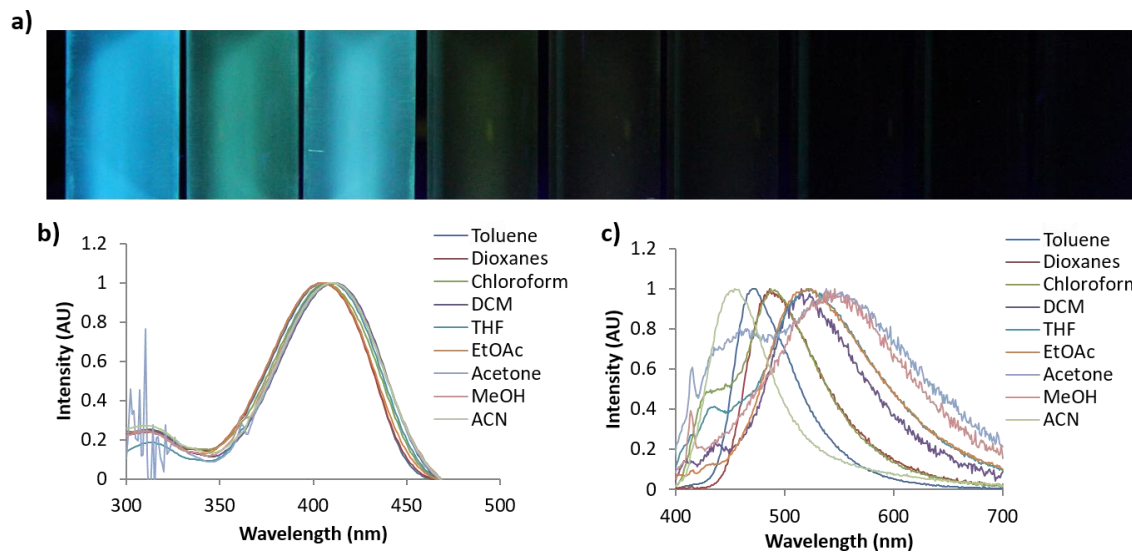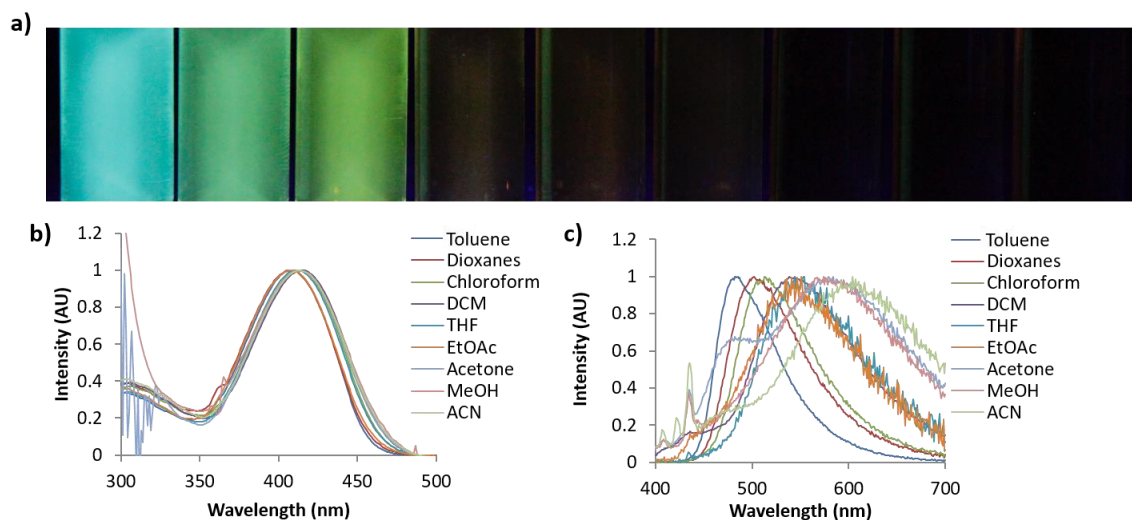**Figure S5.4.** Image of DMA-Br dissolved (from left to right) in toluene, dioxanes, CHCl$_3$, CH$_2$Cl$_2$, THF, EtOAc, MeOH, and ACN (1 x 10^{-5}M) (λ_{ex} = 365 nm) (a), and corresponding absorption (b), and emission (c) spectra. (λ_{ex} = 385 nm).

Figure S5.5. Image of DMA-CF₃ dissolved (from left to right) in toluene, dioxanes, CHCl₃, CH₂Cl₂, THF, EtOAc, MeOH, and ACN (1 x 10⁻⁵M) (λ_{ex} = 365 nm) (a), and corresponding absorption, (b) and emission (c) spectra (λ_{ex} = 385 nm).

Figure S5.6. Image of DMA-COOMe dissolved (from left to right) in toluene, dioxanes, CHCl₃, CH₂Cl₂, THF, EtOAc, MeOH, and ACN (1 x 10⁻⁵M) (λ_{ex} = 365 nm) (a), and corresponding absorption (b), and emission (c) spectra (λ_{ex} = 385 nm).
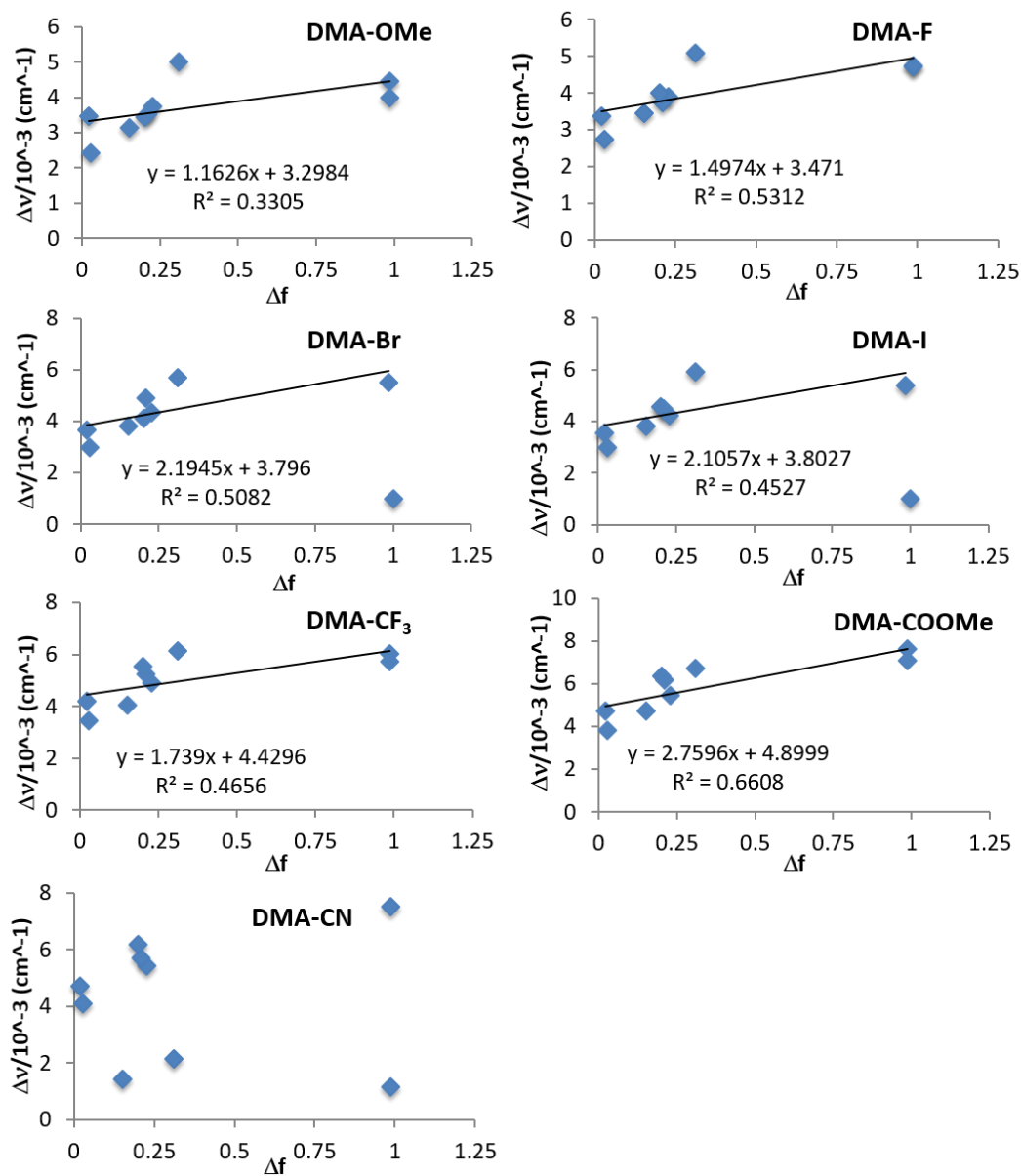
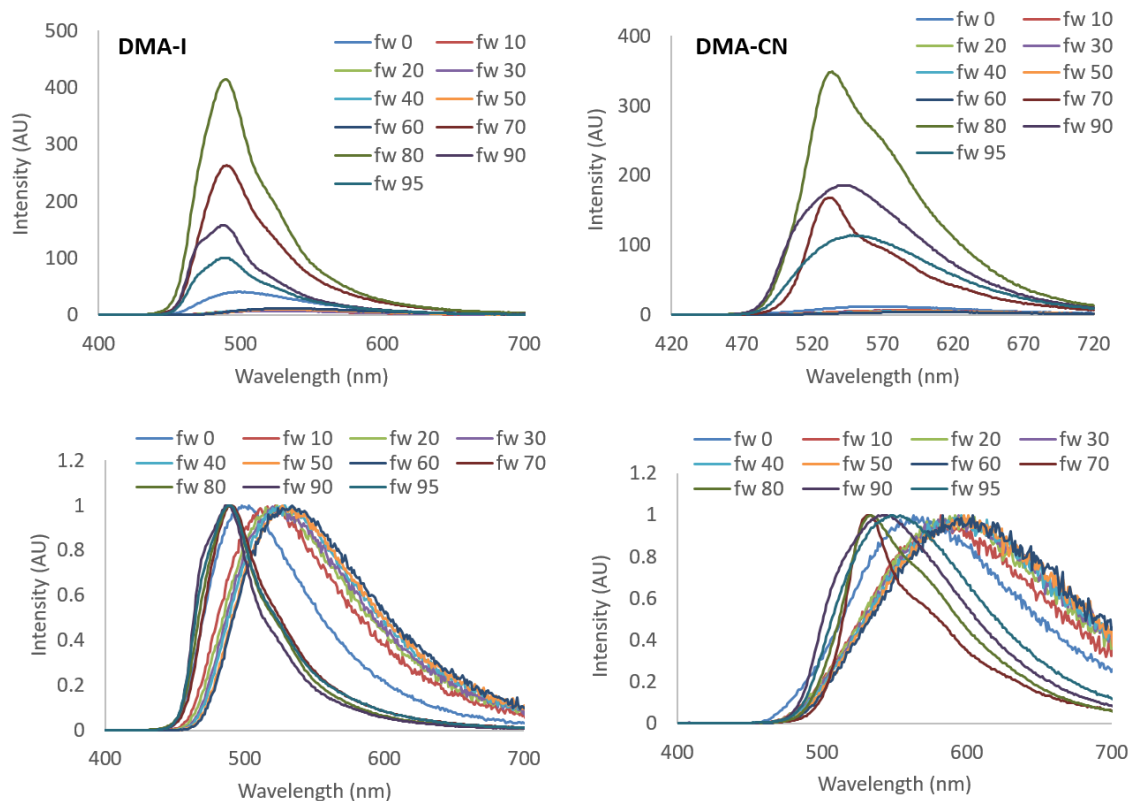**Figure S5.7**. Lippert Mataga plots of DMA substituted diketones.

Figure S5.8. Raw (top) and normalized by peak wavelength (bottom) emission spectra of DMA-I and DMA-CN in THF/H_2O solutions with increasing water fractions (fw, %). (λ_{ex} = 369 nm).
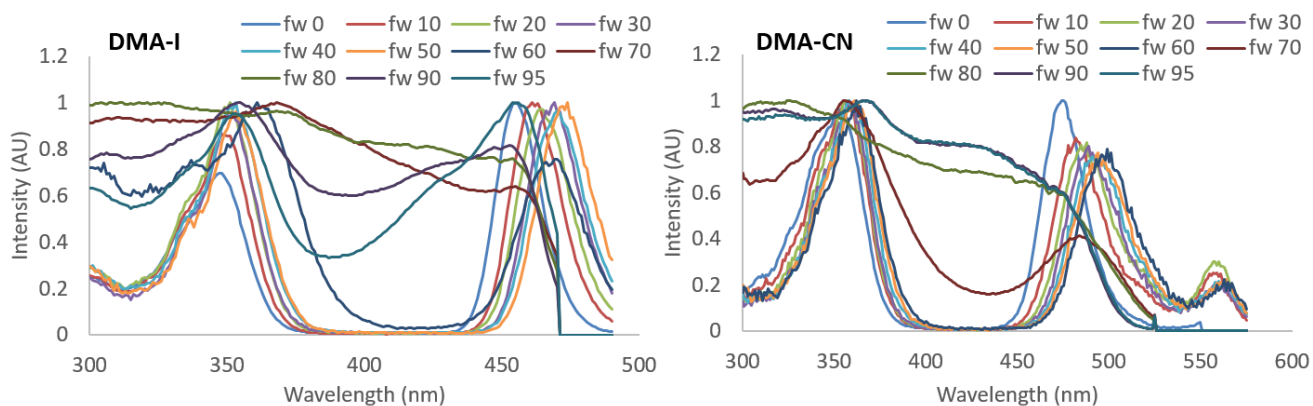

Figure S5.9. Excitation spectra of DMA-I and DMA-CN in THF/H_2O solutions with increasing water fractions (fw, %). (λ_{ex} = 369 nm)
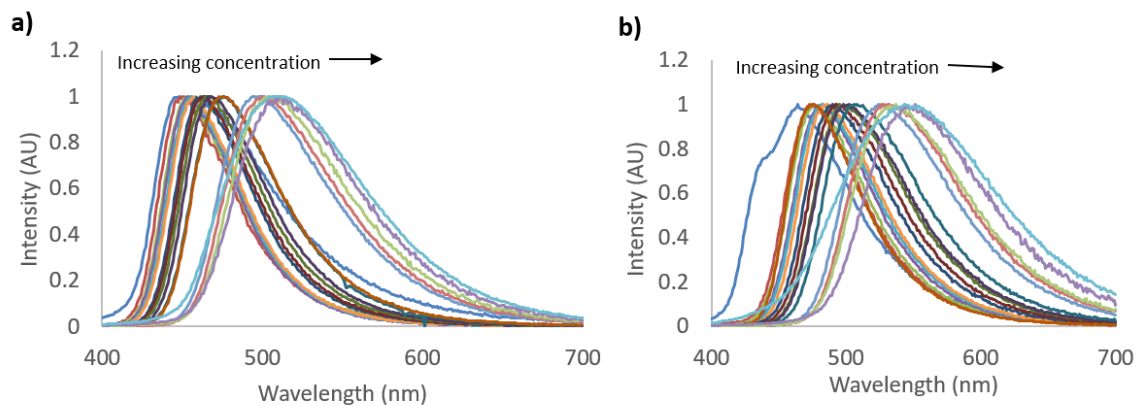
Figure S5.10. Emission spectra of Dye/PS thin films of DMA-I (a) and DMA-CN (b) with increasing dye concentration.
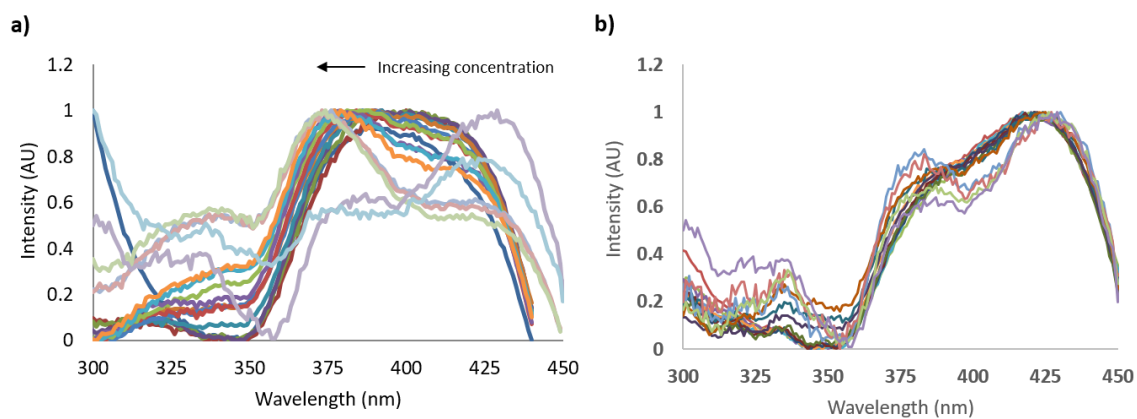

Figure S5.11. Excitation spectra of Dye/PS thin films of DMA-I (a) and DMA-CN (b) with increasing dye concentration.

Figure S5.12. Emission spectra of Dye/CA/PS thin films of DMA-I (a) and DMA-CN (b) with increasing CA concentration.

Figure S5.13. Powder XRD patterns of DMA-I (a) and DMA-CN (b) polystyrene (PS) films doped with camphoric anhydride (CA).
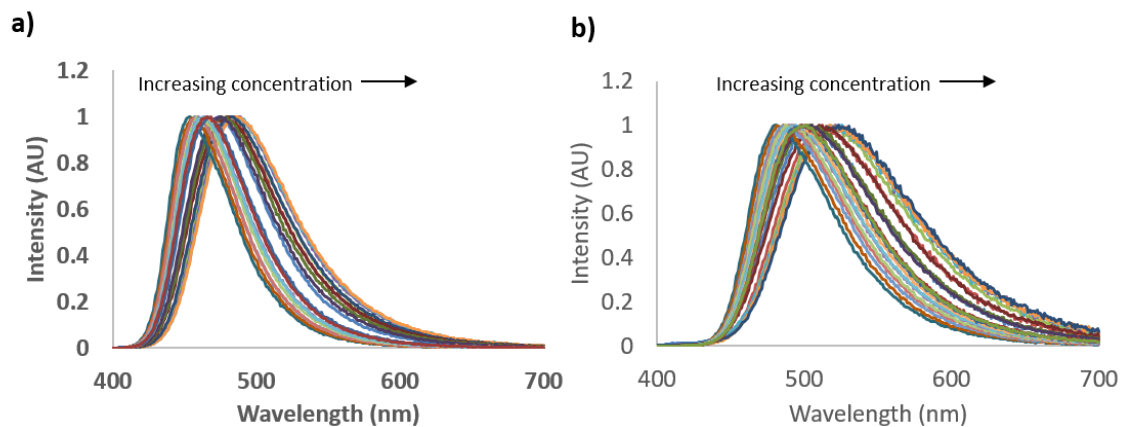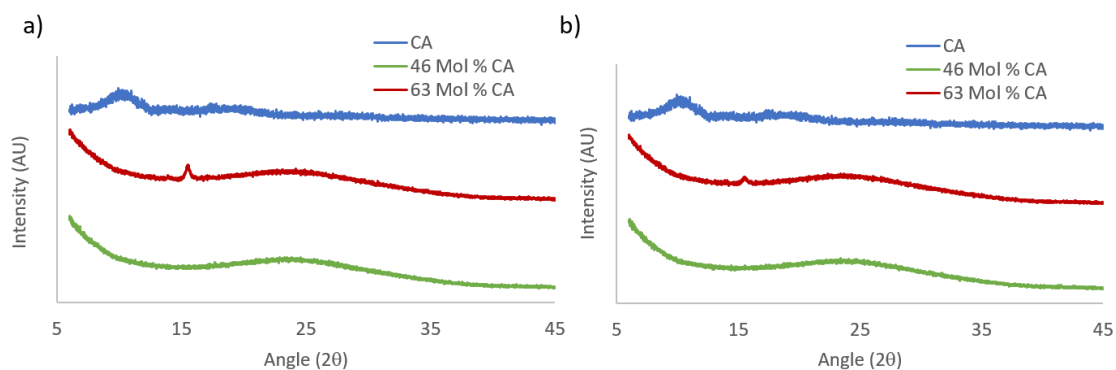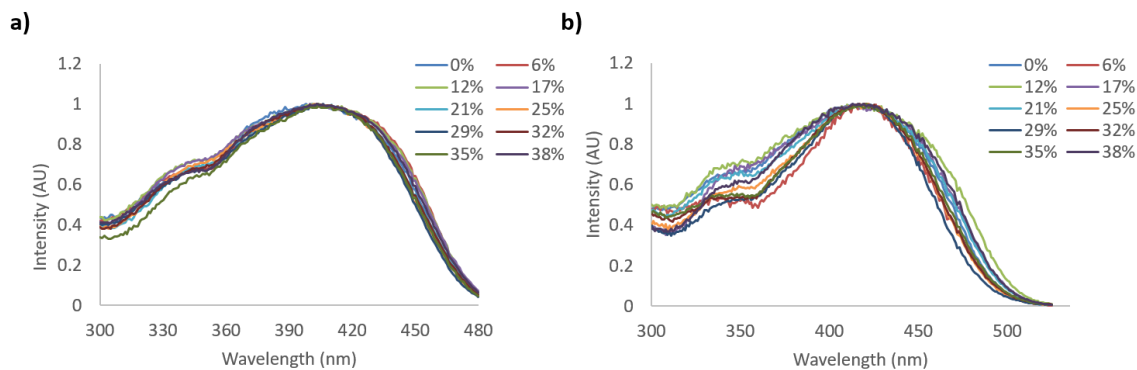
Figure S5.14. Excitation spectra of dye/CA/PS thin films of DMA-I (a) and DMA-CN (b) with increasing CA concentration.
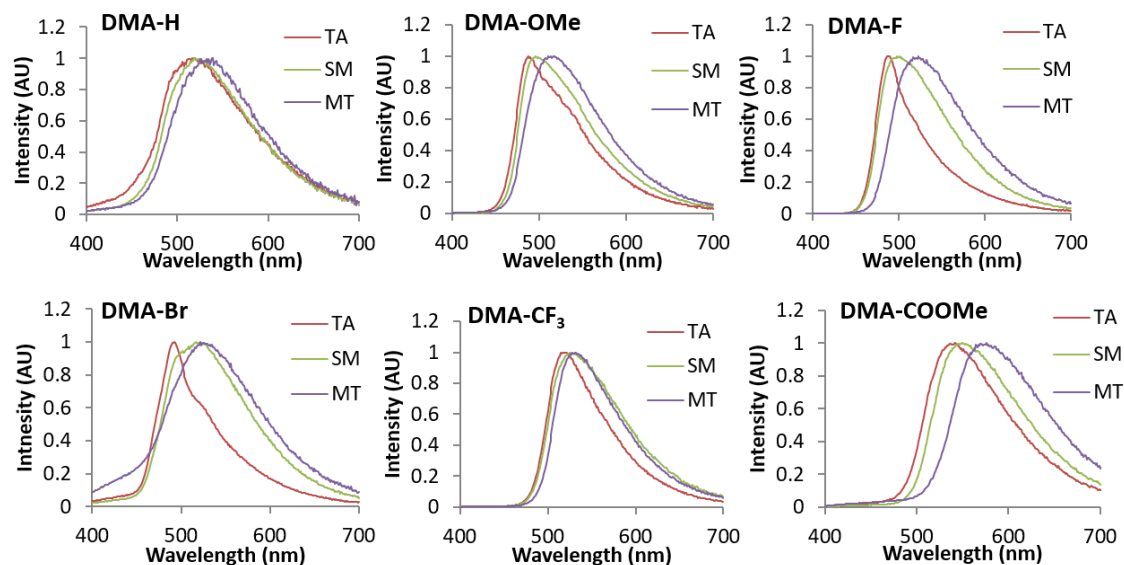
Figure S5.15. Total emission spectra of diketone films on weigh paper substrates in thermally annealed (TA), smeared (SM) and melted (MT) phases. (λ_{ex}= 369 nm).
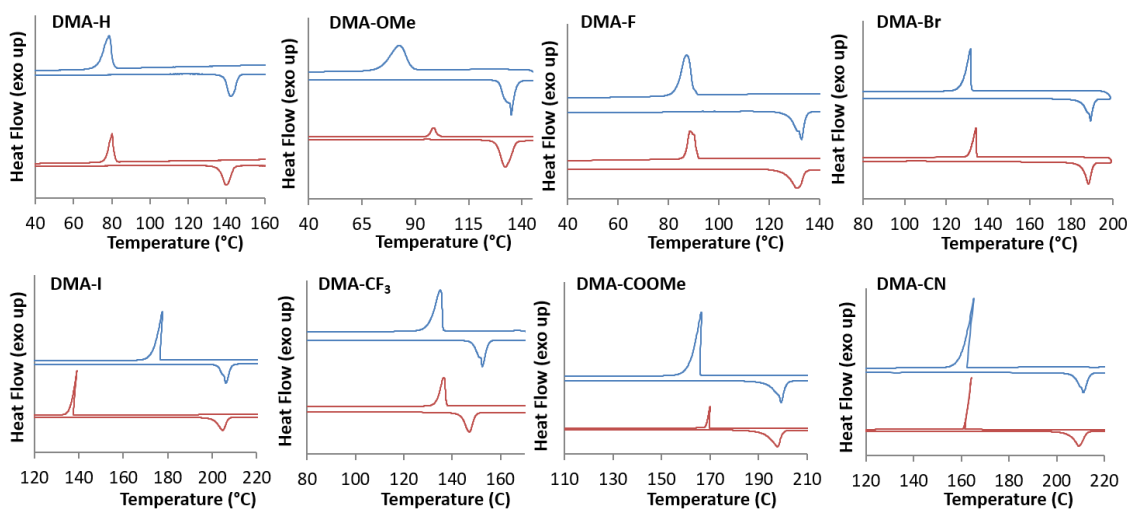
Figure S5.16. Differential scanning calorimetery (DSC) thermograms of diketones. Cooling rate varied between first (blue, 10 ℃/min) and second (red, 1 ℃/min) cycles. (Heating rate = 5 ℃/min)
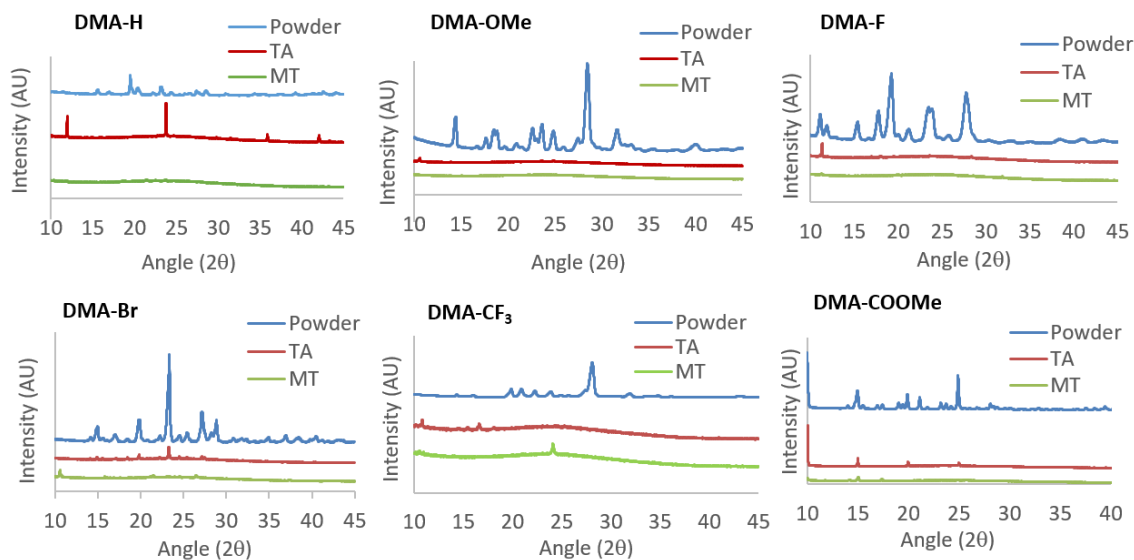
Figure S5.17. Powder X-ray diffraction patterns of diketones as bulk powders and glass films in the thermally annealed (TA) and melted (MT) states.

References

286

1   N. D. Nguyen, G. Zhang, J. Lu, A. E. Sherman and C. L. Fraser, *J. Mater. Chem.*, 2011,
21, 8409–8415.

2   M. J. Frisch, G. W. Trucks, H. B. Schlegel, G. E. Scuseria, M. A. Robb, J. R. Cheeseman,
G. Scalmani, V. Barone, B. Mennucci and G. A. Petersson, *Gaussian 09 Revis. A.1; Gaussian,
Inc. Wallingford, CT*, 2009.

4   R. Tomasi, J.; Mennucci, B.; Cammi, *Chem. Rev.*, 2005, **105**, 2999–3094.

Appendix E

Chapter 6 Supporting Information

Synthetic details

L-F. Yellow powder (0.915 g, 51%). Made as previously described.[1]

L-I. Brown powder (1.588 g, 65 %). ^{1}H NMR (600 MHz, DMSO-d6) δ 17. 36 (s, 1H, ArCOH) 8.04 (s, 4H, 2,3-ArH) 7.51 (s, 2H, 2′-ArH) 7.39 (s, 1H, COCHCO) 3.98 (s, 6H, 3′-OCH$_3$) 3.84 (s, 3H, 4′-OCH$_3$); HRMS (ESI, TOF): m/z calculated for C$_{18}$H$_{18}$O$_5$I 441.0192; found 441.0199 [M+H].

L-CN. Yellow powder (0.546 g, 48%). ^{1}H NMR (600 MHz, DMSO-d6) δ 17. 50 (s, 1H, ArCOH) 8.27 (d, 2H, J = 6, 2-ArH) 8.02 (d, 2H, J = 6, 3-ArH) 7.41 (s, 2H, 2′-ArH) 7.39 (s, 1H, COCHCO) 3.87 (s, 6H, 3′-OCH$_3$) 3.74 (s, 3H, 4′-OCH$_3$); HRMS (ESI, TOF): m/z calculated for C$_{19}$H$_{18}$NO$_5$ 340.1175; found 340.1185 [M+H].

B-F. Yellow powder (0.274 g, 69%). ^{1}H NMR (600 MHz, CDCl$_3$) δ 8.10 (d, 2H, J = 6, 3,5-ArH) 7.28 (s, 2H, 2′-ArH) 7.18 (d, 2H, J = 6, 2,6-ArH), 7.01 (s, 1H, COCHCO) 3.97 (s, 3H, 4′-OCH$_3$) 3.94 (s, 6H, 3′-OCH$_3$); HRMS (ESI, TOF): m/z calculated for C$_{18}$H$_{16}$BO$_5$F$_2$ 361.1058; found 361.1059 [M-F].

B-I. Yellow powder (0.221 g, 39%). ^{1}H NMR (600 MHz, CDCl$_3$) δ 8.09-8.04 (m, 4H, 2,3-ArH) 7.85 (s, 1H, COCHCO) 7.58 (s, 2H, 2′-ArH) 3.91 (s, 6H, 3′-OCH$_3$) 3.82 (s, 3H, 4′-OCH$_3$); HRMS (ESI, TOF): m/z calculated for C$_{18}$H$_{16}$BO$_5$FI 469.0123; found 469.0120 [M-F].

B-CN. Orange powder (0.256 g, 75%). ^{1}H NMR (600 MHz, CDCl$_3$) δ 8.18 (d, 2H, J = 6, 2-ArH) 7.82 (d, 2H, J = 6, 3-ArH) 7.34 (s, 2H, 2′-ArH) 7.08 (s, 1H, COCHCO) 4.01 (s, 3H, 4′-OCH$_3$) 3.96 (s, 6H, 3′-OCH$_3$); HRMS (ESI, TOF): m/z calculated for C$_{19}$H$_{16}$BO$_5$F 368.1100; found 368.1106 [M-F].

Full computational details

L-F
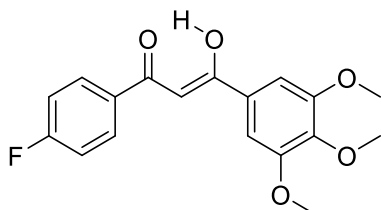
E(TD-HF/TD-KS) = -1172.23552818 a.u.
Dipole Moment = 3.57 Debye

C	4.93036	-1.18976	0.21524
C	6.15977	-0.55508	0.37632
C	5.06606	1.6029	0.05233
C	3.84234	0.95041	-0.09838
C	3.75571	-0.45104	-0.01717
H	4.86667	-2.27092	0.27212
H	2.9619	1.55068	-0.29944
C	2.47162	-1.19629	-0.18072
C	1.21106	-0.50735	-0.1219
H	1.18556	0.55006	0.09374
O	2.5218	-2.44985	-0.3524
C	0.01527	-1.18548	-0.27863
C	-1.31999	-0.55914	-0.22165
C	-1.47378	0.83328	-0.33158
C	-2.44319	-1.38412	-0.05304
C	-2.75071	1.39854	-0.266
H	-0.61204	1.46593	-0.49571
C	-3.72021	-0.81845	0.0207
H	-2.30294	-2.4531	0.02817
O	0.00105	-2.50438	-0.48043
H	5.14547	2.68289	-0.0164
H	7.07019	-1.11521	0.56387
H	0.9709	-2.79676	-0.46806
O	-5.13865	1.12209	-0.08705
C	-3.88228	0.57673	-0.08504
C	-5.61023	1.57109	1.19678
H	-6.60991	1.97549	1.02682
H	-5.66459	0.73261	1.90028
H	-4.95646	2.35466	1.5953
C	6.1978	0.83249	0.29073

```
F              7.39416   1.46291   0.444
C             -1.91      3.62729  -0.55924
H             -1.215     3.5803    0.28753
H             -1.37676   3.41015  -1.49214
H             -2.3518    4.62278  -0.61489
C             -4.77519  -2.95494   0.29889
H             -4.34792  -3.39016  -0.61186
H             -4.17689  -3.25002   1.1688
H             -5.80087  -3.30356   0.42452
O             -4.8661   -1.53169   0.19563
O             -3.00803   2.73152  -0.37381
```
Excitation energies and oscillator strengths:

Excited State   1:   Singlet-A   3.3575 eV 369.27 nm f=0.6435 <S**2>=0.000
      86 -> 88   0.13624
      87 -> 88   0.68949
This state for optimization and/or second-order correction.
Total Energy, E(TD-HF/TD-KS) = -1172.23552818
Copying the excited state density for this state as the 1-particle RhoCI density.

Excited State   2:   Singlet-A   3.4658 eV 357.74 nm f=0.1038 <S**2>=0.000
      86 -> 88   0.68626
      87 -> 88   -0.13669

Excited State   3:   Singlet-A   3.8331 eV 323.46 nm f=0.0020 <S**2>=0.000
      82 -> 88   -0.20486
      83 -> 88   0.61374
      84 -> 88   -0.25345
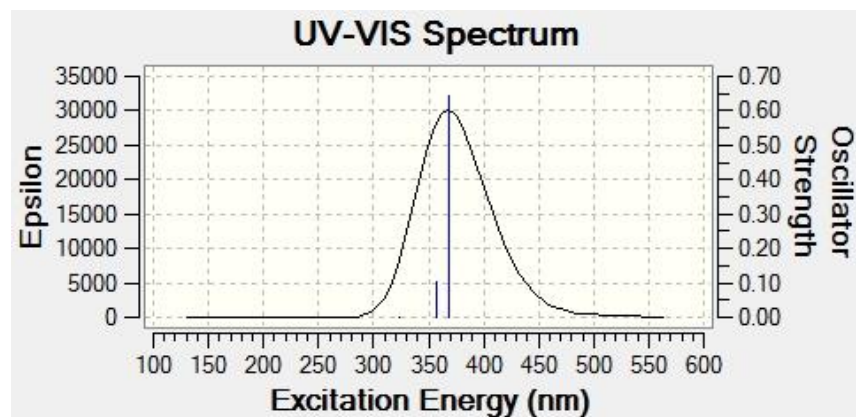
L-I
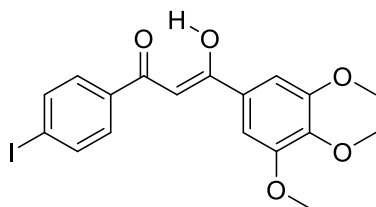
E(TD-HF/TD-KS) = -1083.80361832 a.u.
Dipole Moment = 3.8914 Debye

C	3.05986	-1.95155	0.06811
C	4.35936	-1.45595	0.17424
C	3.51433	0.79336	-0.20505
C	2.21782	0.28327	-0.29912
C	1.97129	-1.09301	-0.16178
H	2.87818	-3.01634	0.1692
H	1.40898	0.97733	-0.50079
C	0.6028	-1.68895	-0.26009
C	-0.56421	-0.85321	-0.19735
H	-0.45641	0.20792	-0.03202
O	0.50269	-2.94543	-0.37886
C	-1.8372	-1.39055	-0.28569
C	-3.08627	-0.60781	-0.21578
C	-3.07637	0.7895	-0.36929
C	-4.29464	-1.28641	0.00968
C	-4.27396	1.50545	-0.28838
H	-2.15147	1.30886	-0.57946
C	-5.4927	-0.56935	0.10057
H	-4.28029	-2.36145	0.12398
O	-2.01197	-2.7054	-0.4259
H	3.68436	1.85807	-0.32197
H	5.1849	-2.13468	0.36107
H	-1.08364	-3.1103	-0.4328
O	-6.67305	1.51982	-0.02342
C	-5.48963	0.83227	-0.04452
C	-6.97941	2.17777	1.2196
H	-7.94028	2.6737	1.06913
H	-7.06492	1.44361	2.02917
H	-6.21276	2.92039	1.46428
C	4.57406	-0.08218	0.03713
C	-3.18972	3.60688	-0.70348
H	-2.47234	3.51421	0.12065
H	-2.7219	3.29024	-1.64307
H	-3.51481	4.64432	-0.78969
C	-6.785	-2.55612	0.46688

H	-6.43864	-3.05995	-0.44294
H	-6.20107	-2.90082	1.32841
H	-7.84073	-2.77713	0.62837
O	-6.7091	-1.13542	0.32839
O	-4.37596	2.85483	-0.44084
I	6.56565	0.69989	0.20188

Excitation energies and oscillator strengths:

Excited State   1:   Singlet-A   3.2374 eV 382.97 nm f=0.7612 <S2>=0.000**
 86 -> 87   0.69390

Excited State   2:   Singlet-A   3.3669 eV 368.24 nm f=0.0949 <S**2>=0.000
  85 -> 87   0.69362

Excited State   3:   Singlet-A   3.7808 eV 327.93 nm f=0.0183 <S**2>=0.000
  80 -> 87   0.55558
  81 -> 87   0.28967
  82 -> 87   -0.20521
  84 -> 87   -0.20853
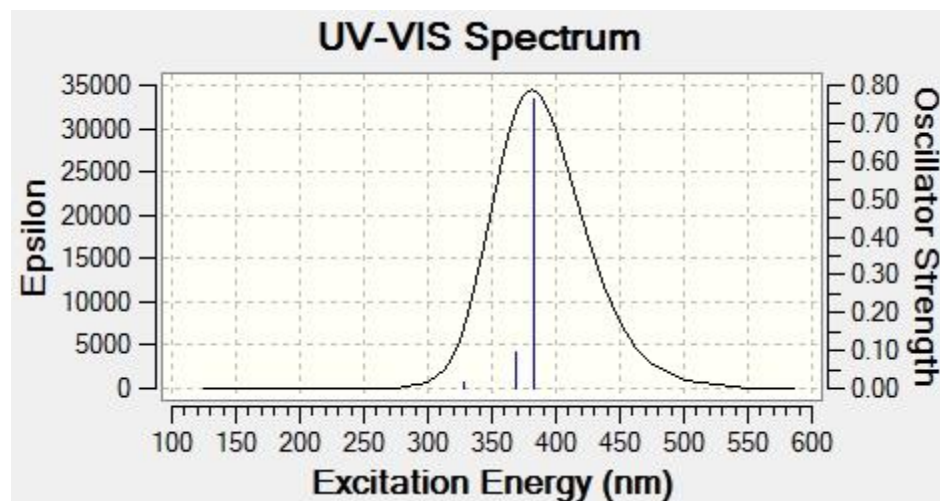
L-CN
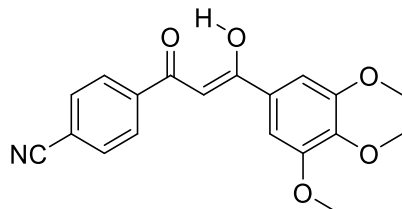
E(TD-HF/TD-KS) = -1165.27154165   a.u.
Dipole Moment = 5.2030 Debye

292

C	4.65547	-1.40272	0.24644
C	5.90048	-0.80398	0.40283
C	4.90445	1.3638	-0.09899
C	3.66194	0.75241	-0.24189
C	3.52119	-0.63484	-0.06828
H	4.54619	-2.47438	0.37134
H	2.81013	1.36684	-0.51168
C	2.20697	-1.34107	-0.2212
C	0.9779	-0.60612	-0.15688
H	0.99548	0.45275	0.05259
O	2.22162	-2.59518	-0.38353
C	-0.24539	-1.2434	-0.29325
C	-1.55486	-0.56917	-0.22547
C	-1.65674	0.82764	-0.34335
C	-2.70599	-1.35105	-0.03822
C	-2.9106	1.44074	-0.26746
H	-0.77367	1.42602	-0.52166
C	-3.95974	-0.73733	0.04663
H	-2.60502	-2.42398	0.04931
O	-0.30667	-2.56088	-0.4833
H	5.00755	2.43435	-0.24309
H	6.77018	-1.40173	0.65586
H	0.64973	-2.89119	-0.48167
O	-5.30323	1.25552	-0.05896
C	-4.06966	0.66262	-0.06742
C	-5.74872	1.71957	1.2292
H	-6.73447	2.15961	1.06707
H	-5.82745	0.88264	1.93209
H	-5.06403	2.47863	1.62312
C	6.02844	0.58648	0.2304
C	-1.99299	3.63513	-0.58832
H	-1.289	3.56952	0.24969
H	-1.48066	3.39222	-1.52655
H	-2.39957	4.64537	-0.64592
C	-5.09197	-2.83001	0.35008
H	-4.69232	-3.2852	-0.56339
H	-4.49521	-3.14336	1.21461
H	-6.12864	-3.13847	0.48936
O	-5.12964	-1.40457	0.24041
O	-3.12008	2.78094	-0.38158
C	7.30914	1.21303	0.38841

N   8.34841 1.72191 0.51785

Excitation energies and oscillator strengths:

Excited State 1:   Singlet-A   3.0763 eV 403.03 nm f=0.5533 <S2>=0.000**
   88 -> 90   -0.11332
   89 -> 90   0.69486

.

Excited State 2:   Singlet-A   3.1679 eV 391.37 nm f=0.0667 <S**2>=0.000
   88 -> 90   0.69255
   89 -> 90   0.11411
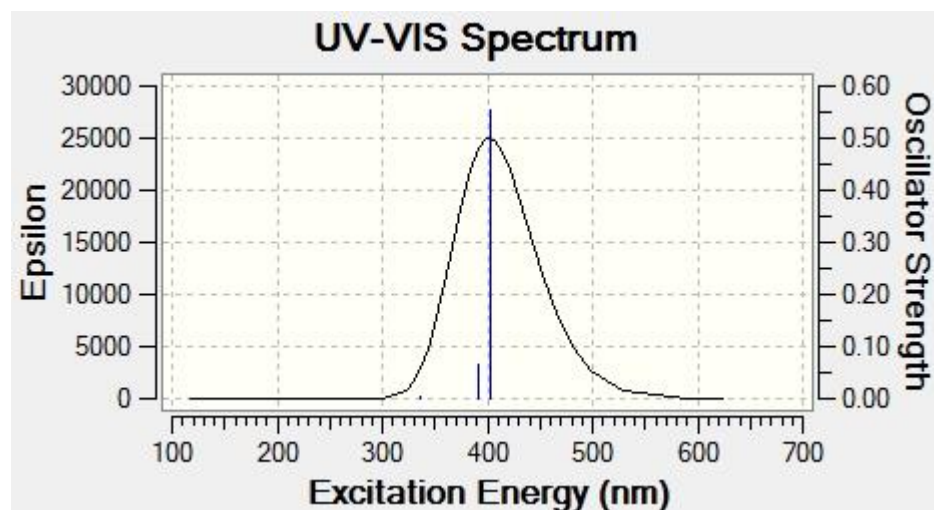
Excited State 3:   Singlet-A   3.6780 eV 337.09 nm f=0.0032 <S**2>=0.000
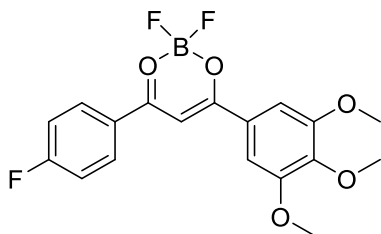   83 -> 90   0.15454
   84 -> 90   -0.28576
   85 -> 90   0.40053
   86 -> 90   0.46796

B-F

E(TD-HF/TD-KS) = -1396.48266073 a.u.
Dipole Moment = 9.5444 Debye

C	0.09129	0.73899	-0.09205
C	-1.06223	-0.0355	0.08702
H	-0.97827	-1.09113	0.28964
O	-0.00374	2.03295	-0.27115
C	-2.32144	0.55711	-0.03143
O	-2.43743	1.84997	-0.20887
B	-1.27853	2.7738	-0.06211
F	-1.37821	3.76861	-1.02212
F	-1.28501	3.30528	1.22956
C	-3.58911	-0.18788	0.01532
C	-4.79891	0.52262	0.14932
C	-3.62905	-1.59359	-0.07483
H	-4.77683	1.60398	0.21889
C	-4.84087	-2.27617	-0.02575
H	-2.71863	-2.16799	-0.20392
C	-6.01772	-0.14712	0.20295
C	-6.01013	-1.5351	0.11463
C	1.45411	0.19259	-0.11137
C	2.53578	1.08847	-0.06247
C	1.6812	-1.19466	-0.17871
C	3.84491	0.6018	-0.06617
H	2.33594	2.14947	-0.00844
C	2.98946	-1.68194	-0.19277
H	0.85213	-1.88446	-0.2532
C	4.08101	-0.78835	-0.12574
C	5.89564	-1.84074	0.99899
H	5.91127	-1.10479	1.8107
H	5.30763	-2.71561	1.29158
H	6.91544	-2.14267	0.7547
C	4.78492	2.80424	0.0431
H	4.26324	3.17201	-0.84773
H	4.23845	3.10192	0.94545
H	5.7943	3.21557	0.07311
O	5.3646	-1.24463	-0.20194
O	4.95407	1.38423	-0.01054
C	2.27064	-3.96607	-0.37238
H	1.63545	-3.94401	0.52089
H	1.66218	-3.8028	-1.26936
H	2.77107	-4.93231	-0.44152
O	3.3198	-2.99853	-0.28156
H	-4.88612	-3.3574	-0.10088
H	-6.9553	0.38759	0.3128

F   -7.19397 -2.19616   0.16415

Excitation energies and oscillator strengths:

Excited State   1:   Singlet-A   2.9339 eV 422.59 nm f=0.1352 <S**2>=0.000
     97 -> 99   0.56267
     98 -> 99   0.42458

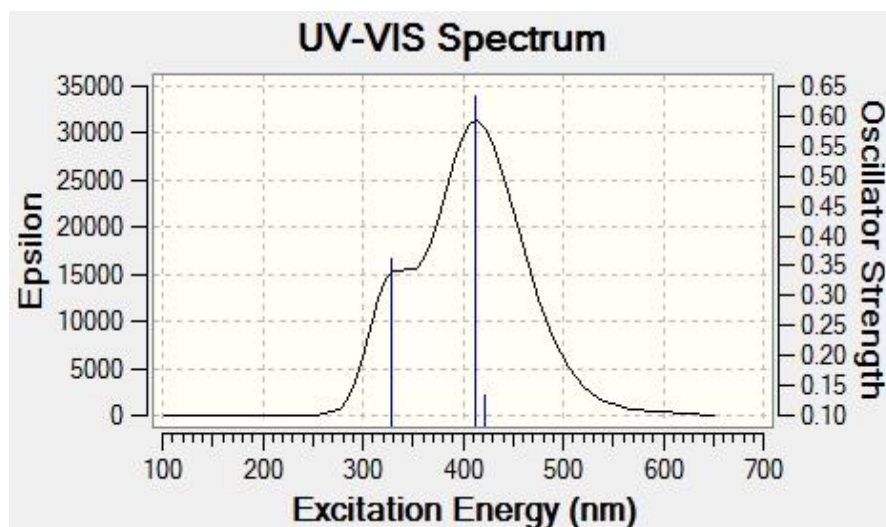Excited State   2:   Singlet-A   3.0045 eV 412.66 nm f=0.6320 <S**2>=0.000
     97 -> 99   -0.42349
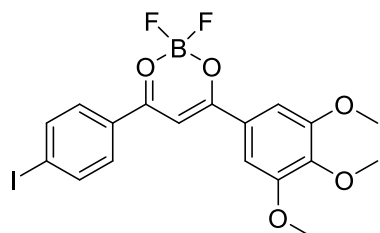   98 -> 99   0.56239

Excited State   3:   Singlet-A   3.7640 eV 329.39 nm f=0.3610 <S**2>=0.000
     96 -> 99   0.69662

B-I

E(TD-HF/TD-KS) = -1307.66525253 a.u.
Dipole Moment = 10.2715 Debye

C   1.76134   0.93916 -0.10632
C   0.48548   0.37593   0.04028
H   0.3781   -0.68148   0.22121

O	1.89683	2.23189	-0.26202
C	-0.64659	1.18335	-0.07995
O	-0.53252	2.47866	-0.2383
B	0.76777	3.18392	-0.06928
F	0.86098	4.18349	-1.02547
F	0.83377	3.70495	1.22532
C	-2.02779	0.67159	-0.05309
C	-3.09631	1.5805	0.06152
C	-2.31391	-0.70372	-0.13969
H	-2.8902	2.6428	0.12803
C	-3.62924	-1.1622	-0.10429
H	-1.51886	-1.43257	-0.25307
C	-4.41541	1.13204	0.10136
C	-4.67129	-0.2391	0.02014
C	3.00694	0.16264	-0.11395
C	4.2285	0.85332	-0.02953
C	2.98798	-1.24181	-0.20673
C	5.43169	0.14366	-0.0212
H	4.21652	1.93184	0.04405
C	4.19012	-1.95171	-0.21127
H	2.0523	-1.77333	-0.30892
C	5.42085	-1.26594	-0.10556
C	6.97559	-2.68483	1.01043
H	7.085	-2.01026	1.86718
H	6.23342	-3.45793	1.22855
H	7.9372	-3.14573	0.77866
C	6.74294	2.14347	0.14319
H	6.31324	2.60926	-0.751
H	6.23886	2.52196	1.03997
H	7.80825	2.36958	0.19855
O	6.60651	-1.93655	-0.16573
O	6.65957	0.7171	0.06941
C	3.08496	-4.07104	-0.44709
H	2.45092	-3.95114	0.43923
H	2.52671	-3.79143	-1.34817
H	3.4096	-5.10895	-0.52682
O	4.28545	-3.30364	-0.3277
H	-3.83056	-2.22516	-0.17777
H	-5.2254	1.84697	0.197
I	-6.69243	-0.94248	0.0871

Excitation energies and oscillator strengths:

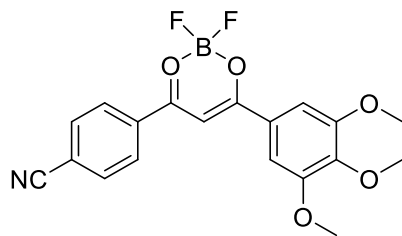Excited State   1:   Singlet-A   2.8223 eV 439.30 nm f=0.3660 <S**2>=0.000
        96 -> 98   0.43385
        97 -> 98   0.55518

Excited State   2:   Singlet-A   2.8820 eV 430.20 nm f=0.4715 <S**2>=0.000
        96 -> 98   0.55502
        97 -> 98   -0.43031

Excited State   3:   Singlet-A   3.4424 eV 360.17 nm f=0.3072 <S**2>=0.000
        95 -> 98   0.69759
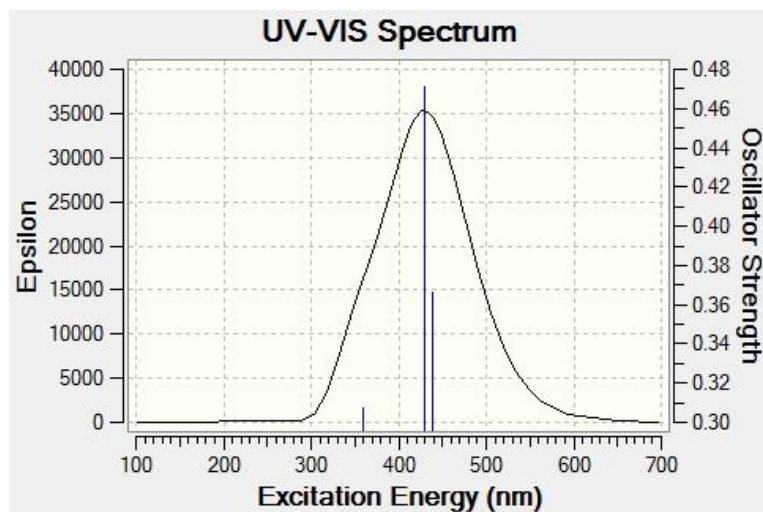
B-CN

E(TD-HF/TD-KS) = -1389.48793883   a.u.
Dipole Moment = 9.2662 Debye

C   0.32055   0.79637 -0.09546
C   -0.87507   0.07576   0.06884
H   -0.84679 -0.98453   0.26235
O   0.28614   2.09234 -0.26109
C   -2.09646   0.7329   -0.04726
O   -2.15569   2.02982 -0.2151
B   -0.95379   2.89917 -0.06758
F   -0.99609   3.88698 -1.03687
F   -0.9418   3.43773   1.21898

C	-3.40494	0.04662	-0.00369
C	-4.57222	0.81176	0.17609
C	-3.51234	-1.34962	-0.14206
H	-4.49483	1.88762	0.28081
C	-4.7547	-1.97091	-0.09436
H	-2.63285	-1.96095	-0.3091
C	-5.81906	0.19916	0.22926
C	-5.91388	-1.19711	0.09464
C	1.65204	0.18388	-0.11143
C	2.77758	1.02456	-0.05629
C	1.80888	-1.2134	-0.18164
C	4.05992	0.4727	-0.05513
H	2.63083	2.09416	0.00007
C	3.09058	-1.76611	-0.19163
H	0.94651	-1.8602	-0.26198
C	4.22575	-0.92846	-0.11523
C	5.96916	-2.10259	1.00622
H	6.01617	-1.38972	1.83699
H	5.33127	-2.95113	1.26938
H	6.97345	-2.45277	0.76264
C	5.11088	2.62366	0.06471
H	4.61421	3.02054	-0.82789
H	4.57554	2.94612	0.96513
H	6.14006	2.98175	0.10165
O	5.48501	-1.44521	-0.1833
O	5.20662	1.19673	0.00744
C	2.25805	-4.01041	-0.38103
H	1.62074	-3.95555	0.50923
H	1.66348	-3.81672	-1.28118
H	2.70956	-5.00056	-0.44757
O	3.35448	-3.09675	-0.28516
H	-4.83202	-3.04696	-0.20791
H	-6.71483	0.79372	0.37442
C	-7.1974	-1.83637	0.1455
N	-8.23815	-2.3561	0.18701

Excitation energies and oscillator strengths:

Excited State   1:   Singlet-A   2.7403 eV 452.44 nm f=0.0711 <S**2>=0.000
    99 ->101   0.60870
    100 ->101   -0.35518

Excited State   2:   Singlet-A   2.8173 eV 440.08 nm f=0.6199 <S**2>=0.000
    99 ->101   0.35471
    100 ->101   0.60928

Excited State   3:   Singlet-A   3.6905 eV 335.96 nm f=0.5341 <S**2>=0.000

299

```
98 ->101        0.68925
100 ->102        0.12864
```
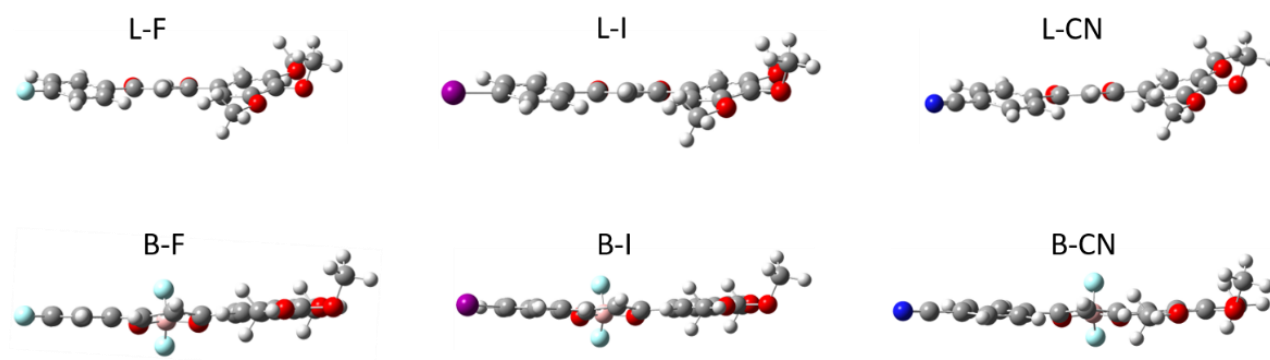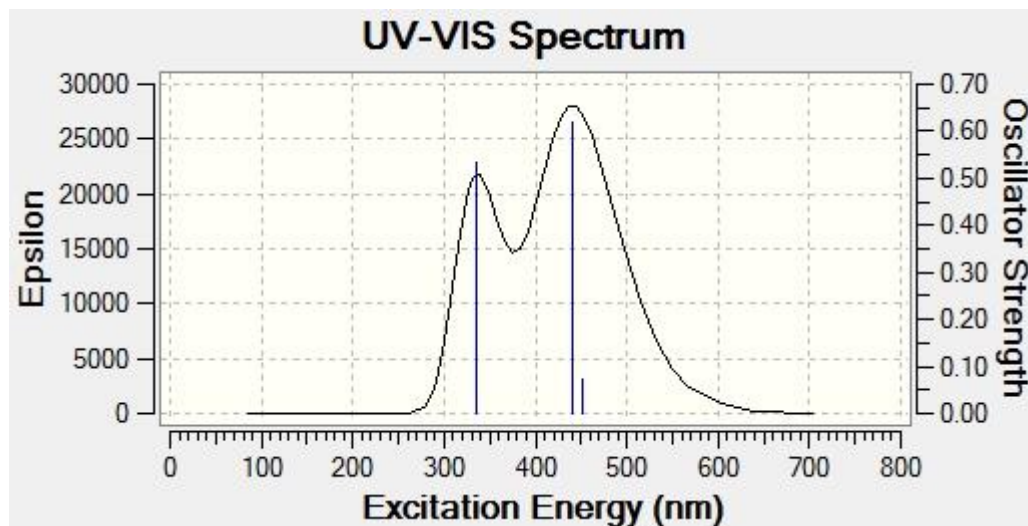

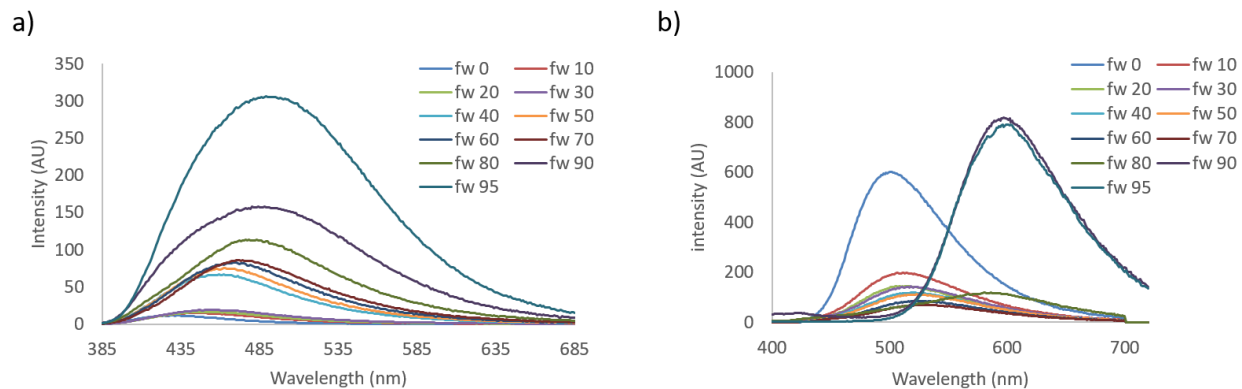**Figure S6.1.** Optimized geometries in dichloromethane for trimethoxy substituted ligands and boron complexes.

Figure S6.2. Emission spectra of L-F (a) and B-F (a) dissolved in THF/H$_2$O solutions with different H$_2$O fractions. (λ_{ex} = 369 nm)
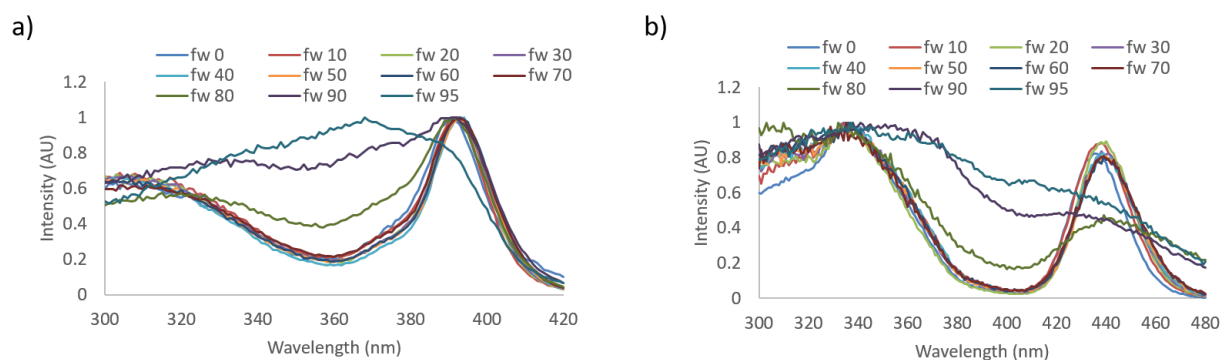

Figure S6.3. Excitation spectra of L-F (a) and B-F (b) dissolved in THF/H$_2$O solutions with different H$_2$O fractions. Excitation was monitored at the peak emission wavelength of each solution. (λ_{ex} = 369 nm)
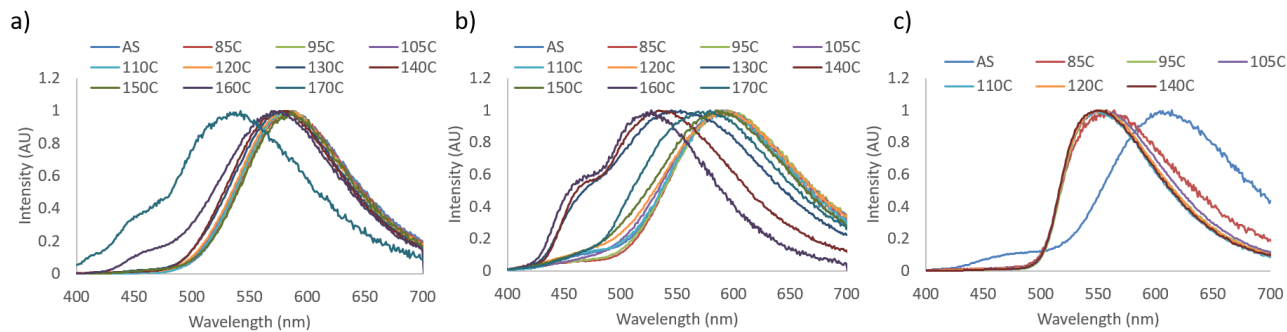
Figure S6.4. Emission spectra of B-F (a), B-I (b), and B-CN (c) glass films heated at different temperatures for 10 min. (λ_{ex} = 369 nm)
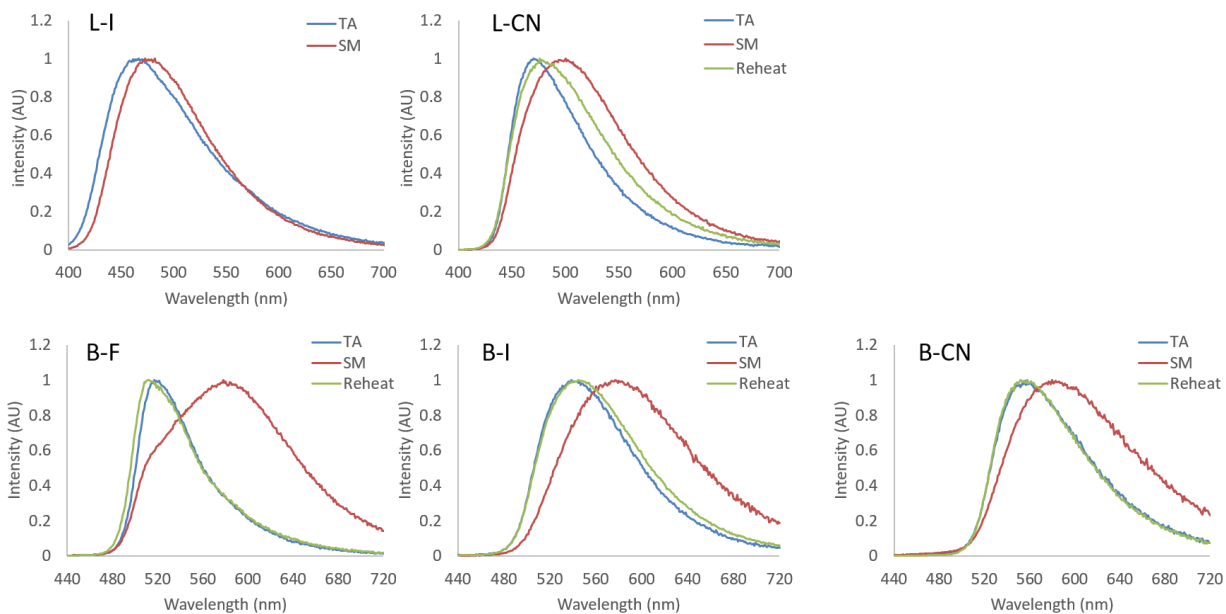
Figure S6.5. Normalized emission spectra of weigh paper films in the thermally annealed (TA), smeared (SM), and reheated states. (λ_{ex} = 369 nm)

Table S6.1. Optical Properties of Weigh Paper Films.[a]

	Thermally Annealed	Smeared	Reheat

	λ_{em}^{b}	FWHM[c]	λ_{em}^{b}	FWHM[c]	λ_{em}^{b}	FWHM[c]
L-I	467	107	482	103		
L-CN	470	81	500	112	476	99
B-F	517	60	578	142	511	63
B-I	539	95	577	129	545	101
B-CN	558	94	580	131	552	93

[a] **Excited at 369 nm, room temperature, air**
[b] **Emission maximum**
[c] **Full width at half maximum**

Appendix F

Chapter 7 Supporting Information

Synthetic Details

Scheme S7.1. Synthetic pathway for phenyl substituted diketones
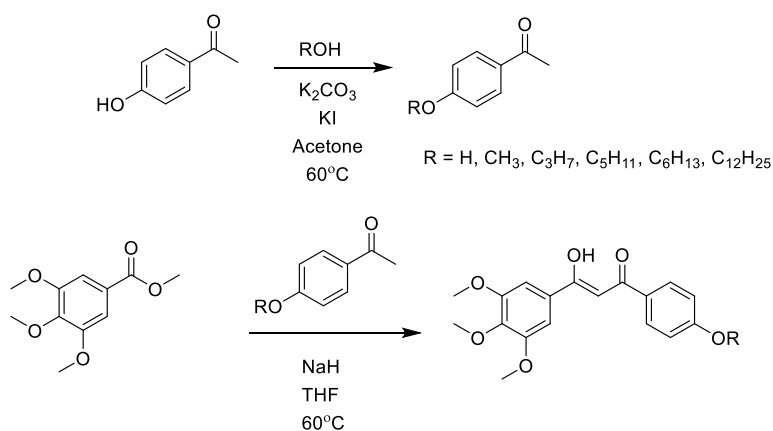
Synthesis. The alkoxy-substituted β-diketones were prepared by Claisen condensation with NaH as previously described.[1] The trimethoxy-substituted ester (methyl 3,4,5-trimethoxy benzoate) was combined with the corresponding para alkylated ketone, prepared via Williamson ether synthesis.[2]

PC3. Colorless crystalline powder (0.687 g, 39%). ^{1}H NMR (600 MHz, DMSO-d6) δ 17.50 (s, 1H, ArCOH) 8.11 (d, 2H, J = 6, 2-ArH) 7.37 (s, 2H, 2′-ArH) 7.18 (s, 1H, COCHCO) 7.04 (d, 2H, J = 6, 3-ArH) 3.99 (t, 2H, J = 9, OCH_2C$_2$H$_6$) 3.87 (s, 6H, 3′-OCH$_3$) 3.72 (s, 3H, 4′-OCH$_3$) 1.71 (m, 2H, J = X, OCH$_2$CH_2CH$_3$) 0.95 (t, 3H, J = 9, OC$_2$H$_4$CH_3); HRMS (ESI, TOF): m/z calculated for C$_{21}$H$_{25}$O$_6$ 373.1646; found 373.1651 [M+H].

PC5. Colorless crystalline powder (1.415 g, 0.47%). ^{1}H NMR (600 MHz, DMSO-d6) δ 17. 50 (s, 1H, ArCOH) 8.11 (d, 2H, J = 6, 2-ArH) 7.37 (s, 2H, 2′-ArH) 7.19 (s, 1H, COCHCO) 7.04 (d, 2H, J = 6, 3-ArH) 4.00 (d, 2H, J = 9, OCH_2C$_4$H$_9$) 3.87 (s, 6H, 3′-OCH$_3$) 3.72 (s, 3H, 4′-OCH$_3$) 1.73-1.69 (m, 2H, OCH$_2$CH_2C$_3$H$_7$) 1.39-1.29 (m, 4H, OC$_2$H$_4$C$_2$H$_4$CH$_3$) 0.86 (t, 3H, J = 9, OC$_4$H$_8$CH_3). HRMS (ESI, TOF): m/z calculated for C$_{23}$H$_{29}$O$_6$ 401.1952; found 401.1964 [M+H].

PC6. Colorless crystalline powder (0.806 g, 27%) ^{1}H NMR (600 MHz, DMSO-d6) δ 17. 50 (s, 1H, ArCO*H*) 8.10 (d, 2H, J = 6, 2-ArH) 7.37 (s, 2H, 2′-ArH) 7.18 (s, 1H, COCHCO) 7.04 (d, 2H, J = 6, 3-ArH) 4.00 (d, 2H, J = 9, OCH2) 3.86 (s, 6H, 3′-OCH3) 3.72 (s, 3H, 4′-OCH3) 1.70-1.68 (m, 2H, OC*H2*C5H11) 1.38-1.35 (m, 2H, OCH2C*H2*C4H9) 1.27-1.24 (m, 4H,C3H6C2*H4*CH3) 0.84 (t, 3H, J = 9, OC5H10C*H3*); HRMS (ESI, TOF): m/z calculated for C24H31O6 415.2112; found 415.2121 [M+H].

PC12. Colorless crystalline powder (1.016 g, 0.43%) ^{1}H NMR (600 MHz, CDCl3) δ 17. 09 (s, 1H, ArCO*H*) 7.95 (d, 2H, J = 6, 2-ArH) 7.33 (s, 1H, COCHCO) 7.20 (s, 2H, 2′-ArH) 6.96 (d, 2H, J = 6, 3-ArH) 4.02 (d, 2H, J = 9, OC*H2*C4H9) 3.90 (s, 3H, 4′-OCH3) 3.88 (s, 6H, 3′-OCH3) 1.81-1.77 (m, 2H, OCH2C*H2*C10H11) 1.47-1.43 (m, 2H, OC2H4C*H2*C9H18CH3) 1.36-1.25 (m, 16H, OC3H6*C8H16*CH3) 0.86 (t, 3H, J = 9, OC11H22C*H3*); HRMS (ESI, TOF): m/z calculated for C30H43O6 499.3055; found 499.3060 [M+H].

Scheme S7.2. Synthetic Pathway for Phenyl-substituted Diketones
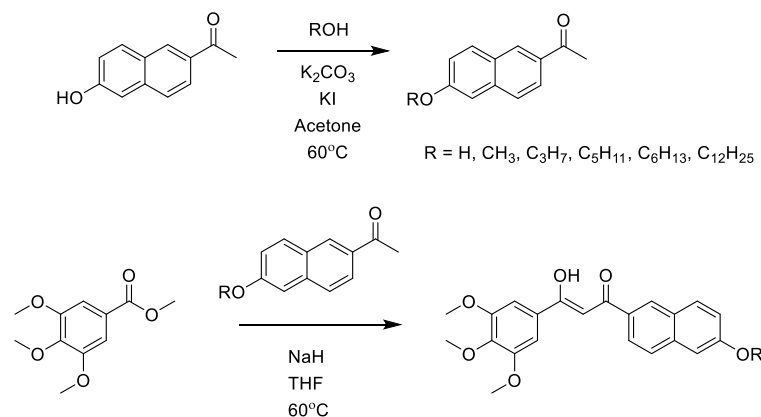
NH. Tan powder (0.517 g, 53%). ^{1}H NMR (600 MHz, CDCl3) δ 16.93 (s, 1H, ArCO*H*) 7.96 (s, 1H, 2-ArH) 7.95-7.94 (m, 1H, 4-ArH) 7.54-7.51 (m, 1H, 9-ArH) 7.93 (d, 1H, J = 6, 10-ArH) 7.42 (s, 2H, 2′-ArH) 7.40 (s, 1H, 7-ArH) 6.74 (s, 1H, COCHCO) 7.24 (d, 1H, J = 6, 5-ArH) 3.89 (s, 6H, 3′-OCH3) 3.88 (s, 3H, 4-OCH3); HRMS (ESI, TOF): m/z calculated for C22H21O5 365.1380; found 365.1389 [M+H].

NC1. Tan powder (0.418 g, 46%). ^{1}H NMR (600 MHz, DMSO-d6) δ 17.10 (s, 1H, ArCO*H*) 8.69 (s, 1H, 2-ArH) 8.17 (d, 1H, J = 6, 4-ArH) 8.01 (d, 1H, J = 6, 9-ArH) 7.93 (d, 1H, J = 6, 10-ArH) 7.42 (s, 2H, 2′-ArH) 7.40 (s, 1H, 7-ArH) 7.37 (s, 1H, COCHCO) 7.24 (d, 1H, J = 6, 5-ArH) 3.89 (s, 6H, 3′-OCH3) 3.88 (s, 3H, 4-OCH3) 3.75 (s, 3H, 4′-OCH3); HRMS (ESI, TOF): m/z calculated for C23H23O6 395.1489; found 395.1495 [M+H].

NC3. Yellow powder (0.515 g, 41%). ^{1}H NMR (600 MHz, DMSO-d6) δ 17.10 (s, 1H, ArCO*H*) 8.43 (s, 1H, 2-ArH) 7.95 (d, 1H, J = 6, 4-ArH) 7.86 (d, 1H, J = 6, 9-ArH) 7.77 (d, 1H, J = 6, 10-ArH) 7.24 (s, 2H, 2′-ArH) 7.21 (d, 1H, J = 6, 5-ArH) 7.14 (s, 1H, 7-ArH) 6.85 (s, 1H, COCHCO)

4.05 (t, 2H, J = 9, OCH_2C$_2$H$_4$) 3.89 (s, 6H, 3′-OCH$_3$) 3.74 (s, 3H, 4′-OCH$_3$) 1.91-1.86 (m, 2H, OCH$_2$CH_2CH3) 1.08 (t, 3H, J = 9, OC$_2$H$_4$CH_3); HRMS (ESI, TOF): m/z calculated for C$_{25}$H$_{27}$O$_6$ 423.1803; found 423.1808 [M+H].

NC5. Tan powder (0.311 g, 35%). ^{1}H NMR (600 MHz, DMSO-d6) δ 17.10 (s, 1H, ArCOH) 8.44 (s, 1H, 2-ArH) 7.96 (d, 1H, J = 6, 4-ArH) 7.86 (d, 1H, J = 6, 9-ArH) 7.77 (d, 1H, J = 6, 10-ArH) 7.24 (s, 2H, 2′-ArH) 7.20 (d, 1H, J = 6, 5-ArH) 7.14 (s, 1H, 7-ArH) 6.85 (s, 1H, COCHCO) 4.09 (t, 2H, J = 9, OCH_2C$_4$H$_9$) 3.96 (s, 6H, 3′-OCH$_3$) 3.93 (s, 3H, 4′-OCH$_3$) 1.88-1.83 (m, 2H, OCH$_2$CH_2C$_3$H$_7$) 1.51-1.46 (m, 2H, OC$_2$H$_4$CH_2C$_2$H$_5$) 1.44-1.38 (m, 2H, OC$_3$H$_6$CH_2CH$_3$) 0.94 (t, 3H, J = 9, OC$_4$H$_8$CH_3); HRMS (ESI, TOF): m/z calculated for C$_{27}$H$_{31}$O$_6$ 451.2113; found 451.2121 [M+H].

NC6. Tan powder (0.730 g, 51%). ^{1}H NMR (600 MHz, DMSO-d6) δ 17.10 (s, 1H, ArCOH) 8.67 (s, 1H, 2-ArH) 8.15 (d, 1H, J = 6, 4-ArH) 7.98 (d, 1H, J = 6, 9-ArH) 7.90 (d, 1H, J = 6, 10-ArH) 7.41 (s, 2H, 2′-ArH) 7.37 (s, 1H, 7-ArH) 7.36 (s, 1H, COCHCO) 7.23 (d, 1H, 5-ArH) 4.08 (t, 2H, J = 9, OCH_2C$_5$H$_{11}$) 3.89 (s, 6H, 3′-OCH$_3$) 3.74 (s, 3H, 4′-OCH$_3$) 1.76-1.71 (m, 2H, OCH$_2$CH_2C$_4$H$_9$) 1.42-1.38 (m, 2H, OC$_2$H$_4$CH_2C$_3$H$_7$) 1.30-1.25 (m, 4H, C$_3$H$_6$C$_2$H$_4$CH$_3$) 0.84 (t, 3H, J = 9, OC$_5$H$_{10}$CH_3); HRMS (ESI, TOF): m/z calculated for C$_{28}$H$_{33}$O$_6$ 465.2271; found 465.2277 [M+H].

NC12. Tan powder (0.429 g, 29%). ^{1}H NMR (600 MHz, CDCl$_3$) δ 17.10 (s, 1H, ArCOH) 8.69 (s, 1H, 2-ArH) 8.17 (d, 1H, J = 6, 4-ArH) 8.00 (d, 1H, J = 6, 9-ArH) 7.91 (d, 1H, J = 6, 10-ArH) 7.42 (s, 2H, 2′-ArH) 7.40 (s, 1H, 7-ArH) 7.37 (s, 1H, COCHCO) 7.23 (d, 1H, 5-ArH) 4.10 (t, 2H, J = 9, OCH_2C$_{11}$H$_{23}$) 3.89 (s, 6H, 3′-OCH$_3$) 3.74 (s, 3H, 4′-OCH$_3$) 1.77-1.74 (p, 2H, J = X, OCH$_2$CH_2C$_{10}$H$_{21}$) 1.43-1.39 (m, 2H, OC$_2$H$_4$CH_2C$_9$H$_{19}$) 1.33-1.29 (m, 2H, OC$_3$H$_6$CH_2C$_8$H$_{17}$) 1.27-1.18 (m, 14H OC$_4$H$_8$C$_7$H$_{14}$CH$_3$) 0.82 (t, 3H, J = 9, OC$_{11}$H$_{22}$); HRMS (ESI, TOF): m/z calculated for C$_{34}$H$_{45}$O$_6$ 549.3212; found 549.3216 [M+H].
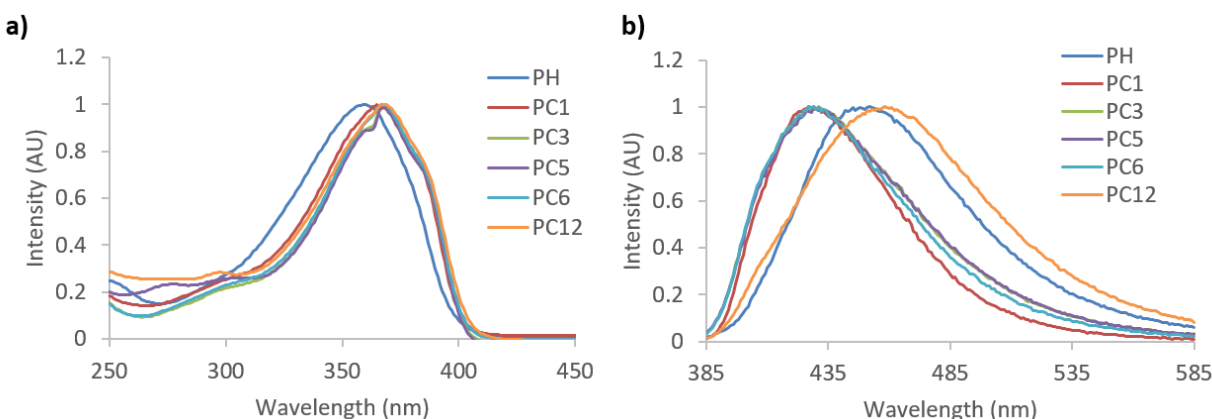

Figure S7.1. Absorption (a) and normallized emission (b) spectra of phenyl-substituted diketones. (λ_{ex} = 369 nm)

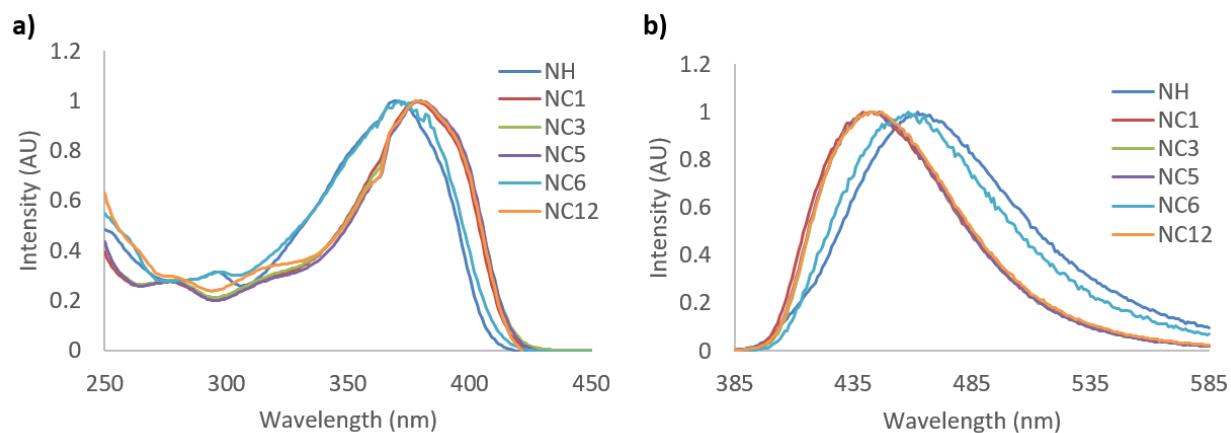**Figure S7.2**. Absorption (a) and normalized emission (b) spectra of phenyl substituted diketone. (λ_{ex} = 369 nm)

Table S1. Optical Properties of SCL Derivatives in Dichloromethane Solution. [a]

Compound	λ_{abs}[b] (nm)	ε ($M^{-1}cm^{-1}$)	λ_{em}[c] (nm)	Φ (%)	τ (ns)
PH	359	75000	452	0.9	0.28
PC1[d]	365	64000	427	0.3	0.31
PC3	367	63000	431	0.6	0.01
PC5	367	58000	429	0.7	0.28
PC6	367	54000	427	0.7	0.40
PC12	367	59000	458	1.0	0.29
NH	370	66000	462	2.0	0.31
NC1	378	65000	442	1.7	0.10
NC3	379	55000	442	1.9	0.10
NC5	380	81000	442	2.3	0.06
NC6	371	74000	458	1.5	0.15
NC12	379	57000	444	2.2	0.10

[a] Excited at 369 nm, room temperature, air, [b] Absorbance maximum, [c] Emission maximum, [d] Data taken from Ref 3.[3]
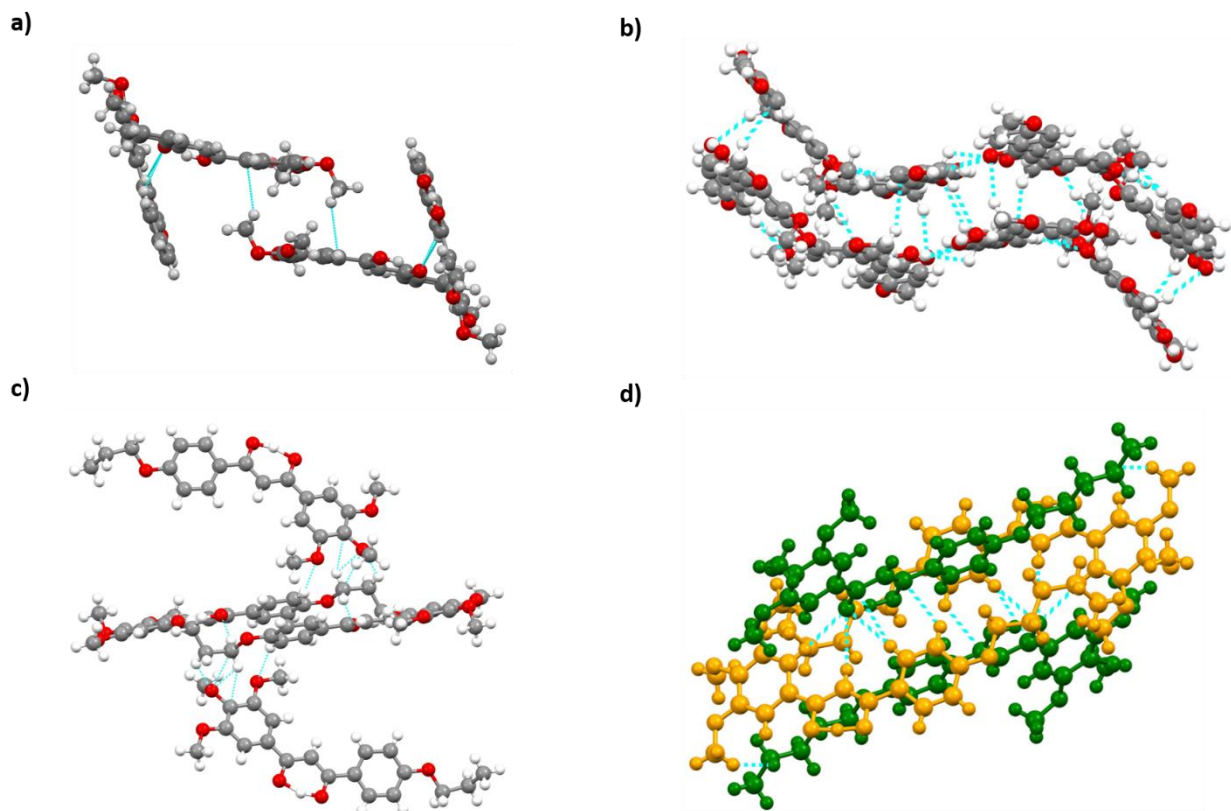
Figure S7.3. Unit cells of PH (a), PC1(b), PC3 (c) and PC5 (d). Green (α-PC5) and orange (β-PC5) were used to designate different molecualr conformations in the unit cell.
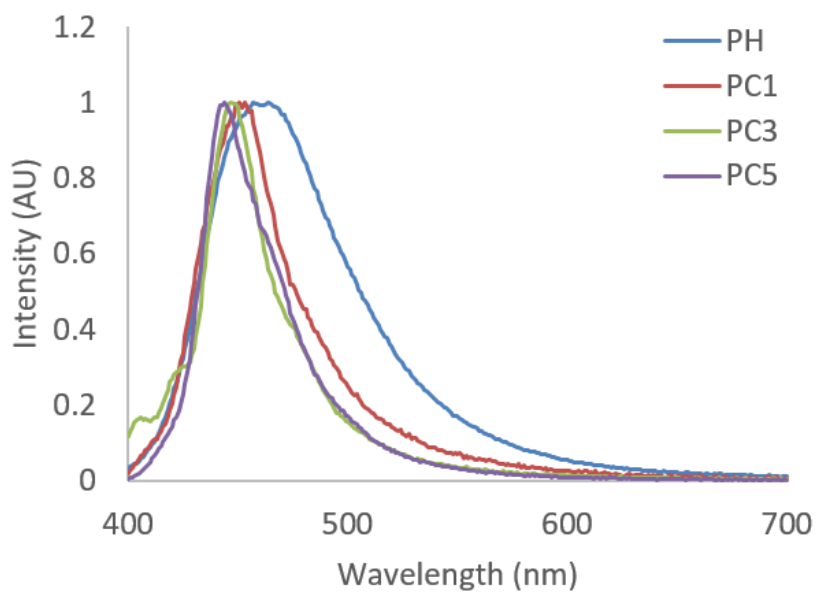

Figure S7.4. Normalized emission of single crystals. (λ_{ex} = 369 nm)